technische universität
dortmund

Advanced EPR Spectroscopic Investigation of Iron-Sulfur Clusters Along the Hydrogen Evolution Pathway

Dissertation submitted for the degree of

Doctor of Natural Sciences

Faculty of Chemistry and Chemical Biology

TU Dortmund

Melanie Heghmanns

Dortmund, August 2023

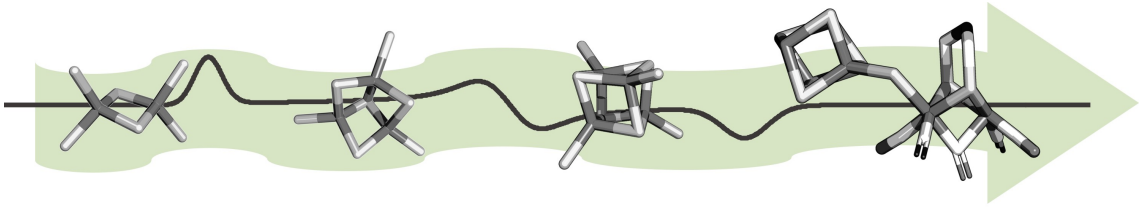

Abstract

Iron-sulfur (FeS) clusters are essential cofactors found in all living organisms. Acting as versatile electron carriers they are indispensable for life-sustaining processes, contributing to respiration, nitrogen fixation, and hydrogen production. Several proteins containing single and multiple FeS clusters are involved in the pathway to hydrogen evolution. Electron paramagnetic resonance (EPR) spectroscopy was used to characterize their FeS clusters providing valuable information about their magnetic properties, structural features, redox states, and biological function. Understanding and tuning the complex interplay of these proteins and their clusters is required for efficient biotechnological H_2 production to sustainably meet the requirements of the world's increasing energy demand.

The journey along the photobiological hydrogen evolution pathway starts with [2Fe2S] cluster-containing ferredoxins (Fdxs) found in the green alga *C. reinhardtii*. Under certain conditions, *Cr*Fdx1 accepts photosynthetic electrons and redirects them to the [FeFe]-hydrogenase HydA1, responsible for H_2 production. This crucial linkage suffers from competing metabolic pathways and limited electron transfers, with the latter being influenced by the difference in midpoint potential between the two redox partners. We established pulsed EPR monitored redox potentiometry, performed at higher frequencies than usual, for determining the midpoint potentials of Fdxs and variants. Exchanging a single amino acid residue in *Cr*Fdx1 fine-tuned the midpoint potential of its [2Fe2S] cluster by approximately 170 mV. Additionally, the [4Fe4S] cluster of catalytically inactive apo-HydA1 was investigated. The observation of multiple paramagnetic species for one cluster led to a comparison with apo-HydA2, suggesting structural differences as the cause of their presence. Continuing along the path, the *in vivo* formation of a fully active hydrogenase requires apo-HydA1 to be maturated in a multi-step process. The exact role and magnetic properties of one of the involved enzymes, the maturase HydF, are still highly debated. The performed EPR investigation of HydF confirmed some unusual features observed for the single [4Fe4S] cluster but raised further questions.

After gaining insight into single cluster-containing FeS proteins, the characterization of fully maturated and more complex [FeFe]-hydrogenases harboring multiple distinct FeS clusters was addressed. One of the main drawbacks of efficient hydrogen production is the oxygen sensitivity of the H-cluster. A newly discovered oxygen-protection mechanism in the [FeFe]-hydrogenase from *C. beijerinckii* led to a comprehensive EPR spectroscopic study, characterizing not only the H-cluster states but also discovering a new radical $R^{\bullet ox}$. Advanced spectroscopic methods explored its origin and function. Eventually, the spectral features of the [FeFe]-hydrogenase CpI from *C. pasteurianum* were revisited, revealing exchange interactions between the H-cluster and the neighbored [4Fe4S] cluster. Variants showed a change in the strength of the exchange coupling and were explored to investigate its effect on the biological function.

The studies presented in this thesis, including the fine-tuning of the midpoint potential of Fdxs, the discovery and characterization of an unusual radical signal and the investigation of exchange coupling interactions in [FeFe]-hydrogenases, shed light on the magnetic properties and functional roles of FeS clusters in essential electron transfer processes and hydrogen evolution pathways.

Zusammenfassung

Eisen-Schwefel-Cluster (FeS) sind essentielle Cofaktoren, die in allen lebenden Organismen vorkommen. Die vielseitigen Elektronenüberträger sind unverzichtbar für lebenserhaltende Prozesse und tragen so zur Atmung, Stickstofffixierung und Wasserstoffproduktion bei. Verschiedene FeS Proteine sind an der Wasserstoffproduktion beteiligt. Mit Hilfe der elektronenparamagnetischen Resonanzspektroskopie (EPR-Spektroskopie) wurden ihre FeS-Cluster charakterisiert, was Informationen über ihre magnetischen Eigenschaften, Struktur, Redoxzustände und biologischen Funktionen liefert. Das Verständnis und die Kontrolle über das komplexe Zusammenspiel dieser Proteine und ihrer Cluster ist für eine effiziente, biotechnologische Wasserstoffproduktion erforderlich um den Anforderungen des weltweit steigenden Energiebedarfs nachhaltig gerecht zu werden.

Der Weg zur photobiologischen Wasserstoffproduktion beginnt mit einfachen Ferredoxinen (Fdxn), die [2Fe2S] Cluster enthalten und in der Grünalge *C. reinhardtii* vorkommen. Unter bestimmten Bedingungen nimmt *Cr*Fdx1 photosynthetische Elektronen auf und leitet sie an die [FeFe]-Hydrogenase HydA1 weiter, die H_2 produziert. Diese Verbindung ist durch konkurrierende Stoffwechselwege und einem geringen Elektronentransfer eingeschränkt. Letzteres wird unter anderem durch den Unterschied der Redoxpotenziale zwischen den beiden Redoxpartnern kontrolliert. Zur Bestimmung der Redoxpotenziale von den Fdxn und ihren Varianten haben wir die Methode der gepulsten EPR-überwachten Redoxpotentiometrie, die mit höheren Frequenzen als üblich durchgeführt wurde, etabliert. Austausche eines einzelnen Aminosäurerests in *Cr*Fdx1 führten zu einer Feinjustierung des Redoxpotenzials des [2Fe2S] Clusters um 170 mV. Zusätzlich wurde das [4Fe4S] Cluster des katalytisch inaktiven apo-HydA1 Proteins untersucht. Die Detektierung mehrerer paramagnetischer Spezies bei nur einem Cluster führte zu einem Vergleich mit apo-HydA2, was auf strukturelle Unterschiede als Ursache für deren Vorhandensein hindeutete. Auf dem weiteren Weg Richtung Wasserstoffentwicklung, erfordert die Bildung einer aktiven Hydrogenase die *in vivo* Reifung von apo-HydA1. Die genaue Funktion und die magnetischen Eigenschaften eines der beteiligten Enzyme, der Maturase HydF, sind umstritten. Die durchgeführten EPR-Untersuchungen von HydF bestätigten einige der ungewöhnlichen Merkmale, die für das einzelne [4Fe4S] Cluster beobachtet wurden.

Nach einem Einblick in FeS-Proteine mit einzelnen Clustern, wurde als nächstes die Charakterisierung von aktiven und komplexeren [FeFe]-Hydrogenasen, die mehrere unterschiedliche FeS-Cluster enthalten, adressiert. Die Sauerstoffempfindlichkeit des H-Clusters ist einer der Nachteile für eine effiziente Wasserstoffproduktion. Ein neu entdeckter Sauerstoffschutzmechanismus in der [FeFe]-Hydrogenase von *C. beijerinckii* führte zu einer umfassenden EPR-spektroskopischen Studie, bei der nicht nur die H-Cluster-Zustände charakterisiert wurden, sondern auch ein neues Radikal, $R^{\bullet ox}$, entdeckt wurde. Dessen Ursprung und Funktion wurde durch fortschrittliche spektroskopische Methoden erforscht. Schließlich wurden die spektralen Eigenschaften der komplexen [FeFe]-Hydrogenase CpI aus *C. pasteurianum* erneut untersucht, wobei Austauschwechselwirkungen zwischen dem H-Cluster und dem benachbarten [4Fe4S] Cluster aufgedeckt wurden. Im direkten Vergleich zu sauerstoffresistenteren Varianten wurde der Einfluss der Austauschkopplung auf die biologische Funktion untersucht.

Die in dieser Arbeit vorgestellten Studien, einschließlich der Feinabstimmung des Redoxpotenzials von Fdxn, der Entdeckung und Charakterisierung eines ungewöhnlichen Radikalsignals und der Untersuchung von Austauschwechselwirkungen in [FeFe]-Hydrogenasen, beleuchten die magnetischen Eigenschaften und die funktionelle Rolle von FeS-Clustern in wichtigen Elektronentransferprozessen und Wasserstoffproduktionswegen.

List of Publications and Presentations

Publications in Peer-Reviewed Scientific Journals

- **Heghmanns, M.**, Rutz, A., Kutin, Y., Engelbrecht, V., Winkler, M., Happe, T. and Kasanmascheff, M., The oxygen-resistant [FeFe]-hydrogenase CbA5H harbors an unknown radical signal, Chemical Science, 2022, 13, 7289-7294.
- **Heghmanns, M.**, Günzel, A., Brandis, D., Kutin, Y., Engelbrecht, V., Winkler, M., Happe, T., and Kasanmascheff, M., Fine-tuning of FeS proteins monitored via pulsed EPR redox potentiometry at Q-band, Biophysical reports, 2021, 1 (2), 100016.

Oral Presentations

- Characterization of the oxygen-resistant [FeFe]-hydrogenase CbA5H using multi-frequency and isotope-sensitive EPR spectroscopy, Hydrogenase Christmas Online Meeting, **2022**.
- Pulsed EPR-Monitored Redox Potentiometry at Q-band: FeS cofactors fine-tuned by their protein environment, 14. Tag der Chemie, TU Dortmund, **2021**.
- EPR-monitored redox potentiometry at Q-band: identifying residue S43 in *Cr*Fdx1 for fine-tuning the midpoint potential, RESOLV Spring Meeting, **2021**.
- First characterization of the oxygen-stable [FeFe]-Hydrogenase from *Clostridium beijerinckii* via EPR spectroscopy, RESOLV Seminar, **2020**.

Poster Presentations

- [FeFe]-hydrogenase CpI revisited: modulation of intercluster exchange coupling as a tool for regulation of catalysis?, 13th International Conference on Hydrogenases, Walla Walla, Washington (USA), **2023**.
- Evidence for an unprecedented radical signal in the oxygen-resistant [FeFe]-hydrogenase CbA5H, 43rd FGMR Discussion Meeting, Karlsruhe (Germany), **and** Gordon Research Conference - Metallocofactors, Newport, Rhode Island (USA), **2022**.
- Evidence for a reversible radical signal in the oxygen-tolerant [FeFe]-hydrogenase CbA5H, RESOLV Klausurtagung, Bad Arolsen (Germany), **2022**.
- First EPR Spectroscopic Characterization of the O_2-tolerant Hydrogenase CbA5H: Discovery of an Unusual Radical, RESOLV Klausurtagung, Harsewinkel (Germany), **2021**.
- Characterization of plant-type ferredoxin isoforms via EPR spectroscopy, 8th EFEPR Summer School, Brno (Czech Republic), **2019**.
- Determination of redox potentials of plant-type ferredoxin isoforms via EPR spectroscopy, EUROISMAR, Berlin (Germany), **and** XIth Conference of the European Federation of EPR groups (EFEPR), Bratislava (Slovakia), **2019**.

Pleasure and pain, sometimes the same.

René Peter Baumann

Table of Contents

List of Figures

List of Tables

List of Abbreviations

C. acetobutylicum	*Clostridium acetobutylicum*
C. beijerinckii	*Clostridium beijerinckii*
C. pasteurianum	*Clostridium pasteurianum*
C. reinhardtii	*Chlamydomonas reinhardtii*
D. desulfuricans	*Desulfovibrio desulfuricans*
D. vulgaris	*Desulfovibrio vulgaris*
E. coli	*Escherichia coli*
M. elsdenii	*Megasphaera elsdenii*
P. furiosus	*Pyrococcus furiosus*
S. oleracea	*Spinacia oleracea*
Sh. oneidensis	*Shewanella oneidensis*
T. maritima	*Thermosipho maritima*
T. melanesiensis	*Thermosipho melanesiensis*
T. neapolitana	*Thermosipho neapolitana*
adt	azadithiolate
CW	continuous wave
DEER	Double Electron Electron Resonance
DFT	density functional theory
ENDOR	Electron Nuclear DOuble Resonance
EPR	electron paramagnetic resonance
ESE	electron spin echo
ET	electron transfer
Fdx	ferredoxin
FeS	iron-sulfur
FIC	potassium ferricyanide
FID	free induction decay
FNR	ferredoxin:$NADP^+$ reductase
FTIR	Fourier-transform infrared spectroscopy
HiPIPs	High Potential Iron-Sulfur Proteins
hs	high-spin
HYSCORE	Hyperfine Sublevel Correlation
ICP-AES	inductively coupled plasma atomic emission spectroscopy
MW	microwave
NaDT	sodium dithionite
NMR	nuclear magnetic resonance
NRVS	Nuclear Resonance Vibrational Spectroscopy
PCET	proton-coupled electron transfer
pdt	propanedithiolate
PTP	proton transfer pathway

RF	radio frequency
ROS	reactive oxygen species
S/N	signal-to-noise ratio
SAM	S-adenosyl-L-methionine
SHE	standard hydrogen electrode
SLBB	soluble-ligand binding β-grasp
SRT	shot repetition time
TIP	temperature-independent buffer
XAS	X-ray absorption spectroscopy

1

Introduction

In Earth's early history, when the atmosphere lacked oxygen and was predominantly reducing, the first cofactors of life emerged.[1] The wide availability of ferrous iron and sulfide likely enabled the spontaneous self-assembly of iron-sulfur (FeS) clusters within ancient proteins, which today represent the largest class of metalloproteins.[2] The simplest FeS cluster consists of a single iron atom ligated by four cysteine (Cys) residues embedded within a polypeptide environment. More frequently found forms are [2Fe2S], [3Fe4S] and [4Fe4S] clusters, where inorganic sulfide bridges the Fe ions (Figure 1.1).[3] The possible interconversion between cluster types underlines their modular nature.[4,5]

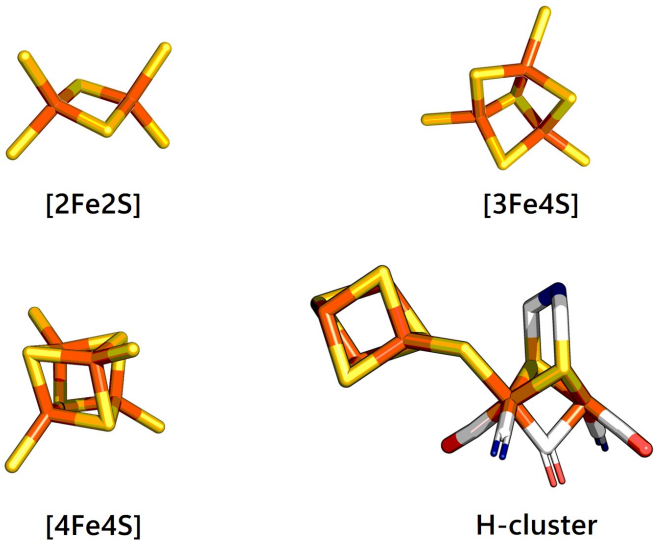

Figure 1.1: Structures of the most common FeS clusters and the H-cluster, which consists of a [4Fe4S] cluster bridged to a diiron subcluster carrying inorganic ligands from [FeFe]-hydrogenases. The crystal structures are derived from human ferredoxin 2 ([2Fe2S] cluster, PDB ID: 2Y5C), *Rhodopseudomonas palustris* HaA2 ferredoxin ([3Fe-4S] cluster, PDB ID: 4ID8), high potential FeS protein from *Thermochromatium tepidum* ([4Fe4S] cluster, PDB ID: 1IUA) and [FeFe]-hydrogenase CbA5H from *Clostridium beijerinckii* (H-cluster, PDB ID: 6TTL). Atomic colouring: Fe: orange, S: yellow, C: grey, O: red, N: blue.

During the course of evolution, the increasing accumulation of oxygen in the atmosphere posed a major challenge to organisms harboring FeS clusters.[6] Oxygen and derived species can decompose FeS clusters, which generates further damaging reactive oxygen species (ROS).[7–9] Therefore, these organisms had to develop mechanisms to protect their clusters from oxygen, resulting in oxygen-tolerant or oxygen-resistant enzymes.[10–13] Furthermore, subtle changes in the cluster's environment lead to a broad diversity of FeS clusters, which have efficiently adapted to specific functions.[2] The modular clusters eventually fused or evolved into higher-order

derivatives by incorporating metal ions and/or bridging ligands.[14,15] One classical example are [FeFe]-hydrogenases, which catalyze the reversible oxidation of molecular hydrogen (H_2) and are used for biotechnological hydrogen gas production.[16] The enzyme's active site contains an unusual [6Fe6S] cluster, consisting of a [4Fe4S] cluster bridged to a diiron subcluster carrying inorganic ligands (Figure 1.1).[17] Today, FeS clusters are ubiquitous throughout all living organisms catalyzing simple and multiple electron transfers (ETs), proton-coupled electron transfer (PCET), anchorage of external ligands or act as catalytic centers.[18–22] Their vulnerability to oxygen is exploited for sensing reactions and regulatory mechanisms induced by cluster changes, such as degradation, interconversions, or redox processes.[4,6,23–27]

Nevertheless, the ability to accept and donate electrons is the most frequent task performed and mainly involves the oxidation states Fe^{2+} and Fe^{3+}.[2] The respective redox enzymes, referred to as ferredoxins (Fdxs) (derived from 'ferrum' *lat.:* iron and 'redox'),[28,29] contain one or more FeS clusters, which effectively shuttle electrons between the clusters or catalytic centers and external redox partners. Multiple clusters can be found for example in the life-sustaining photosynthetic or mitochondrial respiratory chains, as well as complex [FeFe]-hydrogenases.[30,31] The clusters are typically spaced by 10 to 14 Å and form a relay for fast electron transfers.[32] The electron transfer rate is most efficient if the redox potential difference between redox couples is sufficiently small.[11,20] Thus, a wide range of redox potentials, spanning from -600 to +400 mV, is found for FeS clusters.[33]

Their role as one-electron transfer proteins usually conditions that at least one redox state of the FeS cluster is paramagnetic, i.e., having an unpaired electron. Simple [2Fe2S] clusters were first discovered more than six decades ago in reduced plant-type Fdxs *via* electron paramagnetic resonance (EPR) spectroscopy.[34–36] EPR spectroscopy allows for the investigation of electronic and magnetic properties, as well as structural features of paramagnetic systems. It has emerged as a powerful tool for the identification and characterization of all kinds of FeS proteins.[37–43] The application includes among others the deconvolution of multiple clusters in one enzyme,[44,45] the determination of midpoint potentials, identification of structural features with isotope-labeling, and distance determinations between clusters.[43–48]

1.1 Plant-type Ferredoxins from *Chlamydomonas reinhardtii*

Simple [2Fe2S] clusters are sometimes referred to as 'plant' or 'plant-type' ferredoxins but are also found in cyanobacteria and mammals.[49,50] The well-studied green microalga *Chlamydomonas reinhardtii* (*C. reinhardtii*) represents a model organism for the investigation of oxygenic photosynthesis within chloroplasts.[51,52] The alga harbors no less than 12 different plant-type Fdxs (Fdx1-12), which are only partially characterized to date regarding their biological function.[53–56] Their gene sequences exhibit conserved binding motifs required for [2Fe2S] cluster ligation.[57] The presence of multiple isoforms suggests that each of them has evolved distinctly, which is also reflected in their diverse functions.[54–56,58,59]

Fdx1 (also known as PetF) plays a central role in *C. reinhardtii* and is the most abundant isoform. In contrast, Fdx2-6 are expressed less than 1 % in cells.[60] Fdx1 was initially isolated and purified in 1966.[61] Its relatively negative midpoint potential of $-410\,\mathrm{mV}$ makes it an effective natural electron acceptor for photosystem I ($E_m = -550\,\mathrm{mV}$).[62,63] Photosystem I is an integral membrane protein involved in photosynthesis; a fundamental process in plants and algae converting light energy into chemical energy.[64–66] The light-harvesting complex absorbs energy from light through chlorophylls and pigments. Electrons excited in photosystem II are transferred through several intermediates in the thylakoid membrane to photosystem I (see Figure 1.2 for main reaction steps). A second excitation passes the electrons on to Fdx1, which distributes them to various metabolic pathways (Figure 1.2).[63,67] The missing electrons in photosystem II are replenished by water oxidation. The downhill movement of electrons is determined by the E_m difference between redox partners. Under photosynthetic conditions, the primary electron acceptor for Fdx1 is ferredoxin:NADP$^+$ reductase (FNR) ($E_\mathrm{m} = -320\,\mathrm{mV}$), which catalyzes the production of NADPH for carbon fixation.[63,66]

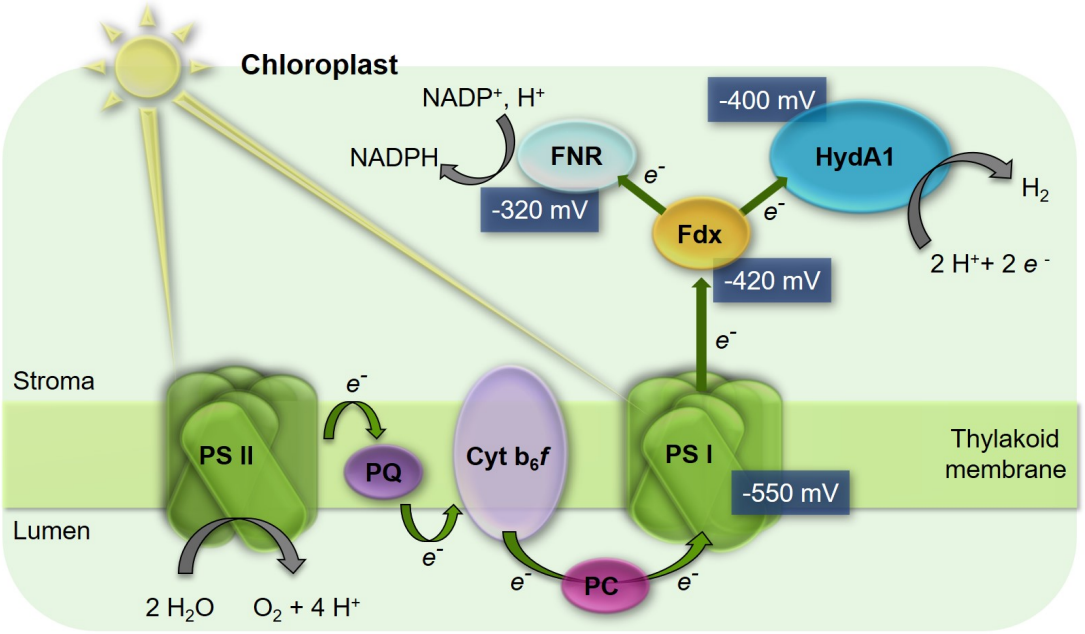

Figure 1.2: Scheme of the electron transfer chain during photosynthesis involving ferredoxin (Fdx) and redox partners. The electrons, generated from light-induced splitting of water, are transferred via photosystem II (PS II), plastoquinone (PQ), cytochrome b_6f (Cyt b_6f), plastocyanine (PC) and photosystem I (PS I) to Fdx, which acts as electron donor to ferredoxin:NADP$^+$ reductase (FNR) and [FeFe]-hydrogenase (HydA1) as well as other redox enzymes (not shown).

In addition, Fdx1 has been found to potentially interact with 78 other proteins, including thioredoxins, sulfite reductases, glutamate synthase, and the [FeFe]-hydrogenases HydA1 and HydA2,[53,68–70] which emphasizes the competitiveness of different metabolic pathways.[66]

Under anaerobic conditions, the electron flow is directed towards H_2 production, involving the [FeFe]-hydrogenases.[68,71] These enzymes facilitate the reversible reduction of H^+ to H_2 under various conditions.[69,72,73] The redirection of photosynthetic electrons mediated by Fdxs to hydrogen-producing enzymes plays a crucial role in the establishment of sustainable H_2 production from water and light as renewable energy sources by microalgae systems.[65,74,75] Therefore, many studies aimed to enhance the efficiency of the Fdx1-HydA1 interaction, as microalgal systems currently face challenges, such as low electron transfer rates and competition from native metabolic pathways like FNR.[76,77] The efficiency of electron transfer is thereby determined by several factors, such as the distance between the electron donor and acceptor, protein-protein interactions, and variations in midpoint potentials.[56]

The midpoint potential of biomolecules can be experimentally determined by different electrochemical techniques, such as direct electron transfer or protein film voltammetry.[78,79] The absorption of a protein onto an electrode surface, however, is challenging and may not reflect the natural environment. Moreover, the assignment of the outcoming current to a specific redox-active species in a multi-cofactor enzyme is uncertain. Another established method is redox potentiometry. This spectroelectrochemical approach provides the midpoint potential by applying defined potentials on the redox system of interest, while the undergoing spectral changes of the oxidation-reduction are monitored with spectroscopic methods, such as UV/Vis, Fourier-transform infrared spectroscopy (FTIR) or EPR spectroscopy.[48,80–82] EPR spectroscopy is advantageous for the unambiguous detection of paramagnets, the deconvolution of multiple species, and limits effects from background impurities by spectral simulations.

1.1.1 Factors Fine-tuning the Midpoint Potential in Ferredoxins

Most plant-type Fdxs exhibit a negative midpoint potential, E_m, of approximately $-400\,mV$, whereas adrenodoxins commonly have higher potentials.[83] Multiple factors can influence the E_m of [2Fe2S] clusters. One key role plays the type, redox state, and possible transitions of metal ions, which determine the range of achievable E_m values.[84] A change of charge or redox state on one metal ion will directly influence the E_m and redox states of neighboring metals, respectively, and affect the overall system. Another primary influence is induced by the coordinating ligands, which can change the geometry and electronic properties of the cluster.[84] This effect can, in particular, be observed for non-cysteine ligands, such as glutathione, S-adenosyl-L-methionine (SAM), or other protein-based residues.[85] Rieske [2Fe2S] clusters, for example, exhibit higher potentials compared to typical plant-type Fdxs. The E_m difference is attributed to the presence of fewer electron-donating histidine residues, which replace two cysteine ligands in Rieske Fdxs.[86,87] Conversely, the stabilization of higher oxidation states by hard ligands (higher charge and lower radii) decreases the E_m.[84]

While the modification of metal ions and ligating residues represents a major intervention with the risk of cluster loss, the secondary coordination sphere can be more easily manipulated (Figure 1.3). Therefore, several ferredoxins from distinct organisms have been targeted with site-directed

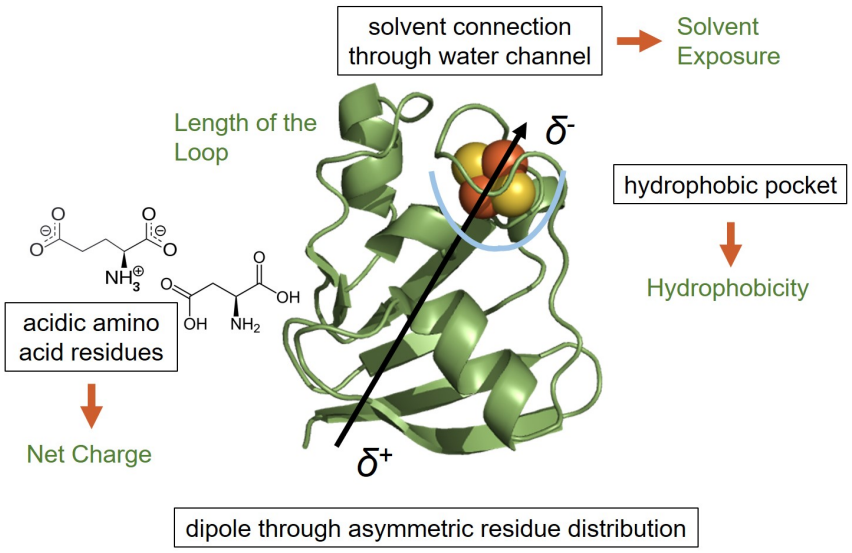

Figure 1.3: Crystal structure of *Cr*Fdx2 with the [2Fe2S] cluster depicted as spheres (PDB ID: 4ITK) and factors affecting its midpoint potential, E_m.

mutagenesis to define general concepts (see Table 1.1). However, the influence of those changes can be difficult to estimate and may affect or even prevent the interaction with redox partners. In the following, several secondary coordination sphere effects on the E_m are reviewed. First, long-range interactions are considered. The asymmetric arrangement of acidic amino acid residues on the protein surface induces a dipole with its negative end showing towards the [2Fe2S] cluster. The electrostatic distribution was shown to be important for interaction with external redox partners.[86] Additionally, exchanges of the N-terminus in *Arabidopsis thaliana* Fdx were found to alter the electronic properties at the active site by inducing conformational rearrangement at or in the vicinity of the cluster, resulting in an altered E_m.[84,88] Second, the [2Fe2S] cluster is embedded in a hydrophobic pocket, that increases the E_m due to greater destabilization of higher oxidation states.[84] This desolvation also accounts for the lower E_m values observed for more solvent-exposed organic model complexes.[84] Moreover, a solvent connection through a water channel in the C-terminal region of Fdxs facilitates the reduction of one Fe ion.[83] Thus, the introduction of bulky hydrophobic amino acids can potentially prevent solvent access to the cluster and cause an increase in the E_m as observed in *Bos taurus* N1a and *Thermosipho maritima* (*T. maritima*) HydC mutants.[80,89]

Third, hydrogen bonding is considered as one of the major determinants of the E_m.[84] In *Anabaena* sp. 7120 Fdx, a mutation of alanine at position 45 to serine increased the E_m in comparison to the wild-type enzyme by 24 mV. This increase is attributed to an additional H-bond from the hydroxyl group of serine to the sulfur atom of a ligating cysteine.[90] The decreased electron density on the sulfur ligand leads to a stabilization of the lower oxidation state and was supported by EPR spectroscopic data. An opposite effect is observed in bovine adrenodoxin, where the exchange of threonine leads to the removal of a H-bond and results in lower E_m values.[91] Similar observations were made in site-directed mutagenesis experiments in *Tm*HydC and *Spinacia oleracea* (*S. oleracea*) Fdx1.[80,92] Fourth, alterations of the electrostatic environment or net charge were observed in *So*Fdx1.[92] The exchange of the negatively charged glutamic acid residue to neutral or positively charged amino acids each increased the E_m by stabilizing lower oxidation states.[84] In contrast, the exchange of charged residues showed little

Table 1.1: Overview of selected site-directed mutagenesis performed on [2Fe2S] cluster-containing proteins from distinct organisms and their impact on the midpoint potential, ΔE_m, compared to the wild-type enzyme.

Organism	Protein	E_m /mV	Mutation	ΔE_m /mV	Annotation	Literature
E. coli	N1a		N142M/V96P	-100	NxM: hydrogen bond to bridging sulfide, PxV: replaces a backbone secondary amide	[89]
B. taurus			M153N	+ 88		
Y. lipolytica			M149N/P103V	+163		
T. Maritima	HydC		A85P and V131N		saturation mutagenesis	[80]
C. reinhardtii	Fdx2	-331	M62F r95Y double-mutant	-69 -19 -27		[95]
A. thaliana	Fdxs		recombinant chimeras with combined subdomains		largest differences resulted from exchange of N-terminus	[88]
Anabaena sp. 7120	Fdx	-406	A45S	+24	H-bond from S45 to C41	[90]
S. oleracea	Fdx	-401	E92K E92Q E92A	+93 +73 +78	neg. -> positive neg. -> neutral E92 forms H-bond to S45	[92]
Bovine adrenodoxin	Adx	-274	T54S T54A	-55 -66	removal of H-bond	[91]

effect on the E_m of the [2Fe2S] cluster N1a from different organisms.[89] This may be due to different orientations of side chains and backbone dipoles relative to the cluster, resulting in distinct electrostatic effects.[93] Eventually, structural features in the vicinity of the [2Fe2S] cluster, such as exchanging the cluster coordinating loops were shown to affect the E_m in N1a.[89]

To gain a first insight into the factors influencing the midpoint potential of Fdxs from *C. reinhardtii*, Fdx1 can be compared to the sequence-like Fdx2 (68 %).[55] Fdx2 exhibits a higher midpoint potential of $E_m = -331\,\text{mV}$ at pH 7 and also interacts with FNR and HydA1, but with lower rate constants than Fdx1.[53,94] Structural modeling suggested that differences in the surface charge distribution between both Fdxs are responsible for the distinct affinities.[60] A structural comparison revealed single amino acid residues in the vicinity of the [2Fe2S] cluster that upon site-directed mutagenesis lowered the midpoint potential of Fdx2 to a value comparable to Fdx1 (see Table 1.1).[95] The lower E_m in the Fdx2 variants favors electron transfer to HydA1 and increased the H_2 production rate twofold in comparison to wild-type Fdx2.[95] Thus, the adjustment of the E_m difference between redox partners can help to increase the efficiency of a chosen metabolic pathway. Developing methods for precise measurements of E_m and determining factors that affect its magnitude are therefore important first steps towards understanding structure-function relationships facilitating electron transfer processes in both native and rationally designed proteins.

1.2 [FeFe]-hydrogenases

The enzymes responsible for high-yield H_2 production are [FeFe]-hydrogenases, which catalyze the simple, yet challenging reversible reduction of protons to molecular hydrogen: $2H^+ + 2e^- \rightleftharpoons H_2$.[17] The reaction can be directed towards H_2 reduction or H^+ oxidation, termed the 'bias'.[96] The prototypical role of hydrogenases comprises two purposes: as an electron donor, they generate energy for organisms by splitting H_2 or, as a sink for reducing equivalents, they produce H_2 and thereby regulate the redox potential of the cell.[97] The reaction is catalyzed at a metal center, on which basis hydrogenases can be divided into three classes: [Fe]-only, [NiFe] and [FeFe]-hydrogenases.[98–100] [Fe]-hydrogenases are only found in hydrogenotrophic methanogenic archaea and harbor one redox-inactive Fe guanylyl-pyridinol cofactor.[101,102] It catalyzes the reversible hydride transfer from splitting of H_2 to methylentetrahydromethanopterin, which represents one reaction step in methane formation from CO_2 and H_2. [NiFe]-hydrogenases consist of a binuclear Ni-Fe center coordinated by four cysteine residues. The redox-inactive low-spin Fe(II) is further coordinated by three diatomic ligands, whereas the Ni changes its redox state during the catalytic reaction.[17,103] [FeFe]-hydrogenases are found in anaerobic prokaryotes, such as *Clostridia* and *Desulfovibrio* species, as well as in some anaerobic eukaryotes, and green algae, like *Chlamydomonas* species.[97,99] Their active site, better known as the H-cluster (from the 'hydrogen-activating cluster') consists of a diiron subsite, $[2Fe]_H$, that is connected to $[4Fe]_H$, a [4Fe4S] cluster (Figure 1.4). The dinuclear cluster is coordinated by inorganic ligands and bridged by an azadithiolate (adt) ligand. A more detailed insight is provided in Section 1.2.2. Of the three classes, [FeFe]-hydrogenases are the most active enzymes with turnover frequencies of $\approx 21,000 \pm 12,000$ H_2 s^{-1} at pH 7,[104] and are the main focus of this work.

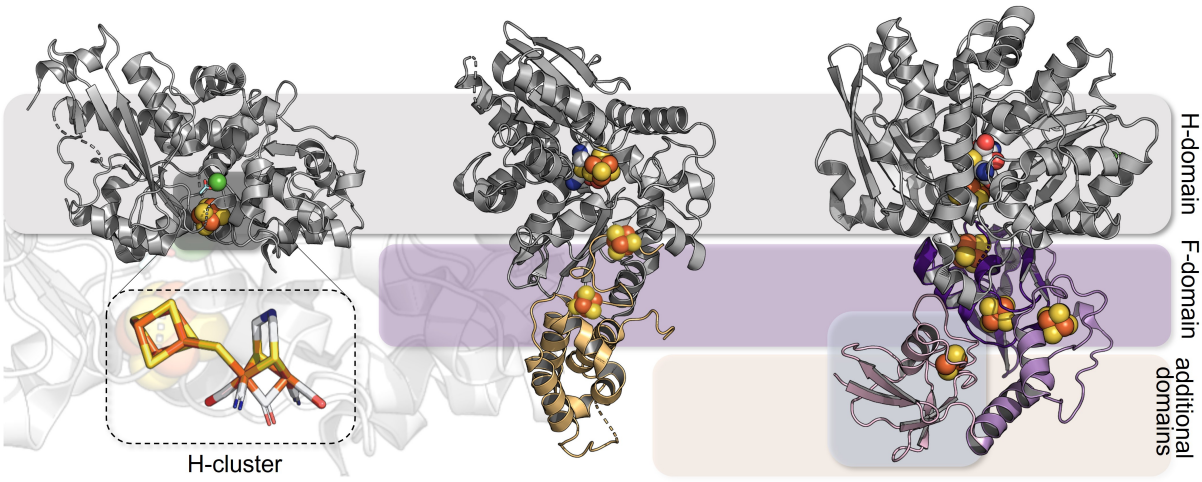

Figure 1.4: Crystal structures of distinct types of [FeFe]-hydrogenases. Left: apo-*Cr*HydA1 from *C. reinhardtii* (PDB-ID: 31X4), whose structure lacks the complete H-cluster shown in the inset below. Middle: CbA5H from *C. beijerinckii* (PDB-ID: 6TTL). Right: CpI from *C. pasteurianum* (PDB-ID: 3C8Y). The H-domain (grey), the F-domain (purple), and the additional soluble-ligand binding β-grasp-domain (orange) are shown as ribbons. The accessory FeS clusters and the H-clusters are shown as spheres. Atomic colouring: Fe: orange, S: yellow, C: grey, O: red, N: blue.

The first hydrogen-producing enzymes were investigated at the beginning of the 20th century and eventually named hydrogenases in 1931.[105,106] Already in the 70s, researchers acknowledged the world's increasing energy demand and the potential of hydrogenases as an alternative energy source.[105] The production of hydrogen from biomass or waste materials generated an

increasing interest and research on these systems. In 1998, the first crystal structure of the [FeFe]-hydrogenase CpI from *Clostridium pasteurianum* (*C. pasteurianum*) was reported and enabled a view of the active site and overall structure.[30] Advancing technological innovations, such as recombinant overexpression,[107–109] and the incorporation of artificial cofactors yielding semi-synthetic enzymes,[110,111] significantly accelerated their characterization. Spectroscopic methods, such as EPR, Mössbauer, and IR-spectroscopy, provided further insight into the catalytic states, their redox potentials, and accessory FeS clusters and eventually enabled the depiction of a (still fragmentary) catalytic cycle.[112] To date, hydrogenases are explored for application in biohybrid nanomaterials, serve as a blueprint for synthetic mimics, and for industrial H_2 production with microalgae as bioenergy producing biomass, although their efficiency is still limited.[65,66,100,113,114]

Approximately 40 hydrogenases have been investigated thus far, from which only a few were biochemically characterized.[97] Their highly modular genetics produced a plethora of distinct enzymes with both monomeric and multi-domain structures. Several attempts were made to classify this comprehensive diversity,[98,115,116] resulting in three groups A-C based on amino acid sequence phylogeny.[117] Group A comprises prototypical and bifurcating hydrogenases, where either Fdx or both Fdx and NAD(H) act as redox partners for hydrogen evolution, respectively.[117,118] Group A can be further divided into subgroups, depending on additional domains and their quarternary structure.[118] Nonetheless, every [FeFe]-hydrogenase consists of a core domain of approximately 40 kDa, which carries the highly conserved H-cluster.[97] One of the simplest [FeFe]-hydrogenases is HydA1 from *C. reinhardtii*, which consists of the H-domain only and belongs to the subgroup M1 (M = monomeric).[69,72,119] Most hydrogenases have one or more closely spaced ($\approx$ 11 Å) accessory FeS clusters (F-clusters), which serve as electron transfer relays from external donors to the catalytic site and vice versa.[120,121] The associated domain is termed F-domain. The function and influence of the F-clusters will be reviewed in Section 1.2.5. Further representatives of Group A containing F-domains are the prototypical [FeFe]-hydrogenases CbA5H from *Clostridium beijerinckii* (*C. beijerinckii*) (M2c),[122–124] and the well-investigated CpI from *C. pasteurianum* (M3) (Figure 1.4).[30,125] Additional domains, such as the soluble-ligand binding β-grasp (SLBB) domain in CbA5H might serve further functions. Group B and C represent thus far uncharacterized ancestral hydrogenases and putative sensory hydrogenases, respectively. Sensory hydrogenases show only very low H_2 evolution activity. Their Per-Arnt-Sim sensory domain can regulate gene expression, e.g., for biosynthesis of hydrogenases by structural changes upon sensing external stimuli, such as molecular hydrogen bonding.[116,126] Related hydrogenases were termed HydS and have attracted broad interest lately.[127,128]

1.2.1 The Apoprotein and its Maturases: Assembly of the H-cluster

The generation of an active hydrogenase, referred to as HydA, requires a stepwise assembly of the unique $[4Fe]_H$ and $[2Fe]_H$ subsites of the H-cluster, including the biosynthesis of the CO and CN^- ligands, as well as installment of the adt bridgehead.[129] *In vivo*, the F-clusters and the $[4Fe]_H$ subcluster are assembled by the cell's own FeS cluster machinery.[119,130,131] In contrast, the formation of $[2Fe]_H$ requires the three enzymes HydG, HydE, and HydF, which are also referred to as maturases.[119,132] Although extensive research has been conducted over the past decades, the exact pathway and role of the maturases in the assembly process are not fully

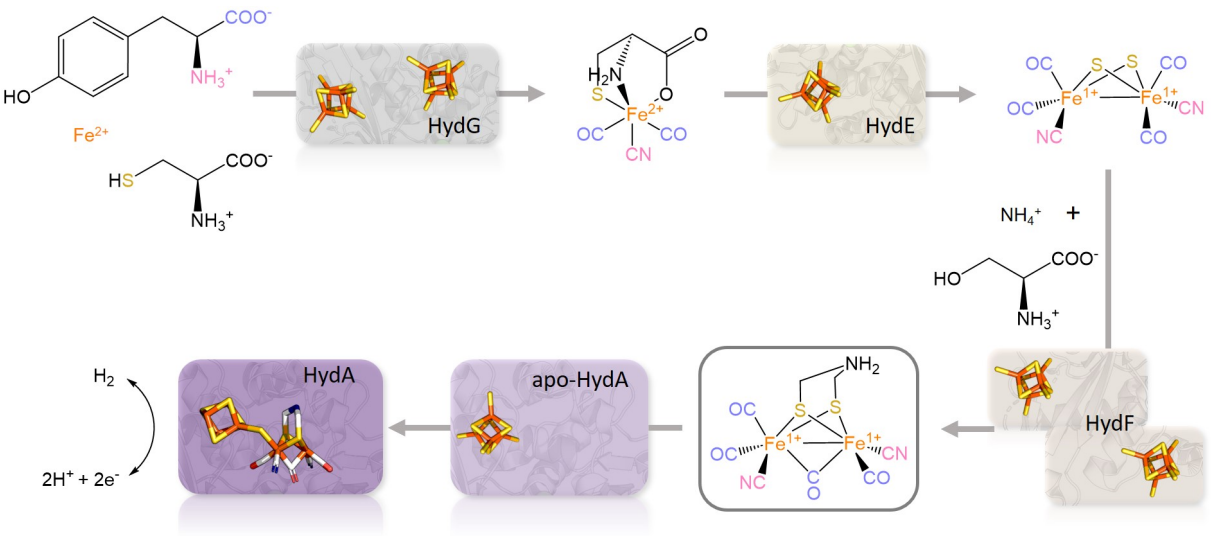

Figure 1.5: Scheme of the *in vivo* maturation process of [FeFe]-hydrogenases involving the three maturases HydG, HydE and HydF (adapted from Britt et al. [129]).

established. This knowledge, however, is crucial for the optimization of bioinspired catalysts and enzyme purification. Moreover, the identification of the necessary enzymatic components allows for a cheap and site-selective incorporation of isotope labels, which can provide further insight into the mechanism of H_2 production.[129,133,134] The first maturase involved in the assembly of $[2Fe]_H$ is HydG, a radical SAM enzyme that contains a SAM-binding [4Fe4S] cluster and an auxiliary FeS cluster. The radical cleavage of tyrosine leads to the formation of CO and CN^- and subsequently to the formation of an organometallic $[Fe(cysteinate)(CO)_2(CN)]^-$ complex (Figure 1.5).[135–139] This complex is supposedly dimerized by the second radical SAM maturase HydE, yielding a $[Fe_2S_2(CO)_4(CN)_2]^{2-}$ precursor, which is still lacking the adt bridgehead.[140,141] A recent study showed that in the absence of HydE and HydG, the synthetic precursor and HydF are sufficient to form an intact H-cluster.[142] This finding is supported by the activation of HydA with a fully defined enzymatic system, where serine and an aminomethyl-lipoyl-H-carrying protein were shown to provide the CH_2 and NH groups of the adt bridgehead, as revealed by isotope-labeled ENDOR experiments.[134,143,144] Hence, the third maturase HydF is suggested to play a fundamental role in the installation of the adt bridgehead and to serve as a scaffold for transfer of $[2Fe]_H$ to the active site.[142] The final incorporation of $[2Fe]_H$ is suggested to be a multistep process, involving several electrostatic contacts and structural reorganization of the protein environment.[119,145,146]

In vitro, the accessory F-clusters and the $[4Fe]_H$ cluster can be reconstituted with iron ions.[147] But in the absence of maturases, e.g., during recombinant overexpression of HydA in *Escherichia coli* (*E. coli*), only the [4Fe4S] subcluster occupies the active site, known as apo-HydA.[119,132] In 2013, Esselborn et al. [111] discovered that the elaborate maturation process, including the simultaneous synthesis of all H-cluster components,[134] can be circumvented by incubating apo-HydA with a synthetic mimic of the diiron subsite, $[2Fe]_{MIM}$. This artificial cofactor, which is EPR-inactive in solution, carries an additional terminal CO ligand instead of the bridging CO and lacks an open coordination site. The incorporation of $[2Fe]_{MIM}$ in apo-HydA can in turn be monitored by

dissociation of one of the four CO ligands.[110,111,148,149] This drastically simplified the *in vitro* assembly and enabled high-yield purification of spectroscopically indistinguishable enzymes and incorporation of artificial cofactors.[150,151] One example for the latter is the propanedithiolate (pdt) cofactor, which introduces a methylene bridgehead. Hydrogenases maturated with pdt show similar structural and spectral properties, but almost no catalytic activity.[110,145,152,153] This circumstance can simplify the spectral analysis and be used to advantage, e.g., for redox potentiometries.[44] Similarly, the incorporation of other cofactors can enable the trapping of intermediate H-cluster states.[150,151]

1.2.2 The H-cluster and its Redox States

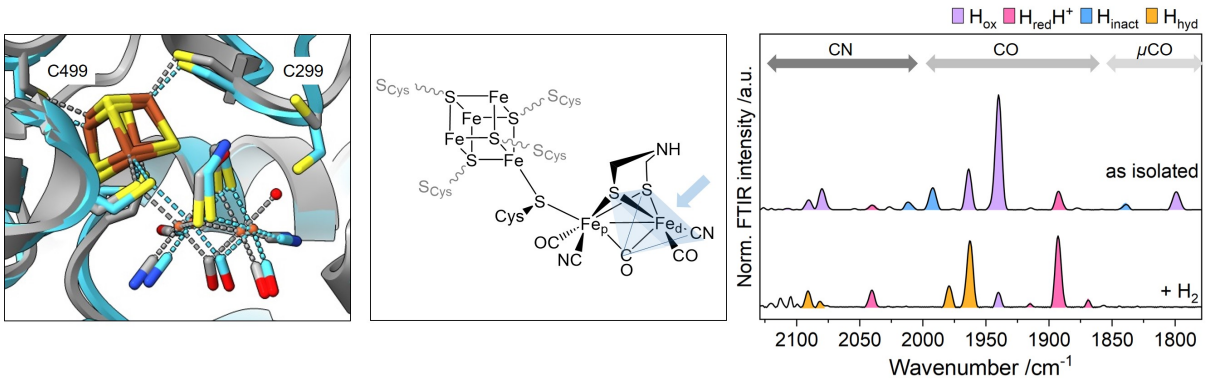

Figure 1.6: The H-cluster of [FeFe]-hydrogenases and corresponding FTIR spectra. (**Left:**) Overlay of the crystal structures of CbA5H (PDB ID: 6TTL, blue) and CpI (PDB ID: 3C8Y, gray). The cysteine residue codes are associated with CpI. Atomic colouring: Fe: orange, S: yellow, C: grey, O: red, N: blue. (**Middle:**) Schematic overview of the H-cluster with the rotated motif of Fe_d (blue shaded areas) and open coordination site (blue arrow) as indicated (adapted from Kleinhaus et al. [100]). (**Right:**) FTIR spectra of CbA5H in the as isolated state and treated with H_2. The vibrational regions associated with the CN, CO and μCO ligands are indicated with gray arrows.

The H-cluster consists of a cubane [4Fe4S] cluster that is scaffolded by four cysteine residues of which one is shared with a binuclear [2Fe2S] cluster (Figure 1.6).[17,30,105,154–156] The proximal (Fe_p) and distal Fe (Fe_d) ions of $[2Fe]_H$ relative to $[4Fe]_H$ carry each a terminal carbon monoxide (CO) and cyanide (CN^-) ligand, that stabilize the metals in low-oxidation states. In contrast to an octahedral ligand environment at Fe_p, a shared carbonyl ligand (μCO) yields square-pyramidal coordination with an open binding position at Fe_d, referred to as 'rotated geometry'.[157–159] The Fe ions of $[2Fe]_H$ are interconnected by two inorganic sulfur atoms of a bridging dithiolate, whose central headgroup remained long unidentified.[30,154,160] It was eventually resolved by a Hyperfine Sublevel Correlation (HYSCORE) study as an amine, being part of an adt ligand. The amine serves as a hydrogen-bond donor to the apical ligands and as a proton relay connecting Fe_d over a nearby cysteine residue with the conserved proton transfer pathway (PTP).[47,151,161] The latter includes arginine and glutamic acid residues interconnected with cysteine, serine, and a small water cluster.[162] Mutations of those residues have been shown to affect the PTP.[100] A vacant position at Fe_d (see Figure 1.6) enables not only the binding of substrates (H^+, H_2) but also inhibitors (CO, O_2, SH, and CN),[163–170] that can access the buried H-cluster by selective channels from the surface.[171,172] In conjunction with the complex interplay of the two electronically coupled H-cluster subsites, a multitude of redox and protonation states (18 different H-cluster states are reviewed in Kleinhaus et al. [100]) were discovered, whose order and

involvement in the catalytic cycle are highly debated. During catalytic turnover, the inorganic ligands at $[2Fe]_H$ are flexible and change their position. The resulting characteristic vibrational bands in the range of 2120−1750 cm^{-1} can be monitored with FTIR spectroscopy to distinguish the various redox and protonation states of the H-cluster (Figure 1.6).[173–175] Complementary to FTIR, EPR spectroscopy is an excellent tool for monitoring and characterizing distinct H-cluster states, as the exchange of electrons and protons between the two H-cluster moieties generates different valence distributions resulting in several paramagnetic species (Figure 1.7).[176–181] The results obtained from spectroscopic techniques, are supported by molecular modeling and density functional theory (DFT) calculations. Crystal structures capturing the H-cluster into specific intermediate states, however, are widely unavailable.[182] In the following, the most widely accepted catalytic states of the H-cluster will be reviewed. Note, that the nomenclature of states changed throughout the years. An encompassing discussion is available in Senger et al. [179]. Moreover, details on the potential catalytic cycle(s) are found in Section 1.2.3.

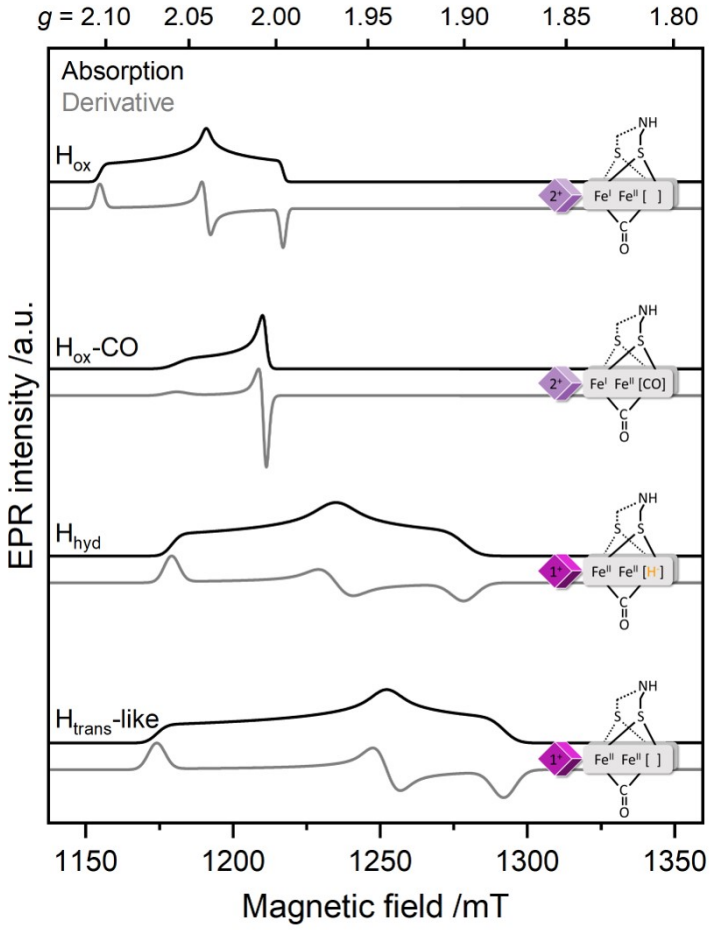

Figure 1.7: Spectral simulations of EPR spectra (10 K, 34 GHz) of typical paramagnetic H-cluster states observed in [FeFe]-hydrogenases using *Cr*HydA2 as an example. The simulations are shown as absorption (black traces) and first derivative (gray traces). The proposed electronic configuration of the H-cluster is depicted on the right.

The $\mathbf{H_{ox}}$ state is the oxidized resting state of the H-cluster, where oxidized refers to the absence of reducing agents or H_2. H_{ox} can be induced by treatment with mild oxidizing agents, such as thionine or neutral red, or by auto-oxidation under an inert atmosphere.[124,183,184] H_{ox} is assumed to have an open coordination site, however, crystal structures of CpI suggest a bound or adjacent water molecule.[30,160] Its electronic structure is best described by a mixed-valence,

paramagnetic $[2Fe]_H$ ($S = 1/2$) site and a diamagnetic $[4Fe4S]^{2+}$ ($S = 0$).[155,185,186] Due to intercluster exchange interactions of $J = 20\,cm^{-1}$ between the two subsites of the H-cluster,[187] some spin density is transferred from $[2Fe]_H$ to $[4Fe]_H$ enabling the detection of weak magnetic hyperfine interactions of ^{57}Fe of $a_{iso} = 9.9\,MHz$ in the former diamagnetic $[4Fe4S]_H$ via Mössbauer or Electron Nuclear DOuble Resonance (ENDOR) spectroscopy.[155,188] Its characteristic rhombic EPR signal, with $g = 2.10, 2.04, 2.00$, has been observed in every [FeFe]-hydrogenase thus far, and shows only minor differences between organisms. The electronic structure of $[2Fe]_H$, however, is still controversial. Based on isotope-labeled ENDOR, IR- and Mössbauer spectroscopy, as well as computational studies,[185,187,189,190] some groups found evidence for a $Fe_p^{2+}Fe_d^{1+}$ site. Other groups suggested the reverse assignment or reported a distributed electron density over both Fe atoms.[156,183,191] This discrepancy may be traced back to experimental limitations or represents an inherent feature that varies within distinct enzymes.[100]

A protonated version of the oxidized resting state, $\mathbf{H_{ox}H}$, is formed under acidic conditions in the presence of sodium dithionite (NaDT)[179,180] or in partially dehydrated protein films treated with mild reductants.[192] The overall redox state of the H-cluster is the same as for H_{ox}, whereas the exact position of protonation has yet to be verified. The formation of $H_{ox}H$ was observed by spectral differences in IR[180] and Nuclear Resonance Vibrational Spectroscopy (NRVS)[193] and is amplified with increasing proton concentrations. However, DFT supported studies hint at the protonation of a terminal cysteine ligating the $[4Fe]_H$ (Cys417 in *Cr*HydA1). The state is suggested to be an intermediate at the end of the catalytic cycle before H_{ox}.[180,193]

The **H_{ox}-CO** state is the CO-inhibited form of the H-cluster, which can intentionally be induced by purging the enzyme with CO gas.[168] Moreover, H_{ox}-CO is frequently observed as a result of low-level degradation, whereupon damaged H-cluster release CO ligands that in turn inhibit intact H-clusters.[184] The binding of CO occurs at the open coordination site at Fe_d and subsequently inactivates the enzyme.[168,194,195] A crystal structure of CO-inhibited CpI indicated spin density at the apical position of Fe_d, that is in conjunction with an unidentified diatomic ligand.[168] Most groups favor an apical CO ligand, which is supported by spin polarization measurements,[196] although a CN^- ligand, possible due to the rotational freedom of Fe_d, was also proposed based on IR spectroscopic data and DFT calculations. The apical CN^- may be stabilized by weak H-bonds to the amine of the adt bridgehead.[151,173,184,197,198] Thus, the arrangement of apical or equatorial CN^- or CO ligands is still under investigation. The H_{ox}-CO state ($S = 1/2$) exhibits an axial EPR signal with $g = 2.06, 2.006, 2.006$.[199,200] In contrast to H_{ox}, the spin density is suggested to be extensively distributed over both subclusters due to an increased intercluster exchange coupling of $J = 150\,cm^{-1}$, yielding a valence-delocalized $[2^+]$-$Fe^{1.5+}Fe^{1.5+}$ state.[173,187,201] The spin delocalization is suggested to be the cause of the axial EPR signal, compared to the rhombic EPR signal of H_{ox}, as the anisotropy of the g-tensor is reduced.[189] Furthermore, **$\mathbf{H_{ox}H}$-CO** is formed under acidic conditions.[180] The state's EPR spectrum, however, is not known thus far.

Recent crystal structures also suggest the binding of CN^- to Fe_d in apical position in CpI and *Dd*HydAB from *Desulfovibrio desulfuricans* (*D. desulfuricans*).[164,202] Similar to H_{ox}-CO, the formation of the state can either be induced by damaged $[2Fe]_H$ clusters, or by intentional addition of CN^-. The respective states can be found in wild-type hydrogenases, but are readily accumulated in variants, where the native PTP is impaired. The rhombic EPR signal with $g = 2.06, 1.98, 1.91$ is similar to the H_{trans} state (see Section 1.2.4) and was termed H_{trans}-like.

Interestingly, purging the as-isolated variants with CO showed no effect, suggesting that the binding site is already occupied by irreplaceable CN^-.[202]

To induce further H-cluster states, the enzyme can be either reduced with H_2 or an excess of NaDT (E_m = -660 mV at pH 7), which compensates for the lack of a physiological electron donor.[100] The addition of NaDT results in H_2 evolution, whereas H_2 treatment results in H_2 uptake. The application of both approaches can indicate whether the formed states are part of the reversible catalytic cycle or dead-end products.[100]

The H_{ox} state reversibly transforms upon one-electron reduction to the diamagnetic H_{red} and $H_{red'}$ (active "reduced") states. In $\mathbf{H_{red'}}$, sometimes denoted as H_{red}, the $[4Fe]_H$ subsite gets reduced.[153,174,203] The $[2Fe]_H$ configuration is similar to H_{ox} and, likewise, the addition of CO yields the reduced, CO-inhibited $\mathbf{H_{red'}}$**-CO** state.[197] This state was also observed as an intermediate shortly after the incorporation of $[2Fe]_{MIM}$ into apo-HydA1 *in vivo*, that rapidly oxidizes to H_{ox}-CO.[112,204] Moreover, similar to $H_{ox}H$, the protonation of $[4Fe]_H$ is proposed, yielding $\mathbf{H_{red'}H}$.[179,180]

For $\mathbf{H_{red}}$, the reducion occurs at $[2Fe]_H$, yielding a homovalent $[2^+]$-$Fe^{1+}Fe^{1+}$ subsite.[179] However, contradictory models were reported for the ligand connecting the two Fe atoms, such as a semi-bridging CO[153,174,205] or bridging hydride, μH^-.[206] The transition between $H_{red'}$ and H_{red} is associated with a pH-dependent electron transfer between both subsites and in favor of H_{red} under acidic conditions.[174,193] The protonation of $\mathbf{H_{red}H^+}$ is suggested to occur either at a cysteine of $[4Fe]_H$,[159] the adt bridgehead,[207], or forms a terminal hydride at $[2^+]$-$Fe^{2+}Fe^{2+}$.[208] For the latter, an interconnecting μCO ligand is proposed.[209,210] The catalytical relevance of H_{red} and $H_{red}H^+$ are under debate.[100,182] The derivatives of H_{red} and $H_{red'}$ are diamagnetic as well.[153,211]

Upon further reduction of H_{red}, the superreduced state $\mathbf{H_{sred}}$ with $[1^+]$-$Fe^{1+}Fe^{1+}$ is attained. This intermediate state with $S = 1/2$ exhibits a rhombic g-tensor ($g = 2.076, 1.943, 1.868$) and is ascribed to arise from $[4Fe]_H$. It was observed in *Cr*HydA1 under reducing conditions.[211] In [FeFe]-hydrogenases with multiple FeS clusters however, H_{sred} is proposed to be a transient species, where the additional cubane electron is readily released *via* the F-clusters.[46,211] Recently, a different axial EPR signal with $g = 2.15, 1.86, 1.86$ was attributed to H_{sred}. The authors suggested that the previously reported rhombic species should be ascribed to the tautomer $H_{hyd:red}$.[212]

The $\mathbf{H_{hyd}}$ state adopts a $[1^+]$-$Fe^{2+}Fe^{2+}$-H^- configuration, where a terminal hydride binds at the apical position.[175,192,213,214] The rhombic EPR signal with $g = 2.07, 1.93, 1.88$ is associated with the [4Fe4S] cluster, which is presumably protonated at a cysteine as well.[46,159] The H_{hyd} state is suggested to be an intermediate state during the catalytic cycle, that was found in CbA5H under H_2 or can be trapped in 'standard' hydrogenases under acidic conditions, by disruption of the PTP, or by exchange of the $[2Fe]_H$ bridgehead.[124,173,175,215] Recently, further tautomers of H_{hyd}, namely $H_{hyd:red}$, $H_{hyd:ox}$ and $H_{hyd}H^+$, have been proposed.[212]

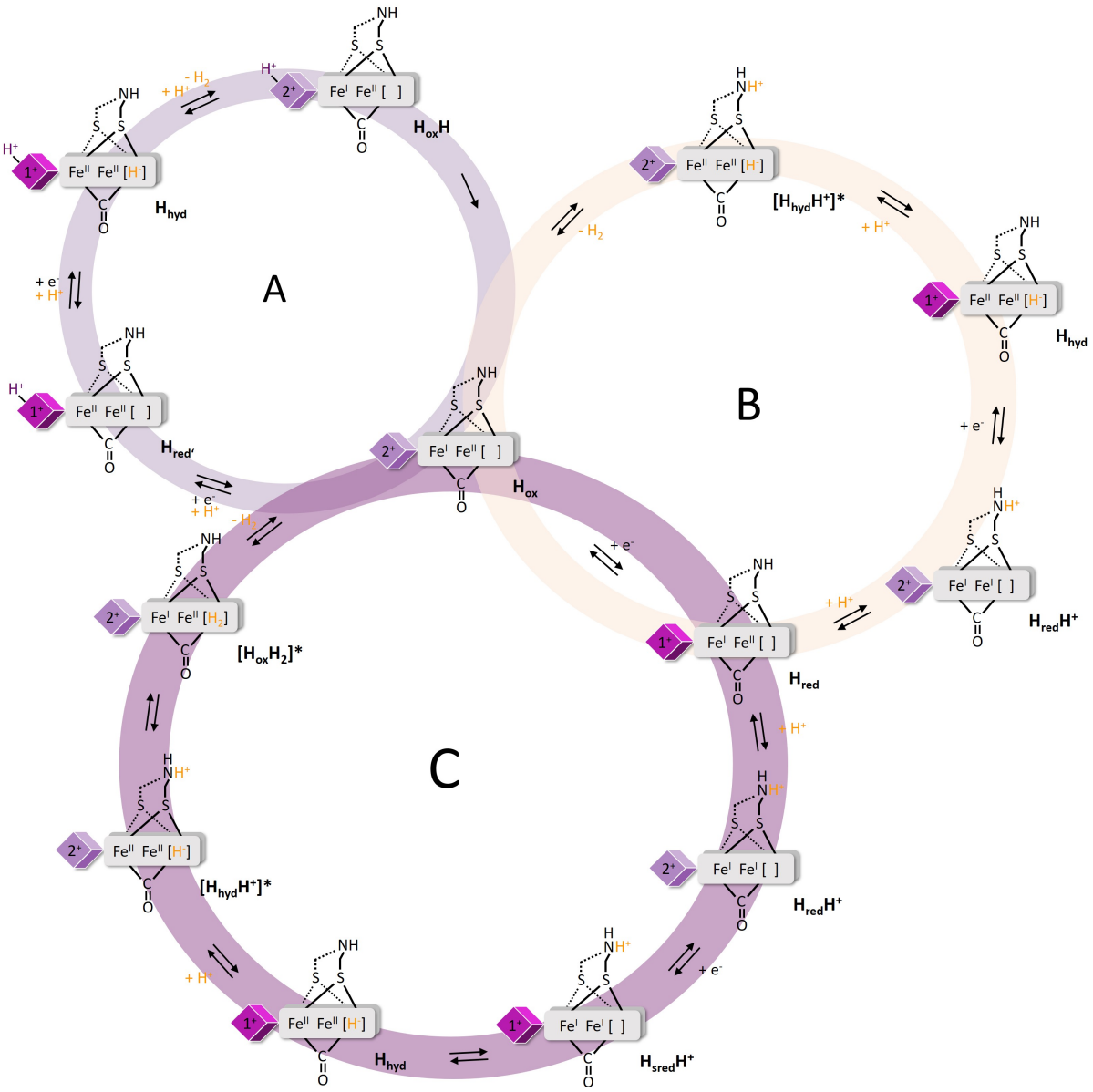

Figure 1.8: Catalytic cycle(s) of reversible hydrogen evolution. Transient states are marked with an asterisk (scheme adapted from Kleinhaus et al. [100]).

1.2.3 The Catalytic Cycle(s)

As was already evident in the previous section, the presence, configuration, and relevance of the catalytic states of the H-cluster are controversially discussed on the basis of contradictory results. These discrepancies can also be transferred to the mechanistic sequence, resulting in at least three distinct proposals for the catalytic cycle (A-C) as summarized by Kleinhaus et al. [100].

Cycles A and B/C can generally be distinguished by the type of proton and electron transfers between the states, which are suggested to be electronically coupled in cycle A and to occur sequentially in cycles B and C. The common starting point of each cycle is $\mathbf{H_{ox}}$, from where the first reduction occurs at $[4Fe]_H$. In cycle A, a PCET yields $\mathbf{H_{red'}}$, where the proton is suggested to reside at one of the ligating cysteine residues of $[4Fe]_H$. In cycles B and C, a simple electron transfer leads to the formation of $\mathbf{H_{red}}$. The next common state is the terminal hydride-carrying $\mathbf{H_{hyd}}$ state, whose formation mechanism differs between each cycle. In cycle A, a second PCET

directly forms H_{hyd} out of $H_{red'}$. In cycle B, the adt ligand is protonated (NH_2^+), whereupon the electron tunnels from $[4Fe]_H$ to Fe_d, forming the $\mathbf{H_{red}H^+}$ state. Subsequently, the proton moves to Fe_d and the diiron site is oxidized by two electrons, resulting in H_{hyd}. In cycle C, the second one-electron reduction of $H_{red}H^+$ forms $\mathbf{H_{sred}H^+}$, which isomerizes to H_{hyd}, similar to cycle B. From H_{hyd} on, protonation of the adt amine leads in all cycles to the formation of a proton-hydride pair, which combines to H_2, and eventually to regeneration of H_{ox} *via* distinct intermediates. In cycle A, the irreversible intermediate state $H_{ox}H$ has the proton still residing at one of the ligating cysteines of $[4Fe]_H$. In cycles B and C, transient H-cluster states, such as $H_{hyd}H^+$ and/or $H_{ox}H_2$ are suggested to be involved.

Recent results disprove the protonation at $[4Fe]_H$ and involvement of PCET in cycle A by showing that the midpoint potential of $[4Fe]_H$ is independent of pH.[216] This finding, however, is in contrast to earlier studies showing a pH-dependent $H_{ox} \leftrightarrow H_{red'}$ transition.[179] Thus, further studies are necessary to illuminate the extensive redox chemistry of the H-cluster. Besides the (more or less) relevant active catalytic states, distinct inactive states were discovered upon exposure to oxygen, that ought to protect the enzyme and associated clusters from oxygen-induced degradation.

1.2.4 Oxygen-Induced Degradation and Protection Mechanisms

[FeFe]-hydrogenases are usually highly sensitive to even trace amounts of oxygen and irreversibly inactivate within seconds. As their oxygen sensitivity is a major drawback for effective hydrogen production applications, increased interest evolved in recent years in the finding and investigation of oxygen-resistant enzymes. In [FeFe]-hydrogenases, oxygen can enter the deeply buried pocket of the H-cluster *via* gas channels.[217] The subsequent binding of oxygen at Fe_d initiates the decomposition of the subsite in a multi-step process and catalyzes the formation of ROS, such as O_2^-, OOH^- or H_2O_2.[166,218] The binding of superoxide at Fe_d can promote two distinct processes, where either $[2Fe]_H$ or $[4Fe]_H$ are the initial targets of degradation.[219–222] Oxygen-induced inhibition is mainly irreversible, whereas short-time oxygen exposures enabled partially reversible reactivation.[165,166,223,224] The [FeFe]-hydrogenase *Dd*HydA1 of the sulfate-reducing bacterium *D. desulfuricans* was the first one found to adopt an inactive, oxygen-protected state after aerobic purification, termed $\mathbf{H_{inact}}$.[225] It forms by bonding of exogenous sulfide, presumably in the form of H_2S at low pH, to Fe_d.[169,226,227] Its $[Fe^{2+}]$-$Fe^{2+}Fe^{2+}$state is diamagnetic.[185,228] One-electron reduction at $[4Fe]_H$ yields a transient state, $\mathbf{H_{trans}}$, that exhibits a characteristic EPR spectrum.[212,225] Subsequent electron transfer from the cubane to $[2Fe]_H$ activates the H-cluster but prevents recapturing of H_{inact} and in turn, restores the enzyme's oxygen sensitivity.[165,185,229] A similar behavior was observed in the [FeFe]-hydrogenases *Dv*HydA1 from *Desulfovibrio vulgaris* (*D. vulgaris*) Hildenborough, and *Cr*HydA1, but was found to be absent in CpI.[124,169,230] An enzyme that exhibits a unique, sulfide-independent protection mechanism is the [FeFe]-hydrogenase CbA5H, which was first discovered by Morra et al. [122] in 2016. CbA5H can spontaneously convert into the H_{inact} state under oxidizing conditions, i.e., treatment with oxidizing agents, oxygen exposure, or high applied potential.[122–124] Notably, the conversion is reversible, so that reductive reactivation results in a mixture of active states, whose spectroscopic features are very similar to *Dd*HydA1.[124] Morra et al. [122] reported a full recovery of the enzyme after at least two 10 min exposures to air and subsequent reactivation, while later studies

showed a continuous decrease of enzyme activity after multiple cycles.[123,124,231] In contrast to *Dd*HydA1, however, the transition between the active state and H_{inact} is a direct one-electron transfer reaction, omitting the formation of H_{trans}.[124] CbA5H, however, is unresponsive to sulfide exposure and shows slightly shifted H_{inact} vibrations.[122,124] Experimental and theoretical data excluded the involvement of uncommon exogenous molecules or oxygen-derived species.[124] A crystal structure of aerobically purified CbA5H compared to anaerobically purified CpI eventually revealed crucial differences near the H cluster: a peptide loop (termed "TSC-loop") undergoes a conformational flip and translocates the cysteine residue C367 in binding position to Fe_d in CbA5H (S-Fe_d: 3.1 Å *vs.* 5.9 Å in CpI) and thus, prevents binding of external molecules. The suggestion that both anaerobic inactivation and resistance to O_2-induced damage depend on the relocation of C367 was supported by two site-directed variants C367A, and C367D, where no H_{inact} formation but irreversible inactivation was observed upon oxygen exposure.[123]From a kinetic point of view, three distinct species are suggested to be involved in H_{inact} formation: two active forms, "A_1" and "A_2", and one inactive form, "I", were derived from chronoamperometric measurements, following the biphasic model:[123]

$$A_1 \underset{k_{-1}}{\overset{k_1}{\rightleftarrows}} A_2 \underset{k_{react}}{\overset{k_{inact}}{\rightleftarrows}} I, \tag{1.1}$$

where k_i are the rate constants of the reactions. The active form A_1 is considered to be the starting point of H_{inact} formation, where the enzyme takes on a similar structure as standard hydrogenases.[123] A conformational change, occurring on a time scale of seconds, is suggested to trigger the formation of A_2, where C367 is still unbound. The final inactivation step eventually translocates C367 closer to Fe_d.[123] A series of site-directed mutations of amino acid residues located far from the active site were shown to alter individual rate constants and impact the kinetics of H_{inact} formation.[123,231] Three residues in the TSC-loop were identified to be mainly responsible for the loop's flexibility and enable the relocation of C367 for coordination to Fe_d. Substitution of the involved amino acids led to an altered flexibility, which slowed down H_{inact} formation and subsequently the oxygen resistance.[123] In contrast, the substitution of a methionine residue to glutamic acid, M382E, located approximately 18 Å away from the active site, generated a more oxygen-resistant variant of CbA5H.[231] The exchanged residue, which stabilized the local environment, led to an increased flexibility of a particular loop located next to the TSC loop. Moreover, the activation energy of the A_2 to I interconversion was lowered. In conjunction with the gained structural flexibility, M382E allows for a faster coordination of C367 to Fe_d and results in a more efficient protection against oxygen binding.[231] Only recently binding of a cysteine and H_{inact} formation were shown to occur in the group B [FeFe]-hydrogenases CpIII and MeII from *Megasphaera elsdenii* (*M. elsdenii*).[232] The residues responsible for an enhanced flexibility of the TSC loop, however, are not conserved in these enzymes. Contrarily, an additional cysteine residue is suggested to relocate the proximal cysteine (C367 in CbA5H) closer to Fe_d. However, CpIII was found to be sensitive to oxygen. One possible explanation is a sluggish H_{inact} formation, which can not prevent O_2 binding to the active site in time.[232] Besides distinct structural features of the direct protein environment, oxygen resistance was shown to depend on the regulation of O_2 diffusion and proton delivery to the active site, or the presence of accessory FeS clusters.[173,229,233,234]

1.2.5 The Influence of the Accessory F-clusters

The main function of single or multiple closely spaced accessory FeS clusters is the electron transfer to and from external donors to the catalytic site,[120,121] but they are also suggested to take on further functions. One factor that might be influenced by the F-clusters is the 'catalytic bias',[182,235] which describes the ratio of the H_2 oxidation and production rates.[96] Moreover, an increase in oxygen stability was observed for the [FeFe]-hydrogenase *Clostridium acetobutylicum* (*C. acetobutylicum*), which harbors four additional F-clusters, whereas the cluster-free *Cr*HydA1 hydrogenase was more prone to oxygen-induced damage.[224] It is suggested that the oxygen stability is increased by provision of stored electrons from the F-clusters, which reduce the present oxygen to water and prevent formation of damaging ROS.[170,182,220] A contrasting observation was made when the N-terminal domain harboring two F-clusters from the [FeFe]-hydrogenase *Me*HydA was removed. While the truncation had no effect on the oxygen stability, the catalytic bias was shifted towards H_2 production.[236] Furthermore, the presence of F-clusters is suggested to affect the catalysis of the H-cluster by redox anticooperative behavior.[182] This phenomenon was detected in the [FeFe]-hydrogenases *Dd*HydAB and CpI harboring multiple F-clusters and manifests in lower redox potentials of the H-cluster states in the presence of reduced F-clusters.[216,237] Redox anticooperativity describes a change of the midpoint potential of one cluster in dependence of a second adjacent cluster. In CpI for example, the $H_{ox} \leftrightarrow H_{red}$ transition has a midpoint potential of $-438\,\mathrm{mV}$, when the proximal and medial F-clusters are oxidized, but decreases by $-111\,\mathrm{mV}$, when both F-clusters are reduced, resulting in $-549\,\mathrm{mV}$ for the H-cluster and *vice versa*.[216] This effect is thought to arise from electrostatic repulsion between clusters and can also be observed in the respective FTIR and EPR spectra.[182,216,237] During catalysis, when FS4A is reduced, the electron transfer from $[4Fe]_H$ to $[2Fe]_H$ is enhanced, which leads to the protonation of the H-cluster and eventually in the production of H_2.[182] In the opposite direction, during H_2 oxidation, the process is reversed. The protonated H-cluster releases H_2, and the electron moves from $[2Fe]_H$ to $[4Fe]_H$, while deprotonating the H-cluster. Concomitantly, the electron at FS4A is transferred to the next F-cluster. It is suggested, that in the presence of FS4A the formation of the double-reduced state $H_{sred}H^+$, frequently observed in the cluster-free *Cr*HydA1, is omitted, as FS4A can store the second electron for the H-cluster. Moreover, with redox anticooperativity, the H_{red} state has a higher pK_a (less acidic) and is less prone to protonation limiting catalysis. Thus, in comparison to *Cr*HydA1, the protonated $H_{red}H^+$ state ($[2^+]$-$Fe^{1+}Fe^{1+}$) is favored due to the anticooperative effect of the F-clusters, whereas H_{red} is destabilized by the reduced FS4A ($[1^+]$-$Fe^{2+}Fe^{1+}$).[182]

1.3 Structure of This Work

Despite years of extensive research on FeS proteins, the application of EPR spectroscopy for the investigation of single and multiple FeS clusters remains a challenging task, especially with regard to their electronic properties and structure-function relationships. The advancement of modern EPR spectrometers enables the use of higher microwave power, higher frequencies, and tailored pulses. These innovations offer better resolution, expand the investigative toolbox and provide further insight into FeS clusters.

This work leads along the hydrogen evolution pathway, which is lined by a variety of FeS proteins, from an EPR spectroscopist's perspective. **Chapter 2** provides the theoretical foundation of EPR spectroscopy and describes the applied techniques and relevant magnetic properties of different FeS cluster types relevant for the present study. **Chapter 3** investigates simple [2Fe2S] cluster-containing Fdxs found in the green alga *C. reinhardtii*. The method of pulsed EPR monitored redox potentiometry, performed at higher frequencies than usual, is established for determining their midpoint potentials. After validating the method with well-characterized Fdxs, it is applied to unexplored isoforms and novel engineered variants. Exchanges of single amino acids are performed to fine-tune the midpoint potential of the [2Fe2S] cluster of *Cr*Fdx1. **Chapter 4** investigates one of the main electron acceptors of *Cr*Fdx1 under anaerobic conditions, the [FeFe]-hydrogenase HydA1. Different sample preparations of apo-HydA1 surprisingly reveal the presence of multiple paramagnetic species for one single [4Fe4S] cluster. This observation is confirmed by a subsequent redox potentiometry allowing for the separation of two species and approximation of their midpoint potentials. The direct comparison with EPR spectra of apo-HydA2 suggests structural differences as a cause for the presence of more than one paramagnetic species. **Chapter 5** encounters the maturase HydF, which harbors another single [4Fe4S] cluster with unusual spectroscopic properties. The present work confirms some of the unusual features observed for the single [4Fe4S] cluster in the maturase HydF and raises further questions. The following chapters deal with the investigation of multiple cluster-containing [FeFe]-hydrogenases. **Chapter 6** delves into the characterization of an oxygen-resistant [FeFe]-hydrogenase from *C. beijerinckii* exhibiting a unique oxygen protection mechanism. This work determines not only the H-cluster states, but also discovers a new radical $R^{\bullet ox}$, whose origin is explored by multi-frequency experiments, site-directed mutagenesis and isotope-labeled ENDOR spectroscopy. Its origin and function is further explored in **Chapter 7** and put into context with the recent literature. A second, even more complex [FeFe]-hydrogenase, CpI from *C. pasteurianum*, is introduced in **Chapter 8**. Temperature-dependent and multi-frequency spectra in conjunction with elaborate spectral simulations reveal an exchange coupling interaction between the H-cluster and neighbored [4Fe4S] cluster, overseen by previous investigations. The strength of the exchange coupling is determined and shown to be modulable by site-directed mutagenesis in the vicinity of the active site. The implication of a changed exchange interaction on the biological function is further explored. **Chapter 9** summarizes and evaluates the obtained results and provides a further outlook.

2

Theory: Electron Paramagnetic Resonance

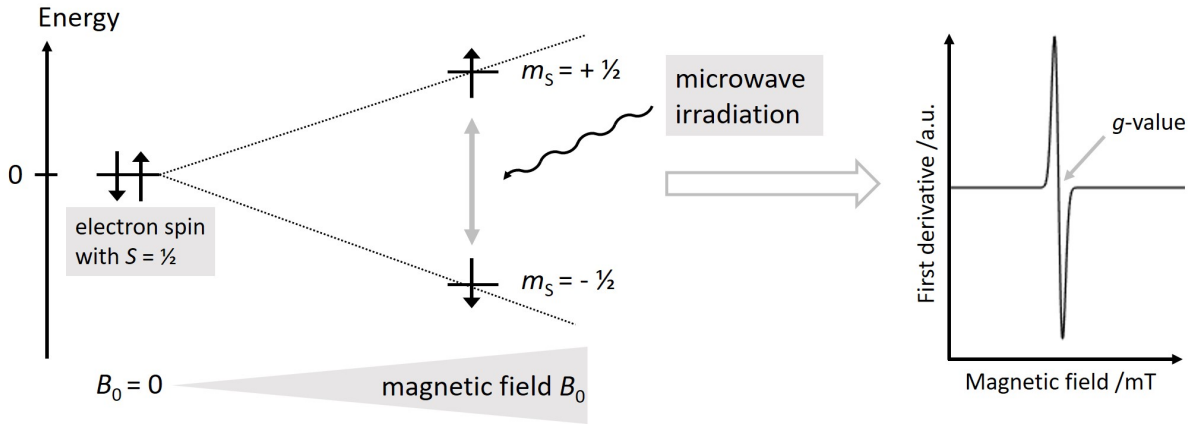

Figure 2.1: Illustration of the splitting of the energy level of a single electron with $S = 1/2$ in an external magnetic field B_0. Irradiation with microwaves of frequency ν that fulfills the resonance condition lead to a transition between the Zeeman energy levels. As a result, an EPR spectrum can be recorded, from which the g-value is obtained.

In this chapter the theoretical foundation of EPR spectroscopy and related techniques, such as ENDOR, and Double Electron Electron Resonance (DEER), as well as spectroscopic features of FeS clusters will be discussed. EPR spectroscopy investigates the electronic and magnetic properties of paramagnetic species, while providing valuable insights into their structure and dynamics. The basic principle of EPR spectroscopy is the interaction of the magnetic moment of unpaired electrons with an external magnetic field that exhibit a resonance transition upon electromagnetic irradiation (Figure 2.1). Since the first EPR experiment performed in 1944,[238,239] a rapid development of instrumentation and techniques made EPR spectroscopy a powerful tool applicable to a wide range of systems, including FeS clusters, free radicals, and metalloenzymes. More detailed introductions into the world of EPR spectroscopy are provided in the textbooks of Schweiger et al. [240], Weil et al. [241], and Goldfarb [242].

2.1 The Spin Hamiltonian

Each electron possesses spin, which is a type of intrinsic angular momentum that has no classical counterpart. The existence of electron spin was demonstrated in the 1920s by the famous Stern-Gerlach experiment, in which a beam of silver atoms passed through a magnetic field and separated into two distinct beams. Those beams correspond to two different spin states of the atoms, which can only attain discrete values.[243] In quantum mechanics, spin angular momentum is represented by the electron spin vector operator $\hat{\mathbf{S}}$, which has a primary spin quantum number $S = 1/2$, quantized in units of $\hbar$, and often simply denoted as "spin".[244]‡

The effect of the electron spin placed in an external magnetic field on the energy of the system can be described by the static *spin Hamiltonian*, $\hat{\mathcal{H}}_{\mathrm{S}}$, which was introduced by Abragam and Pryce in 1951.[245] The spin Hamiltonian depends on the positions and momenta of all particles in the system. EPR resonances arise not only from interactions of unpaired electrons with an applied magnetic field, but also from interactions with their surroundings, other nuclei and unpaired electrons. Therefore, the spin Hamiltonian comprises a sum of individual contributions

$$\hat{\mathcal{H}}_{\mathrm{S}} = \hat{\mathcal{H}}_{\mathrm{EZ}} + \hat{\mathcal{H}}_{\mathrm{NZ}} + \hat{\mathcal{H}}_{\mathrm{HF}} + \hat{\mathcal{H}}_{\mathrm{EE}} + \hat{\mathcal{H}}_{\mathrm{ZF}} + \hat{\mathcal{H}}_{\mathrm{NQ}}, \tag{2.1}$$

where the terms in listing order are: *Zeeman interactions* of electron or nuclear spins with the external magnetic field, *hyperfine interactions* between electron and nuclear spins, *electron-electron interactions* between electron spins, *zero-field splittings* for spin systems with $S > \frac{1}{2}$, and *nuclear quadrupole interactions*. Some terms can be neglected if their contribution is not relevant for the system under investigation. Thus, the latter two are excluded in the present work.

2.1.1 Zeeman Interactions

A particle of mass m and charge q with an intrinsic angular momentum $\hbar\boldsymbol{S}$ is associated with a magnetic dipole moment[240]

$$\boldsymbol{\mu} = \frac{q}{2m}\hbar\boldsymbol{S}. \tag{2.2}$$

The magnetic moment of an electron in the ground state with mass m_e and charge $-e$ yields the *Bohr magneton*[246]

$$\beta_e = \frac{|e|\hbar}{2m_e}. \tag{2.3}$$

The proportionality constant $\gamma_{\mathrm{e}} = -g_{\mathrm{e}}\beta_e/\hbar$, also known as *gyromagnetic ratio* of a free electron, converts the angular momentum to the magnetic moment in quantum mechanics. It introduces the gyromagnetic factor (g-factor) for a free electron, $g_e = 2.00231930436$,[247] which is one of the most precisely determined physical quantities. Thus, the magnetic moment spin operator of an electron is defined as

$$\hat{\boldsymbol{\mu}}_{\boldsymbol{e}} = \gamma_{\mathrm{e}}\hbar\hat{\boldsymbol{S}} = -g_e\beta_e\hat{\boldsymbol{S}}. \tag{2.4}$$

Projecting $\hat{\boldsymbol{S}}$ along the axes of an orthogonal frame results in the spatial components $\hat{S}_x, \hat{S}_y, \hat{S}_z$, with their eigenvalues ranging from $-S$ to $+S$ with $(2S+1)$ possible components along each orientation quantized in $\hbar$. As only one spatial component can be determined at a time with

‡Operators are indicated by circumflexes, and vectors and matrices are set in bold.

certainty, the $\hat{S}_z$ component is usually chosen as a point of reference. Following from above, the eigenvalues of $\hat{S}_z$ are restricted to the secondary quantum numbers $m_S = \pm 1/2$. The associated magnetic dipole moment along the z-axis is defined as:

$$\hat{\mu_z} = -g_e \beta_e \hat{S}_z. \tag{2.5}$$

When placing the unpaired electron in a static magnetic field, the interaction is determined by

$$\hat{\mathcal{H}} = -\hat{\boldsymbol{B}}^{\mathsf{T}} \cdot \hat{\boldsymbol{\mu}} = -\hat{B}_z \hat{\mu_z}, \tag{2.6}$$

where $\hat{\boldsymbol{B}}$ is the magnetic field operator[‡] taken along z in the second term. The insertion of the above equations yields the *electron Zeeman* spin Hamiltonian:[246]

$$\hat{\mathcal{H}}_{\mathrm{EZ}} = g_e \beta_e B_0 \hat{S}_z, \tag{2.7}$$

where B_0 is the magnetic induction.[240] Two energy levels α and β with the spin oriented either parallel ($m_S = +1/2$) or antiparallel ($m_S = -1/2$) exist, when B_0 is applied. The resulting energies are:

$$\begin{aligned} E_\alpha &= +g_e \beta_e B_0 1/2 \\ E_\beta &= -g_e \beta_e B_0 1/2. \end{aligned} \tag{2.8}$$

A transition between the two energy levels can be induced, when the frequency ν of an oscillating electromagnetic field B_1 is oriented perpendicular to B_0 and fulfills the *resonance condition*:

$$\Delta E = h\nu = E_\alpha - E_\beta = g_e \beta_e B_0. \tag{2.9}$$

The transition between the energy levels is accordingly $\Delta m_{\mathrm{S}} = \pm 1$.

In real systems, unpaired electrons are not free and affected by their local environment. Their spin and orbital angular momenta interact through *spin-orbit coupling* due to the electrons' motion around a charged nucleus.[248] The local magnetic fields generated by this coupling add to the external magnetic field, B_0, and can be more conveniently compensated for by introducing an *effective* g-factor $g = g_e + \Delta g$, which results in a characteristic g-factor for every paramagnetic species. The deviation Δg depends on the spin-orbit coupling constant, which increases with increasing atomic number.[248]

As the spin-orbit coupling is related to the orbital motion, which is a directional quantity, the g-value is a measure of the anisotropy of the paramagnetic center and is expressed as a tensor. The g-tensor can be represented by a 3 x 3 matrix, with three principal values g_1, g_2, and g_3 along the diagonal. The g-tensor can attain different symmetries, defined as isotropic ($g_1 = g_2 = g_3$), axial ($g_1 = g_2 \neq g_3$), or rhombic ($g_1 \neq g_2 \neq g_3$).

In liquid solutions the spins are rapidly tumbling and the g-anisotropy is averaged out by motion yielding an isotropic g-tensor $g_{\mathrm{iso}} = \frac{g_1+g_2+g_3}{3}$. Isotropic samples have a homogeneously broadened linewidth, i.e., the line shape is the same for each dipole, resulting in a Lorentzian line

[‡]As it has a constant value in the following, the circumflex is omitted hereafter. The superscript T denotes the transpose of a matrix or vector.

shape.[241] At cryogenic temperatures or in powder samples, every spin has a different, immobile orientation with respect to the magnetic field. The EPR linewidth is inhomogenously broadened due to supersition of many lines and in the case of isotropic systems often resembles a Gaussian shape.[241] Another dominant source of line broadening is molecular disorder, known as 'strain'. The g-strain describes a distribution of g-values of indiviual molecules around a mean value. It is induced by freezing and arises, e.g., from fixed orientations of metal-ligand bonds of individual molecules in the sample. The increasing orbital contribution results in a larger deviation Δg from g_e and therefore in broader linewidths.[50,249]

Equivalent to electron spins, some nuclei possess a nuclear spin described by the nuclear spin operator $\hat{\boldsymbol{I}}$ having a nuclear spin quantum number $I = 1/2, 1, 2/3$, etc., and an associated magnetic dipole moment. The coupling of a nuclear spin to B_0 is described by the *nuclear Zeeman* spin Hamiltonian

$$\hat{\mathcal{H}}_{\mathrm{NZ}} = -g_n \beta_n B_0 \hat{\boldsymbol{I}}, \tag{2.10}$$

where g_n is the nuclear g-factor and β_n is the nuclear magneton. This spectroscopic phenomenon, which is analogous to EPR, is known as nuclear magnetic resonance (NMR). Similarly, the transition between energy levels is given by $\Delta m_{\mathrm{I}} = \pm 1$. The interaction of the unpaired electron with magnetic nuclei, however, results in a complex hyperfine structure.

2.1.2 Hyperfine Interactions

The hyperfine interaction between an electron and nuclear spin is independent of the magnetic field and described by the sum of isotropic or Fermi contact interactions $\hat{\mathcal{H}}_{\mathrm{FC}}$ and spin dipolar couplings $\hat{\mathcal{H}}_{\mathrm{SD}}$[240]

$$\hat{\mathcal{H}}_{\mathrm{HF}} = \hat{\mathcal{H}}_{\mathrm{FC}} + \hat{\mathcal{H}}_{\mathrm{SD}} = \hat{\mathbf{S}} \cdot \boldsymbol{A} \cdot \hat{\mathbf{I}}, \tag{2.11}$$

where the hyperfine coupling tensor $\boldsymbol{A}$ represents the magnetic interaction energy. For multi-electron systems, additional spin polarization effects, i.e., contributions from outer unpaired electron spins affecting inner electron pairing, contribute to $\hat{\mathcal{H}}_{\mathrm{FC}}$. Moreover, if the unpaired electron resides in p-, d- or f-orbitals, where the electron spin density at the nucleus, $|\psi_0|^2$, is usually zero, spin polarization or hyperconjugation effects can transfer significant spin density to neighbouring or the respective nuclei resulting in detectable hyperfine couplings.[250,251] $\boldsymbol{A}$ can be directly extracted from the EPR spectrum, if its magnitude sufficiently exceeds the line width, or in the case of smaller $\boldsymbol{A}$, determined by double resonance experiments, such as ENDOR (Section 2.2.2). $\boldsymbol{A}$ is composed of a_{iso}, the isotropic coupling constant, and $\boldsymbol{T}$, the dipolar coupling constant

$$\boldsymbol{A} = a_{\mathrm{iso}} \mathbf{1}_3 + \boldsymbol{T}, \tag{2.12}$$

where $\mathbf{1}_3$ is the 3×3 unit matrix. In this principal axes representation, which includes only diagonal terms, the dipolar interaction matrix $\boldsymbol{T}$ is both symmetric and traceless. Thus, when a molecule in solution undergoes fast rotational motion, the anisotropic component is averaged out, and only isotropic hyperfine interactions are detected. The isotropic hyperfine coupling constant is directly related to a finite probability of electron spin density at the nucleus in s-orbitals

$$a_{\mathrm{iso}} = \frac{2}{3} \frac{\mu_0}{\hbar} g_e \beta_e g_n \beta_n |\psi_0|^2, \tag{2.13}$$

where ψ_0 is the electronic wavefunction evaluated at the nucleus' position, and μ_0 the vacuum permeability.

In anisotropic systems the dipolar interaction between the electron and nuclear magnetic dipoles connected by an inter-spin vector $\boldsymbol{r}$ is described by the orientation-dependent spin-dipolar Hamiltonian:

$$\hat{\mathcal{H}}_{\mathrm{SD}} = \frac{\mu_0}{4\pi\hbar} g_e \beta_e g_n \beta_n \left[\frac{\hat{\boldsymbol{S}}^{\intercal} \cdot \hat{\boldsymbol{I}}}{r^3} - \frac{3(\hat{\boldsymbol{S}}^{\intercal} \cdot \boldsymbol{r})(\hat{\boldsymbol{I}}^{\intercal} \cdot \boldsymbol{r})}{r^5} \right]. \tag{2.14}$$

Considering only the wavefunction of the ground state ψ_0 and integrating over the spatial variables yields

$$\hat{\mathcal{H}}_{\mathrm{SD}} = \hat{\boldsymbol{S}}^{\intercal} \cdot \boldsymbol{T} \cdot \hat{\boldsymbol{I}}, \tag{2.15}$$

where $\boldsymbol{T}$ represents the traceless and symmetric dipolar coupling tensor.

The dipolar interaction in the hyperfine principal axes system is given by

$$\boldsymbol{T}^{\mathrm{d}} = \frac{\mu_0}{4\pi\hbar} \frac{g_e \beta_e g_n \beta_n}{r^3} \begin{pmatrix} -1 & & \\ & -1 & \\ & & 2 \end{pmatrix} = \begin{pmatrix} -T & & \\ & -T & \\ & & 2T \end{pmatrix}, \tag{2.16}$$

which is only valid for an isotropic electron Zeeman interaction.

2.1.3 Electron-Electron Interactions

The electron-electron interaction between two distinct unpaired electrons can generally be divided into two terms, depending on the inter-spin distance r and orientation between them.[252] Electron-electron interaction can occur (i) due to the direct overlap of orbitals or interaction between them via mediating atoms, or (ii) through dipole-dipole interaction when the paramagnetic centers are farther apart. The electron exchange interaction is operative "through bond", electrostatic in nature, important over short distances (0.5 to 1.5 nm) and can be orders of magnitude stronger than dipolar interactions, which are operative "through space", purely magnetic in nature and significant over long distances.[42,252] The exchange interaction can be described by the exchange spin Hamiltonian

$$\hat{\mathcal{H}}_{\mathrm{EX}} = \hat{\boldsymbol{S}}_{\mathrm{A}}^{\intercal} \cdot \boldsymbol{J}_{\mathrm{AB}} \cdot \hat{\boldsymbol{S}}_{\mathrm{B}}, \tag{2.17}$$

where $\hat{\boldsymbol{S_A}}$ and $\hat{\boldsymbol{S_B}}$ are the electron spin operators of two paramagnetic centers A and B, respectively, and $\boldsymbol{J}$ is a 3 x 3 matrix accounting for the electron exchange interaction. It can be decomposed into the sum of an isotropic, antisymmetric and anisotropic tensor[252]

$$\hat{\mathcal{H}}_{\mathrm{EX}} = J \cdot \hat{\boldsymbol{S}}_{\mathrm{A}} \cdot \hat{\boldsymbol{S}}_{\mathrm{B}} + \boldsymbol{d} \cdot \hat{\boldsymbol{S}}_{\mathrm{A}} \times \hat{\boldsymbol{S}}_{\mathrm{B}} + \hat{\boldsymbol{S}}_{\mathrm{A}}^{\intercal} \cdot \boldsymbol{D}_{\mathrm{ex}} \cdot \hat{\boldsymbol{S}}_{\mathrm{B}}, \tag{2.18}$$

yielding the following expression[253]

$$\boldsymbol{J} = \underbrace{\begin{pmatrix} J & & \\ & J & \\ & & J \end{pmatrix}}_{\text{isotropic}} + \underbrace{\begin{pmatrix} 0 & d_z & -d_y \\ -d_z & 0 & d_x \\ d_y & -d_x & 0 \end{pmatrix}}_{\text{antisymmetric}} + \underbrace{\begin{pmatrix} D_{xx} & D_{xy} & D_{xz} \\ D_{yx} & D_{yy} & D_{yz} \\ D_{zx} & D_{zy} & D_{zz} \end{pmatrix}}_{\text{anisotropic}}, \tag{2.19}$$

where J is a scalar, $\boldsymbol{d}$ is a polar vector, and $\boldsymbol{D}_{\mathrm{ex}}$ is a symmetric traceless tensor. The first term arises from isotropic exchange interactions and is characterized by J.[252] Note, that in the literature conflicting conventions exist for the isotropic exchange coupling, such as $\pm 2J$, or $-J$. The second term is the anti-symmetric exchange, whereas the third term comprises the sum of the anisotropic exchange and dipole-dipole interactions.[254] The anisotropic exchange contributions result from spin-orbit coupling.[253] It is expected, that larger spin-orbit couplings result in larger anisotropic exchange interactions. Furhtermore, they are suggested to be more important over short distances. General concepts, however, have not been established thus far and delocalized pathways might provide higher contributions than anticipated.[253] For two isotropic spin centers A and B with $\Delta g = g_{\mathrm{A}} - g_{\mathrm{B}}$, the spectral line shape depends on the relative magnitudes of $|J|$, and $|\Delta g \beta_e B_0|$.[255] Three distinct situations are encountered under the condition that the isotropic exchange interaction greatly exceeds the anisotropic contributions (Figure 2.2):[255]

(i) $|\Delta g \beta_e B_0| \ll |J|$, where a single line is observed at $g_{\mathrm{AB}} = (g_{\mathrm{A}} + g_{\mathrm{B}})/2$.

(ii) $|\Delta g \beta_e B_0| \approx |J|$, where the spectrum shows four lines of which two are centered around g_{AB} and splitted by $\{[J^2 + (\Delta g \beta_e B_0)^2\}^{1/2} - J]/g_{\mathrm{AB}}\beta_e$ and two with lower intensity each separated by $|J|/g_{\mathrm{AB}}\beta_e$ in field units.

(iii) $|J| \ll |\Delta g \beta_e B_0|$, where two doublets with similar intensity are centered around g_{A} and g_{B} splitted by $|J/g_{\mathrm{AB}}\beta_e|$.

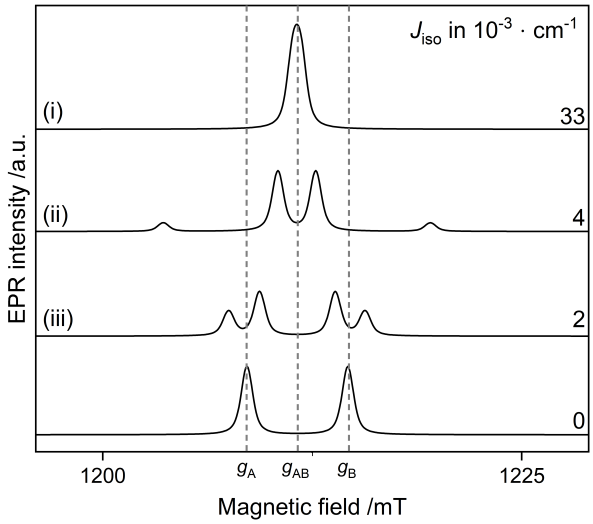

Figure 2.2: Simulated EPR spectra (34 GHz) of two interacting paramagnetic centers **A** and **B** ($S = 1/2$) with distinct isotropic g-values $g_{\mathrm{A}} = 2.01$ and $g_{\mathrm{B}} = 2.00$, respectively, a common g-value $g_{\mathrm{AB}} = (g_{\mathrm{A}} + g_{\mathrm{B}})/2$ and increasing isotropic exchange coupling J.

Analogous to the electron-nuclear dipolar Hamiltonian (Eq. 2.14), the dipolar spin Hamiltonian can be expressed as

$$\hat{\mathcal{H}}_{\mathrm{ED}} = \hat{\boldsymbol{S}}_{\mathrm{A}}^{\intercal} \cdot \boldsymbol{D}_{\mathrm{AB}} \cdot \hat{\boldsymbol{S}}_{\mathrm{B}} = \frac{\mu_0}{4\pi\hbar} g_{\mathrm{A}} g_{\mathrm{B}} \beta_e^2 \left[\frac{\hat{\boldsymbol{S}}_{\mathrm{A}}^{\intercal} \cdot \hat{\boldsymbol{S}}_{\mathrm{B}}}{r^3} - \frac{3(\hat{\boldsymbol{S}}_{\mathrm{A}}^{\intercal} \cdot \boldsymbol{r})(\hat{\boldsymbol{S}}_{\mathrm{B}}^{\intercal} \cdot \boldsymbol{r})}{r^5} \right], \tag{2.20}$$

where $\boldsymbol{D}$ is the dipolar interaction matrix. For two spins aligned with the static magnetic field in the high-field approximation ($\hat{\mathcal{H}}_{\mathrm{EZ}} >> \hat{\mathcal{H}}_{\mathrm{NZ}}$), the expression simplifies to:

$$\boldsymbol{D}^{\mathrm{d}} = \frac{\mu_0}{4\pi\hbar}\frac{g_e g_n \beta_e^2}{r^3}\begin{pmatrix} -1 & & \\ & -1 & \\ & & 2 \end{pmatrix} = \begin{pmatrix} -\omega_{\mathrm{dip}} & & \\ & -\omega_{\mathrm{dip}} & \\ & & 2\omega_{\mathrm{dip}} \end{pmatrix}. \tag{2.21}$$

Thus, the strength of the magnetic interaction is dependent on the cubic inverse distance r^{-3}. The dipolar coupling in angular frequencies is given by

$$\omega_{\mathrm{dip}} = 2\pi(1 - 3\cos^2\theta)\nu_{\perp}, \tag{2.22}$$

where θ is the angle between the inter-spin vector and B_0 and $\nu_{\perp}$ is the perpendicular component of the dipole-dipole interaction tensor ($\theta = 90°$).

2.2 Applied EPR Experiments

In an EPR experiment, a sample containing a paramagnetic center is placed inside a resonator, and an external magnetic field B_0 is applied along z. The magnetic moments align either parallel (β) or antiparallel (α) to B_0, resulting in a population difference between the two energy levels with number N given by the Boltzmann distribution

$$\frac{N_\alpha}{N_\beta} = \exp\left(\frac{-g|\beta_e|B_0}{k_{\mathrm{B}}T}\right), \tag{2.23}$$

where k_{B} is the *Boltzmann constant* and T the temperature of the lattice. The excess of spins in β results in a net magnetization $\boldsymbol{M}$ oriented along B_0, that is the sum of all magnetic moments of the individual electron spins multiplied by the inverse sample volume. The population difference increases with decreasing temperature, which is one of the reasons why cryogenic temperatures are often used. From a classical point of view, the magnetization precesses around the magnetic field axis with the *Larmor frequency*, $\omega_{\mathrm{S}} = -\gamma_{\mathrm{e}}B_0$. As a result, a stationary magnetization, $\boldsymbol{M}_0$, is established when a large number of spins is present. The resonator, e.g., a cylindrical cavity, increases the coupling between the sample and microwave (MW) radiation by providing a spatial distribution of increased magnetic and decreased electric field intensities. The typical MW frequencies used in EPR spectroscopy are approximately 9 GHz (X-band), 34 GHz (Q-band), or 94 GHz (W-band). When MW radiation is applied, a magnetic field B_1 oriented perpendicular to B_0 is induced, which oscillates with a frequency of ω_0. Under resonance conditions, for which $\omega_S = \omega_0$, the coordinate system can be more easily visualized by rotating it with an angular velocity of ω_S. In this rotating frame, B_0 disappears, while B_1 appears stationary. The magnetization M_0 starts to precess with an angular frequency ω_0 around B_1 as long as the MWs are applied. The absorption of MW radiation and the resulting transition between spin energy levels causes a decoupling of the resonator, which leads to reflection of a signal to the detector. EPR experiments can generally be divided into two categories: continuous wave (CW) and pulsed EPR methods. In CW EPR, the MW radiation is continuously applied, while the magnetic field is swept. This method is widely applied and considered a standard technique for

measuring parameters such as the g-factor, linewidth, and spin concentration. Pulsed EPR, on the other hand, involves applying short pulses of MW radiation to the sample, and detecting the resulting EPR signal after a certain time delay. Basic pulsed EPR experiments, such as free induction decay (FID) and field-swept electron spin echo (ESE) experiments provide similar spectral information as CW EPR, but can also yield direct information on spin relaxation times. More advanced techniques, such as ENDOR and DEER, allow further manipulation of the spin system and gathering information about dynamics, distances, or hyperfine interactions.

2.2.1 Field-Sweep Experiments

Even though EPR spectroscopy is an absorption technique, a first derivative spectrum is obtained with CW EPR because field modulation and lock-in detection are used to enhance the sensitivity. Thereby, the modulation of the magnetic field leads to an oscillating absorption signal, whose integrated amplitude is detected, whereas non-resonant absorption is neglected. With increasing modulation amplitude, the signal-to-noise ratio (S/N) of the resulting first derivative spectrum increases. The magnitude, however, is experimentally limited by approximately 1/3 of the smallest peak-to-peak line width due to the risk of overmodulation. Contrarily, signals with a line width exceeding the achievable modulation amplitude, such as FeS clusters at the Q-band, can be challenging to detect due to very small signal oscillations.[256] The application of MW pulses allows the selective manipulation of electron spins, which can significantly increase the spectral resolution.

The simplest pulsed EPR experiment, known as FID, consists of one single MW pulse with length t_p, that tips the magnetization $\boldsymbol{M}$ by an angle α according to $\alpha = -\gamma_e|B_1|t_\mathrm{p}$. The term 'free' refers to the absence of B_1 after the end of the pulse, when the spatial components of $\boldsymbol{M}$ relax towards their respective equilibrium. The spin-lattice relaxation time T_1 describes the recovery of the longitudinal magnetization M_z along the z-axis, whereas the the spin-spin relaxation time T_2 describes the decay of the transverse magnetization $M_{x,y}$. The relaxation times can be determined by pulsed EPR methods, such as inversion or saturation recovery experiments and Hahn echo decay.[240] In real systems the shorter phase memory time, T_m, which includes diffusion effects, is often obtained instead of T_2. Moreover, the length of the pulse influences the bandwidth of excitation, which represents the range of frequencies over which the signal is detected: Long, selective pulses have a small excitation bandwidth, whereas short, non-selective pulses result in a larger excitation bandwidth. Most commonly rectangular pulses with a constant amplitude and duration are used. One of their disadvantages is the existence of sidebands, which can lead to spectral distortion, particularly for samples with broad, inhomogeneous EPR linewidths.[257] This effect is prevented by the use of bell-shaped gaussian pulses. As they exhibit a slightly narrower bandwidth at the same B_1 field, the length of the pulse has to be increased to achieve a similar spin inversion.[257] Long pulses up to 1000 ns can reduce field-dependent modulations arising from interactions with nuclear spins. By detecting the integrated FID of a long pulse while sweeping the magnetic field, an EPR spectrum closely resembling the CW EPR spectrum can be obtained.[153] Pseudo-modulating the obtained absorption spectra can simulate the effect of field-modulation in pulsed EPR spectra, which is used, e.g., to improve the resolution of subtle spectral features.[256,258]

However, FID-detection usually comes at the expense of signal intensity, as the dead time is often comparably large relative to T_m or T_2.[242] In contrast, a sequence of pulses can be used resulting in a so called *spin echo*, while maintaining a higher echo intensity.

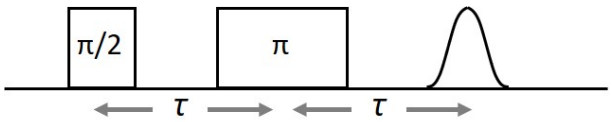

Figure 2.3: Scheme of the Hahn echo sequence.

The spin echo sequence was invented in 1950 by Erich Hahn,[259] and is also known as the Hahn echo sequence. It consists of two consecutive pulses separated by the time interval τ : $\frac{\pi}{2}$-τ-π-τ-echo (Figure 2.3). Equivalent to the FID, $\boldsymbol{M}$ is tipped by the first $\frac{\pi}{2}$ pulse from the z-axis to the xy-plane. The spin packets precess with different rates, which leads to their dephasing during time τ. The subsequent π pulse flips $\boldsymbol{M}$ to the -xy-plane. After interval τ, they attain equal phasing, build up a signal and decay like an FID, which is also called electron spin echo (ESE).[241] For a field-swept ESE-detected EPR experiment, the spin echo intensity is measured as a function of B_0, resulting in an absorption spectrum. To obtain a sufficient S/N, the experiment is repeated when the spins have relaxed back to equilibrium. The limiting factor is the T_1 relaxation time, which determines the shot repetition time (SRT) between consecutive pulse sequences. A good approximation, in which most of the magnetization has been recovered, is $\mathrm{SRT} = 5 \cdot T_1$.[260] If the SRT is chosen too short (around T_1 or less), the EPR signal decreases, known as saturation. In general, the signal intensity is affected by several factors, such as the spin concentration, temperature, MW power or relaxation times, while the line shape offers information regarding dynamics, and paramagnetic center geometry, and can change with temperature. As previously mentioned, hyperfine interactions from neighbouring nuclei can be obscured under inhomogeneously broadened linewidths. To resolve the respective hyperfine couplings, e.g., ENDOR can be applied.

2.2.2 Electron Nuclear Double Resonance

A combination of EPR and NMR principles is used in Electron Nuclear Double Resonance (ENDOR) spectroscopy to study interactions between unpaired electrons and nearby nuclear spins.[240] It is a double-frequency experiment, where both electron and nuclear spins must satisfy the resonance condition.[261] By selectively exciting nuclear spins with a resonant radio frequency (RF) field, ENDOR can provide hyperfine coupling constants, nuclear quadupole constants for $I > 1/2$, and nuclear Larmor frequencies, yielding valuable information about the nuclei in the local environment of the paramagnetic center.

In the following, a two-spin system with $S = 1/2$ and $I = 1/2$ in an external field B_0 is considered. The static spin Hamiltonian can be written as:

$$\hat{\mathcal{H}}_{\mathrm{S}} = \hat{\mathcal{H}}_{\mathrm{EZ}} + \hat{\mathcal{H}}_{\mathrm{NZ}} + \hat{\mathcal{H}}_{\mathrm{HF}}. \tag{2.24}$$

When considering only the isotropic g-value and hyperfine interaction in the high-field approximation with B_0 oriented along z, the energy of the system, expressed in angular frequency units, can be rewritten as

$$\hat{\mathcal{H}}_{\mathrm{S}} = \omega_S \hat{S}_z - \omega_I \hat{I}_z + a_{iso} \hat{S}_z \hat{I}_z, \tag{2.25}$$

where $\omega_S = g_e \beta_e B_0/\hbar$ and $\omega_I = \pm g_n \beta_n B_0/\hbar$ and the first-order eigenvalues are

$$\omega(m_S, m_I) = \omega_S m_S - \omega_I m_I + a_{iso} m_S m_I, \tag{2.26}$$

resulting in four different energy levels (labeled as 1-4 in Figure 2.4).

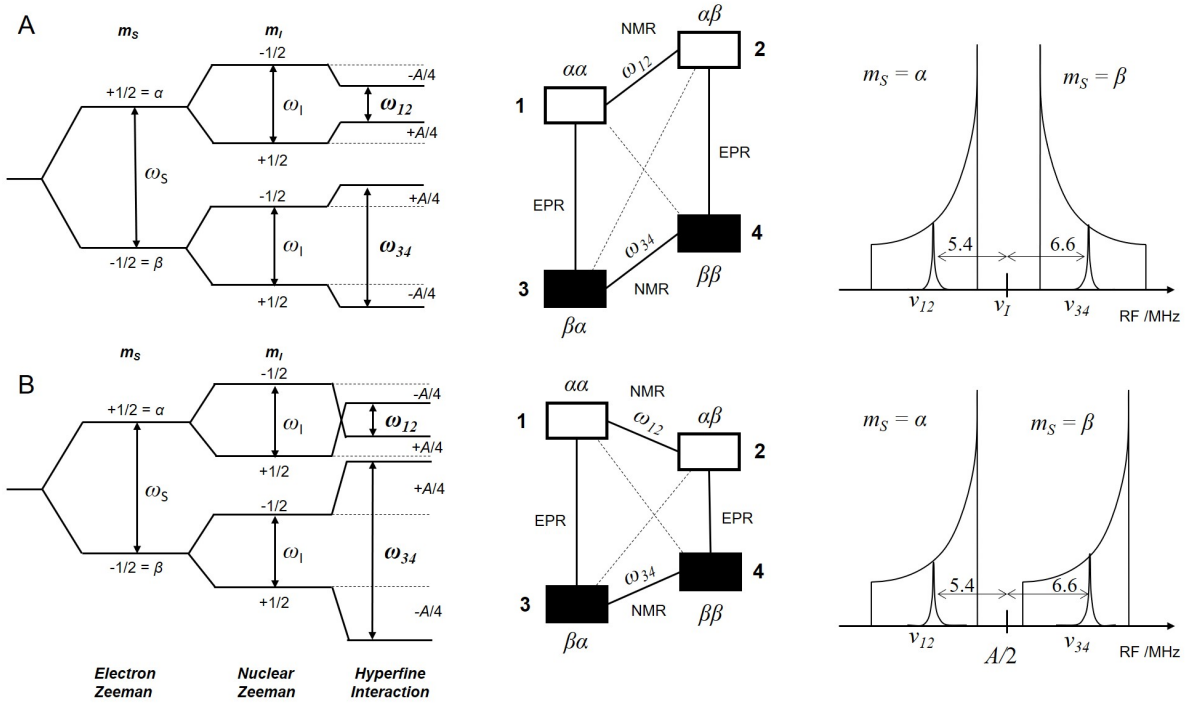

Figure 2.4: Left: Energy level diagrams ($S = 1/2$, $I = 1/2$). **Middle:** Corresponding four-level systems with allowed (solid lines) and forbidden transitions (dashed lines), where the filled boxes illustrate the population difference. **Right:** Resulting ENDOR spectra with two peaks and the powder average for (**A**) the weak coupling case ($A > 0, A < |2\omega_I|$), and (B) the strong coupling case ($A > 0, A > |2\omega_I|$). In both cases, the anisotropic hyperfine coupling causes a shift in frequencies resulting in asymmetrical centered ENDOR transitions. The figure was adapted from Goldfarb [242].

The selection rules for EPR and NMR transitions dictate the number of allowed transitions in each case. For EPR, the selection rules are $\Delta m_S = \pm 1$ and $\Delta m_I = 0$, resulting in $2S + 1$ allowed transitions at $\omega_{\mathrm{EPR}} = \omega_S \pm a_{\mathrm{iso}}/2$. In contrast, the selection rules for NMR transitions are $\Delta m_S = 0$ and $\Delta m_I = \pm 1$ and the resonances occur at $\omega_{\mathrm{NMR}} = |\omega_I \pm a_{iso}/2|$. Depending on the sign and strength of the hyperfine coupling a_{iso} with respect to the nuclear Zeeman interaction, the transitions are either symmetrically centered around the nuclear Larmor frequency, $|\omega_I|$, and split by a_{iso} (weak coupling case, where $|2\omega_I| > |a_{\mathrm{iso}}|$) or the transitions are centered at $|a_{\mathrm{iso}}|/2$ and split by $|2\omega_I|$ (strong coupling case, where $|2\omega_I| < |a_{\mathrm{iso}}|$), as shown in Figure 2.4A.

In the case of anisotropic hyperfine coupling, the ENDOR transitions can exhibit a shift in frequencies (relative to ω_I or $A/2$) if the magnetic field vector B_0 is no longer aligned with the hyperfine interaction tensor. Thus, the spin Hamiltonian from Eq. 2.25 is expanded to[242]

$$\hat{\mathcal{H}}_{\mathrm{S}} = \omega_S \hat{S}_z - \omega_I \hat{I}_z + A\hat{S}_z\hat{I}_z + B_x\hat{S}_z\hat{I}_x + B_y\hat{S}_z\hat{I}_y, \tag{2.27}$$

where A and $B_{\mathrm{x,y}}$ describe the secular and pseudo-secular (off-diagonal) anisotropic hyperfine terms, respectively. As a consequence, the resulting nuclear frequencies are asymmetrically spaced from the center.[242]

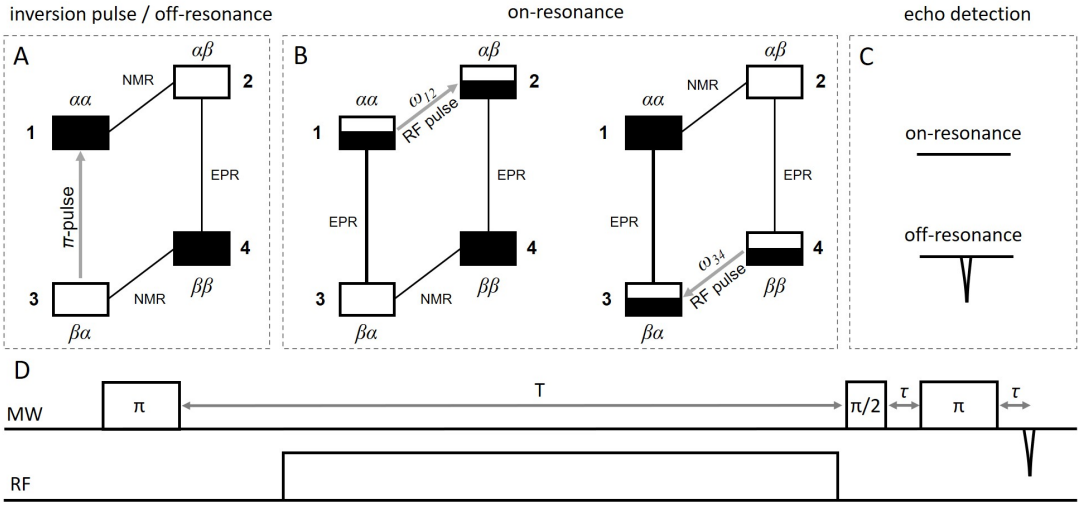

Figure 2.5: Scheme of the Davies ENDOR sequence and respective four-level energy diagrams. The filled boxes indicate a larger spin population. (**A**) A selective MW π pulse inverts the polarization of levels (1,3). The energy level populations remain the same when an off-resonant radiofrequency (RF) pulse is applied. (B) During the time interval T, a selective RF pulse is applied. If one of the NMR transitions (1↔2 or 3↔4) is driven by an on-resonance RF pulse (illustrated by half-filled boxes), the population difference of (1,3) is reduced. (C) The EPR intensity of the off-resonance inverted echo is decreased when on-resonance. (**D**) Pulse sequence of the Davies ENDOR experiment.

The two standard sequences used for pulsed ENDOR were developed by Davies[262] and Mims[263] and named accordingly. A scheme of the Davies ENDOR sequence and associated evolution of the spin populations are illustrated in Figure 2.5. The basic prinicple is shown on a simple spin system, where one electron spin $S = 1/2$ is coupled to one nuclear spin $I = 1/2$. The population difference among the resulting four energy levels (1-4) is illustrated in Figure 2.5. The relative populations are determined by the Boltzmann equation (Eq. 2.23), where under thermal equilibrium levels (3,4) have larger populations (represented by filled boxes) compared to (1,2). The application of a selective MW π pulse inverts the polarization of levels (1,3). The inversion pulse results in a reduced EPR intensity burning a narrow 'hole' in the EPR spectrum. During the time interval T, a selective RF pulse is swept over a desired frequency range. Under off-resonance conditions, an inverted echo is usually detected due to the holeburning of the inversion pulse. If one of the NMR transitions (1↔2 or 3↔4) is driven by an on-resonance RF pulse, the population difference of (1,3) is reduced and the EPR intensity of the inverted echo is decreased. The resulting ENDOR spectrum represents the increase of the EPR intensity due to the NMR transitions driven by the applied RF pulse as a function of RF.

One disadvantage of Davies ENDOR is the low-power inversion pulse, that decreases the sensitivity of the experiment for weakly coupled nuclei. For smaller hyperfine couplings, the more sensitive Mims ENDOR experiment is often used. Mims ENDOR is based on a three-pulse echo sequence: $\frac{\pi}{2} - \tau - \frac{\pi}{2} - T - \frac{\pi}{2} - \tau -$ echo. The first two non-selective $\frac{\pi}{2}$ pulses separated by delay τ create a periodic pattern in M_z. Its period is approximately proportional to $\frac{1}{\tau}$, resulting in blind spots in the ENDOR spectrum. A selective RF pulse applied during time interval T induces an NMR transition when on resonance, causing a τ-dependent frequency-shift and defocusing of the EPR transition. The third $\frac{\pi}{2}$ pulse tips the magnetization to $M_{x,y}$ and a stimulated echo is detected. To compensate for the presence of blindspots, Mims ENDOR is often performed at different τ-values.

2.2.3 Double Electron-Electron Resonance

The distance and relative orientation between two paramagnetic centers can be determined using double electron-electron resonance (DEER) spectroscopy. The method relies on the isolation of dipole-dipole interaction between two paramagnetic centers A and B, whose strength is inversely proportional to the cube of the distance according to Eq. 2.21. The inhomogeneous linewidth of the EPR spectra usually exceeds the dipolar interactions, which is why they have to be separated from unresolved hyperfine couplings and g-anisotropy.[264] With this method large distances within biomolecules, ranging from approximately 1.8 to 8 nm, can be measured.[264,265] The most commonly applied four-pulse DEER experiment manipulates the dipolar interactions between an detect spin A and a pump spin B using two different frequencies ω_A and ω_B, respectively (Figure 2.6).

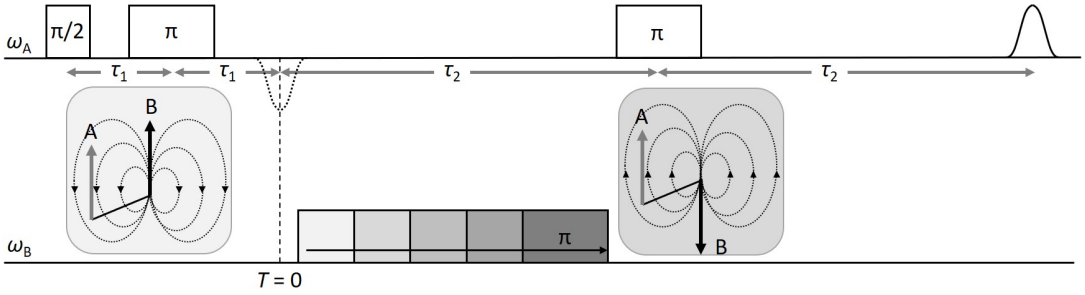

Figure 2.6: Scheme of the four-pulse DEER experiment. A Hahn-echo sequence at the detect frequency ω_A refocuses all interactions of spin A. The inset on the left shows spin A, and spin B and its local field. An incremented π pulse at the pump frequency ω_B inverts the state of spin B and simultaneously the local field at spin A as indicated by the inverted local field inset on the right.

The experiment starts with a Hahn-echo sequence at ω_A, which refocuses all interactions of spin A including dipole-dipole interactions with a second spin B and allows to detect the echo intensity $V(T)$ of A.[264–267] The π pulse at the pump frequency ω_B inverts the state of spin B after time T, with inversion efficiency $\lambda < 1$, and reintroduces the coupling between A and B. The inversion of spin B changes the Larmor frequency of spin A by $\pm\omega_{dip}$, leading to an imperfect refocusing, and thus, to a phase gain of spin A, which exclusively depends on the dipolar coupling between A and B. Incrementing the starting position T of the inversion pulse induces a periodic modulation of spin A according to $V(T) = V(0)\cos(\omega_{dip}T)$, where $V(0)$ is the echo intensity at $T = 0$. A final π pulse at ω_A refocuses all, but dipolar interactions, yielding a refocused echo.

The resulting time-dependent signal is composed of the intramolecular interactions, $V(T)_{\text{intra}}$, between two spins in one molecule, as well as the intermolecular interactions, $V(T)_{\text{inter}}$, between spins in different molecules:[268]

$$V(T) = V(T)_{\text{intra}} \times V(T)_{\text{inter}}. \tag{2.28}$$

The fraction of inverted B spins, λ_{B} (also known as inversion efficiency of the pump pulse), can be quantified using[265,269]

$$V(T) = V(0)(1 - \lambda_{\text{B}}(1 - \cos(\omega_{\text{dip}}T)), \tag{2.29}$$

and depends on the excitation bandwidth, flip angle, pulse length, and frequency of the pump pulse.

For extraction of the distance from the obtained DEER trace, the initial step is the isolation of $V(T)_{\text{intra}}$ by removing the $V(T)_{\text{inter}}$ contributions with a background-correction function $B(T)$. The background-corrected DEER trace is also known as the form factor $F(T)$. In the absence of orientation selection, the final distance distribution can be obtained by the application of a Tikhonov regularization. The modulation depth is defined as

$$\Delta = 1 - (1 - \lambda_{\text{B}})^{(N-1)}, \tag{2.30}$$

where N is the number of coupled spins involved in an N-spin system with $N(N-1)/2$ pairwise distances. It can be obtained from the DEER trace after background subtraction, where the modulations of $V(T)_{\text{intra}}$ have dampened:

$$\Delta = 1 - F(T)(T \to \infty). \tag{2.31}$$

In the presence of multiple distinctly behaving spins with varying transversal relaxation times, T_2, a scaling factor needs to be introduced to account for the different signal intensities:

$$\Delta = \frac{\sum_i s_i x_i \Delta_i}{\sum_i s_i x_i}. \tag{2.32}$$

Some restrictions apply to this method particularly for distance determinations among polynuclear clusters. First, the electronic exchange coupling is assumed to be negligible for the above described approach. Thus, a point-dipole model may insufficiently account for systems with significant spin delocalization and the application of a local spin model has to be considered.[270] Second, the largest possible measured distance is limited by the phase-memory time T_m of the detect spin A,[242] as at least one oscillation period during time interval T is necessary for a reliable distance determination.

2.3 EPR Spectroscopy of Iron-Sulfur Clusters

Iron is a transition metal that can exist in four distinct oxidation states in biological systems: as Fe^{1+} in [FeFe]-hydrogenases, as Fe^{4+} in monooxygenases, but most commonly as Fe^{2+} and Fe^{3+}.[2] In FeS clusters, high-spin (hs) iron is usually pseudo-tetrahedrally coordinated by sulfur, which occurs either as inorganic sulfide (S^{2-}) or as thiolate sulfur (RS^{-}) stemming from cysteine residues.[271] The net charge of FeS clusters is calculated by the sum of the iron oxidation states and the number of sulfurs. Mononuclear [FeS] clusters, such as rubredoxins, have an $S = 5/2$ (Fe^{3+}, hs-d^5) and an $S = 2$ (Fe^{2+}, hs-d^6) state.[272] Depending on the amount of modular [FeS] building blocks, distinct spin states can be attained in polynuclear clusters due to exchange coupling and electron delocalization (Figure 2.7).[273]

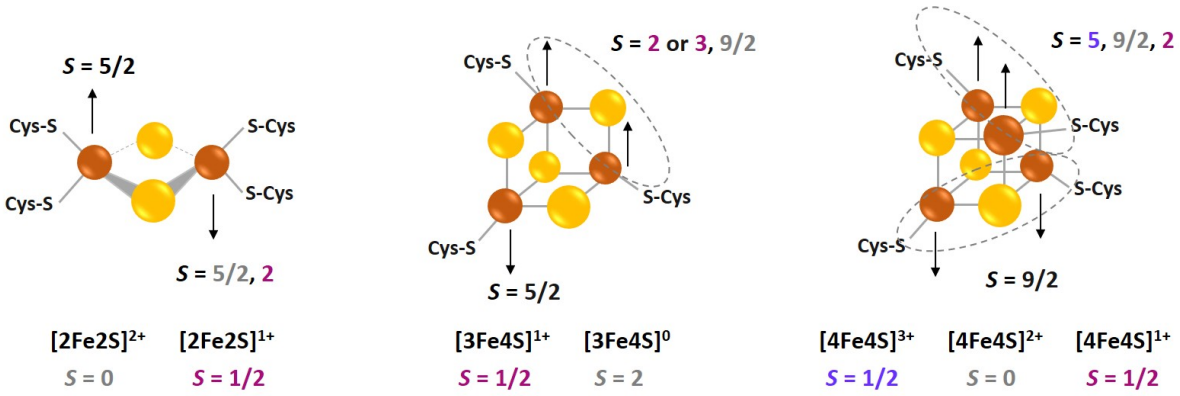

Figure 2.7: Structures of three distinct types of FeS clusters including spin states and orientations of individual iron sites and the resulting total spin states upon different oxidation states. Atomic coloring: Fe, orange; S, yellow.

Considering a simple diiron system with two spins, S_1 and S_2, a range of spin states can occur.[3,274] Heisenberg exchange coupling of the individual spin states (see also Section 2.1.3) yields a total spin S_t with values ranging from $| S_1 + S_2 |$ to $| S_1 - S_2 |$ with integer spacings and favors the antiferromagnetic (antiparallel) alignment of spins.[271] Thus, the spin ground state S of FeS clusters usually arises from antiferromagnetic alignment, resulting in localized valences.[273] For a mixed-valence dimer, such as $Fe^{2+}Fe^{3+}$, however, additional electron delocalization effects have to be considered.[271] The ferromagnetic (parallel) alignment has a bias towards electron delocalization, creating a $Fe^{2.5+}Fe^{2.5+}$ pair with two equivalent irons due to delocalized electron spin density between them. Electron delocalization is usually more pronounced in mixed-valence [3Fe4S] and [4Fe4S] clusters.[275] The competing effects of the antiferromagnetic alignment of the exchange coupling and the ferromagnetic alignment of the electron delocalization determine the local parameters of the individual iron sites.[276]

EPR Spectroscopy of [2Fe2S] Clusters Oxidized $[2Fe2S]^{2+}$ clusters are in general diamagnetic due to antiferromagnetic alignment of $Fe^{3+}Fe^{3+}$ ($S = 0$). The reduction of one iron leads to a paramagnetic state with localized electronic structure ($S = 1/2$).[273,277] A valence-delocalized $S = 9/2$ state due to ferromagnetic alignment was generated in thioredoxin-like Fdx by a ligand exchange from cysteine to serine.[278]

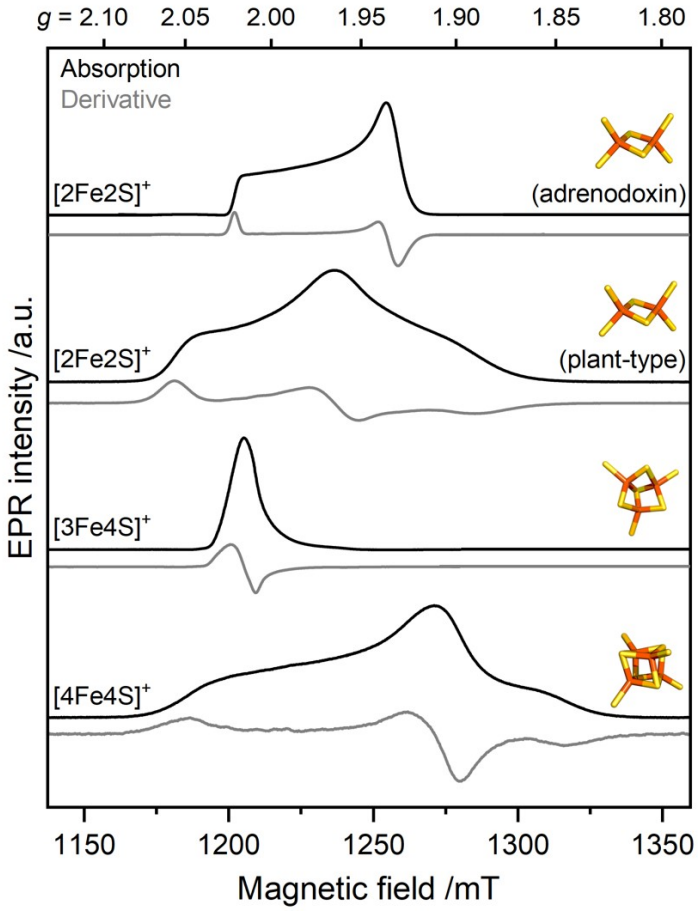

Figure 2.8: Pulsed EPR spectra (34 GHz, $T = 10 - 15K$) of distinct FeS clusters recorded as absorption spectra (black traces) normalized to their maximum signal amplitude and first-derivative spectra derived from pseudo-modulation (grey traces). The spectra from top to bottom originate from: adrenodoxin, plant-type ferredoxin Fdx1 from *C. reinhardtii*, oxidized HydF from *T. melanesiensis*, and apo-HydA1 from *C. reinhardtii*.

The g-tensor of the $S = 1/2$ state of a diirion center is given by:[36]

$$\boldsymbol{g}_{\mathrm{Fe}} = \tfrac{7}{3}\boldsymbol{g}_{\mathrm{III}} - \tfrac{4}{3}\boldsymbol{g}_{\mathrm{II}}, \tag{2.33}$$

where $\boldsymbol{g}_{\mathrm{III}}$ and $\boldsymbol{g}_{\mathrm{II}}$ are the local g-tensors of Fe^{3+} and Fe^{2+}, respectively. Fe^{3+} is relatively insensitive to its coordination environment.[249] The d^5 electrons of Fe^{3+} have a spherical electron distribution resulting in an isotropic hyperfine coupling.[41] As the spin orbit coupling is relatively small, the $\boldsymbol{g}_{\mathrm{III}}$-tensor is approximately 2.[249] For Fe^{2+}, the orbital contribution to the magnetic moment is larger due to the unsymmetrical electron distribution of its hs d^6 configuration.[41] The resulting strong anisotropy, where the strongest hyperfine coupling is observed along g_1, yields a larger deviation of up to -0.2 from 2. The $\boldsymbol{g}_{\mathrm{II}}$-tensor dominates the range of $\boldsymbol{g}_{\mathrm{Fe}}$ values resulting in $\boldsymbol{g}_{\mathrm{Fe}} < 2.0$.[249]

Thus, EPR spectra of [2Fe2S] clusters can be classified according to their average g-value, g_{av}, that is influenced by the cluster's protein and ligand environment.[279] Plant-type [2Fe2S] clusters often exhibit a rhombic EPR spectrum where $g_{av} \approx 1.96$ (Figure 2.8). Rieske-type [2Fe2S] clusters, however, have usually lower g-values where $g_{av} \approx 1.91$.[280] Putidaredoxin and human Fdx, also called adrenodoxin, are more axial with a narrower linewidth (Figure 2.8).[49]

EPR Spectroscopy of [3Fe4S] Clusters The trinuclear clusters are rarer found, e.g., in bacteria or as a product of oxidative damage to [4Fe4S] clusters in proteins.[86] In their reduced state [3Fe4S] clusters have a ground state $S = 2$.[279] Upon oxidation, antiferromagnetic exchange interactions among the three $S = 5/2$ Fe^{3+} sites result in a $S = 1/2$ ground state. This spin state is derived from exchange coupling of two Fe^{3+} yielding $S = 2$ or 3 and its coupling with the remaining Fe^{3+} resulting in $S = 1/2$. The intra-cluster exchange coupling and partial delocalization in between the Fe ions lead to alternative charge distributions on distinct iron pairs, known as valence isomerism.[275] Here, two distinct $S = 1/2$ states can exist, which can be each described by a set of spin coupling coefficients $\{K_i\}$, also known as spin projection factors.[14,279] Provided that the ground and excited states are sufficiently separated, the g-tensor is obtained by

$$g_{\mathrm{Fe}} = \sum K_i' g_i, \tag{2.34}$$

where g_i are the local g-tensors and the K_i' values can be determined, e.g., from Eq. 2.33, and depend on K_i and J_i.[279] The resulting g-values for [3Fe4S] clusters are in the range of $2.08 - 1.97$, when inserting the g-values of tetrahedral coordinated Fe^{3+}.[279] Indeed, oxidized $[3Fe4S]^{+}$ clusters generally show a characteristic $g_{av} \approx 2.01$ value and an asymmetric lineshape (Figure 2.8).[277,280] In general, two distinct forms can be distinguished based on their g-anisotropy and relaxation behavior.[37,279] Those unusual properties, observed for the rather environmentally insensitive Fe^{3+} ions, are suggested to arise from admixing with low-lying excited states refuting Eq. 2.34.

EPR Spectroscopy of [4Fe4S] Clusters The [4Fe4S] clusters can form three stable oxidations states *via* single electron transfers ranging from $[4Fe4S]^{1+}$ to $[4Fe4S]^{3+}$. The $[4Fe4S]^{2+}$ cluster can be pictured as two antiferromagnetically coupled layers, where each layer consists of a ferromagnetically coupled, delocalized $Fe^{2.5+}$ pair.[273] The antiferromagnetic coupling of the two layers yields a total spin $S = 0$, that changes with the addition or removal of electrons. The $[4Fe4S]^{1+}$ cluster, for example, consist of two $Fe^{2.5+}$ antiferromagnetically coupled to two Fe^{2+} ions ($S = 1/2$), where the additional electron is partially delocalized and resides on a pair of Fe ions.[275] Thus, there are six different arrangements of Fe ions forming a mixed-valence pair, and in turn six possible valence isomers exist, which are energetically inequivalent. Changes in the first coordination sphere of [4Fe4S] clusters were shown to impact the distribution of valence isomers.[275] The $[4Fe4S]^{3+}$ has a $S = 1/2$, that is well separated from higher energy states, whereas the $[4Fe4S]^{1+}$ cluster can attain ground states with $S = 1/2, 3/2$ and $7/2$, with lower lying excited states.[273] Moreover, ligand exchange, solvent effects, and asymmetries can promote exchange coupling resulting in valence localized $Fe^{2+}Fe^{3+}$ pairs.[249] Similar electronic arrangements are observed for the $[3Fe4S]^{0}$ and $[3Fe4S]^{1+}$ pair.[3] These variations in spin localization and charge are reflected in the distinct electronic and magnetic properties of the polynuclear cluster states, which are difficult to generalize. The $[4Fe4S]^{1+} \leftrightarrow [4Fe4S]^{2+}$ couple has a low redox potential and belongs to the 'classical' FeS clusters. The line shape of the EPR-active reduced clusters is similar to those of rhombic $[2Fe2S]^{1+}$ clusters and characterized by $g_1 \approx 2.03 - 2.10$ and $g_{2,3} \approx 1.96 - 1.85$ (Figure 2.8).[49,277] The $[4Fe4S]^{2+} \leftrightarrow [4Fe4S]^{3+}$ couple is usually found in High Potential Iron-Sulfur Proteins (HiPIPs), which have a completely different protein structure and exhibit comparably high redox potentials.[49] The oxidized $[4Fe4S]^{3+}$ site ($S = 1/2$) displays an axial EPR signal with $g_1 \approx 2.11 - 2.14$ and $g_{2,3} \approx 2.04$.[280]

As is evident from Figure 2.8, the spectral line shapes of [2Fe2S] and [4Fe4S] clusters, can be very similar. The relaxation times of isolated FeS clusters increase in the following order: $FeS^{+} > [2Fe2S]^{1+} > [3Fe4S]^{1+} > [4Fe4S]^{3+} >$ ferredoxin-type $[4Fe4S]^{1+}$, and thus, can be used as a hint for identifying an unknown cluster.[277] The relaxation times of the mononuclear cluster are the slowest due to weak coupling with the lattice and very large ligand-field energy.[50] Two different situations are encountered for [3Fe4S] clusters, where fast- and slow-relaxing centers (relaxation broadening starting from 9 or 100 K) are observed.[279] $[4Fe4S]^{1+}$ clusters interact stronger with the lattice than $[4Fe4S]^{+3}$ clusters because of their 'ferrous' character, resulting in a faster relaxation rate.[50] However, this is not generally true for simple or polynuclear FeS clusters due to additional effects, such as exchange interactions.[281] Moreover, there are a few examples of [2Fe2S] and [4Fe4S] clusters with equal relaxation rates at cryogenic temperatures, wherefore the relaxation rate can be an unreliable factor.[50]

The subsequent chapters describe the results of the presented methods applied for the investigation of FeS clusters and their role in distinct enzymes.

3

Fine-tuning of FeS proteins Monitored via Pulsed EPR Redox Potentiometry at Q-band

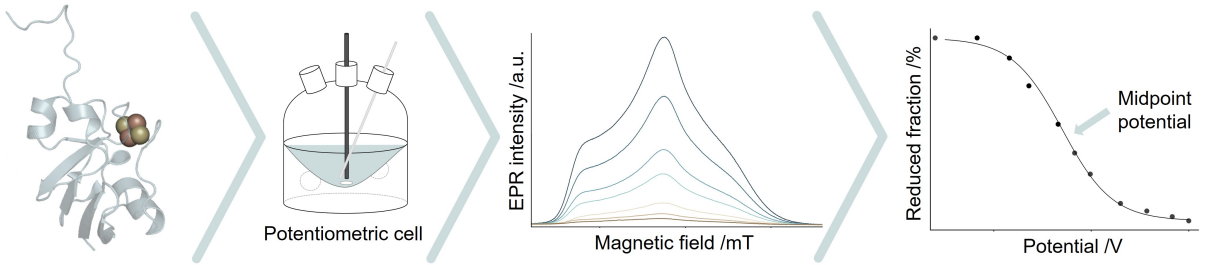

This research was originally published as:

Heghmanns, M., Günzel, A., Brandis, D., Kutin, Y., Engelbrecht, V., Winkler, M., Happe, T., and Kasanmascheff, M., *Fine-tuning of FeS proteins monitored via pulsed EPR redox potentiometry at Q-band*, 2021, Biophysical reports, 1, (2), 100016.

- Alexander Günzel expressed and purified all *Cr*Fdx isoforms and variants
- I performed the redox potentiometries and EPR experiments of wild-type *Cr*Fdx isoforms and analyzed all spectrosopic data
- Dörte Brandis performed the redox potentiometries and EPR experiments of *Cr*Fdx1 variants and analyzed the spectrosopic data under my supervision
- I wrote the first draft of the manuscript and was involved in further editing
- Yury Kutin, Vera Engelbrecht, Alexander Günzel and Müge Kasanmascheff edited the manuscript
- All authors discussed the results and commented on the manuscript

Biophysical Reports

ARTICLE

Fine-tuning of FeS proteins monitored via pulsed EPR redox potentiometry at Q-band

Melanie Heghmanns,[1] Alexander Günzel,[2] Dörte Brandis,[1] Yury Kutin,[1] Vera Engelbrecht,[2] Martin Winkler,[2] Thomas Happe,[2,*] and Müge Kasanmascheff[1,*]

[1]TU Dortmund University, Department of Chemistry and Chemical Biology, Dortmund, Germany and [2]Ruhr University Bochum, Faculty of Biology and Biotechnology, Photobiotechnology, Bochum, Germany

ABSTRACT As essential electron translocating proteins in photosynthetic organisms, multiple plant-type ferredoxin (Fdx) isoforms are involved in a high number of reductive metabolic processes in the chloroplast. To allow quick cellular responses under changing environmental conditions, different plant-type Fdxs in *Chlamydomonas reinhardtii* were suggested to have adapted their midpoint potentials to a wide range of interaction partners. We performed pulsed electron paramagnetic resonance (EPR) monitored redox potentiometry at Q-band on three Fdx isoforms for a straightforward determination of their midpoint potentials. Additionally, site-directed mutagenesis was used to tune the midpoint potential of *Cr*Fdx1 in a range of approximately −338 to −511 mV, confirming the importance of single positions in the protein environment surrounding the [2Fe2S] cluster. Our results present a new target for future studies aiming to modify the catalytic activity of *Cr*Fdx1 that plays an essential role either as electron acceptor of photosystem I or as electron donor to hydrogenases under certain conditions. Additionally, the precisely determined redox potentials in this work using pulsed EPR demonstrate an alternative method that provides additional advantages compared with the well-established continuous wave EPR technique.

WHY IT MATTERS In this work, we determined midpoint potentials of distinct ferredoxin isoforms found in *Chlamydomonas reinhardtii* using pulsed electron paramagnetic resonance spectroscopy at Q-band. Site-directed mutagenesis was used to tune the midpoint potential of ferredoxin 1, known as PetF, in a range of −338 to −511 mV. Our results serve as a basis to design new experiments for unraveling the distinct functions of ferredoxin isoforms and illuminate the decisive role of individual positions in the secondary ligand sphere of the cofactor in tuning the midpoint potential of redox proteins.

INTRODUCTION

Proteins containing iron-sulfur (FeS) clusters are one of the major electron transfer protein classes in biology (1–3). The midpoint potential (E_m) difference between an FeS protein and its partner determines the kinetics and efficiency of electron transfer reactions (4,5). The redox range of FeS proteins is wide and mostly dictated by the protein environment in the immediate vicinity of the bound FeS cluster (6–9). Developing methods for precise measurements of E_m and determining factors that affect its magnitude are therefore important first steps toward understanding structure-function relationships that control electron transfer processes in both native and rationally designed proteins.

Primary ligands play a major role in the coarse adjustment of the E_m range of FeS clusters. Long-range protein effects and interactions of the metal cluster with the secondary coordination sphere fine-tune the E_m values and thus electron transfer processes (8,10). Multiple types of interactions have been shown to drastically influence the potentials of metal centers in protein environments, including hydrogen bonding interactions, hydrophobicity and solvent exposure, aromatic interactions, and net charge effects (10–12).

Ferredoxins (Fdxs) are ubiquitous FeS proteins that function as electron acceptors and donors in diverse metabolic pathways. Interestingly, the evolution of more complex FeS proteins is discussed to have started

Submitted May 20, 2021, and accepted for publication August 30, 2021.

*Correspondence: thomas.happe@rub.de or muege.kasanmascheff@tu-dortmund.de

Melanie Heghmanns and Alexander Günzel contributed equally to this work.

Editor: Paul Schanda.

https://doi.org/10.1016/j.bpr.2021.100016

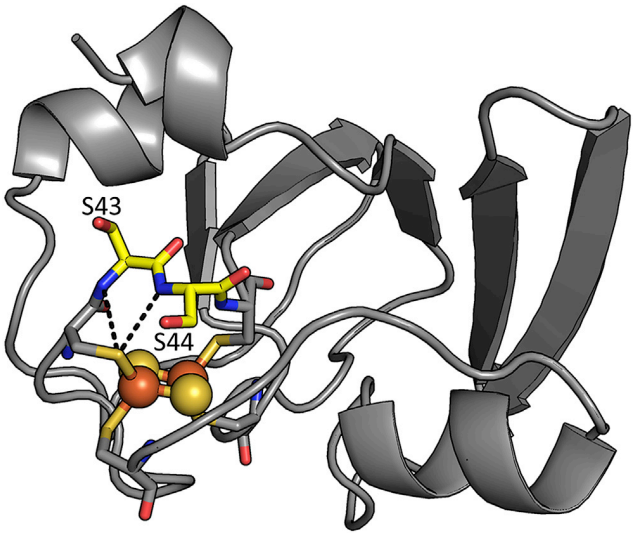

FIGURE 1 Cartoon structure of *Cr*Fdx1 (Protein Data Bank, PDB: 6lk1). [2Fe2S] cluster with ligating cysteines shown as a ball and stick model. Serine 43 and serine 44 are shown as yellow sticks. Potential hydrogen bonds from amide nitrogen atoms (*blue*) to sulfur atoms (*dark yellow*) of the ligating cysteine are shown with black dashed lines.

from ancient Fdxs, which were incorporated into larger electron transfer chains or adapted toward metallocofactors of higher complexity (13). Plant-type Fdxs, which are mainly found in the chloroplasts of photosynthetic algae, cyanobacteria, and higher plants (14), are characterized by their relatively low midpoint potentials ranging from −230 to −420 mV (15). Their [2Fe2S] cluster in its oxidized state has usually two high-spin Fe^{3+} ions ($S = 5/2$) antiferromagnetically coupled, yielding a total spin $S_T = 0$ in the ground state. Upon reduction of one Fe^{3+} ion to high-spin Fe^{2+} ($S = 2$), the ground state has a total spin $S_T = 1/2$, producing a paramagnetic species with a localized electronic structure that can be identified and characterized via electron paramagnetic resonance (EPR) spectroscopy (16,17). As small (∼10 kDa) and soluble metalloproteins having the same fold and FeS cluster binding motif (3), the versatile plant-type Fdxs are effective models for assessing the influence of the protein surroundings on FeS clusters.

The unicellular green alga *Chlamydomonas reinhardtii* (Cr) is known to provide an unusual wealth of 12 different Fdx isoforms (*Cr*Fdx1–12) (18,19). All genes encode for plant-type Fdxs with characteristic [2Fe2S] clusters and a conserved binding motif (Fig. 1) (20). Thus far, only some of the *Cr*Fdx isoforms were assigned to specific functions and interaction partners under certain environmental conditions. The most abundant isoform *Cr*Fdx1, also known as PetF, plays an essential role as an electron acceptor of photosystem I (21,22). Under anaerobiosis and nutrient deprivation, *Cr*Fdx1 becomes the electron donor to the hydrogenase HydA1, which catalyzes the reversible reduction of H^+ to H_2 (23). Furthermore, *Cr*Fdx2–5 are suggested to be involved in nitrite reduction, nitrogen assimilation, glycolysis, and hydrogenase maturation, respectively (24–26). E_m values of *Cr*Fdx1 (−410 mV (22)) and *Cr*Fdx2 (−331 mV (26)), which have been determined previously by distinct methods, such as cyclic voltammetry, ultraviolet-visible spectroscopy (UV/Vis), and continuous wave (cw) EPR-monitored redox titrations, differ substantially (22,25,26). By comparing the sequences and structures of these Fdxs, Boehm et al. (26) were able to shift the E_m of *Cr*Fdx2 closer to that of *Cr*Fdx1 by exchanging a single amino acid. The same mutation also led to shifts in detected *g*-values, indicating the role of this residue in fine-tuning the electronic properties of the [2Fe2S] cluster residing in *Cr*Fdx2. Yet electrochemical data on the other isoforms is scarce.

Cyclic voltammetry, UV/Vis, and EPR-monitored redox potentiometry are established and highly effective methods for the determination of E_ms of Fdxs (11,27–29). EPR spectroscopy serves to monitor the spectral changes during oxidation-reduction reactions that are driven by the mediated application of defined potentials on redox proteins with at least one paramagnetic state (30). Additionally, it provides structural insights into the protein under study while simultaneously enabling the deconvolution of multiple redox-active species in one protein. In contrast to UV/Vis, EPR-monitored redox potentiometry overcomes the difficulty of separating the contribution from most mediator dyes and is more precise, particularly for Fdxs as they exhibit low extinction coefficients. Moreover, misinterpretations because of background signals or minor impurities can be avoided by comparing the experimental and simulated EPR data.

Herein, we determined the unknown midpoint potential of the isoform *Cr*Fdx3 using pulsed EPR spectroscopy at Q-band (34 GHz). As it was suggested that *Cr*Fdx3 might interact with the [FeFe]-hydrogenases HydA1 and HydA2 from *C. reinhardtii* (24), its redox properties are of high interest. Furthermore, we investigated the effect of substituting specific amino acids surrounding the [2Fe2S] cluster on the midpoint potential of *Cr*Fdx1. This enabled us to identify S43 as a key position to fine-tune the midpoint potential in *Cr*Fdx1 and thus presented a new target for future studies aiming to modify its catalytic activity.

MATERIALS AND METHODS

Protein expression and purification

The *C. reinhardtii* sequences encoding ferredoxins *Cr*Fdx1 (National Center for Biotechnology Information accession number XP_001692808.1), *Cr*Fdx2 (XP_001697912.1), and *Cr*Fdx3 (XP_001691381.1) were amplified from complementary DNA isolated out of total RNA from

culture samples of *C. reinhardtii* strain CC-124. In all cases, known or predicted sequences that may encode transit peptides were omitted. *Cr*Fdx sequences were cloned into vector pASK-IBA7, following a sequence encoding an N-terminal Strep-tagII and a factor Xa cleavage site, according to manufacturer recommendations (IBA Lifesciences, Göttingen, Germany; www.iba-lifesciences.com).

Expression constructs for site-directed mutagenesis variants of *Cr*Fdx1 were generated following the procedure described in the QuikChange-PCR manual from Agilent Technologies (Santa Clara, CA), using the corresponding 5′ overlapping mismatch primer pairs (Table S1).

For the heterologous expression of the different Fdx isoforms and mutagenesis variants, electrocompetent *Escherichia coli* BL21(DE3) ΔiscR cells were transformed using the respective expression construct. 4 L Vogel-Bonner medium was inoculated with overnight grown LB-preculture to an OD_{550} of 0.05 (31). Main cultures were grown at 37°C in a shaking incubator (180 rpm) until an OD_{550} of 0.5 was reached. Gene expression was induced by adding anhydrotetracycline to a final concentration of 0.2 $\mu g \times mL^{-1}$, and expression cultures were kept for 16 h at 20°C in a shaking incubator (180 rpm) until cell harvest. Cells were harvested by centrifugation (20 min, 9000 g, and 4°C), and cell pellets were resuspended in 0.1 M Tris-HCl (pH 8). Cell disruption was carried out by ultrasonication, and the resulting cell lysate was centrifuged at 165,000 g for 1 h at 4°C. The supernatant was filtered using sterile syringe filters (0.2-μm pore size; SARSTEDT, Newton, NC). The recombinant proteins were purified via affinity chromatography using StrepTag Superflow high-capacity gravity flow columns (IBA Lifesciences), according to manufacturer's recommendations, and concentrated using Amicon Ultracel filters with a 10 kDa cutoff (Merck Millipore, Burlington, MA). Protein concentration was determined via UV/Vis spectroscopy (BioPhotometer D30 from Eppendorf, Hamburg, Germany www.eppendorf.com) at 420 nm applying the Beer-Lambert Law and using a molar extinction coefficient of 9.7 $mM^{-1} \cdot cm^{-1}$ (32). Until further use, all proteins were stored at −80°C in 0.1 M Tris-HCl (pH 8). Fdx from *Spinacia oleracea* (*So*Fdx) and the remaining chemicals used for protein expression and purification were purchased from Sigma-Aldrich (St. Louis, MO).

Redox potentiometry

The FeS cluster occupancy of the purified Fdxs was calculated before each experiment by measuring the absorbance at 420 nm via UV/Vis spectroscopy (NanoDrop 1000; Thermo Fisher Scientific, Waltham, MA). Redox titrations were performed in an anaerobic vinyl tent (~20 ppm O_2; Coy Laboratory Products, Grass Lake, MI) equipped with an electrochemical glass cell (scientific glassblowing service; TU Dortmund University, Dortmund, Germany) built according to the description provided by Wright et al. (29). A final concentration of 200 μM cluster-occupied Fdxs in titration buffer (60 mM HEPES, 40 mM potassium phosphate buffer, and 150 mM NaCl (pH 7.5)) and the following redox mediator dyes of methyl viologen (200 μM), benzyl viologen (200 μM), and 100 μM each of neutral red, safranin O, sodium anthraquinone-2-sulfonate, phenosafranin, and 2-hydroxy-1,4-naphthoquinone were added to the cell. The overall volume of solution within the cell was 770 μL. Under constant stirring, the solution potential was altered by microliter additions of either 2 or 20 mM sodium dithionite (NaDT) solution (reductive titration) or potassium ferricyanide solution (oxidative titration). The potential difference was monitored with a potentiostat (PalmSense4; PalmSens, Houten, the Netherlands) connected to a glass-encased platinum wire, functioning as a working electrode (scientific glassblowing service; TU Dortmund University), and an Ag/AgCl microreference electrode with a 6-mm diameter (Redoxme, Norrköping, Sweden) calibrated with Zobell's solution (33) or a commercially available Ag/AgCl electrode. All herein reported potentials, E_h, are in reference to the standard hydrogen electrode. The potential was altered in ~30 mV steps. After stabilization of ~5–10 min at a given potential, 70 μL of the sample solution was transferred to a 2.8 mm EPR tube (quartz glass capillary ilmasil) and immediately flash frozen in liquid nitrogen. Nine samples were usually withdrawn for each potentiometry series. In addition, an external 200 μM standard of the respective protein was prepared and reduced with 10 mM NaDT for comparison of the spin concentrations.

cw EPR spectroscopy

X-band cw EPR measurements were performed at 15 K using a Bruker ELEXSYS E500 spectrometer equipped with a Bruker ER 4116DM resonator (Bruker, Billerica, MA), Oxford Instruments ESR 900 cryostat (Abingdon, UK), and ITC503 temperature controller. The microwave power level used was 0.63 mW, and magnetic field modulation amplitude was 7 G. The spectra were recorded under nonsaturating conditions.

Q-band cw EPR measurements were performed at 15 and 25 K using a Bruker ELEXSYS E580 spectrometer equipped with a home-built Q-band cw EPR intermediate frequency unit, Bruker ER 5106 resonator, Oxford instruments CF 935 cryostat, and ITC503 temperature controller. The microwave power was in the range of 0.02–20 mW, and magnetic field modulation amplitude was 5 G.

Pulsed EPR spectroscopy

Pulsed EPR (electron spin echo-detected EPR) field-sweep experiments, using a two-pulse Hahn spin echo sequence $\pi/2-\tau-\pi-\tau-$echo without phase cycling, were carried out on a Bruker ELEXSYS E580 Q-band EPR spectrometer equipped with an Oxford Instruments CF935 cryostat and Oxford Instruments MercuryiTC temperature controller. The temperature was kept at 15 K with a sufficiently high flow of liquid He. The Bruker ER 5106QT-2 resonator was critically coupled with the inserted sample height spanning the entire length of the cavity. For comparison of signal intensities, all spectra of a respective sample batch were recorded on the same day under optimized, similar conditions concerning the shot repetition time, pulse lengths, microwave power, τ, and acquisition trigger parameters. The $\pi/2$- and π-pulse lengths varied between 8–11 and 16–22 ns, respectively, whereas τ was kept between 600 and 650 ns and the shot repetition time between 300 and 600 ns, depending on the Fdx type. Either one or two scans with 100 shots/point were accumulated, chosen based on the concentration of the reduced Fdx species. The measurement time varied accordingly between 1.3 and 2.5 min/scan. The phase memory time T_m was measured via a two-pulse echo decay experiment using a $\pi/2-\tau-\pi-\tau-$echo sequence. The relaxation curves were fitted with a stretched exponential function using MATLAB (The MathWorks, Natick, MA). The original pulsed EPR spectra are shown in Fig. S3.

Validation of pulsed EPR at Q-band as an accurate method for determining redox potentials

To validate pulsed EPR as a method for determining redox potentials, the midpoint potential of the well-characterized *So*Fdx was investigated. The rhombic EPR spectrum arising from the reduced [2Fe2S] cluster of *So*Fdx was simulated with $g_{1,2,3} = 2.05, 1.96, 1.89$ (Fig. S1; Table S2), which are in great agreement with the literature values (34). Oxidative potentiometric titrations with *So*Fdx were performed via cw and pulsed EPR spectroscopy at X- and Q-band, respectively (Fig. S2). Both X-band cw and pulsed Q-band EPR spectra of the redox titration series suffered from distinct

background impurities (Figs. S1 and S3). Potential-dependent contributions from the mediator mix, as well as from low amounts of free Mn^{2+} present in the buffer, hampered the uniform background subtraction. Therefore, the EPR intensity of the spectral component at $g_3 = 1.89$, which is well separated from the impurity signals, was used to compare the fractions of the reduced species within a series of titration samples (Fig. S1). The fits to the one-electron Nernst equation, which were almost identical for cw and pulsed EPR measurements, resulted in $E_{m,7.5} = -394 \pm 7$ and ± 5 mV, respectively. A plot of the redox potentials against the logarithm of the concentration ratio of oxidized to reduced (log([Ox]/[Red])) Fdx yields the number of electrons transferred, *n*. Low *n* values can be an indicator of incomplete equilibration during redox potentiometry. The *So*Fdx data set yields $n = 1.02$ (inset in Fig. S2), which is in excellent agreement with the expected one-electron transfer reaction. For the quantitative pulsed EPR measurements, several points were considered. In general, an overcoupled resonator is used for Q-band pulsed EPR experiments, but we found the spectral intensities were often poorly reproducible. To circumvent this issue, we performed the experiments with a critically coupled resonator to maximize the reproducibility. As a result of the high-quality factor, *Q*, pulse microwave power took longer to dissipate and thus required a longer interpulse delay, τ. To control for possible changes in the phase memory time T_m and its effect on the electron spin echo signal intensity, echo decay experiments were carried out for each sample in the series. The T_m time was found to be nearly constant under the varying potential E_h, and thus, its influence on the obtained E_m value was negligible (Figs. S4 and S5; Table S3). This may not be the case for other systems, and we note that the T_m relaxation time needs to be taken into account when pulsed EPR is used for spin quantification. The determination of T_m and the subsequent correction of midpoint potentials, however, is a quick and simple procedure, as explained in the discussion of Table S3.

Here, the identical E_m values obtained from the two datasets established that cw EPR at X-band and pulsed EPR at Q-band are equivalent for quantitative analysis.

Spectral analysis

The EPR spectra were baseline corrected using MATLAB. The absorption spectra were pseudomodulated (modulation amplitude of 3 G) and subsequently simulated with *EasySpin* (35) for a straightforward analysis of *g*-values, where g_1 corresponds to the low-field spectral feature and g_3 to the high-field one. To exclude any background contributions, the simulated pseudomodulated spectra were integrated, if not stated otherwise, over the whole spectral range for the determination of spin concentrations (36). The obtained intensities were then corrected for dilution and compared to the standard sample (of the same Fdx type) showing the highest spectral intensity within the experimental uncertainty. The spin concentration of the standard was set to 100%, whereas the respective potential was chosen to be −0.47 V according to the E_m of NaDT (37). The fractions of the reduced species were plotted against the corresponding potentials E_h. The data were fitted to the Nernst equation:

$$y(x) = \frac{100}{1 + e^{((x-E_m)/Q)}}$$

yielding the midpoint potential E_m (in volts) for a one-electron transfer, with $Q = (RT)/(nF)$ (*R*, universal gas constant; *T*, temperature in Kelvin; *n*, number of electrons transferred; and *F*, Faraday constant) (38).

A semi-log plot of E_h versus the common logarithm of the concentration ratio of oxidized ([Ox]) to reduced ([Red]) Fdx yielded the E_m from the *y*-intercept of the line according to:

$$E_h = E_m + 2.3026 \cdot Q \cdot log \frac{[Ox]}{[Red]}$$

The slope, *b*, was used to calculate the number of electrons transferred, *n*, with $b = 0.059$ V/*n* at 25°C (30,38). The error of the Nernst fit is given within 95% confidence interval. It comprises changes in temperature (±0.3 mV), pH (±1.2 mV), and electrode calibration (39). Errors occurring because of protein denaturation and/or evaporation during the redox titration were averaged out by performing two, namely oxidative and reductive, titrations.

RESULTS

EPR characterization and midpoint potentials of *C. reinhardtii* ferredoxin isoforms

To identify and characterize the [2Fe2S] clusters of the ferredoxin isoforms, we recorded pulsed EPR spectra of *Cr*Fdx1-3 at Q-band. The first-derivative line shapes of the recorded EPR spectra are shown in Fig. 2 *A*. Note that Q-band cw experiments failed to detect EPR signals of at least two isoforms (*Cr*Fdx3 EPR data are shown exemplarily in Fig. S6). A similar observation was reported previously for a different system (40).

All spectra indicate a rhombic symmetry with three principal *g*-values. The *g*-values were determined via spectral simulations, for which *g*-strain was used to fit the linewidths (Table S2). The obtained *g*-values, which varied slightly among the isoforms ($g_1 = 2.048–2.061$, $g_2 = 1.955–1.971$, and $g_3 = 1.879–1.890$), were all in the range for typical [2Fe2S] clusters (17). These differences are attributed to the distinct tetrahedral environment of the ferrous ion (41). Additional physical differences between the *Cr*Fdx isoforms were examined by comparing the width of the g_3 component, rhombicity $\eta = (g_2 - g_3)/(g_1 - g_{iso})$, g_{iso}, and the parameter $\chi = g_2 - g_3$ (Table S2). Wide g_3 peaks and high χ-values indicate enhanced flexibility of the [2Fe2S] cluster (41). η and g_{iso} are correlated with structural changes of the active site and spin localization within the cluster, respectively (41–43). Small deviations of these parameters are expected as the redox-active centers reside in distinct proteins. Their high overall similarity, however, strongly indicates similar spin localization and structural environments of the [2Fe2S] clusters (Table S2).

Next, we determined the E_m values of each Fdx isoform. The Nernst plots obtained by oxidative and reductive redox titrations monitored via pulsed EPR at Q-band are shown in Fig. 2 *B* (see Fig. S3 for details). We note that the determined E_m values of *Cr*Fdx1 ($E_{m,7.5} = -419$ mV) and *Cr*Fdx2 ($E_{m,7.5} = -332$ mV) are in great agreement with the previously reported values (Table S4) (22,25,26). The E_m of *Cr*Fdx3 that is determined here for the first time is

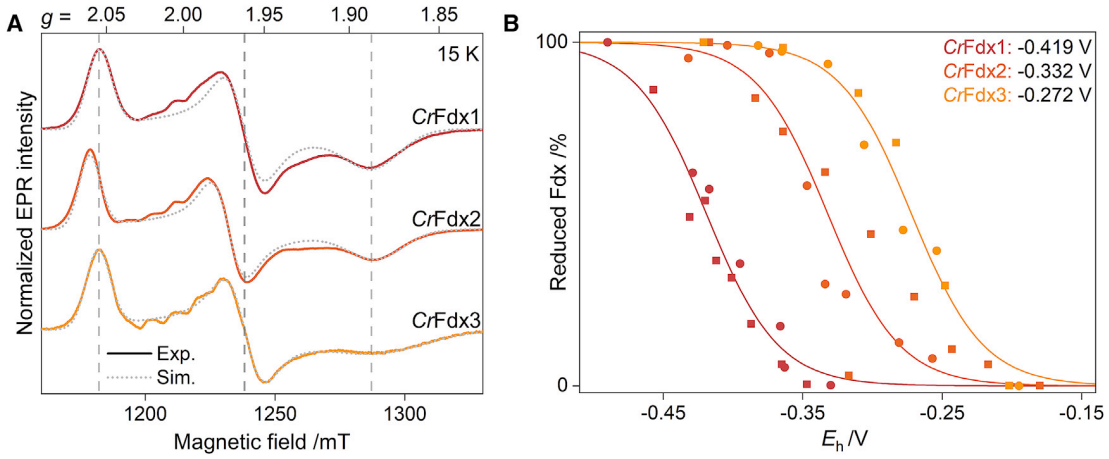

FIGURE 2 (*A*) Comparison of normalized Q-band pseudomodulated pulsed EPR spectra of *Cr*Fdx isoforms. The isoforms were reduced with 10 mM NaDT, and the corresponding simulations are shown with dotted gray lines. The principal *g*-values of *Cr*Fdx1 are marked with vertical dashed lines. Simulation parameters are listed in Table S2. (*B*) Titration curves of the reductive (*circles*) and oxidative (*squares*) redox potentiometry series of the three *Cr*Fdx isoforms monitored via pulsed EPR spectroscopy at Q-band. The reduced Fdx fractions were obtained by double integration of the simulated pseudomodulated pulsed EPR spectra. The data points were fitted to the one-electron Nernst equation yielding the midpoint potential.

−272 mV. Surprisingly, the midpoint potential of this isoform is not only substantially higher than that of *Cr*Fdx1 ($E_{m,7.5} = -419$ mV) but also remarkably high for plant- and cyanobacterial-type Fdxs (25). A comparable $E_{m,7.5} = -243$ mV was recently obtained for the cyanobacterial Fdx2 from *Synechocystis sp.* PCC 6803 (44).

We note that the oxidative and reductive titrations of *Cr*Fdx1–3 resulted in almost identical Nernst fits (Fig. 2 *B*). The results of both titrations were combined before fitting to the one-electron Nernst plots. The semi-log plot analysis yielded $n = 1 \pm 0.1$ for all isoforms validating a poised redox titration.

EPR characterization and midpoint potentials of *Cr*Fdx1 variants

Fig. 1 shows the active site region of *Cr*Fdx1 (45). The highlighted positions S43 and S44 are located in the cluster binding loop region of *Cr*Fdx1 and thus are in proximity to the [2Fe2S] cluster. Whereas S44 is more or less pointing toward the FeS cluster, the hydroxyl group of S43 faces away from it. However, as the loop region of *Cr*Fdx1 is known to be very flexible, which is believed to be important in terms of minimizing the reorganization energy required for rapid electron transfer, the orientation of the side chains at these positions will most likely change in solution. Both primary amides of the protein backbone are situated close enough to one of the bridging cysteine sulfides (3.3 Å) to form a hydrogen bond as part of the NH-S hydrogen bond network unique to plant-type PetF, thus delocalizing the electron density of the cluster (46).

Because of their proximity to and their influence on the FeS cluster, these positions were targeted by site-directed exchange mutagenesis; exchanges to different properties (charge, polarity, size, and hydrophobicity) were implemented for protein variants S43A, S43D, S44D, S44G, and S44R. Subsequently, pulsed Q-band EPR spectra were recorded for all *Cr*Fdx1 variants (Fig. 3). As expected, their rhombic spectra revealed slightly shifted *g*-tensor values in comparison to the wildtype, indicating that the electronic environment of the [2Fe2S] cluster has changed (Table S2). Whereas S44G and S44R exhibit negligible differences in the *g*-tensor values, those of S43A and S44D deviate significantly. Analysis of the EPR spectra did not reveal any correlation between the observed shifts in *g*-values and type and/or position of the mutated amino acids. The detected changes in midpoint potentials of all S44 variants are negligible, whereas S43A and S43D show the highest deviations from the midpoint potential of *Cr*Fdx1 of +80 and −93 mV, respectively (Fig. 3; Table 1). We note that the actual midpoint potential of S43D is possibly even more negative because the midpoint potential of dithionite limited the lowest achievable potential for this variant (37). The potential shift of S43A and S43D goes along with distinct shifts in *g*-values and g_3, respectively (see Fig. 4). For the other variants, no simple correlation between midpoint potential and respective shifts of the *g*-values is observed. Furthermore, S43A presents the highest rhombicity and flexibility among *Cr*Fdx1 variants. In contrast, S43D displays the lowest rhombicity and flexibility.

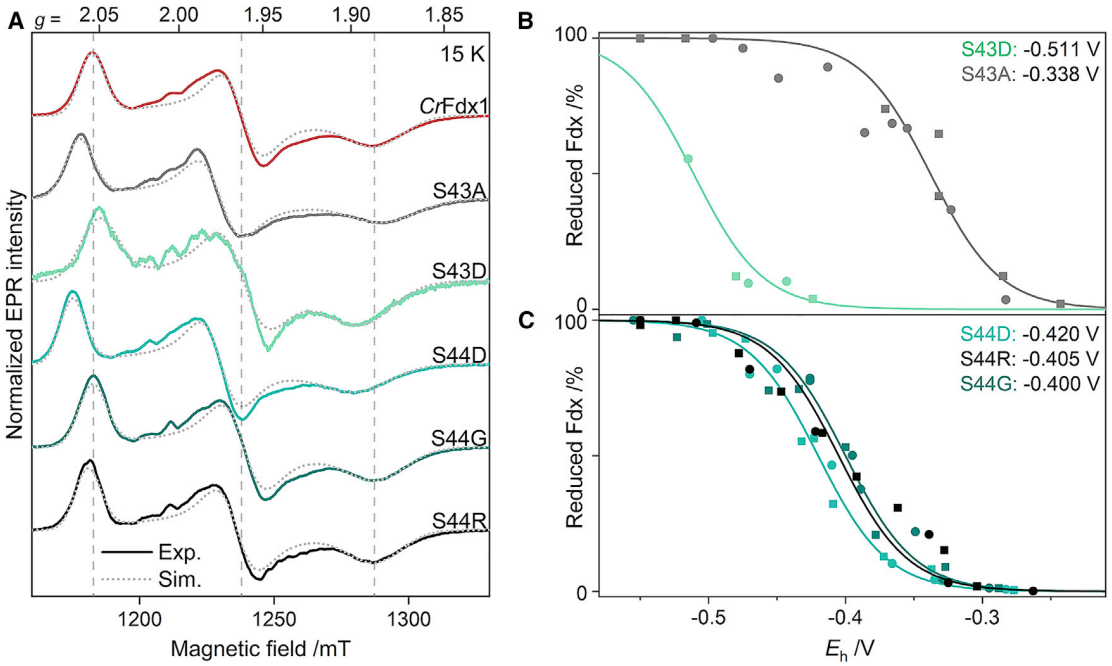

FIGURE 3 (*A*) Comparison of normalized Q-band pseudomodulated pulsed EPR spectra of different *Cr*Fdx1 variants. The samples were reduced with 10 mM NaDT. Simulations are shown with dotted gray traces, and the principal *g*-values of *Cr*Fdx1 are marked with vertical dashed lines. Titration curves of the reductive (*circles*) and oxidative (*squares*) redox potentiometry series of *Cr*Fdx1 variants (*B*) S43 and (*C*) S44 monitored via pulsed EPR spectroscopy at Q-band. The spin concentrations were obtained by double integration of the simulated first-derivative pulsed EPR spectra. The data points were fitted to a one-electron Nernst equation (*solid lines*) yielding the midpoint potential.

DISCUSSION

The precise determination of midpoint potentials is one of the key steps toward understanding the function of a redox protein and its role in complex catalytic reactions. Identifying positions that alter the FeS cluster midpoint potential does not only help to understand the sophisticated and complex influence of the protein environment but also reveals effective parameters for precise manipulation of metalloproteins for biotechnological purposes. It adjusts the metabolic "fate" of the electrons by manipulating the electron carriers (Fdx) as track switches (47,48). In this work, we showed for *Cr*Fdx1 that S43 is an important position close enough to the FeS cluster to alter the electronic structure of the cofactor.

The rhombic EPR line shape of Fdx [2Fe2S] clusters is dominated by *g*-anisotropy. The g_2 and g_3 values are dominated by the strong anisotropy of the Fe^{2+} ion, whereas the low-field value, g_1, is determined by the Fe^{3+} ion (41,49,50). Therefore, shifts in *g*-values suggest structural and/or electrostatic changes within and/or in the vicinity of the active center (41–43). Despite the observed small variations, the *g*-values and also the rhombicity parameter, η, of all Fdx isoforms and variants detected in this work fall into the characteristic average Fe^{3+}-Fe^{2+}-S-C dihedral angle range described by Gambarelli and Mouesca (42) for plant-type Fdxs. These results indicate that the structure around the [2Fe2S] clusters of Fdxs does not change dramatically upon site-directed exchange mutagenesis. This is not always self-evident as shown for the [2Fe2S] cluster of HydC from *Thermotoga maritima* (11). Furthermore, the similar g_{iso} values indicate the absence of strong shifts in the spin localization degree of the [2Fe2S] cluster. A comparison of the physical differences listed in Table S2 and detected E_ms did not establish a correlation among the Fdx isoforms. However, strikingly, for the *Cr*Fdx1 variants S43A and S43D, a possible relation is observed (see Fig. 4).

The origin of the difference in midpoint potentials of *Cr*Fdx1 and *Cr*Fdx2 is not fully understood yet. Structural differences in the vicinity of their [2Fe2S] clusters were suggested to be one of the underlying reasons (26). Primary ligands determine the overall redox potential range of a given metal center. However, interactions with the secondary coordination sphere have been shown to fine-tune the potential of metal cofactors within redox proteins. The midpoint potential of *Cr*Fdx2 was lowered to a value comparable to that of *Cr*Fdx1 by employing the substitution M62F (26). In wildtype *Cr*Fdx1, as observed in many other FeS proteins, the backbone nitrogen atoms in the cluster binding loop area form NH-S hydrogen bonds with the cysteine sulfur atoms and the sulfur atoms of the [2Fe2S] cluster. The backbone amide of S43 is also

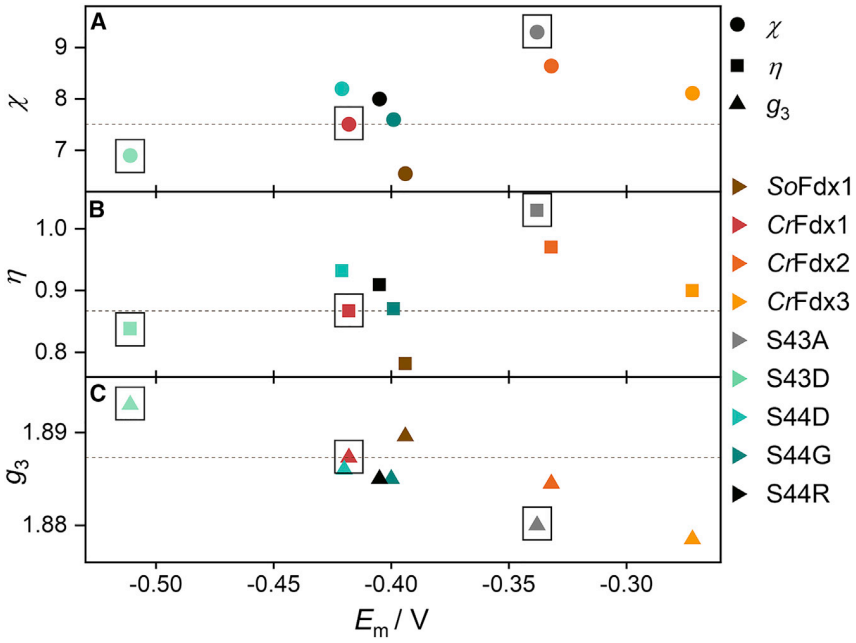

FIGURE 4 Correlation between the midpoint potentials, E_m, of the Fdx isoforms and variants and parameters (*A*) χ, (*B*) the rhombicity η, and (*C*) the g_3 component. *Cr*Fdx1 and its variants that resulted in significant midpoint potential shifts are marked with squares. The dashed lines show the χ-, η-, and g_3 values of *Cr*Fdx1.

involved in a hydrogen bond toward the μ-sulfide atom of the FeS cluster. Thus, the impact of exchanges at this position might be caused by a weakening or disruption of that bond because of steric changes in the protein loop. This is underlined by the detected physical differences, such as χ, η, and the *g*-values, suggesting structural/electrostatic changes nearby and/or within the redox cluster. Among *Cr*Fdx1 variants, S43A, the variant with substantial *g*-shifts and the highest χ- and η-values, displays the highest E_m, whereas the one with the lowest E_m, S43D, shows the lowest χ- and η-values. Interestingly, the g_1 and g_2 values of S43D are highly similar to the ones measured for *Cr*Fdx1, but its g_3 value is distinct. A slight correlation is observed when g_3 values are plotted against detected E_ms (see Fig. 4). Such a relationship has not been reported so far; however, these findings need to be interpreted with care as our data is restricted to a small number of Fdxs investigated in this work. Our results furthermore suggest that the flexibility of the cluster is related to the midpoint potential, as seen in Fig. 4 for S43 variants (χ versus E_m). In *Anabaena* 7120 Fdx1, S47 (corresponding to S43 in *C. reinhardtii*) is prone to structural changes upon reduction of the FeS cluster (51–53). Therefore, this position might be crucial to buffer structural changes in the protein environment, for example by redox transitions. Increasing or restricting the flexibility at this position might therefore in turn have a higher impact on the electronic features and solvent accessibility of the adjacent FeS cluster. The correlation observed between the E_ms of the *Cr*Fdx1 S43 variants and η, which associate with variations of average Fe^{3+}-Fe^{2+}-S-C dihedral angles, further supports the important role of the small structural changes in affecting the redox potentials (54). Yet, further research, including different *Cr*Fdx isoforms and variants along with theoretical calculations, are needed to reveal the significance of the observed relationships.

Apart from the impact of hydrogen bonds, the introduction of net charge was shown to have drastic effects on the midpoint potential (10). We showed that the introduction of a negative charge (S43D) decreased the midpoint potential, whereas exchanging the negative dipole with a noncharged amino acid (S43A) led to a more positive net charge and therefore to a more positive potential. Exchanges of S44 barely changed the midpoint potential. Furthermore, the physical differences between the variants of residue S44 were negligible (Table S2). As S44 shares many attributes with S43 (amide H-bond and proximity to the FeS cluster), this underlines the complex nature of the protein framework and its influence on the bound cofactor. It can be noted that in wildtype *Cr*Fdx1, S44 is H-bonded to S36. Exchanges of S44 might therefore lead to a disruption of this H-bond, which could result in a reorientation of both side chains and associated regions and thus a composition of different effects on the FeS cluster.

Last, we note that although cw EPR spectroscopy at X-band frequencies has been established as a powerful tool for obtaining midpoint potentials, pulsed EPR is beneficial when there exist multiple species with distinct relaxation times. Then, relaxation filtering can be used to separate and/or suppress their signals (see the mediator mix signal marked with an asterisk in Fig. S3 *A* vs. Fig. S3 *B*). This approach can additionally be applied at even higher microwave frequencies when low *g*-anisotropy

TABLE 1 Midpoint potentials, $E_{m,7.5}$, obtained at pH = 7.5 of all Fdxs investigated in this work

Ferredoxin	$E_{m,7.5}$/mV
*So*Fdx	−394 ± 5/7
*Cr*Fdx1	−419 ± 5
*Cr*Fdx2	−332 ± 5
*Cr*Fdx3	−272 ± 4
*Cr*Fdx1 S43A	−338 ± 9
*Cr*Fdx1 S43D	−511 ± 17
*Cr*Fdx1 S44D	−420 ± 4
*Cr*Fdx1 S44G	−400 ± 8
*Cr*Fdx1 S44R	−405 ± 9

See Materials and methods for details of the given error margin.

or multiple species with similar *g*-factors need to be resolved. Furthermore, the required sample volume decreases substantially at higher frequencies (∼150 μL at 9.5 GHz vs. 5–10 μL at 34 GHz vs. 0.5 μL at 94 GHz). Therefore, our pulsed EPR-monitored redox potentiometry technique at Q-band presents an alternative method that overcomes the limitations of the X-band cw EPR technique for certain systems.

CONCLUSIONS

In this study, we determined the midpoint potential of *Cr*Fdx3 for the first time, to our knowledge, using pulsed EPR at Q-band. *Cr*Fdx3 might be a potential target for manipulating catalysis in *C. reinhardtii* as it was suggested to have interactions with [FeFe]-hydrogenases HydA1 and HydA2 in this organism. Furthermore, we showed that single point mutations in the vicinity of the [2Fe2S] cluster of *Cr*Fdx1 tune the midpoint potential in the range of −338 to −511 mV. We identified S43 as an optimal target for manipulating the midpoint potential by introducing or removing the net charge. Our results serve as a basis to design new experiments for unraveling the distinct functions of Fdx isoforms and illuminate the decisive role of individual positions in the secondary ligand sphere of the cofactor in tuning the midpoint potential of redox proteins.

SUPPORTING MATERIAL

Supporting material can be found online at https://doi.org/10.1016/j.bpr.2021.100016.

AUTHOR CONTRIBUTIONS

M.H. performed research, analyzed data, and partially wrote the manuscript. A.G. performed research, analyzed data, and partially wrote the manuscript. D.B. and Y.K. contributed to some of the data acquisition Y.K. and VE helped writing the manuscript. M.W. designed research and helped writing the manuscript. T.H. and M.K. designed and funded research, partially analyzed data, and wrote the manuscript.

ACKNOWLEDGMENTS

We thank Dr. Alexander Schnegg (Max Planck Institute for Chemical Energy Conversion) for providing access to his X-band EPR spectrometer. We thank Dr. Edward Reijerse for helpful discussions.

This work is funded by the Deutsche Forschungsgemeinschaft (German Research Foundation) under Germany's Excellence Strategy (EXC 2033 - 390677874 – RESOLV). T.H. acknowledges finance from the Deutsche Forschungsgemeinschaft (Priority Programme SPP1927 `FeS for Life' and HA 2555/10-1).

DECLARATION OF INTERESTS

The authors declare no competing interests.

REFERENCES

1. Beinert, H. 2000. Iron-sulfur proteins: ancient structures, still full of surprises. *J. Biol. Inorg. Chem.* 5:2–15.
2. Lill, R. 2009. Function and biogenesis of iron-sulphur proteins. *Nature.* 460:831–838.
3. Liu, J., S. Chakraborty, …, Y. Lu. 2014. Metalloproteins containing cytochrome, iron-sulfur, or copper redox centers. *Chem. Rev.* 114:4366–4469.
4. Page, C. C., C. C. Moser, and P. L. Dutton. 2003. Mechanism for electron transfer within and between proteins. *Curr. Opin. Chem. Biol.* 7:551–556.
5. Jin, Q., and C. M. Bethke. 2002. Kinetics of electron transfer through the respiratory chain. *Biophys. J.* 83:1797–1808.
6. Cammack, R., K. K. Rao, …, L. J. Rogers. 1977. Midpoint redox potentials of plant and algal ferredoxins. *Biochem. J.* 168:205–209.
7. Zuris, J. A., D. A. Halim, …, P. A. Jennings. 2010. Engineering the redox potential over a wide range within a new class of FeS proteins. *J. Am. Chem. Soc.* 132:13120–13122.
8. Bak, D. W., and S. J. Elliott. 2014. Alternative FeS cluster ligands: tuning redox potentials and chemistry. *Curr. Opin. Chem. Biol.* 19:50–58.
9. Hosseinzadeh, P., N. M. Marshall, …, Y. Lu. 2016. Design of a single protein that spans the entire 2-V range of physiological redox potentials. *Proc. Natl. Acad. Sci. USA.* 113:262–267.
10. Hosseinzadeh, P., and Y. Lu. 2016. Design and fine-tuning redox potentials of metalloproteins involved in electron transfer in bioenergetics. *Biochim. Biophys. Acta.* 1857:557–581.
11. Birrell, J. A., C. Laurich, …, W. Lubitz. 2016. Importance of hydrogen bonding in fine tuning the [2Fe-2S] cluster redox potential of HydC from Thermotoga maritima. *Biochemistry.* 55:4344–4355.
12. Li, B., P. Steindel, …, S. J. Elliott. 2021. Maximizing (electro)catalytic CO_2 reduction with a ferredoxin-based reduction potential gradient. *ACS Catal.* 11:4009–4023.
13. Mutter, A. C., A. M. Tyryshkin, …, P. G. Falkowski. 2019. De novo design of symmetric ferredoxins that shuttle electrons in vivo. *Proc. Natl. Acad. Sci. USA.* 116:14557–14562.
14. Cammack, R., D. S. Patil, and V. M. Fernandez. 1985. Electron-spin-resonance/electron-paramagnetic-resonance spectroscopy of iron-sulphur enzymes. *Biochem. Soc. Trans.* 13:572–578.
15. Zanello, P. 2014. The competition between chemistry and biology in assembling iron–sulfur derivatives. Molecular structures and electrochemistry. Part II. {[Fe2S2](SγCys)4} proteins. *Coord. Chem. Rev.* 280:54–83.
16. Sands, R. H., and W. R. Dunham. 1974. Spectroscopic studies on two-iron ferredoxins. *Q. Rev. Biophys.* 7:443–504.

17. Beinert, H., R. H. Holm, and E. Münck. 1997. Iron-sulfur clusters: nature's modular, multipurpose structures. *Science.* 277:653–659.
18. Yang, W., T. M. Wittkopp, …, A. R. Grossman. 2015. Critical role of Chlamydomonas reinhardtii ferredoxin-5 in maintaining membrane structure and dark metabolism. *Proc. Natl. Acad. Sci. USA.* 112:14978–14983.
19. Sawyer, A., and M. Winkler. 2017. Evolution of Chlamydomonas reinhardtii ferredoxins and their interactions with [FeFe]-hydrogenases. *Photosynth. Res.* 134:307–316.
20. Bertini, I., C. Luchinat, …, P. R. Vasos. 2002. Browsing gene banks for Fe2S2 ferredoxins and structural modeling of 88 plant-type sequences: an analysis of fold and function. *Proteins.* 46:110–127.
21. Schmitter, J. M., J. P. Jacquot, …, P. Decottignies. 1988. Purification, properties and complete amino acid sequence of the ferredoxin from a green alga, Chlamydomonas reinhardtii. *Eur. J. Biochem.* 172:405–412.
22. Galvan, F., A. Marquez, and E. Fernandez. 1985. Physicochemical properties of ferredoxin from Chlamydomonas reinhardii. *Z. Naturforsch. C.* 40c:373–378.
23. Happe, T., and J. D. Naber. 1993. Isolation, characterization and N-terminal amino acid sequence of hydrogenase from the green alga Chlamydomonas reinhardtii. *Eur. J. Biochem.* 214:475–481.
24. Peden, E. A., M. Boehm, …, A. Dubini. 2013. Identification of global ferredoxin interaction networks in Chlamydomonas reinhardtii. *J. Biol. Chem.* 288:35192–35209.
25. Terauchi, A. M., S.-F. Lu, …, S. S. Merchant. 2009. Pattern of expression and substrate specificity of chloroplast ferredoxins from Chlamydomonas reinhardtii. *J. Biol. Chem.* 284:25867–25878.
26. Boehm, M., M. Alahuhta, …, A. Dubini. 2016. Crystal structure and biochemical characterization of Chlamydomonas FDX2 reveal two residues that, when mutated, partially confer FDX2 the redox potential and catalytic properties of FDX1. *Photosynth. Res.* 128:45–57.
27. Martínez-Espinosa, R. M., D. J. Richardson, …, M. J. Bonete. 2007. Spectopotentiometric properties and salt-dependent thermotolerance of a [2Fe-2S] ferredoxin-involved nitrate assimilation in Haloferax mediterranei. *FEMS Microbiol. Lett.* 277:50–55.
28. Hagedoorn, P.-L., L. van der Weel, and W. R. Hagen. 2014. EPR monitored redox titration of the cofactors of *Saccharomyces cerevisiae* Nar1. *J. Vis. Exp* e51611.
29. Wright, J. J., E. Salvadori, …, M. M. Roessler. 2016. Small-volume potentiometric titrations: EPR investigations of Fe-S cluster N2 in mitochondrial complex I. *J. Inorg. Biochem.* 162:201–206.
30. Dutton, P. L. 1978. Redox potentiometry: determination of midpoint potentials of oxidation-reduction components of biological electron-transfer systems. *Methods Enzymol.* 54:411–435.
31. Vogel, H. J., and D. M. Bonner. 1956. Acetylornithinase of *Escherichia coli*: partial purification and some properties. *J. Biol. Chem.* 218:97–106.
32. Palma, P. N., B. Lagoutte, …, F. Guerlesquin. 2005. Synechocystis ferredoxin/ferredoxin-NADP(+)-reductase/NADP+ complex: structural model obtained by NMR-restrained docking. *FEBS Lett.* 579:4585–4590.
33. Nordstrom, D. K., and F. D. Wilde. 2005. Chapter 6.5. Reduction-oxidation potential (electrode method). *In* U.S. Geological Survey Techniques of Water-Resources Investigations, Book 9: Handbooks for Water-Resources Investigations. F. D. Wilde and D. B. Radtke, eds. U.S. Geological Survey.
34. Aliverti, A., W. R. Hagen, and G. Zanetti. 1995. Direct electrochemistry and EPR spectroscopy of spinach ferredoxin mutants with modified electron transfer properties. *FEBS Lett.* 368:220–224.
35. Stoll, S., and A. Schweiger. 2006. EasySpin, a comprehensive software package for spectral simulation and analysis in EPR. *J. Magn. Reson.* 178:42–55.
36. Aasa, R., and T. Vänngård. 1975. EPR signal intensity and powder shapes: a reexamination. *J. Magn. Reson.* 19:308–315.
37. Mayhew, S. G. 1978. The redox potential of dithionite and SO-2 from equilibrium reactions with flavodoxins, methyl viologen and hydrogen plus hydrogenase. *Eur. J. Biochem.* 85:535–547.
38. Hagen, W. R. 2014. Biomolecular EPR Spectroscopy. CRC Press, Boca Raton, FL.
39. Stombaugh, N. A., J. E. Sundquist, …, W. H. Orme-Johnson. 1976. Oxidation-reduction properties of several low potential iron-sulfur proteins and of methylviologen. *Biochemistry.* 15:2633–2641.
40. Roncaroli, F., E. Bill, …, M.-E. Pandelia. 2015. Cofactor composition and function of a H_2-sensing regulatory hydrogenase as revealed by Mössbauer and EPR spectroscopy. *Chem. Sci. (Camb.).* 6:4495–4507.
41. Bertrand, P., and J. P. Gayda. 1979. A theoretical interpretation of the variations of some physical parameters within the [2Fe-2S] ferredoxin group. *Biochim. Biophys. Acta.* 579:107–121.
42. Gambarelli, S., and J.-M. Mouesca. 2004. Correlation between the magnetic g tensors and the local cysteine geometries for a series of reduced [2Fe-2S*] protein clusters. A quantum chemical density functional theory and structural analysis. *Inorg. Chem.* 43:1441–1451.
43. Orio, M., and J.-M. Mouesca. 2008. Variation of average g values and effective exchange coupling constants among [2Fe-2S] clusters: a density functional theory study of the impact of localization (trapping forces) versus delocalization (double-exchange) as competing factors. *Inorg. Chem.* 47:5394–5416.
44. Schorsch, M., M. Kramer, …, G. T. Hanke. 2018. A unique ferredoxin acts as a player in the low-iron response of photosynthetic organisms. *Proc. Natl. Acad. Sci. USA.* 115:E12111–E12120.
45. Ohnishi, Y., N. Muraki, …, G. Kurisu. 2020. X-ray dose-dependent structural changes of the [2Fe-2S] ferredoxin from Chlamydomonas reinhardtii. *J. Biochem.* 167:549–555.
46. Fukuyama, K. 2004. Structure and function of plant-type ferredoxins. *Photosynth. Res.* 81:289–301.
47. Rumpel, S., J. F. Siebel, …, M. Winkler. 2014. Enhancing hydrogen production of microalgae by redirecting electrons from photosystem I to hydrogenase. *Energy Environ. Sci.* 7:3296–3301.
48. Wiegand, K., M. Winkler, …, M. Rögner. 2018. Rational redesign of the ferredoxin-$NADP^+$-oxido-reductase/ferredoxin-interaction for photosynthesis-dependent H_2-production. *Biochim. Biophys. Acta Bioenerg.* 1859:253–262.
49. Gibson, J. F., D. O. Hall, …, F. R. Whatley. 1966. The iron complex in spinach ferredoxin. *Proc. Natl. Acad. Sci. USA.* 56:987–990.
50. Hearshen, D. O., W. R. Hagen, …, W. R. Dunham. 1986. An analysis of g strain in the EPR of two [2Fe2S] ferredoxins. Evidence for a protein rigidity model. *J. Magn. Reson.* 69:440–459.
51. Dugad, L. B., G. N. La Mar, …, I. Bertini. 1990. Identification of localized redox states in plant-type two-iron ferredoxins using the nuclear Overhauser effect. *Biochemistry.* 29:2263–2271.
52. Morales, R., M. H. Charon, …, M. Frey. 1999. Refined X-ray structures of the oxidized, at 1.3 A, and reduced, at 1.17 A, [2Fe-2S] ferredoxin from the cyanobacterium Anabaena PCC7119 show redox-linked conformational changes. *Biochemistry.* 38:15764–15773.
53. Morales, R., M. H. Charon, …, M. Frey. 2000. A redox-dependent interaction between two electron-transfer partners involved in photosynthesis. *EMBO Rep.* 1:271–276.
54. Ergenekan, C. E., D. Thomas, …, T. Ichiye. 2003. Prediction of reduction potential changes in rubredoxin: a molecular mechanics approach. *Biophys. J.* 85:2818–2829.

Biophysical Reports, Volume *1*

Supplemental information

Fine-tuning of FeS proteins monitored via pulsed EPR redox potentiometry at Q-band

Melanie Heghmanns, Alexander Günzel, Dörte Brandis, Yury Kutin, Vera Engelbrecht, Martin Winkler, Thomas Happe, and Müge Kasanmascheff

Table S1: QuikChange Primers used for site-directed mutagenesis of *Cr*Fdx1. Mismatch positions are presented in bold.

Primer	Sequence
*Cr*Fdx1 S43A fw	CTGGTGCTTGC**G**CCAGCTGC
*Cr*Fdx1 S43A rv	GCGCAGCTGG**C**GCAAGCACC
*Cr*Fdx1 S43D fw	TTGC**GA**CAGCTGCGCCGGCAAGG
*Cr*Fdx1 S43D rv	AGCTG**TC**GCAAGCACCAGCGCGGCAAG
*Cr*Fdx1 S44D fw	GCTCC**GA**CTGCGCCGGCAAGG
*Cr*Fdx1 S44D rv	GGCGCAG**TC**GGAGCAAGCACCAGC
*Cr*Fdx1 S44G fw	TTGCTCC**G**GCTGCGCCGGCAAGG
*Cr*Fdx1 S44G rv	CGGCGCAGC**C**GGAGCAAGCAC
*Cr*Fdx1 S44R fw	TTGCTCCAG**A**TGCGCCGGCAAGG
*Cr*Fdx1 S44R rv	GGCGCA**T**CTGGAGCAAGCAC

Figure S1: The experimental cw and pulsed EPR spectra of *So*Fdx (black lines) and the corresponding simulations (dotted grey lines) are shown. The cw and pulsed EPR spectra were recorded at X- and Q-band, respectively. The pseudo-modulated pulsed EPR spectrum is shown for better comparison. The areas around g_3 used for EPR intensity scaling are shown with a grey rectangle. Simulation parameters are given in Table S2. The experimental conditions were as follows. For X-band cw: T = 15 K, 7 G modulation amplitude, 100 kHz modulation frequency, 82 ms time constant, 82 ms conversion time and 1 scan; for Q-band pulsed EPR: T = 15 K, $\pi/2$ = 8 ns, π = 16, τ = 650 ns, SRT = 300 ms, 200 shots/point. The typical six-line pattern of a Mn^{2+} species present in buffer contributes to the Q-band pulsed EPR spectrum and is marked with an asterisk.

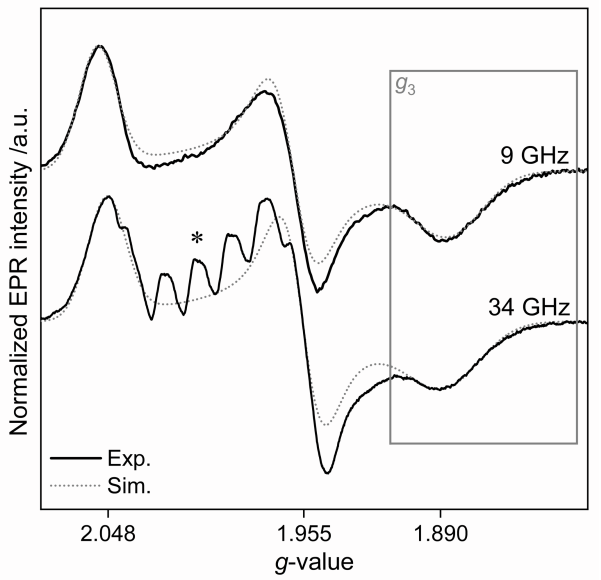

Figure S2: Titration curves of the oxidative redox potentiometry of *So*Fdx monitored via EPR spectroscopy. The reduced Fdx fractions were obtained using the intensities of the components at g_3 = 1.89 in cw X-band (black triangles) and pseudo-modulated pulsed Q-band (grey triangles) EPR spectra (see Figure S1 and S3 for details). The data points were fitted to an adjusted one-electron Nernst equation with a 95 % confidence interval shown in grey. The semi-log plot (inset) of E_h vs. the logarithm of the concentration ratio of oxidized ([Ox]) to reduced ([Red]) *So*Fdx was drawn. The slope of the line yields the actual number of electrons transferred confirming the fidelity of the one-electron Nernst equation for the systems under investigation.

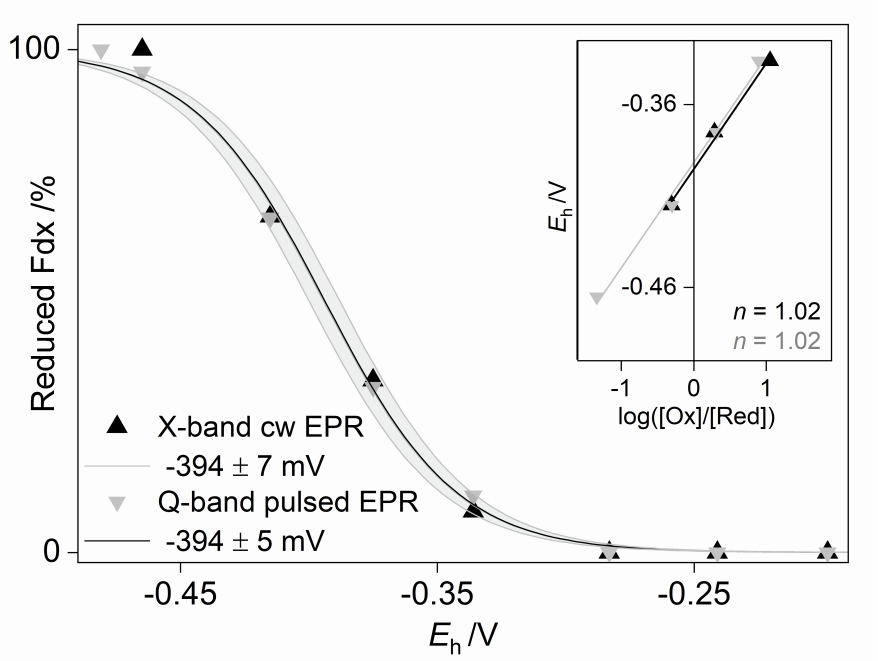

Table S2: *g*-values and *g*-strains used for spectral simulations of the cw and pulsed EPR spectra of ferredoxins from *Spinacia Oleracea* (*So*) and *Chlamydomonas reinhardtii* (*Cr*) recorded at X- and Q-band. g_{iso} is the arithmetic mean of three principal *g*-values. The parameter $\chi = g_2 - g_3$ is related to the stiffness at the active site.[1] The rhombicity parameter η is calculated as $(g_2-g_3)/(g_1-g_{iso})$, with $\eta = 0$ and $\eta = 1$ representing a completely axial and rhombic spectrum, respectively. The linewidth (lw) parameters are given in mT and were determined at Q-band.

Ferredoxin	*g*-values			*g*-strain			g_{iso}	lw at g_3	χ $\times 10^2$	η
*So*Fdx1	2.048	1.955	1.890	0.020	0.019	0.040	1.964	29	6.5	0.78
*Cr*Fdx1	2.055	1.962	1.887	0.019	0.023	0.038	1.968	29	7.5	0.87
*Cr*Fdx2	2.061	1.971	1.885	0.017	0.020	0.036	1.972	30	8.6	0.97
*Cr*Fdx3	2.054	1.960	1.879	0.019	0.022	0.066	1.964	38	8.1	0.90
*Cr*Fdx1 variants										
S43A	2.062	1.973	1.880	0.020	0.023	0.043	1.972	23	9.3	1.03
S43D	2.051	1.962	1.893	0.027	0.027	0.040	1.969	16	6.9	0.84
S44D	2.059	1.968	1.886	0.017	0.021	0.033	1.971	21	8.2	0.93
S44G	2.054	1.961	1.885	0.021	0.003	0.042	1.967	18	7.6	0.87
S44R	2.057	1.965	1.885	0.019	0.023	0.037	1.969	20	8.0	0.91

Figure S3: EPR spectra of the oxidative redox potentiometry series at respective potentials (solid lines) of *So*Fdx recorded via cw EPR at X-band (A) and of Fdx isoforms and variants recorded via pulsed EPR at Q-band: (B-J) as-recorded absorption spectra; (B'-J') pseudo-modulated spectra. The Fdx isoforms and variants are as follows: (B) *So*Fdx, (C) *Cr*Fdx1, (D) *Cr*Fdx2, (E) *Cr*Fdx3, (F) S43A, (G) S43D, (H) S44D, (I) S44G (J) S44R. The first derivatives of the pulsed EPR spectra were obtained by pseudo field modulation with a modulation amplitude of 3 G. The intensities of the respective simulated spectra (grey dashed lines) were normalized to the g_3 components to rule out background contributions and were used for double integration. The background/impurity signals arise from Mn^{2+} and/or the redox mediator mix (marked with an asterisk). All spectra were recorded at 15 K.

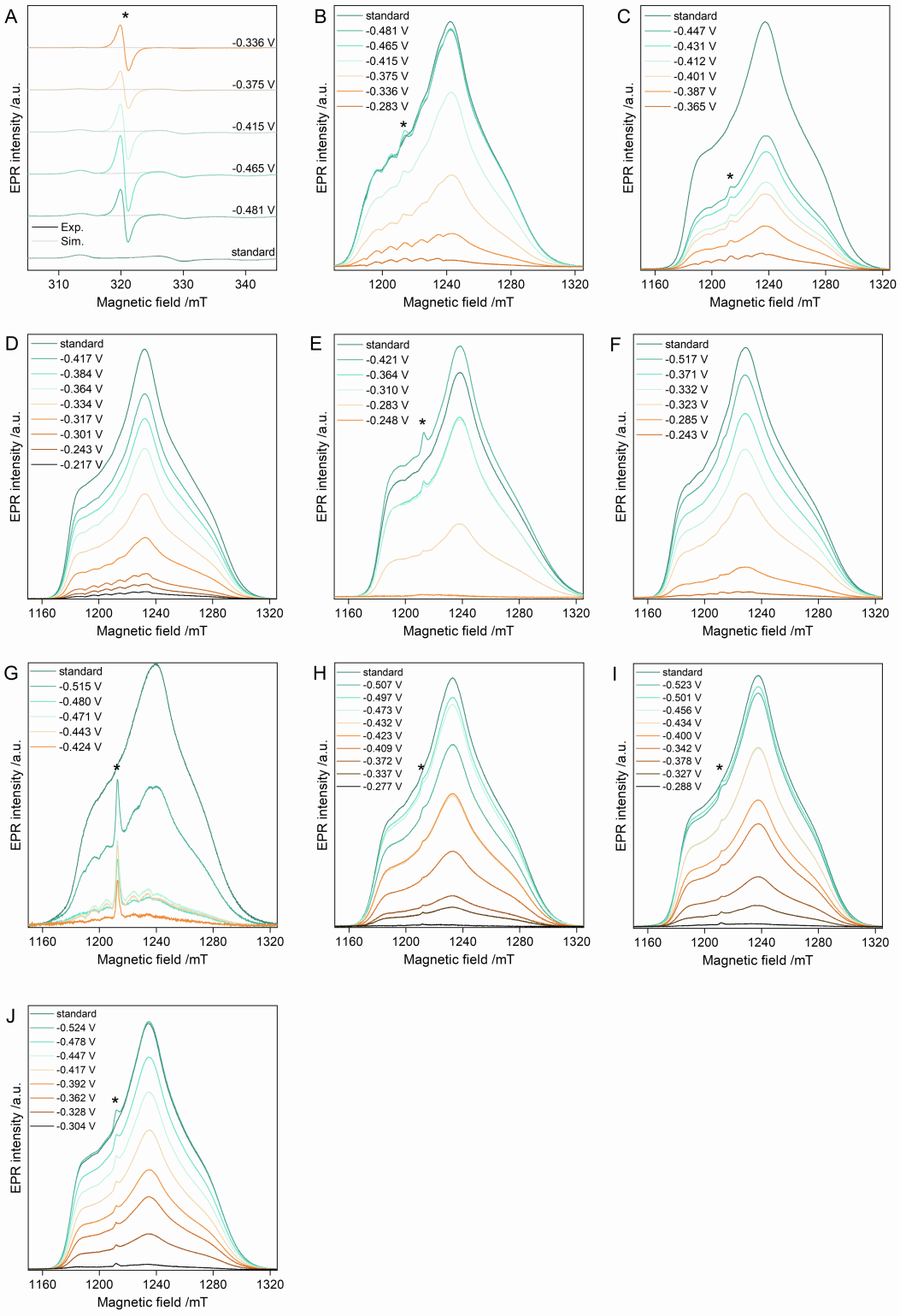
A
B
C
D
E
F
G
H
I
J
EPR intensity /a.u.
Magnetic field /mT
-0.336 V
-0.375 V
-0.415 V
-0.465 V
-0.481 V
Exp.
Sim.
standard
-0.283 V
-0.387 V
-0.401 V
-0.412 V
-0.431 V
-0.447 V
-0.217 V
-0.243 V
-0.248 V
-0.277 V
-0.285 V
-0.288 V
-0.301 V
-0.304 V
-0.310 V
-0.317 V
-0.323 V
-0.327 V
-0.328 V
-0.332 V
-0.334 V
-0.337 V
-0.342 V
-0.362 V
-0.364 V
-0.371 V
-0.372 V
-0.378 V
-0.384 V
-0.392 V
-0.400 V
-0.409 V
-0.417 V
-0.421 V
-0.423 V
-0.432 V
-0.434 V
-0.443 V
-0.447 V
-0.456 V
-0.471 V
-0.473 V
-0.478 V
-0.480 V
-0.497 V
-0.501 V
-0.507 V
-0.515 V
-0.517 V
-0.523 V
-0.524 V

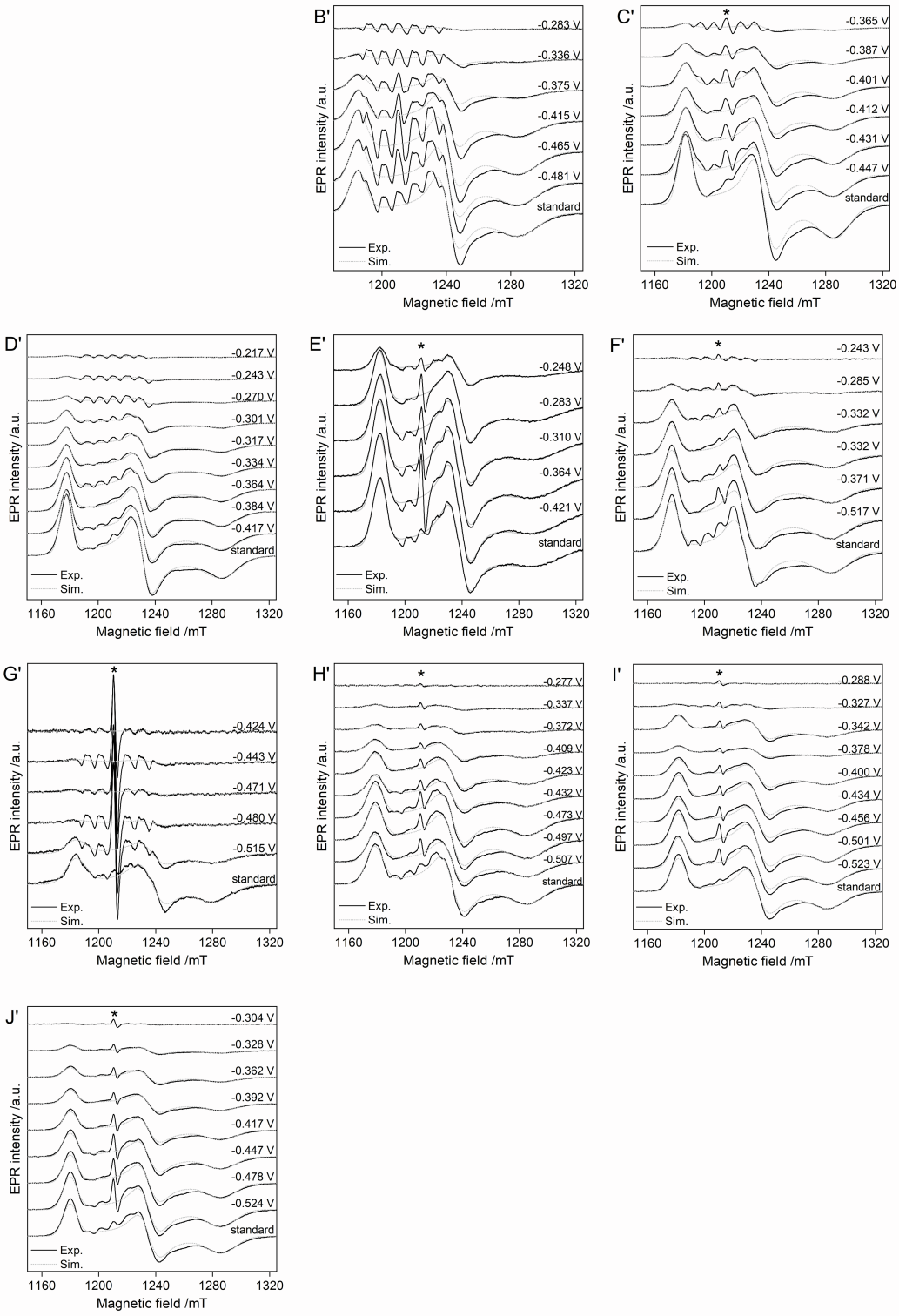
B'
-0.283 V
-0.336 V
-0.375 V
-0.415 V
-0.465 V
-0.481 V
standard
Exp.
Sim.
EPR intensity /a.u.
1200 1240 1280 1320
Magnetic field /mT
C'
*
-0.365 V
-0.387 V
-0.401 V
-0.412 V
-0.431 V
-0.447 V
standard
Exp.
Sim.
EPR intensity /a.u.
1160 1200 1240 1280 1320
Magnetic field /mT
D'
-0.217 V
-0.243 V
-0.270 V
-0.301 V
-0.317 V
-0.334 V
-0.364 V
-0.384 V
-0.417 V
standard
Exp.
Sim.
EPR intensity /a.u.
1160 1200 1240 1280 1320
Magnetic field /mT
E'
*
-0.248 V
-0.283 V
-0.310 V
-0.364 V
-0.421 V
standard
Exp.
Sim.
EPR intensity /a.u.
1160 1200 1240 1280 1320
Magnetic field /mT
F'
*
-0.243 V
-0.285 V
-0.332 V
-0.332 V
-0.371 V
-0.517 V
standard
Exp.
Sim.
EPR intensity /a.u.
1160 1200 1240 1280 1320
Magnetic field /mT
G'
*
-0.424 V
-0.443 V
-0.471 V
-0.480 V
-0.515 V
standard
Exp.
Sim.
EPR intensity /a.u.
1160 1200 1240 1280 1320
Magnetic field /mT
H'
*
-0.277 V
-0.337 V
-0.372 V
-0.409 V
-0.423 V
-0.432 V
-0.473 V
-0.497 V
-0.507 V
standard
Exp.
Sim.
EPR intensity /a.u.
1160 1200 1240 1280 1320
Magnetic field /mT
I'
*
-0.288 V
-0.327 V
-0.342 V
-0.378 V
-0.400 V
-0.434 V
-0.456 V
-0.501 V
-0.523 V
standard
Exp.
Sim.
EPR intensity /a.u.
1160 1200 1240 1280 1320
Magnetic field /mT
J'
*
-0.304 V
-0.328 V
-0.362 V
-0.392 V
-0.417 V
-0.447 V
-0.478 V
-0.524 V
standard
Exp.
Sim.
EPR intensity /a.u.
1160 1200 1240 1280 1320
Magnetic field /mT

Table S3: The phase memory relaxation times (T_m) of samples obtained by redox potentiometry were determined at each potential (E_h) at the g_2 component via the two-pulse echo decay experiment. The decay curves were fitted to a stretched exponential function with the stretching parameter *c* (see the text below, Figure S4 and Material and Methods for details). The estimated error of T_m values is ± 0.1 µs. The standard refers to the Fdx sample with an initial concentration of 200 µM reduced with 10 mM NaDT.

*So*Fdx	*c* = 1.66	*Cr*Fdx3	*c* = 1.25	S43D	*c* = 1.40
E_h /V	T_m /µs	E_h /V	T_m /µs	E_h /V	T_m /µs
standard	2.2	standard	1.3	standard	1.5
-0.481	2.2	standard	1.3	-0.515	1.5
-0.465	2.1	-0.430	1.3	-0.471	1.5
-0.415	2.2	-0.421	1.4		
-0.375	2.2	-0.382	1.3		
-0.336	2.2	-0.365	1.3		
-0.283	2.4	-0.364	1.4		
		-0.332	1.3		
		-0.310	1.4		
		-0.306	1.4		
		-0.283	1.4		
		-0.278	1.4		
		-0.254	1.4		
		-0.248	1.5		
		-0.202	1.5		

S43A	*c* = 1.66	S44D	*c* = 1.80	S44G	*c* = 1.86	S44R	*c* = 1.83
E_h /V	T_m /µs	E_h /V	T_m /µs	E_h /V	T_m /µs	E_h /V	T_m /µs
standard	1.7	standard	1.9	standard	2.0	standard	2.1
standard	1.7	standard	1.9	standard	2.0	standard	2.0
-0.517	1.7	-0.507	1.9	-0.523	2.0	-0.526	2.0
-0.497	1.7	-0.497	1.9	-0.456	2.0	-0.509	2.0
-0.475	1.7	-0.473	2.0	-0.453	2.0	-0.480	2.0
-0.449	1.7	-0.432	2.0	-0.434	2.0	-0.470	2.0
-0.413	1.7	-0.423	2.0	-0.426	2.1	-0.422	2.0
-0.386	1.7	-0.410	2.1	-0.400	2.1	-0.419	2.1
-0.371	1.7	-0.409	2.1	-0.395	2.0	-0.394	2.1
-0.366	1.7	-0.372	2.1	-0.389	2.2	-0.364	2.2
-0.355	1.7	-0.366	2.3	-0.378	2.2	-0.330	2.2
-0.332	1.8	-0.337	2.2	-0.349	2.1	-0.263	2.2
-0.323	1.8	-0.335	2.6	-0.329	2.4		
-0.285	1.9			-0.327	2.3		
-0.243	1.9						

In this study all field-swept EPR spectra were recorded via the primary ESE signal intensity, I_{ESE}. It is proportional to the transverse magnetization $M_{x,y}$ and is strongly affected by the phase memory time, T_m, in concordance with

$$I_{ESE}(t) \propto M_{x,y}(t) = M_{x,y}(0) \cdot e^{-t/T_m}, \quad \text{(eq. S1)}$$

where $M_{x,y}(0)$ is the initial maximum value of the transverse magnetization. For Fdxs used in this study, however, a more complicated stretched exponential function had to be introduced to properly simulate the ESE decay (see Figure S4 and Table S3):

$$I_{ESE}(2\tau) \propto e^{(-2\tau/T_m)^c}, \quad \text{(eq. S2)}$$

where τ is the inter-pulse delay between the first and second MW pulses of the Hahn echo sequence, and c is the stretching parameter, which was kept constant for all samples of the same Fdx type ($1.25 \leq c \leq 1.86$). Since the relaxation process is taking place both before and after the π-pulse, 2τ is used as the function's argument.

Field-swept ESE-detected EPR spectra of all samples within a titration series were recorded with the same τ value. It is possible, however, for T_m to vary from sample to sample within a series. According to eq. S2, a variation in the T_m parameter within a titration series would introduce additional changes in the signal intensities. Such an effect would invalidate the underlying assumption that the signal intensity is strictly proportional to the concentration of the paramagnetic species (reduced state of the Fdx).

Therefore, in order to account for variations in T_m, the signal intensity $I_{ESE}(2\tau)$ would need to be normalized to the stretched exponential term $e^{(-2\tau/T_m)^c}$. Here τ is an experimental parameter chosen based on the ringdown duration and T_m is a property of the sample determined via echo decay experiments. Such normalization extrapolates the signal intensity to $\tau = 0$.

In our case, however, the T_m parameter was found to be nearly constant under the changing potential for all samples within a given series. Deviations were only observed for highly oxidized samples where EPR intensities were very low, and T_m measurements were significantly affected by the underlying background signals. The error of T_m is estimated to be 0.1 µs. For systems where changes in T_m need to be taken into account, the echo decay curves can be measured using an over-coupled resonator to minimize the initial lowest 2τ value, which would likely improve the accuracy of the extrapolated signal intensities at $\tau = 0$.

We note that usual limitations of the ESE-detected EPR might apply in some cases, such as suppression of the signal by very short T_m and a possible distortion of the frozen solution line shape due to a strong ESEEM effect (none of them observed here).

Figure S4: EPR intensity obtained in two-pulse echo decay experiments (see Materials and Methods) of potential-dependent samples of *So*Fdx1 (grey curves) plotted against the time. The standard refers to the Fdx sample with an initial concentration of 200 µM reduced with 10 mM NaDT. The curves were fitted to a stretched exponential decay function (black curves): $y(x) = y(0) \cdot e^{\left(-\frac{x}{T_m}\right)^c}$, with c = 1.66. The curves are shifted vertically for clarity.

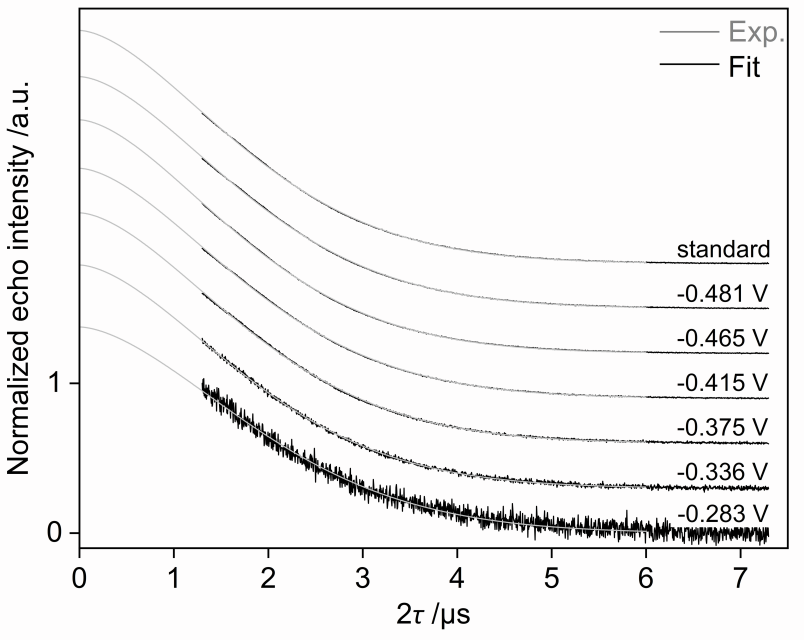

Figure S5: Detected (black triangles) and T_m-corrected (grey triangles) double integrated intensities at g_3 of pulsed EPR *So*Fdx spectra as a function of the respective potential. Fitting to the one-electron Nernst equation (solid lines with 95 % confidence interval in grey) resulted in an identical E_m of -394 ± 5/6 mV. The spectra were recorded at Q-band, T = 15 K.

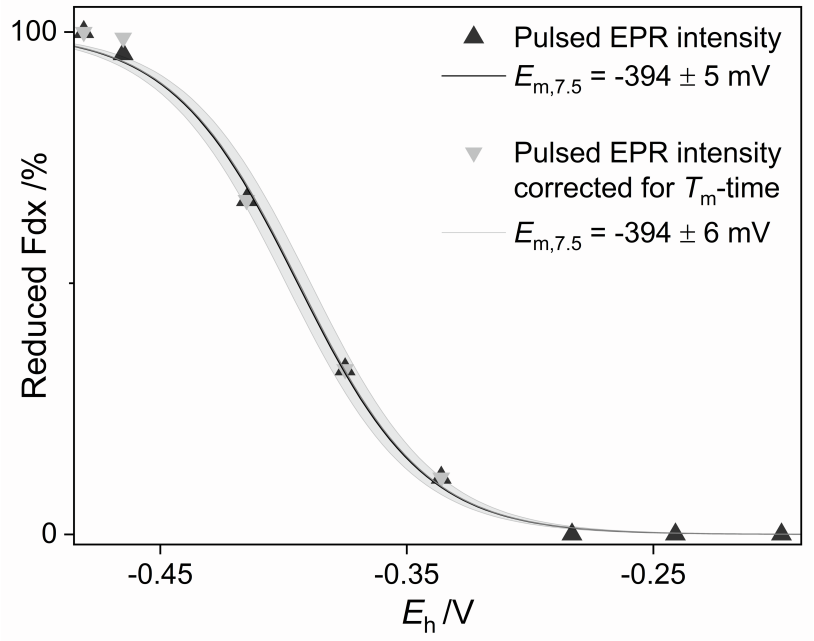

Figure S6: The cw and pulsed EPR spectra of *Cr*Fdx3 at -430 mV recorded at Q-band (T = 15 K) are shown in black and grey, respectively. The first derivative of the pulsed EPR spectrum, obtained by pseudo-modulation with an amplitude of 3 G, is shown for better comparison. A sharp, isotropic signal marked with an asterisk is detected in both EPR spectra and arises from a radical species present in the redox mediator mix. The experimental conditions were as follows. For Q-band cw: T = 15 K, 2 mW power, 5 G modulation amplitude, 100 kHz modulation frequency, 164 ms conversion time and 1 scan; for Q-band pulsed EPR: T = 15 K, π/2 = 10 ns, π = 20, τ = 650 ns, SRT = 0.3 ms, 100 shots/point, 1 scan.

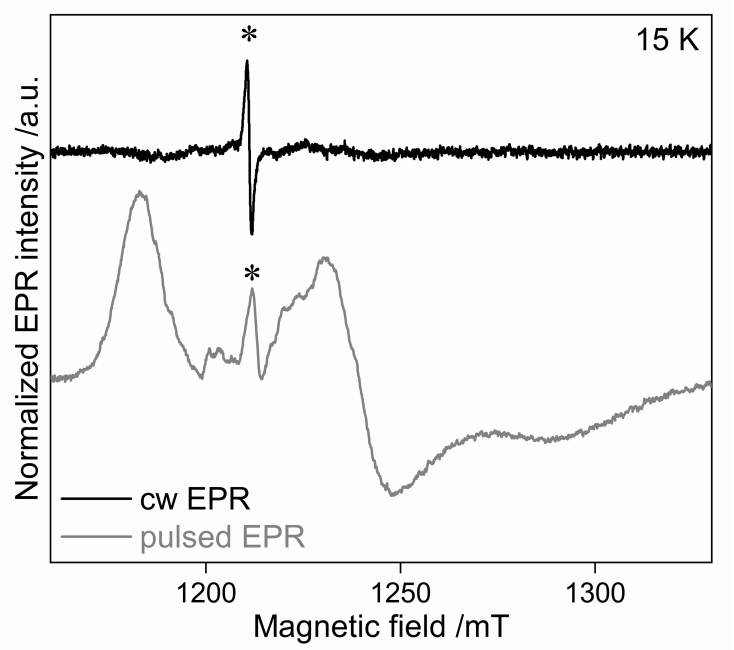

Table S4: Midpoint potentials, E_m, of ferredoxins from *Spinacia oleracea* (*So*) and *Chlamydomonas reinhardtii* (*Cr*) determined by different methods

Ferredoxin	Method	E_m /mV
*So*Fdx	Cyclic voltammetry	$E_{m,7.5}$ = -401(10) [2]
	Cyclic voltammetry	$E_{m,7.0}$ = -420 [3]
	EPR redox titration (this work)	$E_{m,7.5}$ = -394(7)
*Cr*Fdx1	UV/Vis redox titration	$E_{m,7.5}$ = -410 [4]
	Cyclic voltammetry	$E_{m,7.0}$ = -398 [3]
	EPR redox titration (this work)	$E_{m,7.5}$ = -419(5)
*Cr*Fdx2	Cyclic voltammetry	$E_{m,7.0}$ = -321 [3]
	EPR redox titration	$E_{m,7.8}$ = -331(6) [5]
	EPR redox titration (this work)	$E_{m,7.5}$ = -332(5)

References

[1] P. Bertrand, J. P. Gayda, *Biochim. Biophys. Acta* **1979**, *579*, 107–121.

[2] A. Aliverti, W. R. Hagen, G. Zanetti, *FEBS Lett.* **1995**, *368*, 220–224.

[3] A. M. Terauchi, S.-F. Lu, M. Zaffagnini, S. Tappa, M. Hirasawa, J. N. Tripathy, D. B. Knaff, P. J. Farmer, D. Lemaire, T. Hase, et al., *J. Biol. Chem.* **2009**, *284*, 25867–25878.

[4] F. Galvan, A. Marquez, E. Fernandez, *Z. Naturforsch.* **1985**, *40c*, 373–378.

[5] M. Boehm, M. Alahuhta, D. W. Mulder, E. A. Peden, H. Long, R. Brunecky, V. V Lunin, P. W. King, M. L. Ghirardi, A. Dubini, *Photosynth. Res.* **2016**, *128*, 45–57.

4

Discovery of Distinct Species in apo-HydA1 Having a Single Iron-Sulfur Cluster

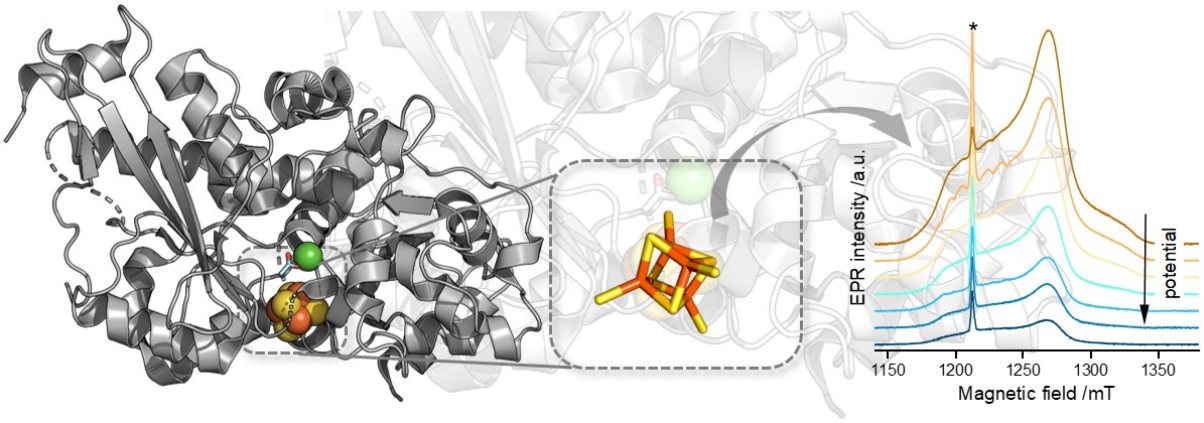

The apo-enzyme of HydA1 from *Chlamydomonas reinhardtii*, referred to as apo-HydA1, harbours one single [4Fe4S] cluster as evidenced by X-ray crystallography (PDB ID: 3LX4, see above Figure), as well as EPR and Mössbauer data.[119,132] The [4Fe4S] cluster is ligated by four cysteine residues (C115, C170, C362 and C366). The first residue was found to be essential for stable cluster assembly and the latter for $[2Fe]_H$-anchoring.[282] The crystal structure of apo-HydA1 revealed an empty cavity for the usual location of $[2Fe]_H$, which showed some residual density.[119] After excluding additional Fe atoms as the source of density, an acetate molecule and chloride ion, both present in the crystallization buffer, were modeled at this site. In the apo-hydrogenase from *C. pasteurianum*, apo-CpI, the cavity is occupied by water molecules and a chloride ion.[145] As until today the crystal structure of maturated HydA1 is unavailable, the 'standard' hydrogenase CpI is used for structural comparison between the apo- and holo-enzyme.

The overlay of apo-HydA1 with maturated CpI revealed significant structural differences in three regions, referred to as "plug", "lock" and "lid".[119,145,146] In apo-HydA1, these regions adopt an open conformation, forming a positively charged channel that connects the empty cavity with the protein surface. Upon insertion of $[2Fe]_H$, the regions are believed to rearrange to a closed conformation blocking the channel and tightly securing the H-cluster in the binding pocket.[119,145,146] Contrarily, a comparison of crystal structures of apo-CpI and maturated CpI revealed that apo-CpI readily crystallizes in the closed conformation, which is very similar to maturated CpI. As synthetic maturation nevertheless provided an active enzyme, an equilibrium between a closed and open conformation is suggested for apo-CpI.[145] Moreover, a phenylalanine residue in contact with $[2Fe]_H$ (F417 in apo-CpI), is relocated by 15 Å in the open conformation of apo-HydA1 in comparison to the closed conformation of apo-CpI.[119,145]

To determine the midpoint potential of the $[4Fe]_H$ cluster, the naturally occurring adt ligand can be replaced by the artificial pdt ligand, which renders the enzyme almost completely inactive.[110] The inability of protonating the pdt bridgehead limits the H-cluster states to H_{ox} and $H_{red'}$, where only $[4Fe]_H$ can change its redox state.[153] The midpoint potential of pdt-maturated HydA1, HydA1(pdt), is therefore associated with $[4Fe]_H$ and was determined with infrared spectroelectrochemical redox titrations to $-345\,mV$ at pH 7,[153] and $-450\,mV$ at pH 7.5.[179] The latter study also found a pH-dependency for the E_m, which supports a PCET event with protonation occurring at one of the cysteines ligating $[4Fe]_H$.[179] In contrast, a recent study found the E_m to be pH-independent with $E_m \approx -360\,mV$.[216] Due to the significant differences in reported midpoint potentials, a redox potentiometry of apo-HydA1 is performed in this study. EPR spectroscopy of apo-HydA compared to the mature hydrogenase allows for the determination of the midpoint potential of the isolated [4Fe4S] cluster while circumventing redox coupling with the diiron subsite. Therefore, optimal measurement conditions were probed first. The appearance of a second species for a single [4Fe4S] cluster led to the investigation of further sample preparations, including distinct buffer compositions with varying pH values. Eventually, apo-HydA1 was compared with the second [FeFe]-hydrogenase from *C. reinhardtii*, apo-HydA2, which exhibits a high sequence similarity but distinct catalytic properties. The absence of a second species in apo-HydA2 points to only one from many possibilities causing the presence of two distinct species in apo-HydA1, which are finally discussed.

4.1 Sample Preparations and Measurement Conditions of apo-HydA1

The unmaturated [FeFe]-hydrogenase from *C. reinhardtii* lacking the diiron subsite, referred to as apo-HydA1, was expressed and purified as described in Engelbrecht et al. [283] by Astrit Veliju of the Photobiotechnology AG, Ruhr-University Bochum. The apo-HydA2 protein was similarly expressed and purified by Kristina Liedtke from the same research group. Different sample preparations frozen in liquid nitrogen, listed in Table 4.1, were provided in 2.8 mm quartz tubes.

Table 4.1: Overview of the measured apo-HydA1 (and as indicated apo-HydA2) samples. The mixed buffer contains each 15 mM sodium acetate, TAPS, CHES, HEPES, and MES. The temperature-independent buffer (TIP) buffer contains 60 mM HEPES, 40 mM potassium phosphate buffer and 150 mM NaCl.

Sample	Buffer	Protein conc. \µM	NaDT conc. \mM	glycerol \%
-	Tris-HCl pH 8	400	5	-
-	Tris-HCl pH 8	400	10	-
Sample 1	Tris-HCl pH 8	800	5	-
-	Tris-HCl pH 8	800	10	-
Sample 2	TIP pH 7.5	500	10	10
pH 6	mixed buffer pH 6	600	5	-
pH 7	mixed buffer pH 7	600	5	-
pH7 + Gly	mixed buffer pH 7	600	5	10
pH 8	Tris-HCl pH 8	600	200	-
pH 9	mixed buffer pH 9	600	5	-
apo-HydA2	Tris-HCl pH 8	1000	5	-

ESE-detected field-sweep experiments, using a two-pulse Hahn spin-echo sequence, were carried out on a Bruker ELEXSYS E580 Q-band EPR spectrometer equipped with a Bruker ER 5106QT-2 resonator, an Oxford Instruments CF935 cryostat, and MercuryiTC temperature controller. Spectra were acquired at different temperatures in the overcoupled mode with gaussian $\frac{\pi}{2} = 12$ ns and $\pi = 24$ ns pulses. The interpulse delay τ was usually set to 250 ns and varied for τ-dependent measurements as indicated below. The shot repetition time varied between 0.2–1.2 ms depending on the sample and temperature. All spectra were normalized to the given frequency, video gain, shots per point, and number of scans. Spectral simulations were performed with *EasySpin* using the implemented function 'pepper'.[284]

Redox Potentiometry of apo-HydA1

The redox potentiometry of apo-CbA5H was performed anaerobically with a final concentration of 500 µM protein and 100 µM redox mediator dyes in TIP buffer with pH 7.5 and 10 % glycerol at room temperature by Astrit Veliju under my supervision. All herein-reported potentials are corrected for the standard hydrogen electrode (SHE). The potentiometry was performed in oxidative direction, i.e., after reduction with NaDT the potential was stepwise increased with µL addition of potassium ferricyanide (FIC). Meanwhile every ~ 50 mV a sample was transferred to an EPR tube and immediately frozen in liquid nitrogen. The samples were measured via ESE-detected field-sweep experiments with the resonator in the critically coupled mode at 10 K and Q-band frequencies. The analysis was performed as described in Chapter 3.

4.2 Results and Discussion

First, EPR spectra of apo-HydA1 in the reduced state were investigated. Optimal sample and measurement conditions were tested by recording spectra of samples with distinct apo-HydA1 and NaDT concentrations and the resonator in critically coupled mode (Figure 4.1). An increase in the protein concentration from 400 to 800 µM is well reflected in the relative spin concentration, which increases by 58 % upon increasing protein concentration. Moreover, a slightly higher signal intensity was observed for samples reduced with 5 mM instead of 10 mM NaDT. All sample preparations showed the same rhombic line shape, which is in agreement with a typical [4Fe4S] cluster ($S = 1/2$). Spectral simulations with a single species, however, resulted in only an insufficient fit. Similarly, no spectral simulations were reported for literature spectra, where the g-values were solely estimated to $g = 2.04, 1.9, 1.9$ (CW EPR at X-band)[119], $g = 2.05, 1.915, 1.852$ (ESE-detected EPR at Q-band)[285], $g = 2.054, 1.921, 1.848$ (ESE-detected EPR at Q-band)[111] and $g = 2.045, 1.926, 1.896$ (FID-detected EPR at Q-band).[282] Notably, the reported g-values show a high discrepancy, which unlikely arises from the different measurement techniques.

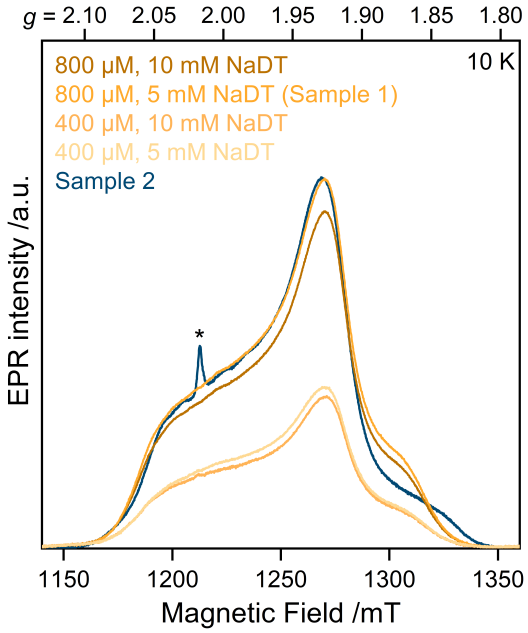

Figure 4.1: ESE-detected EPR spectra ($T = 10$ K, 34 GHz) of 400 µM and 800 µM apo-HydA1 reduced with either 5 mM or 10 mM NaDT in Tris-HCl buffer at pH 8 from one batch (orange traces) and 500 µM apo-HydA1 reduced with 10 mM NaDT in TIP buffer at pH 7.5 with 10 % glycerol from a second batch (Sample 2, blue trace). Differences in the measurement conditions are displayed in Table 4.1. An impurity arising from an organic radical is marked by an asterisk.

To meet the requirements for potentiometric titration, the buffer was exchanged to a TIP buffer (Sample 2). The TIP buffer was used to prevent changes of pH upon freezing,[286] whereas glycerol serves as cryoprotectant and limits evaporation during the potentiometry. Surprisingly, a comparison between the spectra of this sample and one of the previously prepared samples (Sample 1) revealed distinct line shapes, especially in the g_3 region, for this well-characterized monomeric protein containing only one [4Fe4S] cluster (Figure 4.2). As varying protein or NaDT concentrations showed no effect on the line shape, the distinct buffer, pH, or addition of glycerol (compare Table 4.1) have more likely impacted the electronic environment of the cluster. The observation of different spectral properties resonates with previous EPR measurements

of apo-HydA1, where besides the distinct g-values summarized above, a feature varying with different protein preparations was reported.[119,282,285] In the literature, slightly distinct line shapes for one oxidized $[4Fe4S]^{3+}$ cluster were reported, which are inconsistent with one single $S = 1/2$ species.[38] The possible six valence isomers each experience a slightly distinct, asymmetric protein environment and in principle exhibit each their own EPR spectrum.[38,287] A detailed study on HiPIPs from distinct proteins found that three to four spectral components are required for a full spectral simulation of a single cluster.[38] Moreover, a recent study on two defined valence isomers of a $[4Fe4S]^{1+}$ cluster investigated the effect of the first coordination sphere, e.g., ligating residues, on the electron distribution in [4Fe4S] clusters. The population of valence isomers changes, for example, with non-cysteinyl ligation.[275]

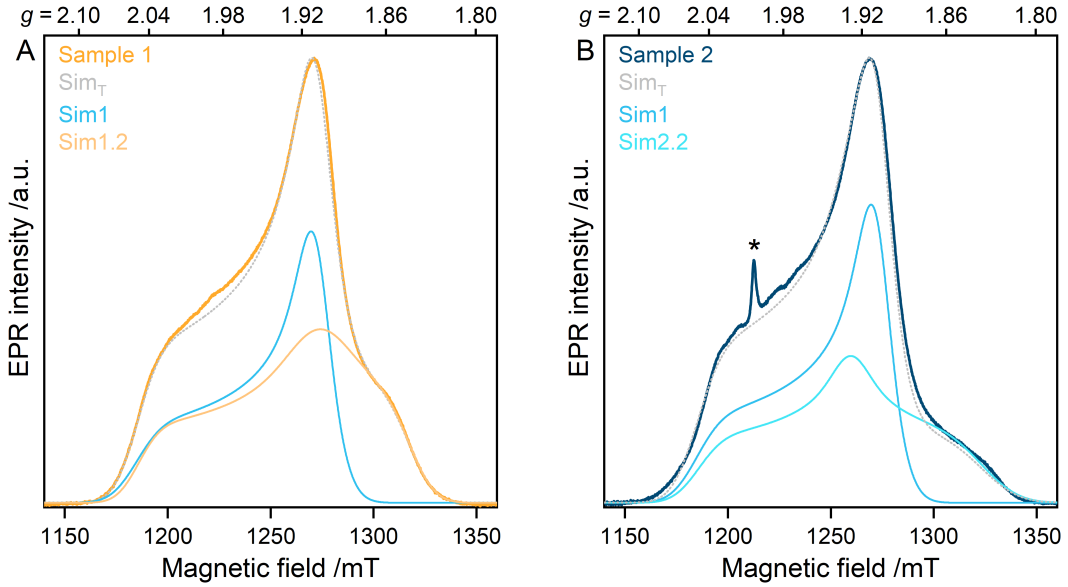

Figure 4.2: ESE-detected EPR spectra (T = 10 K, 34 GHz) of (**A**) Sample 1 and (**B**) Sample 2 of apo-HydA1 (see Table 4.2) and their respective total simulation (Sim_T, grey trace), one simulation that fit both spectra (Sim1, petrol trace) and two individual simulations (Sim1.2/Sim2.2). The simulation parameters are displayed in Table 4.2. An impurity arising from a radical signal is marked by an asterisk.

Table 4.2: Simulation parameters of the two HydA1 samples.

Simulation	g-value	g-Strain
Sim1	2.051, 1.908, 1.901	0.040, 0.018, 0.034
Sim1.2	2.049, 1.907, 1.843	0.034, 0.043, 0.031
Sim2.2	2.047, 1.928, 1.834	0.037, 0.024, 0.045

Thus, spectra of Sample 1 (Tris-HCl buffer) and Sample 2 (TIP buffer) were simulated under the assumption that two different $S = 1/2$ species contribute to each spectrum, that might arise from valence isomers. Indeed, both spectra could be well simulated (Figure 4.2) with one species (Sim1) appearing in both spectra, while individual g-values for the second species had to be introduced for each sample (Sim1.2/Sim2.2). The simulation parameters are presented in Table 4.2. The ratio of each Sim1/Sim2 is almost equal in both samples (Sample 1: 0.89, Sample 2: 1) ruling out minor species arising from contamination. Notably, the g_2-value in both simulations is $g_2 \approx 1.9$, which is attributed to [4Fe4S] clusters with non-cysteine ligands, compared to the usual observed $g_2 \approx 1.94$ in all-cysteine ligated clusters.[288] The crystal structure, however, supports the latter case.

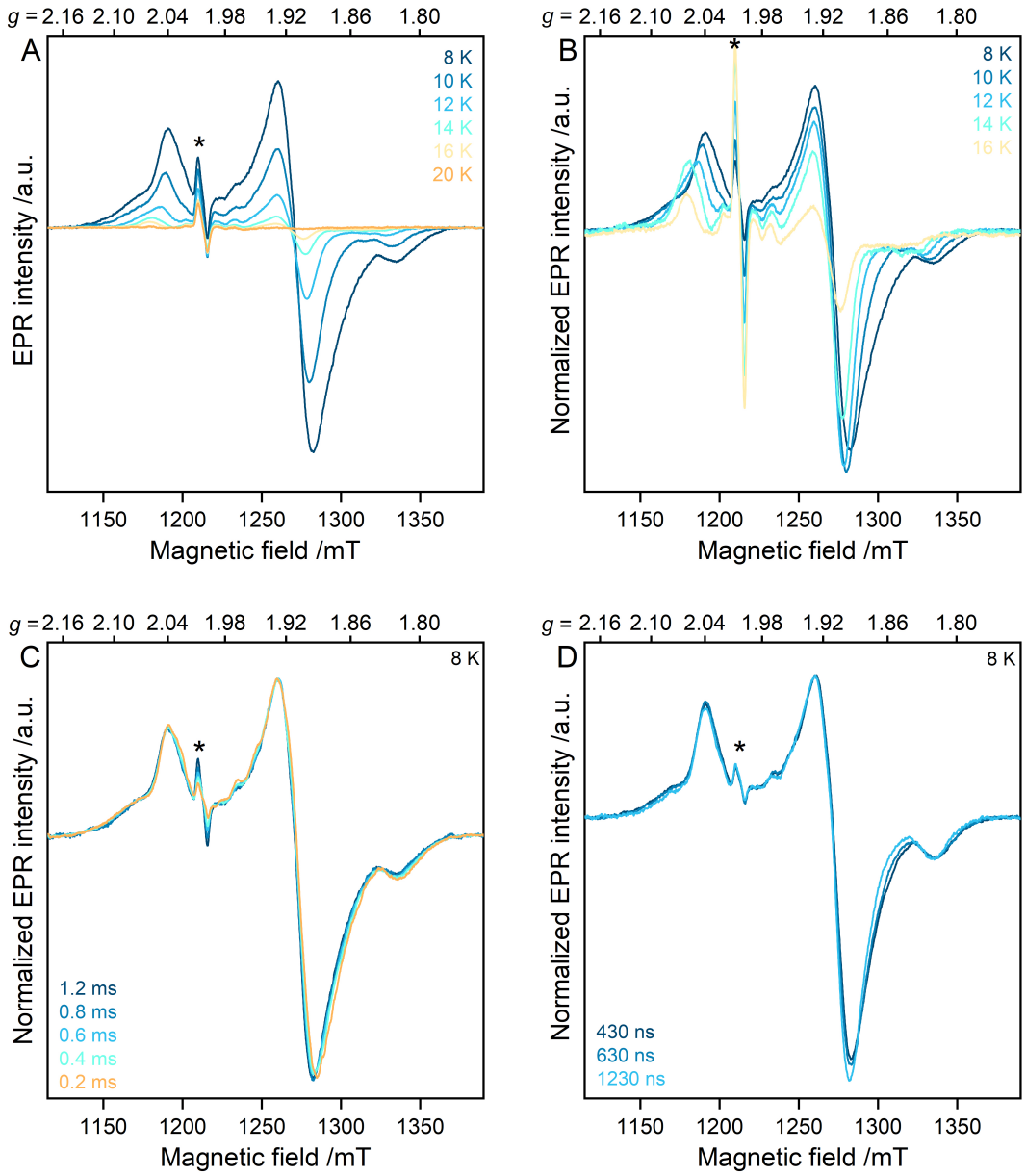

Figure 4.3: Pseudo-modulated ESE-detected EPR spectra (34 GHz) of reduced apo-HydA1 (Sample 2) recorded at different temperatures shown (**A**) as recorded and (**B**) normalized to [0,1] and (**C, D**) recorded at 8 K with (C) the shot repetition time varied between 0.2−1.2 ms and (D) the inter-pulse delay varied between 430−1230 ns. An impurity arising from a radical signal is marked by an asterisk.

The presence of more than one paramagnetic species for only one [4Fe4S] cluster was also observed in the EPR spectra of other FeS proteins. In Isf from *M. thermophila* two instead of one feature were observed in the g_3-region. After the exclusion of spin-spin interactions or proton hyperfine couplings as a cause, the atypical features were attributed to microheterogeneity within the population of Isf molecules.[289] In the reductase APR from *M. tuberculosis* a mixture of [4Fe4S] clusters were assumed to reflect the existence of distinct conformations, whose formations were shown to be unaffected by changes in the pH value.[290] In the corrinoid protein from *C. thermoaceticum*, a superposition of two components with different temperature and power dependences were attributed to distinct $S = 1/2$ electronic states arising from different protein environments of the reduced [4Fe4S] cluster. A single state was isolated by the addition of urea.[291] In comparison to the reviewed literature, here not only two distinct species are observed for one

[4Fe4S] cluster, but they also partially differ upon different sample preparations. Nevertheless, the assignment of two species based on one spectrum is daring as there are too few defined features for an unambiguous assignment.

Thus, in an attempt to deconvolute the species of Sample 2, distinct measurement conditions were tested. Spectra were recorded at varying temperatures up to 20 K (Figure 4.3), beyond which the signal was undetectable. This observation agrees with previous measurements,[119] indicating the presence of at least one fast-relaxing [4Fe4S] cluster and supports the absence of slower-relaxing species, such as [2Fe2S] clusters. Moreover, variation of the shot repetition time and inter-pulse delay τ had no significant effect on the line shape at lower temperatures (Figure 4.3C and D), indicating that the species have similar or too fast relaxation properties for disentanglement. The complex temperature-dependent profile exhibits shifted peak positions of g_1 and g_3 as a function of temperature. This change in line shape prevents an unambiguous assignment of specific g-values valid for all temperatures or assignment to certain species. The g-values obtained from the simulation Sim1, however, are very similar to the spectrum recorded at 16 K. Broad wings at the g_1 and g_3 positions at lower temperatures, that are absent from 16 K on, are indicative of dipolar interactions. However, inter-molecular spin-spin interactions between two [4Fe4S] clusters are unlikely to occur, as the [4Fe4S] cluster binding site is buried inside the protein and the neighboring cavity of $[2Fe]_H$ was shown to be deficient of further Fe ions in the crystal structure.[119] A similar complex temperature dependence including increased broadening was reported for maturated HydA but suggested to arise from the here absent inter-cluster exchange interactions between $[4Fe]_H$ and $[2Fe]_H$.[183]

Overall, at least two distinct species were observed in apo-HydA1, that partially vary within different protein preparations. The temperature-dependent relaxation profile, however, is complex and possibly reflects the presence of valence isomers and/or distinct conformations of the [4Fe4S] cluster in the ground and excited states.[275] Therefore, an EPR-monitored redox potentiometry of apo-HydA1 is subsequently performed to determine the midpoint potential of the [4Fe4S] cluster and attempt to separate distinct species based on their potential.

4.2.1 Redox Potentiometry of apoHydA1 Reveals Two Distinct Species

To determine the midpoint potential of the [4Fe4S] cluster of apo-HydA1, an oxidative redox potentiometry was performed. The spectra of redox potentiometry samples taken at various potentials are compared in Figure 4.4A to Sample 2, here denoted as "standard", which is assumed to contain 100 % reduced clusters. The highest potential sample taken at $E_m = -392$ mV can be well simulated with Sim1 derived from Sample 2 simulations (Figure 4.4B), whereas the lowest potential sample at -509 mV shows a mixture of Sim1 and Sim2.2. Upon increasing potentials, the intensity of the species denoted as Sim2.2 decreases, as is apparent from the continuous disappearance of the g_3-feature. The respective weights used for the total simulations are shown in Table 4.3. As the overall signal intensity decreases concomitantly with increasing potential, a conversion of one species into another is unlikely but rather reflects distinct redox potentials for the two species.

Three different Nernst plots were constructed, where the integrated intensity of each simulation Sim1, Sim2.2, and Sim_T with weights presented in Table 4.3 were plotted as a function of

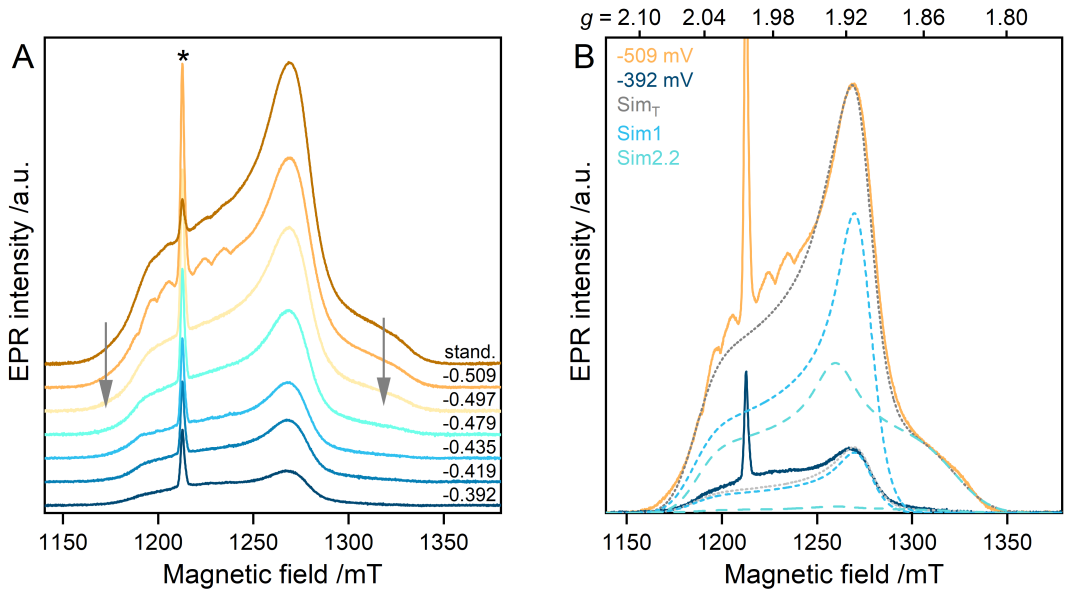

Figure 4.4: ESE-detected EPR spectra (T = 10 K, 34 GHz) of the redox potentiometry samples of apo-HydA1 taken at various potentials (**A**) displayed with a continuous spacing, where the arrows indicate decreasing of the g_1 and g_3 features and (**B**) simulations of the highest (blue trace) and lowest potential samples (orange trace) with adjusted simulations of Sim1 (dashed trace) and Sim2.2 (dashed trace) yielding the total simulation $\mathrm{Sim_T}$ (brown dotted trace). An impurity arising from a radical signal is marked by an asterisk.

Table 4.3: Weights of Sim1 and Sim2.2 used for the total spectral simulations and construction of the Nernst plots as a function of potential E_h.

E_h \mV	Sim1 \%	Sim2.2 \%
standard	54	46
-0.509	54	46
-0.497	57	43
-0.479	68	32
-0.435	74	26
-0.419	75	25
-0.392	85	15

potential. The resulting midpoint potential is the highest for Sim1 (E_m = −474 mV) and lowest for Sim2.2 (E_m = −491 mV), yielding a total potential of E_m,tot = −482 mV. The number of electrons transferred, n, is almost equal to one for Sim2.2 and consistent with a one-electron transfer reaction. In contrast, n is almost halved for Sim1, which can be caused by insufficient equilibration and/or the presence of several redox centers with similar potential.[82,292] As data points are missing at the upper and lower end of the curve, the Nernst fits are only an approximation, and further samples as well as a reductive counterpart are necessary to improve the accuracy and prove the reversibility of the redox reaction. In comparison with the literature, the obtained midpoint potential is best in accordance with the one reported by Senger et al. [179] (E_m = −450 mV at pH 7.5). However, it is questionable, if the present midpoint potential of the isolated [4Fe4S] cluster can be compared with the fully maturated H-cluster experiencing intra-cluster exchange coupling. Nevertheless, the potential-dependent spectra allowed for an unambiguous separation of species Sim1 at higher potentials, whereby redox-dependent changes might reflect the presence of two discernible species.

The formation of multiple redox states of the H-cluster, such as $H_{ox}H$, $H_{red}'H$, or $H_{hyd}H$, were shown to be pH-dependent, e.g., they accumulated mainly under acidic pH. Further studies supported protonation events occurring at the cysteine residues ligating $[4Fe]_H$ independent of the catalytic proton transfer pathway.[179,180] Moreover, increasing concentrations of NaDT accelerated the formation of $H_{ox}H$.[180] Thus, it is tempting to speculate, that such a protonation might as well occur at the [4Fe4S] cluster in the apo-enzyme, which is possibly exposed to bulk water in the open conformation, and might reflect the presence of two distinct species in apo-HydA1.

To investigate the possibility of pH-dependent protonation and in a further attempt to deconvolute the species, spectra of apo-HydA1 in buffers with distinct pH values were recorded.

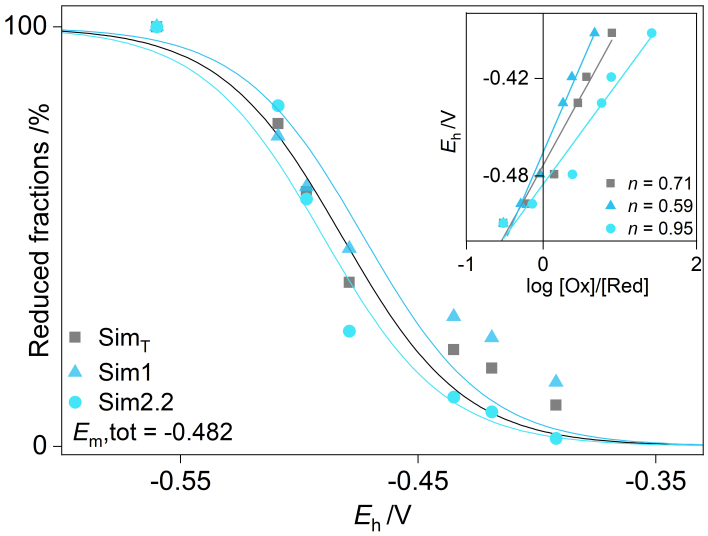

Figure 4.5: Titration curves of the oxidative (squares) redox potentiometry series of apo-HydA1 monitored via pulsed EPR spectroscopy ($T = 10$ K, 34 GHz). The reduced fractions were obtained by integration of the simulated absorption pulsed EPR spectra of either Sim1 (triangles), Sim2.2 (circles), or the total simulation (squares). The data points were fitted to the one-electron Nernst equation yielding the midpoint potential. The slope of the line of the semi-log plot (inset) of the logarithm of the concentration ratio of oxidized ([Ox]) to reduced ([Red]) yields the actual number of electrons transferred, n.

4.2.2 pH-Dependency of HydA1 Confirms Second Species

EPR spectra of apo-HydA1 in buffers with distinct pH values (simply denoted as pH X) and one sample reduced with 200 mM NaDT (pH 8) were recorded at 8 and 14 K, respectively (Figure 4.6). All samples exhibit a rhombic spectrum and share the common $g_2 \approx 1.9$ feature, similar to Sim1, which shifts to a lower magnetic field at elevated temperatures. The latter observation may be a consequence of interconversion between ground and excited states with increasing temperature or arise from distinct valence isomers.[275] The pH 9 and the super-reduced sample (orange traces) lack the broad wing around g_3 at 8 K and seem to consist of only one species contrarily to the pH 6/7 samples (blue traces). However, the g_3 feature becomes more prominent at elevated temperatures and is also visible in the super-reduced sample. Moreover, two new features are present in samples pH 6 and 7, marked with a hashtag. Spectra of the mixed buffer alone showed only the resonator background (data not shown), excluding that these features are artifacts arising from the buffer. Their presence at lower pH values and $g \approx 2$ hint at the presence of

redox-dependent organic radicals, that are absent at pH ≥ 8. The addition of glycerol induces an overall broadening of the line shape, which is attributed to an increase in g-strain (Figure 4.6C). This observation could contribute to explain the differences observed between Sample 1 and Sample 2, where the latter was in buffer with 10 % glycerol.

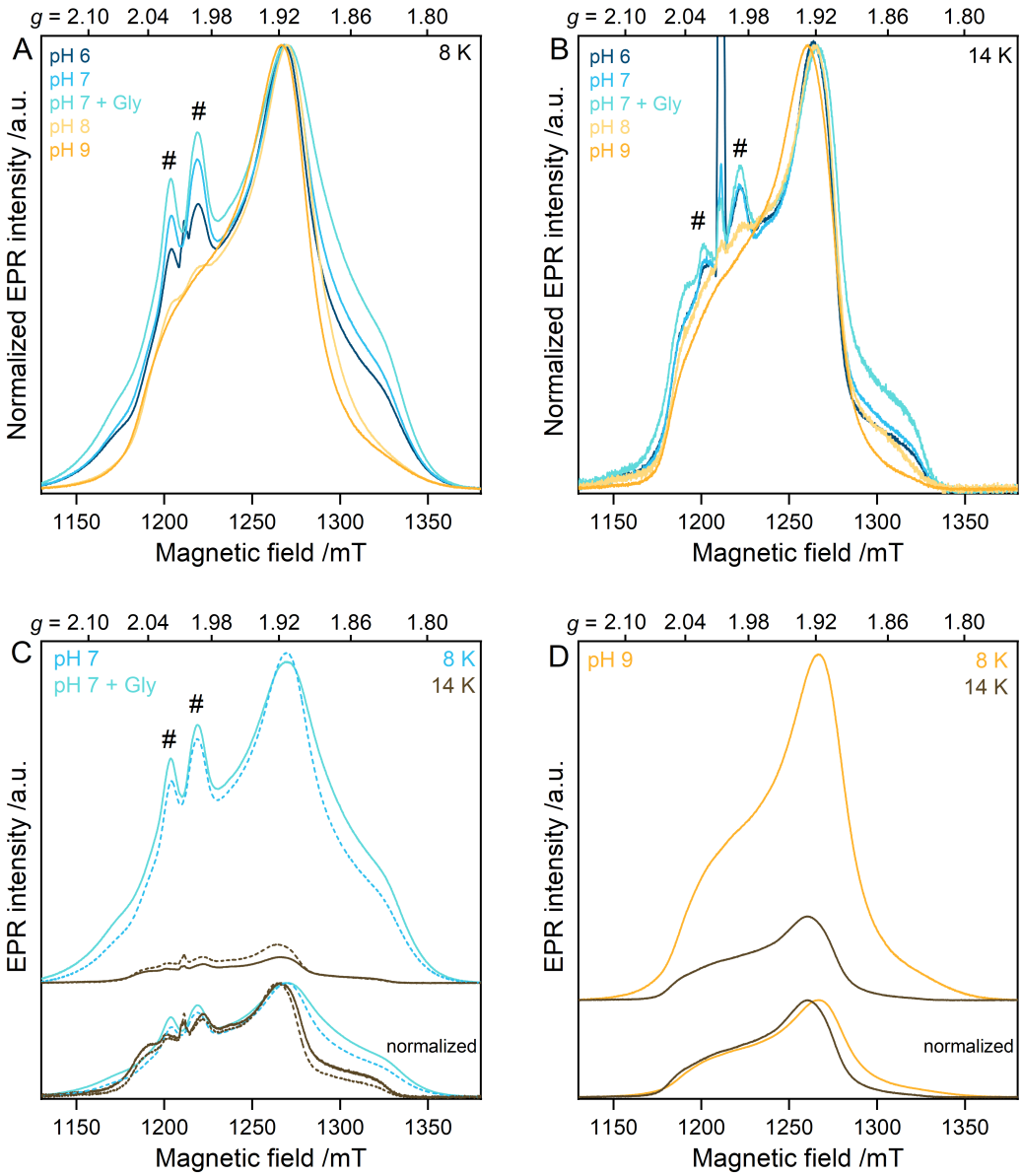

Figure 4.6: ESE-detected EPR spectra (34 GHz) of apo-HydA1 in mixed buffer with distinct pH values (pH 6-9), in the presence of 10 % glycerol (+ Gly) and in Tris-HCl buffer at pH 8 with 200 mM NaDT recorded at (**A**) 8 K and (**B**) 14 K. All spectra were normalized to their maximum signal intensity. The spectra of pH 7 and pH 7 + Gly (**C**) and pH 9 (**D**) recorded at two distinct temperatures are displayed for better comparison of their line shape as recorded (top traces) and normalized to their maximum signal intensity (bottom traces). Unknown features are marked by #. An impurity arising from a radical signal is marked by an asterisk.

Overall, the obtained spectra indicate a pH-dependent variation of the fractions of the two species. Under basic conditions (pH 9) only one species similar to Sim1 is present, whereas under acidic conditions, two species are detectable. However, duplicates are necessary to confirm this observation, as the previously presented data suggest the formation of distinct features

within different sample preparations. Moreover, other reducing agents, or the reduction with a potentiostat should be probed to investigate the influence of NaDT, which is under debate.[293]

4.2.3 Comparison of apo-HydA1 and apo-HydA2

To determine if the unusual features of the [4Fe4S] cluster and the respective distinct species are inherent to apo-HydA1, the second [FeFe]-hydrogenase from *C. reinhardtii*, apo-HydA2, was investigated. HydA2 has a high sequence similarity to HydA1 (73.5 %) and is likewise suggested to consist of the H-domain only.[283] However, no crystal structure is available to date. The catalytic activity of HydA2 is lower compared to HydA1 and biased in favor of H_2 consumption. Contrarily, HydA1 is biased towards H_2 production.[283] The reason for a changed bias is suggested to arise from a hydroxyl group from a nearby threonine introducing a negative dipole near $[4Fe]_H$, that is present in HydA1 (T226) but absent in HydA2 (V229). Exchange mutagenesis of both residues generating T226V and V229T in HydA1 and HydA2, respectively, switched the catalytic bias each in the respective other direction.[283]

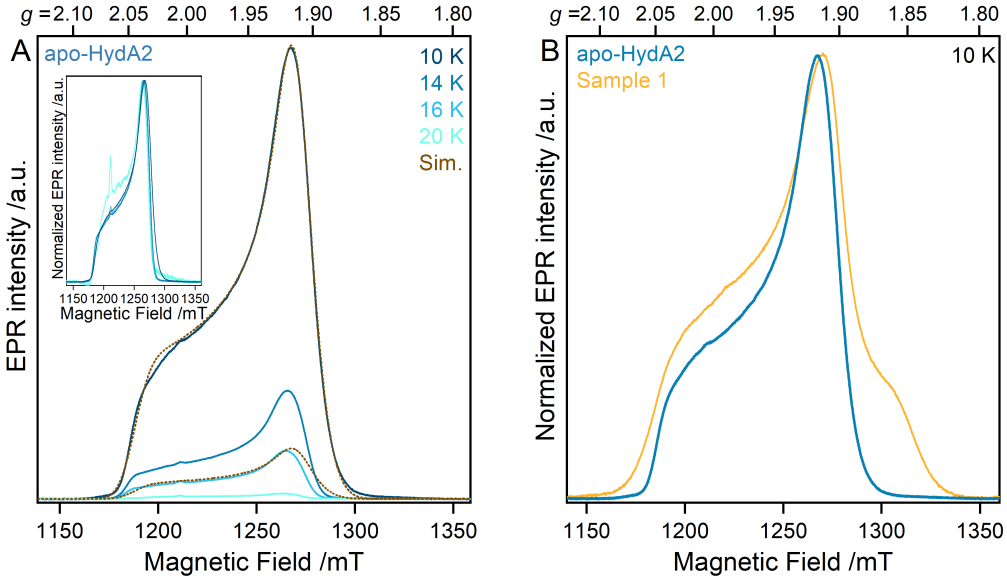

Figure 4.7: Comparison of ESE-detected EPR spectra (34 GHz) of reduced apo-HydA1 (Sample 1) and apo-HydA2. (**A**) Temperature-dependent EPR spectra of apo-HydA2 with the spectral simulation performed at 10 K (brown dotted trace) fitting insufficiently at higher temperatures. (**B**) Comparison of normalized EPR spectra from apo-HydA1 and apo-HydA2 at 10 K prepared under similar conditions.

Temperature-dependent spectra of apo-HydA2 prepared similar to Sample 1 (see Table 4.1) exhibit in contrast to apo-HydA1 a single rhombic signal attributed to a [4Fe4S] cluster (Figure 4.7). Temperature-dependent spectra reveal a similar temperature behavior compared to apo-HydA1, where only residual signal intensity is left at 20 K. The spectrum can be simulated with a single species with $g = 2.045, 1.911, 1.902$. The g-values are comparable to Sim1 from apo-HydA1 ($g = 2.051, 1.908, 1.901$), and possibly reflect the distinct protein environment between the enzymes. Spectral simulations performed at 10 K fit only insufficiently at higher temperatures. The observed upshift in g-values dominating at g_3 indicate, similar to the pH-dependent samples of apo-HydA1, the presence of excited states or valence isomers.

4.3 Summary and Outlook

At least four distinct EPR spectra and respective g-values of reduced apo-HydA1 were previously reported in the literature, whose respective g-values differ. Moreover, to date no EPR spectral simulations or extensive temperature-dependent studies were undertaken. These observations are in conjunction with changing cluster environments within different preparations, as reported in this study, which hamper a simple analysis. An overview of selected recorded spectra is presented in Figure 4.8.

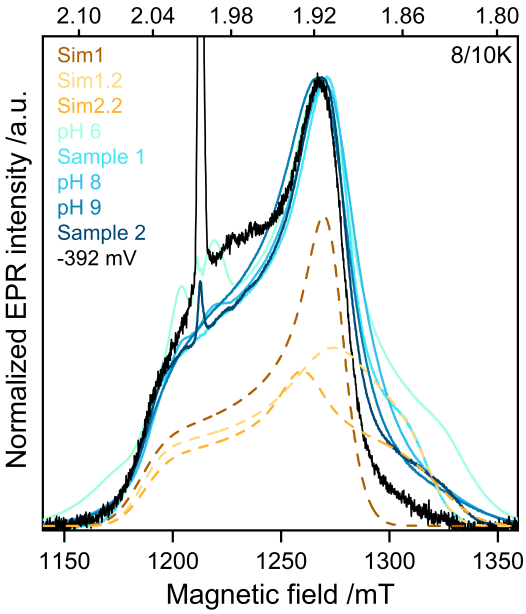

Figure 4.8: Comparison of selected ESE-detected EPR spectra (T = 8/14 K, 34 GHz) of reduced apo-HydA1 derived from distinct sample preparations as shown in Table 4.1. The coloring ranges from dark to light blue, indicating the broadening of the line width, particularly at g_3.

All spectra seem to share a common species with g-values represented by Sim1. A similar species is also observed in the spectrum of apo-HydA2. However, at least one additional species is present in most sample preparations, which varies under distinct conditions and thus, seems to be prone to changes in the cluster environment. Notably, under basic conditions (pH 9) and higher E_m (−392 mV) the spectral line shape is the least broadened and may consist of a single species only. The broadening and appearance of an additional feature most prominent at g_3 increases upon decreasing pH and with lower potential. Eventually, the sample at pH 6 exhibits the most deviating spectrum, whose additional species is not consistent with Sim1.2 or Sim2.2. Several suggestions can be made for the observation of distinct features or species in apo-HydA1 based on the presented results.

First, little is known about the EPR spectral properties of valence isomers or excited states of [4Fe4S] clusters embedded in proteins. A recent study by Skeel et al. [275] revealed the presence of both in synthetic [4Fe4S] clusters limited to two valence isomers. The situation is expectedly more complex in proteins, where the first and second coordination spheres and even distant structural changes can influence the E_m or state of the FeS clusters. Thus, the small upshift in g-values, observed with increasing temperature, may be attributed to the population of excited states, whereas at lower temperatures, the ground state is observed. Additionally, the

presence of two or more valence isomers can not be excluded. Therefore, a study investigating the fundamental properties of [4Fe4S] clusters at distinct temperatures and protein preparations from distinct organisms, supported by isotope-labeled hyperfine spectroscopy, may be necessary.

Second, the broadened wings observed at g_1 and g_3 around the initial Sim1 signal are frequently attributed to dipolar couplings. A gas-phase electrophoretic macromolecule analysis (GEMMA) showed that apo-HydA1 and HydA1 are predominantly present as monomers, however, a dimerized form is observed as well.[294] As the [4Fe4S] cluster is located close to the surface, a possible dimerization may support the inter-cluster interaction of two monomers resulting in changed EPR spectral line shapes. The varying buffer and pH may thereby influence the distribution of monomeric or multimeric forms. A comparable analysis may readily support or exclude this hypothesis.

Third, the change of Tris-HCl to TIP buffer or mixed buffer led to the appearance of several unknown features including $g \approx 2$ at lower pH values, that are absent in a mixed buffer sample devoid of protein. In the crystal structure of apo-HydA1, a sodium acetate molecule was found in the empty cavity adjacent to the [4Fe4S] cluster and suggested to arise from the crystallization buffer.[119] Here, the mixed buffer also contains sodium acetate and thus, it can be speculated that the unknown features might arise from acetate molecules or their binding to the cluster. Moreover, chloride was shown to bind to the Fe ion of a radical SAM [4Fe4S] cluster.[295] Thus, the shift in g_3 observed for samples in Tris-HCl and TIP buffer might arise from the high concentration of 150 mM NaCl in the latter. Labile binding of the cluster is supported by varying amounts of Fe and S^{2-} in between preparations,[132] and site-directed mutagenesis of the ligating cysteine residues. For example, cysteine residue 114 was suggested to be an alternative ligand in C115A variants,[282] which would induce a shift in g-values. Thus, an in-depth study of site-directed mutants or varying buffer and salt conditions, including spectral simulations and temperature-dependent spectra, might help to unravel the unusual features observed here. Moreover, it would be interesting to compare the present samples with CW EPR measurements at X-band frequencies to probe which features persist at distinct microwave powers and to unambiguously exclude spin-spin interactions. Note, that these suggestions are highly speculative. A water-filled cavity of 10 Å diameter neighboured to the [4Fe4S] cluster,[145] however, leaves a lot of room for speculation.

Fourth, the crystal structures of apo-HydA1 and apo-CpI revealed the active site to be either in the open or closed conformation, respectively, while an equilibrium state is believed to exist for the latter. The significant structural rearrangement that the active site undergoes during binding of $[2Fe]_H$ might also occur in the apo-enzyme upon external triggers. Thus, the distinct species observed in the present study might be traced back to (partial) structural arrangement of the "lid", "lock", and/or "plug" region. Distinct species for one [4Fe4S] cluster have been previously associated with structural microheterogeneity arising from distinct conformations of the cluster's protein environment. To investigate this possibility, apo-HydA1 could be studied in the presence of (apo-)HydF, the maturase enzyme suggested to be responsible for the transport of $[2Fe]_H$ to the active site. The presence of (apo-)HydF might stabilize one specific conformation. As HydF also carries at least one [4Fe4S] cluster, that is paramagnetic under reducing conditions, apo-HydF would be a more suitable choice due to the prevention of overlapping species. Further insights into the electronic structure of HydF are presented in the next chapter.

Fifth, the here performed redox potentiometry revealed not only a low redox potential ($E_m = -482\,mV$), which agrees with the one observed by Senger et al. [179], but also enabled the separation of species by potential-dependent variations of the spectral line shape. This indicates the occurrence of a potential-dependent event, such as protonation of the [4Fe4S] cluster. The potential dependence is in agreement with the pH-dependent samples, exhibiting two distinct species at low pH, whereas presumably, only one species is present at higher pH values. To determine if a protonation is involved in the formation of a second species, the redox potentiometries should be performed at distinct pH values, as the midpoint potential is expected to shift upon protonation/deprotonation. However, for the determination of an accurate midpoint potential, first, the respective spectral species have to be defined. Eventually, proton ENDOR spectra in protonated and deprotonated buffers at distinct pH values might provide insights into the direct proton environment of the cluster and reveal the presence of exchangeable protons.

Sixth, the protonation of $[4Fe]_H$ at one of the ligating cysteine residues is proposed for several redox states,[179,180,192] but has been challenged by others.[216,293] The redox titration performed by Rodríguez-Maciá et al. [216] on inactivated HydA1(pdt) was shown to be pH-independent and thus, contradicts the opinion that a PCET, including protonation of $[4Fe]_H$, occurs. Protonation at a ligating cysteine residue is expected to decrease the electron density of the [4Fe4S] cluster and in turn, facilitate its reduction.[180] This effect might explain the change in g-values and would be in conjunction with the lower midpoint potential observed for species Sim2.2 ($E_m = -491\,mV$) in comparison to species Sim1 ($E_m = -474\,mV$). Moreover, the increasing presence of the broad feature at g_3 upon lowering the pH would agree with the observed accumulation of protonated species under acidic conditions. Nevertheless, it is questionable why such a second species is not observable at all in the related apo-HydA2 preparation. Thus, further investigations of site-directed variants may be necessary.

Seventh, the results imply, that apo-HydA1, in contrast to apo-HydA2, has a distinct protein environment promoting the formation of a second species. One cause might be the hydroxyl group of T226 in the vicinity of the [4Fe4S] cluster in HydA1, that is absent in HydA2. The properties of T226 were shown to manipulate the catalytic bias of HydA2.[283] Thus, it is tempting to speculate, that the residue's influence changes the electronic environment of the [4Fe4S] cluster in a way that a second species with changed electronic properties is observable. However, simultaneously the question arises why only fractions of the protein take onto a distinct conformation. Further EPR studies on the Thr/Val variants might help to resolve the differences in the EPR spectral signatures observed for apo-HydA1 and apo-HydA2.

Overall, HydA1 is a prime model for the investigation of first and second coordination sphere effects via EPR spectroscopy, due to the principal lack of overlapping species from F-clusters. Why in the apo-enzyme, harboring one single [4Fe4S] cluster, multiple species are observed, requires further investigations. Eventually, for determination and comparison of the g-values of [4Fe4S] clusters, a careful examination of the sample preparation, buffer, reducing agent, and glycerol content is necessary. This may especially be true, when the cluster is exposed to the surface and/or in contact with bulk water.

5

The Maturase HydF: [2Fe2S], or not [2Fe2S], That is the Question

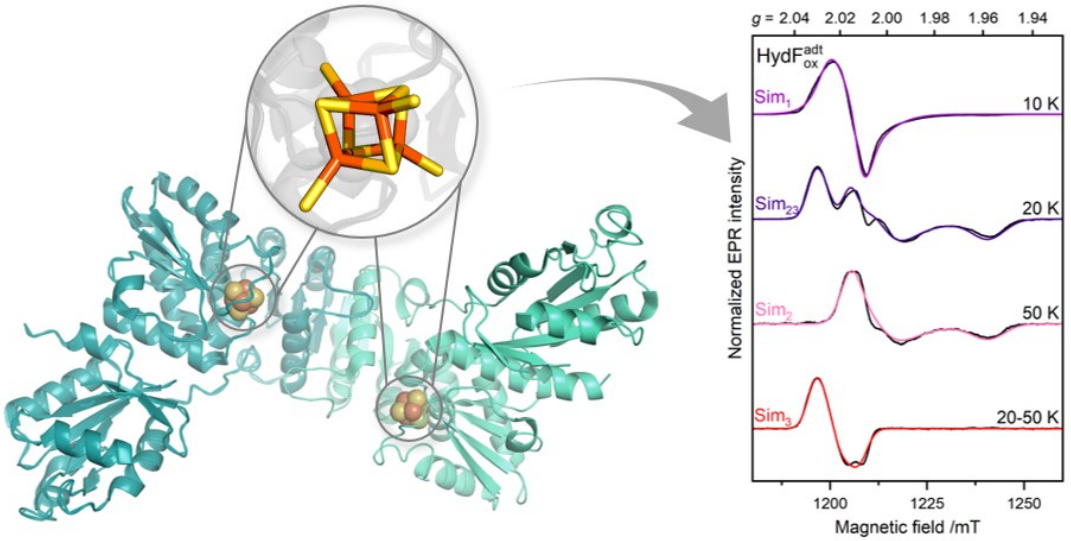

HydF is an enzyme with GTPase activity that exists as a dimer or trimer and has been studied in several organisms.[135,148,204,296–299] Regardless of the organism, there is a consensus that each monomer of HydF contains a single [4Fe4S] cluster, as confirmed by the crystal structure of *Tme*HydF (PDB ID: 5KH0, see Figure above) and spectroscopic data.[110,135,148,285,288,297,298,300,301] The [4Fe4S] cluster is coordinated by three cysteine residues, which are essential for its assembly.[288] Based on X-ray and ENDOR data, the fourth ligand is suggested to be an aspartate, glutamate, histidine, or water-derived species, and varies with the hosting organism.[148,288,302,303] This unique three-cysteine ligation is also reflected in the EPR spectral properties. Under reducing conditions, the [4Fe4S] cluster is paramagnetic ($S = 1/2$) and exhibits a rhombic signal with g-values around $g = 2.05, 1.9, 1.85$. The g-values vary only slightly between different organisms (see Table 5.1). Similar to other three-cysteine ligated [4Fe4S] clusters, the g_2 value is downshifted to $g = 1.9$ in comparison to the typical $g = 1.94$ value observed for all-cysteine ligated [4Fe4S] clusters.[298] In addition, a $S = 3/2$ signal was observed at lower magnetic field in *Tm*HydF.[298] Exchange experiments showed that the fourth ligand of the [4Fe4S] cluster is labile and can be readily accessed and exchanged by exogenous ligands.[148,298] This observation has raised the question whether the precatalyst of $[2Fe]_H$ transferred from HydG can bind to the [4Fe4S] cluster of HydF. The lack of an additional FeS cluster binding motif and a conserved cavity next to the [4Fe4S] cluster supports this view.[148,304] Furthermore, HYSCORE data and DFT calculations suggest a shared CN^- ligand of the [4Fe4S] cluster and diiron subsite in *Ca*HydF^{pdt} and, thus, a transient binding of $[2Fe]_H$.[110]

The suggestion that the diiron precursor binds to the [4Fe4S] cluster of HydF, however, was refuted by a recent study, where [4Fe4S] cluster-less variants were generated via site-directed exchange of the ligating cysteines.[304] After addition of the synthetic mimic $[2Fe]_{MIM}$, the respective FTIR spectra showed the integration of $[2Fe]_{MIM}$ and subsequent transfer to HydA1 *in vitro*. The results demonstrate that neither the [4Fe4S] cluster nor its ligating residues are required for $[2Fe]_{MIM}$ binding. Shifts in FTIR bands observed for the variants in comparison to the wild-type enzyme, however, suggest a proximity of $[2Fe]_{MIM}$ to the [4Fe4S] cluster.[304] Moreover, it is suggested that the diiron subsite remains in the $Fe^{1+}Fe^{1+}$ state, as anticipated previously.[110,304]

Table 5.1: Overview of the EPR-active species and respective *g*-values of reduced and oxidized (denoted with an asterisk) or as-isolated HydF of different organisms (including *C. acetobutylicum*, *T. maritima*, *Thermosipho melanesiensis* (*T. melanesiensis*), *Thermosipho neapolitana* (*T. neapolitana*), and *Shewanella oneidensis* (*Sh. oneidensis*)) derived from this work and the literature. When HydF was expressed in the presence of HydE and HydG it is denoted as "co-expressed". The asterisk marks samples obtained from O_2-oxidized samples.

Enzyme	Temp.	Species	*g*-values	Reference
reducing conditions				
*Tn*HydF	10 K	[4Fe4S]	2.044, 1.895, 1.85	Berto et al. [288]
*Ca*HydF	12-90 K	[2Fe2S]	2.00, 2.00, 1.96	Shepard et al. [135]
co-expressed	12-30 K	[4Fe4S]	2.05, 2.05, 1.89	Shepard et al. [135]
co-expressed	10 K	[4Fe4S]	2.049, 1.902, 1.872	Czech et al. [285]
	15 K	[4Fe4S]	2.053, 1.879, 1.865	Scott et al. [305]
	12 K	[4Fe4S]	2.058, 1.879, 1.862	Balci et al. [144]
+ $[2Fe]_{MIM}$	12 K	[4Fe4S]	2.062, 1.879, 1.858	Balci et al. [144]
*Sho*HydF	20-40 K	[4Fe4S]	2.045, 1.927, 1.927	Kuchenreuther et al. [297]
*Tm*HydF	10 K	[4Fe4S]	2.045, 1.904, -	Brazzolotto et al. [298]
	10 K	[4Fe4S]	-	Berggren et al. [110]
*Tm*HydF + $[2Fe]_{MIM}$	10 K	[4Fe4S]	-	Berggren et al. [110]
*Tme*HydF	10 K	[4Fe4S]	2.046, 1.899, 1.864	Caserta et al. [148]
*Tme*HydF + $[2Fe]_{MIM}$	10 K	[4Fe4S]	2.048, 1.908, 1.867	Caserta et al. [148]
	10 K	[4Fe4S]	2.044, 1.905, 1.866	this work
	20 K	FeS cluster	2.039, 1.916, 1.877	this work
as isolated/O^2-oxidized*				
*Ca*HydF co-expressed	20 K	3Fe or less	2.045, 2.007, 1.906	Czech et al. [285]
	15 K	[3Fe4S]	2.019, 2.010, 1.974	Shepard et al. [301]
	30 K	[2Fe2S] A	2.010, 2.003, 1.961	Shepard et al. [301]
	30 K	[2Fe2S] B	2.045 , 2.008, 1.981	Shepard et al. [301]
co-expressed[1]	25 K	[2Fe2S] A	2.016, 2.004 , 1.961	Scott et al. [305]
co-expressed[1]	25 K	[2Fe2S] B	2.041, 2.008, 1.997	Scott et al. [305]
*Sho*HydF	20-120 K	unknown	2.052, 2.009, 1.971	Kuchenreuther et al. [297]
*Tme*HydF	10 K	no signal	-	Caserta et al. [148]
*Tme*HydF + $[2Fe]_{MIM}$*	10 K	[3Fe4S]	2.023, 2.012, 2.010	this work
*	20-35 K	[3Fe4S]	2.031, 2.023, 2.012	this work
*	10-80 K	unknown	2.015, 2.002, 1.958	this work

[1] samples with visible FTIR bands

Conflicting EPR and X-ray absorption spectroscopy (XAS) data suggest the existence of at least one more paramagnetic species in some organisms. When HydF is expressed without other maturases, either only the [4Fe4S] cluster[110,288,298] or both [4Fe4S] and [2Fe2S] clusters were observed.[135,300,305] Co-expression with HydF and HydG or the addition of $[2Fe]_{MIM}$ to as-isolated HydF led either to small[110,144] or no significant[148,305] changes in the [4Fe4S] cluster signal and/or the observation of additional [2Fe2S] cluster-like species, that are also suggested to arise from $[2Fe]_{MIM}$ precursors, [3Fe4S] clusters or a radical-derived species.[285,297,305] As the exact maturation pathway and role of HydF in terms of assembling or scaffolding the $[2Fe]_H$ precursor is still under investigation and the reported EPR data are conflicting, samples of *Tme*HydF loaded with $[2Fe]_{MIM}$ were investigated with temperature-dependent pulsed EPR.

5.1 Sample Preparations and Measurement Conditions of HydF

The hydrogenase maturation enzyme HydF from *Thermosipho melanesiensis* was expressed and purified as described by Haas et al. [304] by Kristina Liedtke from the AG Photobiotechnologie, Ruhr-University Bochum, and different sample preparations of HydF loaded with the synthetic $[2Fe]_{MIM}$ cofactor listed in Table 5.2 were provided in 2.8 mm quartz tubes.

Table 5.2: Overview of the measured *Tme*HydF samples provided in potassium phosphate buffer at pH 6.8.

Sample	State (Treatment)	Concentration / µM
*Tme*HydF + $[2Fe]_{MIM}$	reduced (25 mM NaDT)	760
*Tme*HydF + $[2Fe]_{MIM}$	oxidized (2 h O_2)	760

ESE-detected field-sweep experiments, using a two-pulse Hahn spin-echo sequence, were carried out on a Bruker ELEXSYS E580 Q-band EPR spectrometer equipped with a Bruker ER 5106QT-2 resonator, an Oxford Instruments CF935 cryostat, and MercuryiTC temperature controller. Spectra were acquired at different temperatures in the overcoupled mode with gaussian $\pi/2 = 24$ ns and $\pi = 26$ ns pulses. The interpulse delay τ was set to 250 ns and the shot repetition time varied between 0.5–3 ms depending on the sample and temperature. The EPR spectra were baseline-corrected using MATLAB. If not stated otherwise, all spectra were normalized to the given frequency, protein concentration, video gain, shots per point, and number of scans. Spectral simulations were performed with *EasySpin* using the implemented pepper function.[284]

5.2 Results and Discussion

The homodimeric *Tme*HydF maturase harbors two [4Fe4S] clusters with one in each monomeric subunit.[148] Here, HydF was loaded with the synthetic $[2Fe]_{MIM}$ cofactor (denoted as $HydF^{adt}$). The ESE-detected EPR spectrum of reduced $HydF^{adt}$ at 10 K (see Figure 5.1) exhibits a rhombic signal, whose spectral simulation is consistent with a [4Fe4S] cluster having $g = 2.044$, 1.905, 1.866. The g-values are in agreement with literature data of previously recorded *Tme*$HydF^{adt}$ (see Table 5.1) and also show no significant change upon integration of $[2Fe]_{MIM}$compared to the as-isolated [4Fe4S] cluster.[144,148] In contrast, Berggren et al. [110] observed an upshift from $g = 1.9$ to $g = 1.93$ in *Tm*HydF upon loading with $[2Fe]_{MIM}$. With increasing temperature, the spectral intensity decreases by approximately 93 % at 20 K and the g-values ($g = 2.039$, 1.915, 1.878) are slightly shifted. This small upshift and the respective g-values are unreported for any HydF preparation and might have been missed due to the low signal intensity or restriction to only one temperature. The second species indicates either the presence of a second [4Fe4S] cluster, an excited state, or reflects a slightly different coordination geometry, arising, e.g., from distinct monomers or binding of $[2Fe]_{MIM}$. The signal intensity eventually vanishes at 30 K and suggests the absence of any slow-relaxing paramagnet, such as [2Fe2S] clusters or $[2Fe]_{MIM}$-derived species. Overall, the results imply that the $[2Fe]_{MIM}$ cluster is in the diamagnetic $Fe^{1+}Fe^{1+}$ state under reducing conditions, as suggested previously.[110,148,285,304]

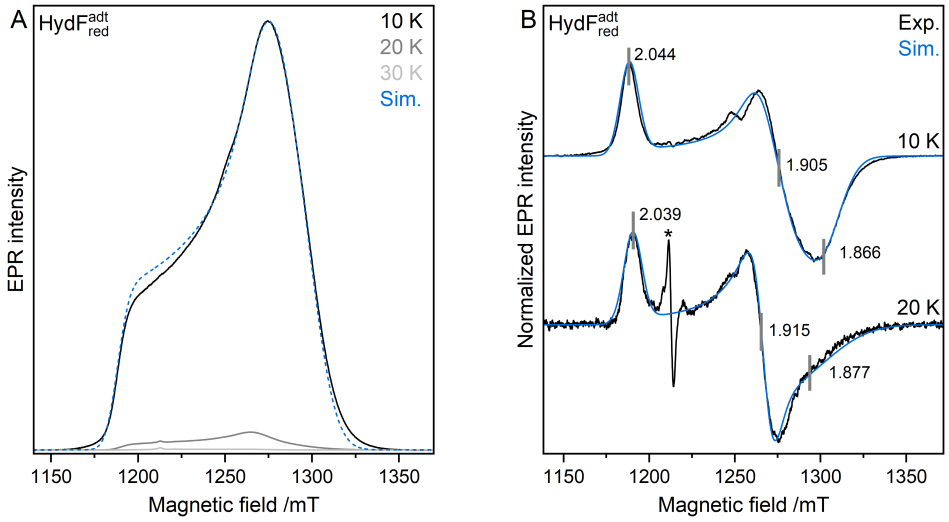

Figure 5.1: ESE-detected EPR spectra ($T = 10 - 30$ K, 34 GHz) of $HydF^{adt}$ treated with 25 mM NaDT (**A**) as recorded and with the total simulated spectrum at 10 K (blue dashed trace) and (**B**) pseudo-modulated spectra (3 mT modulation amplitude) and respective simulations (blue traces) with g-values as indicated. The asterisk denotes a dithionite-derived radical.

Next, temperature-dependent pulsed EPR spectra of an oxidized sample of $HydF^{adt}$ were recorded. A previous EPR study did not detect any signals in oxidized *Tme*HydF, but unfortunately does not comment on oxidized *Tme*$HydF^{adt}$ samples.[148] Here, at least three distinct species were detected, which are distinguished based on their relaxation behavior, i.e., the use of different temperatures.

At 10 K, oxidized $HydF^{adt}$ is dominated by an almost isotropic signal (see Figure 5.2A), that strongly resembles a [3Fe4S] cluster, here termed Sim_1. Its g-values ($g = 2.023$, 2.012, 2.010) and relaxation properties (no longer observable above 20 K) are comparable to the proposed [3Fe4S]

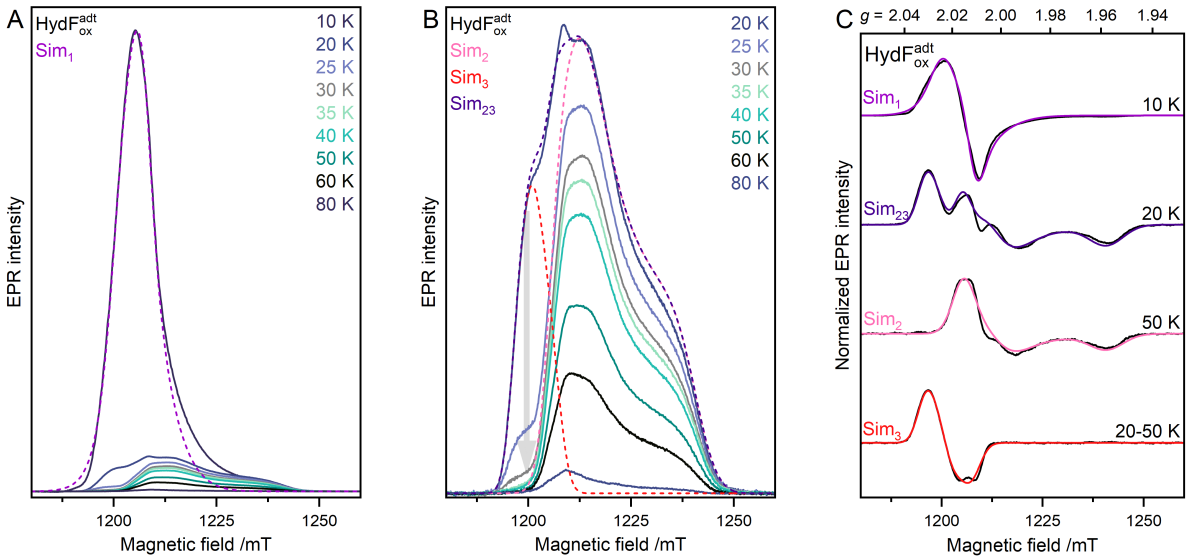

Figure 5.2: Temperature-dependent ESE-detected EPR spectra ($T = 10 - 80$ K, 34 GHz) of O_2-oxidized HydF^{adt} with (**A**) the simulated spectrum at 10 K (Sim_1, magenta dashed line) and (**B**) the simulated spectra of the single species Sim_2 (pink dashed line) and Sim_3 (red dashed line) and their sum Sim_{23} (purple dashed line) at 20 K, where the grey arrow indicates the decrease of Sim_2 with increasing temperature and (**C**) the respective pseudo-modulated EPR spectra and simulations (3 G modulation amplitude).

cluster observed in as-isolated, $[2Fe]_{MIM}$-free *Ca*HydF between 12-20 K (g = 2.019, 2.01, 1.974), although g_3 is reportedly lower for *Ca*HydF.[301] Their assignment of g_3 might be influenced by the overlapping species described in the following. The signal intensity decreases significantly upon increasing temperature and a distinct signal is dominating the spectra from 20 K and above, having at least two species contributing at temperatures up to 40 K (see Figure 5.2B). The second species (Sim_2, pink trace) is observable between 10-80 K (Figure 5.2B), and its spectral simulation with g = 2.015, 2.002, 1.958 can be performed on an isolated species at temperatures above 35 K (Figure 5.2C). Notably, the feature around g_1 and its respective turning point are indicative of the presence of another underlying species. Between 20 and 35 K one outstanding feature is observable at the lower field (marked by a grey arrow). By subtracting the spectrum taken at 50 K from the one at 20 K, a signal well simulated with g = 2.031, 2.023, 2.012 remains (termed Sim_3, red trace). The sum of the spectral simulations Sim_2 and Sim_3 (Sim_{23}) yields an approximate full simulation for the spectrum at 20 K (Figure 5.2C). Similar to Sim_1, the g-values and relaxation behavior of Sim_3 also resemble a [3Fe4S] cluster-derived species with slightly distinct properties. Given that the present sample was treated for 2 h with O_2, it is expected that either no or only a few intact FeS clusters are observed and that they are fully oxidized. Therefore, it is surprising that the species Sim_2 exhibits a relaxation behavior typical for [2Fe2S] clusters or organic radicals. Comparable signals with similar relaxation behavior and g = 2.00, 2.00, 1.96 or g = 2.016, 2.004, 1.961, were observed in photo-reduced or as-isolated *Ca*HydF, respectively. HydF was either (i) solely expressed[135,306] or (ii) co-expressed showing FITR bands associated with $[2Fe]_{MIM}$.[305] This observation excludes that the species arises from the introduced $[2Fe]_{MIM}$ cofactor, as suggested previously.[110,148,285,304] Indeed, it was previously assigned to a redox active [2Fe2S] cluster.[305,306] Moreover, slightly deviating g-values were reported for a species with a similar relaxation profile as Sim_2 in as-isolated *Sho*HydF. The authors suggested that it is either a protein-associated radical or a [3Fe4S] cluster.[285] In conjunction with the present results, the species associated with Sim_2 seems to be independent

of the organism, reducing or oxidizing conditions, and the presence or absence of $[2Fe]_{MIM}$. As the present sample was treated with O_2 for a prolonged time, it seems highly unlikely, that [2Fe2S] clusters withstand oxidative degradation, unless they are deeply buried inside of the protein. Moreover, according to the suggested midpoint potential of $E_m \geq -200$ mV,[301] the [2Fe2S] cluster should be completely oxidized in the present sample and, therefore, diamagnetic. Interestingly, the g-values of Sim_2 are very well in agreement with type 2 [3Fe4S] clusters.

Distinct types of [3Fe4S] clusters were classified into two types by Duderstadt et al. [307] and Telser et al. [37]. Both [3Fe4S] cluster types have $g_{max} = 2.03$, whereby type 1 is characterized by $g_{mid} = 2.00$ and a sharp resonance, e.g., in aconitase, whereas type 2 has $g_{mid} = 1.95$ and a broader high-field feature arising from antisymmetric exchange, e.g., in Fdx from *Pyrococcus furiosus* (*P. furiosus*).[37] Moreover, the [4Fe4S] cluster forms of both aconitase and *Pf*Fdx are coordinated by a non-cysteinyl ligand and are in line with the glutamate coordination in *Tme*HydF. According to this classification, species Sim_1 and Sim_3 can be attributed to a type 1 [3Fe4S] cluster, whereas Sim_2 falls into the type 2 category. However, relating to the present literature, [3Fe4S] clusters are usually only observable up to 50 K, which is not satisfied for Sim_2. Notably, additional slow-relaxing species were observed up to 100 K in *Pf*Fdx under aerobic purification, that were attributed to [2Fe2S] clusters based on their relaxation behavior and suggested to arise from oxygen-induced damage.[308] Eventually, the contradicting g-values and relaxation properties prevent a definite assignment but might be associated with the unusual cluster ligation.

Furthermore, the presented spectroscopic features of *Tme*HydF agree well with the one reported for the methyltransferase RumA from *E. coli* containing one single [4Fe4S] cluster as well.[309] The authors reported two distinct species with similar g-values and relaxation properties as observed in this study. Likewise, they attribute the faster relaxing species observable at lower temperatures to a [3Fe4S] cluster. The second slower relaxing species observable from 40 K and above is suggested to arise either from a closely spaced disulfide radical, although the g-values are in disagreement, or some novel type of oxidized [2Fe2S] cluster. The latter is also highly similar to a species found in the SdhC domain of the archaeal respiratory complex II from *S. tokodaii*, which was attributed to a novel [2Fe2S] cluster based on EPR and resonance raman experiments.[310] The observed g-values are explained by the unusual ligation environment: -YXGC-//-CCG-//-PCSXC-,[310] which is different for the [4Fe4S] cluster in *Tme*HydF, where a conserved -$CXHX_4$6-$_5$3HCXXC- motif was derived from the crystal structure.[148] It is moreover worth noting, that Guigliarelli et al. [279] predicted already in 1999 the not yet confirmed discovery of non-diamagnetic $[4Fe4S]^{2+}$ clusters.

In summary, at least one [4Fe4S] cluster was observed in the reduced *Tme*HydF enzyme, whose g-values at lower temperatures are in agreement with the literature. The upshift in g-values at elevated temperatures might be associated with the binding of $[2Fe]_{MIM}$, but an unloaded *Tme*HydF sample is necessary for verification. The higher resolution of the magnetic field axis at the Q-band, as well as temperature-dependent studies, enabled the deconvolution of at least three distinct species in the oxidized state. Their spectral features strongly resemble those of *Ca*HydF. However, a $g_{max} = 2.04/2.05$ feature, detected in as-isolated *Sho*HydF and *Ca*HydF, is absent in this preparation. The species dominating at 10 K can be attributed to a [3Fe4S] cluster. Upon increasing temperature, the signal is replaced by a mixture of two unknown species. The spectral

properties of Sim_3 are in agreement with a (distinct) [3Fe4S] cluster, whereas the features of Sim_2 are attributed to the controversially discussed redox-active [2Fe2S] cluster, [3Fe4S] cluster or radical-derived species.[285,297,305] Further studies are necessary to provide a comprehensive explanation for the presence of multiple yet unidentified species and elucidate the mechanism of $[2Fe]_{MIM}$ binding.

The recently generated [4Fe4S] cluster-less variants[304] might help to illuminate the nature and origin of the additional species present in different HydF enzymes and preparations. First, in the absence of [4Fe4S] clusters, no degradation products, such as [3Fe4S] or [2Fe2S] clusters should be observable, except there is an additional binding domain or position beyond the mutated cavity, as suggested by Shepard et al. [306]. Second, as the [4Fe4S] cluster-free variants are still able to bind $[2Fe]_{MIM}$, it might provide the first chance to unambiguously refute that $[2Fe]_{MIM}$ changes its redox state to a paramagnetic species under oxidizing or reducing conditions. Third, ENDOR spectra of isolated species could help to elucidate the paramagnet's environment and narrow down its classification as a FeS cluster or radical-derived species.

6

The Oxygen-Resistant [FeFe]-hydrogenase CbA5H Harbors an Unknown Radical Signal

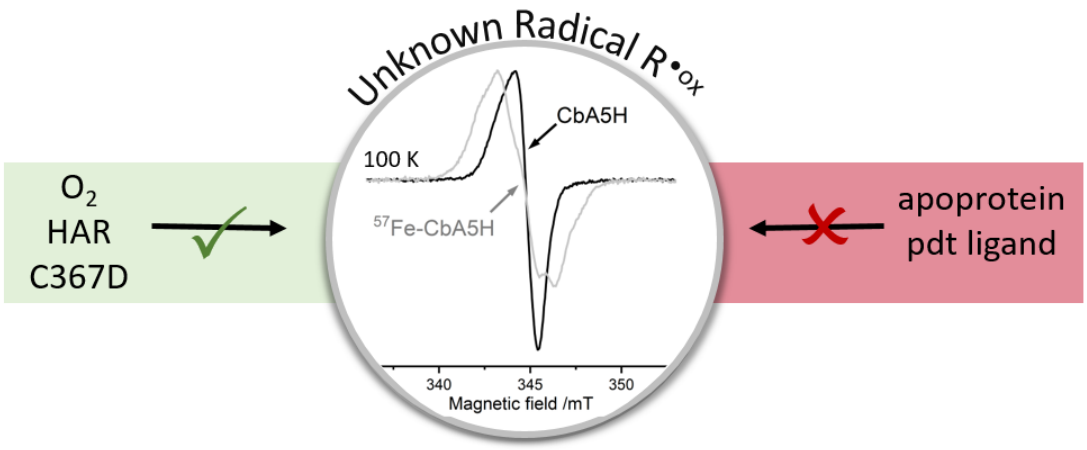

This research was originally published as: Heghmanns, M., Rutz, A., Kutin, Y., Engelbrecht, V., Winkler, M., Happe, T. and Kasanmascheff, M., *The oxygen-resistant [FeFe]-hydrogenase CbA5H harbors an unknown radical signal*, Chemical Science, 2022, 13, 7289-7294.

- Andreas Rutz prepared all protein samples and performed and analyzed activity assays and FTIR spectroscopic experiments
- I performed all EPR experiments and analyzed the respective data
- I wrote the first draft of the manuscript and was involved in further editing
- Müge Kasanmascheff edited the manuscript
- All authors discussed the results and commented on the manuscript

Chemical Science

ROYAL SOCIETY OF CHEMISTRY

EDGE ARTICLE

View Article Online
View Journal | View Issue

Check for updates

Cite this: *Chem. Sci.*, 2022, **13**, 7289

All publication charges for this article have been paid for by the Royal Society of Chemistry

Received 20th January 2022
Accepted 28th May 2022

DOI: 10.1039/d2sc00385f

rsc.li/chemical-science

The oxygen-resistant [FeFe]-hydrogenase CbA5H harbors an unknown radical signal†

Melanie Heghmanns, ‡[a] Andreas Rutz, ‡[b] Yury Kutin,[a] Vera Engelbrecht,[b] Martin Winkler,[c] Thomas Happe *[b] and Müge Kasanmascheff *[a]

[FeFe]-hydrogenases catalyze the reversible conversion of molecular hydrogen into protons and electrons with remarkable efficiency. However, their industrial applications are limited by their oxygen sensitivity. Recently, it was shown that the [FeFe]-hydrogenase from *Clostridium beijerinckii* (CbA5H) is oxygen-resistant and can be reactivated after oxygen exposure. In this work, we used multifrequency continuous wave and pulsed electron paramagnetic resonance (EPR) spectroscopy to characterize the active center of CbA5H, the H-cluster. Under oxidizing conditions, the spectra were dominated by an additional and unprecedented radical species. The generation of this radical signal depends on the presence of an intact H-cluster and a complete proton transfer pathway including the bridging azadithiolate ligand. Selective ^{57}Fe enrichment combined with isotope-sensitive electron-nuclear double resonance (ENDOR) spectroscopy revealed a spin density distribution that resembles an H-cluster state. Overall, we uncovered a radical species in CbA5H that is potentially involved in the redox sensing of CbA5H.

Introduction

Molecular hydrogen is a promising alternative to fossil fuels in meeting the world's increasing energy demand.[1,2] Unlike platinum-based systems, metalloenzymes such as [FeFe]-hydrogenases use only earth-abundant metals to produce and oxidize H_2 under mild conditions and with high turnover rates (10 000 molecules per second).[3,4] The catalytic properties of these enzymes inspired the development of cheap and efficient H_2 catalysts for carbon-neutral hydrogen production.[5] Yet, their industrial application is hindered by their intrinsic O_2-sensitivity.[6,7] Despite the extensive research, engineering [FeFe]-hydrogenases with improved oxygen stability has not been entirely successful.[8]

The active site of [FeFe]-hydrogenases harbors the so-called H-cluster: a cubane [4Fe4S] cluster ($[4Fe]_H$) linked by a cysteine to a unique [2Fe2S]-subsite ($[2Fe]_H$).[3] The distal (Fe_d) and proximal (Fe_p) iron atoms of $[2Fe]_H$ are coordinated by two CN^- and three CO ligands and are bridged by an azadithiolate (adt) ligand.[9,10] The binding of O_2 to the open coordination site at Fe_d initiates a degradative process causing irreversible damage to the H-cluster.[7,11–13] Partial reduction and protonation of dioxygen, leading to H-cluster destruction, was assumed to be inherent to all [FeFe]-hydrogenases until the discovery of the hydrogenase from *Clostridium beijerinckii*, termed CbA5H (Fig. 1).[14] The H-cluster of CbA5H can reversibly switch from the oxygen-sensitive and active H_{ox} state to the oxygen-stable but inactive H_{inact} state.[14,15] Recently, the air-exposed crystal structure revealed that this outstanding ability is reached by the binding of a conserved cysteine residue (C367) to Fe_d shielding the cofactor from O_2.[16] Structural elucidation of the H_{inact} state combined with spectroscopic and electrochemical investigations[14,15] of CbA5H strongly indicate a novel oxygen resistance mechanism that does not involve direct O_2 binding to the H-cluster. Understanding the unusual oxygen resistance mechanism of CbA5H might present an important step toward facilitating the use of [FeFe]-hydrogenases as carbon-neutral energy carriers.

The work presented here expands our understanding of CbA5H and its exceptional oxygen resistance by characterizing its paramagnetic centers under oxidative and reductive conditions using isotope-sensitive electron paramagnetic resonance (EPR) spectroscopy. Along with the well-known H-cluster states in the active CbA5H, we detected an unusual radical species dominating the oxygen-treated spectra, which has not been reported in other [FeFe]-hydrogenases under similar conditions. Our investigation suggests that this radical is unique to CbA5H and potentially plays a role in the redox-sensing of the enzyme.

[a]TU Dortmund University, Department of Chemistry and Chemical Biology, Otto-Hahn-Straße 6, 44227 Dortmund, Germany. E-mail: muege.kasanmascheff@tu-dortmund.de

[b]Ruhr University Bochum, Faculty of Biology and Biotechnology, Photobiotechnology, Universitätsstr. 150, 44801 Bochum, Germany. E-mail: thomas.happe@ruhr-uni-bochum.de

[c]Technical University of Munich Campus Straubing for Biotechnology and Sustainability, Professorship for Electrobiotechnology, Uferstrasse 53, 94315 Straubing, Germany

† Electronic supplementary information (ESI) available: Material and methods, sample descriptions, experimental details and additional experimental data. See https://doi.org/10.1039/d2sc00385f

‡ Contributed equally.

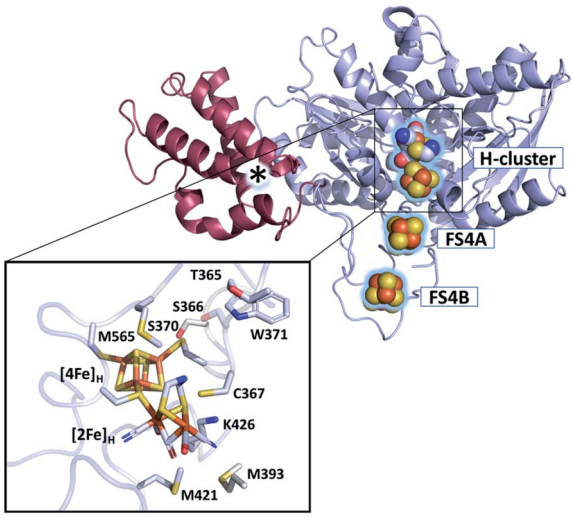

Fig. 1 Structure of CbA5H (PDB ID 6TTL). X-ray structure of CbA5H displayed as a monomer with SLBB – (soluble ligand-binding beta-grasp) domain (dark-red), and H- and F-cluster containing domain (light-blue). Positions of the FeS clusters are highlighted and depicted as spheres. The asterisk indicates electron density whose nature could not be unambiguously identified yet. The lower panel shows the active site of CbA5H representing $[4Fe]_H$ and $[2Fe]_H$ embedded in the protein environment.

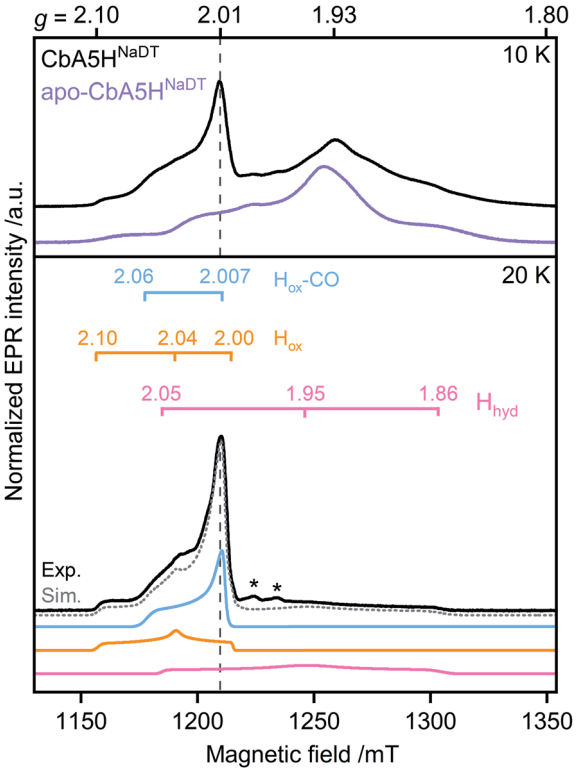

Fig. 2 Pulsed EPR spectra (34 GHz) of CbA5H (black) and apo-CbA5H (purple). The samples were reduced with 10 mM NaDT and measured at 10, and 20 K. Suppression of fast-relaxing FeS clusters at 20 K enabled the complete simulation of holo-CbA5H (dotted grey trace). H_{ox}, H_{ox}–CO, H_{hyd} and $R^{\bullet ox}$ were included in the simulation (Fig. S1†). Details of the experiments and analysis are given in ESI.† Dashed vertical lines mark the additional signal at $g \approx 2.01$. A Mn^{2+} impurity signal is marked with asterisks.

Results and discussion

Analysis of reduced states of apo- and holo-CbA5H

First, to investigate the paramagnetic H-cluster states, the enzyme was reduced either with H_2 or with varying concentrations of sodium dithionite ($CbA5H^{NaDT}$). Additionally, we performed NaDT-free control measurements (see ESI†). Analysis of the respective EPR spectra is facilitated by using elevated temperatures at which signals from fast-relaxing, accessory FeS clusters, the so-called F-clusters, are undetectable (20 K *vs.* 10 K spectra in Fig. 2, S1 and S2†).[17] The EPR spectrum of the active CbA5H recorded at 20 K exhibits the characteristic, well-known H-cluster states H_{ox},[18–27] H_{ox}–CO,[12,23,24,28] and H_{hyd} [29–31] (Fig. 2, S1, S2 and Tables S2 and S3†). Their presence is also confirmed *via* Fourier-transform infrared (FTIR) spectroscopy (Fig. S3 and ref. 15†). Interestingly, an additional signal at $g \approx 2.01$, which can be observed even up to 180 K, is also detected (Fig. S2, S4 and S5†). The origin of this unidentified species, termed $R^{\bullet ox}$, is discussed below.

Next, to characterize the accessory FeS clusters, we employed multi-frequency EPR on the inactive apoenzyme that lacks the $[2Fe]_H$ subsite but harbors the F-clusters and $[4Fe]_H$ (apo-CbA5H) (Fig. 2, S2 and S6†). The EPR spectrum at 10 K (Fig. 2, purple trace) is dominated by a broad signal centered around $g = 1.93$. This signal is broadened beyond detection at 20 K, confirming the presence of fast-relaxing $[4Fe4S]^{1+}$ clusters (Fig. S2†).[32,33] Furthermore, its spectral features are frequency-dependent (Fig. S6†). In conjunction with the signal's significant width, the frequency dependence clearly indicates spin–spin interaction between the F-clusters.[35,36] This observation is not surprising as the clusters are adjacent (Fig. 1).[16] Spectral simulation using parameters for two FeS clusters similar to those reported in the literature resulted in a good fit for the experimental apo-$CbA5H^{NaDT}$ spectrum (Fig. S2†). Note that the $R^{\bullet ox}$ signal found in the holoenzyme of CbA5H is absent in the apoprotein. This relates $R^{\bullet ox}$ to the presence of an intact H-cluster.

The H_2–O_2 cycle

Unlike other [FeFe]-hydrogenases (from *Desulfovibrio desulfuricans* (*Dd*HydAB) and *Desulfovibrio vulgaris* Hildenborough), the inactive H_{inact} state of CbA5H can undergo several cycles of oxidative inactivation and reductive reactivation.[14,15] We investigated this reversible transformation by monitoring the spectral changes of the anaerobically isolated enzyme repeatedly treated with H_2 and O_2 (termed $CbA5H^{H_2}$ and $CbA5H^{O_2}$, respectively) (Fig. 3 and S4†). At cryogenic temperatures, EPR spectra of $CbA5H^{H_2}$ reveal a complex line shape (Fig. 3) arising from paramagnetic H-cluster states and F-clusters (see also Fig. 2). The overall signal intensity of $CbA5H^{H_2}$ is reduced by approximately 40% after the first cycle (see ESI† on the H_2–O_2 cycle). This observation agrees with activity assays and FTIR

View Article Online
Edge Article Chemical Science

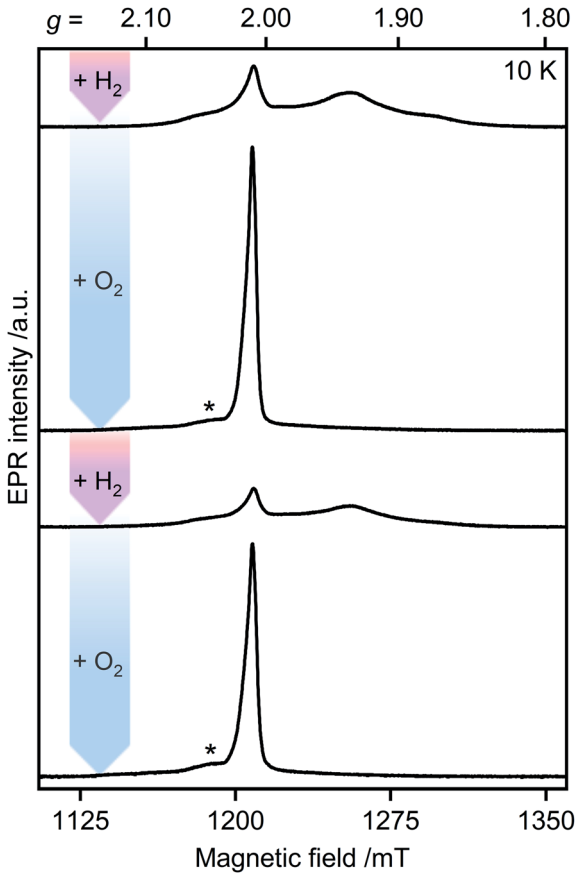

Fig. 3 Pulsed EPR spectra of CbA5H (34 GHz). As-isolated CbA5H was treated alternately with H_2 (pink arrows) and O_2 (blue arrows). Asterisks indicate residual H_{ox}–CO signals (see also ESI† on the H_2–O_2-cycle).

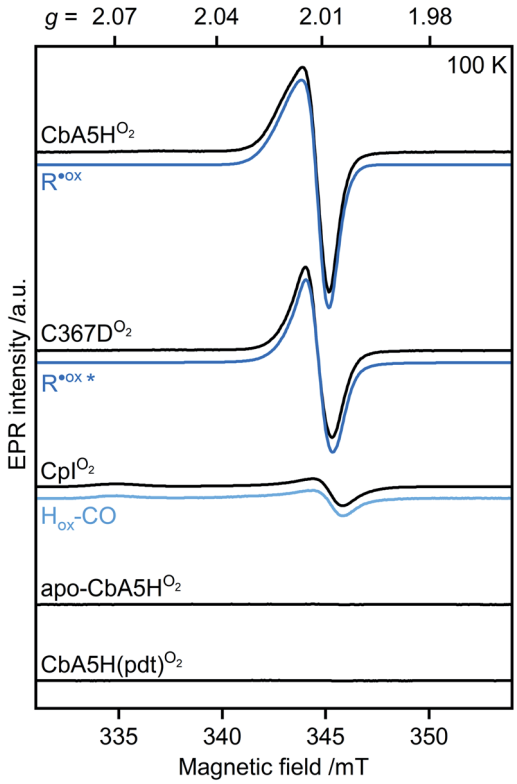

Fig. 4 Continuous-wave (cw) EPR spectra of oxygen-treated samples (9.7 GHz, T = 100 K). CbA5H, C367D, CpI, apo-CbA5H, and CbA5H(pdt) were treated with O_2. Blue lines represent simulations of $R^{\bullet ox}$ detected in CbA5H and variant C367D, and of H_{ox}–CO detected in CpI. The asterisk indicates a change in the $R^{\bullet ox}$ line shape for variant C367D (see Fig. S15†).

spectra (Fig. S3, S7 and ref. 15†), confirming the partial reactivation of CbA5H after O_2-treatment.

When $CbA5H^{H_2}$ is exposed to O_2, all identified signals from the F-clusters and H-cluster disappear. This was expected as most FeS clusters are EPR-inactive in the oxidized state, and H_{inact}, the only H-cluster state present in $CbA5H^{O_2}$ (see Fig. S3†), is suggested to be EPR-silent.[15] The EPR spectra of $CbA5H^{O_2}$ (Fig. 3), however, are dominated by the nearly isotropic signal at $g = 2.01$ (Fig. 4). Its EPR signature is distinct from typical signals of H_{ox}–CO and degraded FeS clusters (Fig. S4 and S7†). Its three principal g-values were determined as $g = 2.019, 2.010, 2.006$ *via* a global fit at the X- and Q-band frequencies (see Table S2† for details). Surprisingly, its intensity decreases only by 5–13% after two H_2–O_2 cycles and cryo-annealing, while the amount of active protein drops significantly (ESI on the H_2–O_2 cycle, Fig. 3 and S4–S7†). Even though $R^{\bullet ox}$ is present in $CbA5H^{H_2}$, its EPR-intensity is considerably higher in the oxidized enzyme (Fig. 3 and S4†). The high stability of $R^{\bullet ox}$ contradicts the observed degradation of H_{inact} during the cycle, as shown *via* FTIR (Fig. S3†), indicating that the H_{inact} state itself is not the source of $R^{\bullet ox}$. Moreover, the generation of $R^{\bullet ox}$ by treatment with the mild oxidant hexamine ruthenium(III) chloride (HAR) showed that O_2 is not the only catalyst triggering its formation (Fig. S9†). Similar results were reported for the generation of H_{inact},[15] emphasizing the connection between H_{inact} formation and the $R^{\bullet ox}$ signal. This is reminiscent of the EPR signals observed for the proximal [4Fe3S] cluster of O_2-tolerant [NiFe]-hydrogenases under oxidative conditions, even in the absence of O_2,[37] which turn out to be a strong indicator for the underlying O_2 tolerance mechanism. These intriguing properties of the $R^{\bullet ox}$ species prompted us to investigate its identity further.

Investigation of $R^{\bullet ox}$ formation under various conditions

First, we analyzed the EPR spectra of O_2-exposed CbA5H compared to CpI (Fig. 4 and S10†). CpI, a 'standard' [FeFe]-hydrogenase, was purified and oxidized using the same procedure for CbA5H. In agreement with reported CpI data,[34] $R^{\bullet ox}$ was not detected in EPR spectra of CpI^{O_2}, demonstrating that the signal is unique to CbA5H. These data also exclude the possibility of $R^{\bullet ox}$ being an artifact related to the protein preparation procedures or a radical species generated due to external factors such as the buffers used. This conclusion is further supported by (i) the almost identical EPR signature of $R^{\bullet ox}$ in aerobically and anaerobically isolated CbA5H (Fig. S11†) and (ii) the absence of the $R^{\bullet ox}$ signal in EPR spectra of apo-CbA5H (reduced or oxidized). The only signal detected in the oxidized apoenzyme originates from a $[3Fe4S]^+$ cluster in sub-stoichiometric amounts, possibly from mild oxidative damage to the FeS clusters (Fig. S6, S8 and S12†).

We, therefore, explored whether an active enzyme is necessary to generate $R^{\bullet ox}$. Apo-CbA5H was maturated with a chemically altered cofactor ($[Fe_2(pdt)(CO_4)(CN_2)]^{2-}$, CbA5H(pdt)) yielding a catalytically inactive enzyme due to the non-protonatable bridgehead.[35] This artificial ligand does not interfere with the native structure of the hydrogenases but disrupts the proton-transfer pathway to and from Fe_d.[36,38,39] The complex EPR spectrum of H_2-reduced CbA5H(pdt) (Fig. S13†) resembles the corresponding spectrum reported for CpI(pdt).[17] The spectrum of O_2-treated CbA5H(pdt) shows sub-stoichiometric amounts of a $[3Fe4S]^+$ cluster (Fig. S13†), similar to the one detected in apo-CbA5H^{O_2}. Strikingly, none of the EPR spectra recorded for CbA5H(pdt) exhibit the $R^{\bullet ox}$ signal (Fig. 4 and S13†), although the formation of the H_{inact} state in CbA5H(pdt) was verified by FTIR measurements (Fig. S14†). This again excludes H_{inact} as the source of $R^{\bullet ox}$.

To this point, our results on EPR characteristics (*g*-values and temperature-dependency) of $R^{\bullet ox}$ hint at a protein-based radical species whose generation is dependent on the presence of an active H-cluster and the native adt ligand, ensuring an intact proton transfer pathway. The cysteine residue C367 is one of the closest amino acids to the H-cluster and is involved in the H_{inact} formation.[16] Therefore, we investigated whether the oxidation of C367 results in the $R^{\bullet ox}$ signal.

We recorded EPR spectra of the O_2-treated CbA5H in which C367 is replaced with aspartate (C367D) (Fig. 4 and S15†). This variant prevented the formation of the H_{inact} state while retaining 20% of the H_2-production activity compared to the wild-type enzyme.[16] Temperature-dependent spectra exhibit the $R^{\bullet ox}$ signal but with a narrower line shape and decreased intensity. Although these results exclude C367 as the source of $R^{\bullet ox}$, they show that the identity of residue 367 affects its electronic structure.

Furthermore, the characteristics of our EPR and UV-vis data conflict with those of typical (i) amino acid radicals, (ii) sulfur-based radicals, (iii) peroxyl radicals, and (iv) semiquinone radicals (Fig. S16 and ESI Discussion† on the identity of $R^{\bullet ox}$). Yet, an unusual organic radical near, on, or bound to the H-cluster with anomalous spectroscopic properties, as observed with the tryptophane cation radical found in cytochrome c peroxidase[40,41] cannot be ruled out. Candidates that might be considered are residues M393, S370 or M565, M421, and W371 (Fig. 1), of which the last three represent highly conserved positions among other [FeFe]-hydrogenases.

^{57}Fe-labeling and isotope-sensitive studies of $R^{\bullet ox}$

EPR studies combined with ^{57}Fe labeling provided invaluable information on iron-containing metalloproteins, including elucidation of the electronic structure of H-cluster states from different organisms.[9,27,42,43] The presence of a ^{57}Fe nucleus with a nuclear spin $I = \frac{1}{2}$ results in EPR line broadening due to hyperfine interaction (hfi). To investigate whether $R^{\bullet ox}$ is associated with the H-cluster, we selectively labeled the apoprotein ($[4Fe]_H$ and F-clusters) with ^{57}Fe and subsequently maturated it with ^{56}Fe–$[2Fe]_H$. The *g*-value of $R^{\bullet ox}$ did not change upon labeling. However, ^{57}Fe enrichment resulted in EPR line broadening of the $R^{\bullet ox}$ spectra due to strong hfis between ^{57}Fe nuclei and $R^{\bullet ox}$ (Fig. S17†).

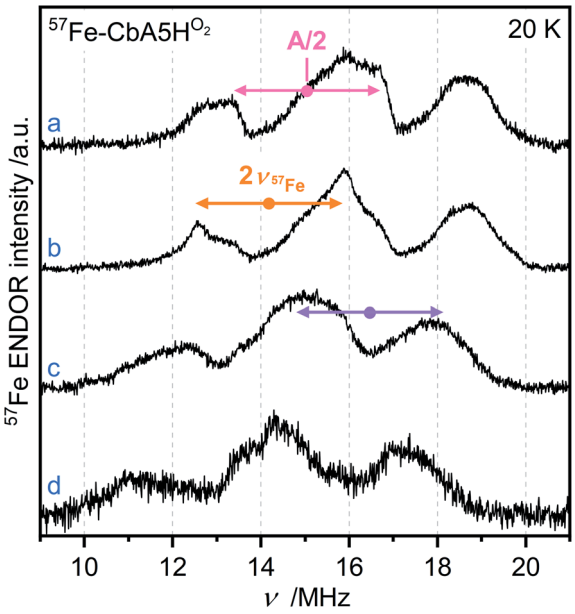

Fig. 5 Orientation-selective Davies ENDOR spectra of ^{57}Fe-labeled CbA5H^{O_2} recorded at 20 K, Q-band and (a) $g = 2.008$ (b) $g = 2.012$ (c) $g = 2.018$ (d) $g = 2.022$. At least three different ^{57}Fe hyperfine couplings are observable, centered at $A/2$ (dots), and split by twice the Larmor frequency (arrows). All experimental details are given in ESI.†

Next, we recorded orientation-selective ^{57}Fe electron-nuclear double resonance (ENDOR) spectra of $R^{\bullet ox}$ (Fig. 5). The ENDOR line shape shows three broad features symmetrically centered around $|A|/2$ (A is the hyperfine coupling constant) and split by twice the Larmor frequency $\nu_{^{57}Fe}$ due to strong hfis with several ^{57}Fe nuclei. At least three ^{57}Fe nuclei needed to be introduced to simulate the experimental ENDOR line shape (Fig. S18†). At this point, however, a complete and unique analysis of the orientation-selective ^{57}Fe ENDOR pattern is not possible, as only a few features of the overlapping signals are resolved at Q-band. Nonetheless, the hf couplings of all observed ^{57}Fe nuclei are in the range of 25–35 MHz, very similar to those observed for the $[4Fe]_H$ subcluster in the H_{ox}–CO state from other hydrogenases.[9,43] These data suggest that $R^{\bullet ox}$ is either a unique H-cluster state or located close to the intact H-cluster and thus coupled to $[4Fe]_H$. Note that the F-clusters in their native conformation can be excluded as the source of observed hfis because (i) $R^{\bullet ox}$ is not generated in the absence of an intact H-cluster, *i.e.*, in apo-CbA5H, (ii) slow relaxation behavior of $R^{\bullet ox}$ is inconsistent with a typical $[4Fe4S]^{1+}$ cluster, (iii) substituting the C367 residue residing close to $[2Fe]_H$ perturbs the EPR line shape of $R^{\bullet ox}$, and (iv) the isotropic hfis determined for $R^{\bullet ox}$ are significantly different from the ones observed for the standard $[4Fe4S]^{1+}$ clusters displaying $|A_{iso}|$ of around 15 MHz for their ferrous Fe^{2+}–Fe^{2+} pair.[44]

Next, we performed orientation-selective proton (^{1}H) ENDOR experiments on $R^{\bullet ox}$ (Fig. S19†). The spectra revealed overlapping signals due to contributions from several protons having hfis not larger than 9 MHz. As our ^{57}Fe EPR data showed

effective spin density on the H-cluster, we compared ^{1}H ENDOR spectra of $R^{\bullet ox}$ with those of H_{ox}, H_{ox}–CO, and H_{hyd} from different [FeFe]-hydrogenases.[45–47] As with the ^{57}Fe data, the strength of the hfis and the spectral shape of $R^{\bullet ox}$ ^{1}H ENDOR resemble those detected with H_{ox}–CO assigned to β-protons of the cysteine ligands of $[4Fe]_H$.[45–47]

To demonstrate that the detected ^{57}Fe and ^{1}H hfis do not arise from the underlying H_{ox}–CO species, we recorded FTIR spectra for oxygen-treated ^{57}Fe–CbA5H (Fig. S3†) and ^{1}H ENDOR spectra with $CbA5H^{air}$ whose EPR spectrum is composed of $R^{\bullet ox}$ and H_{ox}–CO (Fig. S19†). The absence of an H_{ox}–CO FTIR signature in ^{57}Fe–$CbA5H^{O_2}$ and the presence of additional features in ^{1}H ENDOR spectra of $CbA5H^{air}$ showed that the observed hfis belong to $R^{\bullet ox}$. The similarities detected in hfis strongly imply a similar spin density distribution for $R^{\bullet ox}$ and H_{ox}–CO, which features a paramagnetic $[2Fe]_H$ ($S = 1/2$) exchange coupled to the diamagnetic $[4Fe]_H{}^{2+}$.

Interestingly, the F-cluster-truncated form of the [FeFe]-hydrogenase from *Megasphaera elsdenii*, harboring the H-cluster, displayed an EPR signal similar to $R^{\bullet ox}$ upon CO-treatment.[6] This signal was attributed to the H_{ox}–CO state. However, the EPR signature differs substantially from the H_{ox}–CO state observed for the as-isolated enzyme and other known [FeFe]-hydrogenases. As the FTIR spectrum of this redox state was similar to those of other hydrogenases, the unusual change in the EPR spectrum could not be explained. Here, we can exclude the well-known H_{ox}–CO state as the origin of the $R^{\bullet ox}$ signal because we can distinguish the features of H_{ox}–CO and $R^{\bullet ox}$ in our temperature-dependent EPR and ENDOR data (Fig. S8 and S19†).

Lastly, we investigated the presence of exchangeable protons by recording ^{1}H ENDOR spectra of $R^{\bullet ox}$ in the D_2O buffer. Indeed, we detected differences in the proton ENDOR spectra of $R^{\bullet ox}$ in H_2O or D_2O buffers. In addition, the ^{2}H Mims ENDOR spectrum revealed at least two proton hfis arising from the exchangeable protons (see Fig. S19–S20†). These associate $R^{\bullet ox}$ with coordinating water or solvent-derived protonated species, *e.g.*, an amino acid residue with an exchangeable proton. One might hypothesize that the flexible loop around the H-cluster of CbA5H facilitates the movement of conserved water/s that is part of the proton-transfer pathway (see Fig. S6 in ref. 16†).

Overall, our EPR and ENDOR data show a spin density distribution at the H-cluster similar to the H_{ox}–CO state and exclude C367 and H_{inact} as the source of $R^{\bullet ox}$. Therefore, it would be intriguing to interpret $R^{\bullet ox}$ as an H-cluster state distinct from H_{ox}, H_{ox}–CO, H_{inact}, and H_{hyd}. However, the absence of the corresponding FTIR data that could be associated with $R^{\bullet ox}$ prevents an unambiguous assignment at this moment.

Conclusions

In this study, we provided direct spectroscopic evidence for the presence of an unprecedented radical species in CbA5H, named $R^{\bullet ox}$. We showed that the formation of $R^{\bullet ox}$ under oxidizing conditions is dependent on the presence of an active H-cluster harboring the native adt ligand that ensures an intact proton transfer pathway. While advanced spectroscopic and biochemical studies are underway aiming to reveal the identity of $R^{\bullet ox}$, the combined results of our temperature-dependent and isotope-sensitive spectroscopic investigations already narrow down its location within the protein to either the H-cluster or its immediate vicinity. In line with the early onset of anaerobic oxidative inactivation and the formation of H_{inact}, the $R^{\bullet ox}$ signal appears either in the presence of O_2 or upon applying oxidative conditions in the absence of it. Similar to the intact proton transfer pathway to Fed, $R^{\bullet ox}$ formation seems to be part of the redox sensing process that determines the reversible formation of H_{inact} in CbA5H.

Data availability

All experimental data associated with the paper can be found in the article or in the ESI.†

Author contributions

MH (first shared author): data curation, formal analysis, investigation, writing – original draft. AR (first shared author): data curation, formal analysis, investigation. YK: supervision, data curation, validation, writing – review & editing. VE: writing – review & editing. MW: conceptualization, writing – review & editing. TH (corresponding author): supervision, validation, resources, funding acquisition, conceptualization, writing – review & editing. MK (corresponding author): methodology, validation, supervision, resources, funding acquisition, conceptualization, writing – original draft, review & editing.

Conflicts of interest

There are no conflicts to declare.

Acknowledgements

We are grateful to Shanika Yadav and Ulf-Peter Apfel for the adt and pdt ligands. We thank Silke Leimkühler for the ICP measurement. T. H. thanks the Deutsche Forschungsgemeinschaft for funding (RTG 2341 and HA 2555/10-1). We also thank the Studienstiftung des deutschen Volkes for supporting V. E. and A. R. This work is funded by the Deutsche Forschungsgemeinschaft (German Research Foundation) under Germany's Excellence Strategy (EXC 2033-390677874-RESOLV).

References

1 J. Tollefson, *Nature*, 2010, **464**, 1262–1264.
2 M. K. Singla, P. Nijhawan and A. S. Oberoi, *Environ. Sci. Pollut. Res.*, 2021, **28**, 15607–15626.
3 W. Lubitz, H. Ogata, O. Rüdiger and E. Reijerse, *Chem. Rev.*, 2014, **114**, 4081–4148.
4 B. R. Glick, W. G. Martin and S. M. Martin, *Can. J. Microbiol.*, 1980, **26**, 1214–1223.

5 S. Gao, W. Fan, Y. Liu, D. Jiang and Q. Duan, *Int. J. Hydrogen Energy*, 2020, **45**, 4305–4327.
6 G. Caserta, C. Papini, A. Adamska-Venkatesh, L. Pecqueur, C. Sommer, E. Reijerse, W. Lubitz, C. Gauquelin, I. Meynial-Salles, D. Pramanik, V. Artero, M. Atta, M. del Barrio, B. Faivre, V. Fourmond, C. Léger and M. Fontecave, *J. Am. Chem. Soc.*, 2018, **140**, 5516–5526.
7 J. Esselborn, L. Kertess, U. P. Apfel, E. Hofmann and T. Happe, *J. Am. Chem. Soc.*, 2019, **141**, 17721–17728.
8 A. Dubini and D. Gonzalez-Ballester, in *Algae Biotechnology*, 2016, pp. 165–193.
9 A. Silakov, E. J. Reijerse, S. P. J. Albracht, E. C. Hatchikian and W. Lubitz, *J. Am. Chem. Soc.*, 2007, **129**, 11447–11458.
10 Z.-P. P. Liu and P. Hu, *J. Am. Chem. Soc.*, 2002, **124**, 5175–5182.
11 A. Kubas, C. Orain, D. De Sancho, L. Saujet, M. Sensi, C. Gauquelin, I. Meynial-Salles, P. Soucaille, H. Bottin, C. Baffert, V. Fourmond, R. B. Best, J. Blumberger and C. Léger, *Nat. Chem.*, 2017, **9**, 88–95.
12 K. D. Swanson, M. W. Ratzloff, D. W. Mulder, J. H. Artz, S. Ghose, A. Hoffman, S. White, O. A. Zadvornyy, J. B. Broderick, B. Bothner, P. W. King and J. W. Peters, *J. Am. Chem. Soc.*, 2015, **137**, 1809–1816.
13 S. Mebs, R. Kositzki, J. Duan, L. Kertess, M. Senger, F. Wittkamp, U. P. Apfel, T. Happe, S. T. Stripp, M. Winkler and M. Haumann, *Biochim. Biophys. Acta, Bioenerg.*, 2018, **1859**, 28–41.
14 S. Morra, M. Arizzi, F. Valetti and G. Gilardi, *Biochemistry*, 2016, **55**, 5897–5900.
15 P. S. Corrigan, J. L. Tirsch and A. Silakov, *J. Am. Chem. Soc.*, 2020, **142**, 12409–12419.
16 M. Winkler, J. Duan, A. Rutz, C. Felbek, L. Scholtysek, O. Lampret, J. Jaenecke, U.-P. Apfel, G. Gilardi, F. Valetti, V. Fourmond, E. Hofmann, C. Léger and T. Happe, *Nat. Commun.*, 2021, **12**, 756.
17 J. H. Artz, D. W. Mulder, M. W. Ratzloff, C. E. Lubner, O. A. Zadvornyy, A. X. Levan, S. G. Williams, M. W. W. Adams, A. K. Jones, P. W. King and J. W. Peters, *J. Am. Chem. Soc.*, 2017, **139**, 9544–9550.
18 H. J. Grande, W. R. Dunham, B. Averill, C. van Dijk and R. H. Sands, *Eur. J. Biochem.*, 1983, **136**, 201–207.
19 W. R. Hagen, A. van Berkel-Arts, K. M. Krüse-Wolters, W. R. Dunham and C. Veeger, *FEBS Lett.*, 1986, **201**, 158–162.
20 M. W. Adams, *J. Biol. Chem.*, 1987, **262**, 15054–15061.
21 A. J. Pierik, W. R. Hagen, J. S. Redeker, R. B. G. Wolbert, M. Boersma, M. F. J. M. Verhagen and H. J. Grande, *Eur. J. Biochem.*, 1992, **209**, 63–72.
22 B. Bennett, B. J. Lemon and J. W. Peters, *Biochemistry*, 2000, **39**, 7455–7460.
23 S. P. J. Albracht, W. Roseboom and E. C. Hatchikian, *J. Biol. Inorg Chem.*, 2006, **11**, 88–101.
24 C. Kamp, A. Silakov, M. Winkler, E. J. Reijerse, W. Lubitz and T. Happe, *Biochim. Biophys. Acta, Bioenerg.*, 2008, **1777**, 410–416.
25 A. Adamska, A. Silakov, C. Lambertz, O. Rüdiger, T. Happe, E. Reijerse and W. Lubitz, *Angew. Chem., Int. Ed.*, 2012, **51**, 11458–11462.
26 G. Caserta, L. Pecqueur, A. Adamska-Venkatesh, C. Papini, S. Roy, V. Artero, M. Atta, E. Reijerse, W. Lubitz and M. Fontecave, *Nat. Chem. Biol.*, 2017, **13**, 779–784.
27 G. Rao and R. D. Britt, *Inorg. Chem.*, 2018, **57**, 10935–10944.
28 W. Roseboom, A. L. De Lacey, V. M. Fernandez, E. C. Hatchikian and S. P. J. Albracht, *J. Biol. Inorg Chem.*, 2006, **11**, 102–118.
29 D. W. Mulder, M. W. Ratzloff, M. Bruschi, C. Greco, E. Koonce, J. W. Peters and P. W. King, *J. Am. Chem. Soc.*, 2014, **136**, 15394–15402.
30 D. W. Mulder, Y. Guo, M. W. Ratzloff and P. W. King, *J. Am. Chem. Soc.*, 2017, **139**, 83–86.
31 M. Winkler, M. Senger, J. Duan, J. Esselborn, F. Wittkamp, E. Hofmann, U. P. Apfel, S. T. Stripp and T. Happe, *Nat. Commun.*, 2017, **8**(16115).
32 R. Cammack, *Adv. Inorg. Chem.*, 1992, **38**, 281–322.
33 H. Rupp, K. K. Rao, D. O. Hall and R. Cammack, *Nat. Commun.*, 1978, **537**, 255–269.
34 M. W. W. Adams, *Biochim. Biophys. Acta, Bioenerg.*, 1990, **1020**, 115–145.
35 G. Berggren, A. Adamska, C. Lambertz, T. R. Simmons, J. Esselborn, M. Atta, S. Gambarelli, J. M. Mouesca, E. Reijerse, W. Lubitz, T. Happe, V. Artero and M. Fontecave, *Nature*, 2013, **499**, 66–69.
36 M. M. Roessler, R. M. Evans, R. A. Davies, J. Harmer and F. A. Armstrong, *J. Am. Chem. Soc.*, 2012, **134**, 15581–15594.
37 J. Esselborn, C. Lambertz, A. Adamska-Venkatesh, T. Simmons, G. Berggren, J. Noth, J. Siebel, A. Hemschemeier, V. Artero, E. Reijerse, M. Fontecave, W. Lubitz and T. Happe, *Nat. Chem. Biol.*, 2013, **9**, 607–609.
38 W. Lubitz, E. Reijerse and M. van Gastel, *Chem. Rev.*, 2007, **107**, 4331–4365.
39 J. Esselborn, N. Muraki, K. Klein, V. Engelbrecht, N. Metzler-Nolte, U. P. Apfel, E. Hofmann, G. Kurisu and T. Happe, *Chem. Sci.*, 2016, **7**, 959–968.
40 M. Sivaraja, D. B. Goodin, M. Smith and B. M. Hoffman, *Science*, 1989, **245**, 738–740.
41 A. L. P. Houseman, P. E. Doan, D. B. Goodin and B. M. Hoffman, *Biochemistry*, 1993, **32**, 4430–4443.
42 C. V. Popescu and E. Münck, *J. Am. Chem. Soc.*, 1999, **121**, 7877–7884.
43 R. Gilbert-Wilson, J. F. Siebel, A. Adamska-Venkatesh, C. C. Pham, E. Reijerse, H. Wang, S. P. Cramer, W. Lubitz and T. B. Rauchfuss, *J. Am. Chem. Soc.*, 2015, **137**, 8998–9005.
44 J. M. Mouesca, L. Noodleman, D. A. Case and B. Lamotte, *Inorg. Chem.*, 1995, **34**, 4347–4359.
45 J. Telser, M. J. Benecky, M. W. Adams, L. E. Mortenson and B. M. Hoffman, *J. Biol. Chem.*, 1987, **262**, 6589–6594.
46 A. Silakov, E. J. Reijerse and W. Lubitz, *Eur. J. Inorg. Chem.*, 2011, 1056–1066.
47 A. Adamska-Venkatesh, T. R. Simmons, J. F. Siebel, V. Artero, M. Fontecave, E. Reijerse and W. Lubitz, *Phys. Chem. Chem. Phys.*, 2015, **17**, 5421–5430.

Supporting Information

for

The oxygen-resistant [FeFe]-hydrogenase CbA5H harbors an unknown radical signal

Melanie Heghmanns[1‡], Andreas Rutz[2‡], Yury Kutin[1], Vera Engelbrecht[2], Martin Winkler[3], Thomas Happe[2*], Müge Kasanmascheff[1*]

[1] Technical University of Dortmund, Department of Chemistry and Chemical Biology, Otto-Hahn-Straße 6, 44227 Dortmund, Germany

[2] Ruhr University Bochum, Faculty of Biology and Biotechnology, Photobiotechnology, Universitätsstr. 150, 44801 Bochum, Germany

[3] Technical University of Munich Campus Straubing for Biotechnology and Sustainability, Professorship for Electrobiotechnology, Uferstrasse 53, 94315 Straubing, Germany

[‡] Contributed equally

[*] Corresponding authors (thomas.happe@rub.de, muege.kasanmascheff@tu-dortmund.de)

Material and Methods

Cw EPR spectroscopy

All X-band cw EPR spectra recorded at 100 K were obtained using a Bruker EMX-Nano Benchtop spectrometer equipped with a continuous-flow nitrogen cryostat. The experimental conditions were 100 kHz modulation frequency, 4 G modulation amplitude, and variable parameters given in figure captions.
X-band cw EPR measurements shown in Figures S6 and S12 were performed at 15-20 K using a Bruker ELEXSYS E580 X-band EPR spectrometer, equipped with a Bruker ER 4118X-MD5 resonator and an Oxford Instruments ER 4118CF cryostat. The experimental conditions were 100 kHz modulation frequency, 7 G modulation amplitude, and variable parameters given in figure captions. All EPR spectra were baseline-corrected using MATLAB. If not stated otherwise, all spectra were normalized to the given frequency, protein concentration, microwave power, and the number of scans. Spectral simulations were performed with *EasySpin* using the implemented *pepper* function. [1]

Pulsed EPR spectroscopy

Pulsed EPR (electron spin echo detected EPR, ESE-detected EPR) field-sweep experiments, using a two-pulse Hahn spin-echo sequence $\pi/2–\tau–\pi–\tau–$echo without phase cycling, were carried out on a Bruker ELEXSYS E580 Q-band EPR spectrometer equipped with a Bruker ER 5106QT-2 resonator, an Oxford Instruments CF935 cryostat and Oxford Instruments MercuryiTC temperature controller. The cryogenic temperatures were kept with a sufficiently high flow of liquid He. If not stated otherwise, spectra were acquired in the overcoupled mode with gaussian $\pi/2$- and π-pulses whose lengths were optimized before each experiment and varied between 10–13 and 20–26 ns, respectively. The interpulse delay τ was usually set between 220–300 ns and the shot repetition time (SRT) between 0.3–25 ms, depending on the sample and temperature. As a rule, the SRT was long enough to prevent saturation. For most measurements at 10 K, however, an SRT of 3 ms was chosen for time-efficient measurements: prolonged SRTs led to higher signal intensities, but no change in line shape was observed. The EPR spectra were baseline-corrected using MATLAB. If not stated otherwise, all spectra were normalized to the given frequency, protein concentration, video gain, shots per point, and number of scans. Spectral simulations were performed with *EasySpin* using the implemented *pepper* function. [1]

Electron Nuclear Double Resonance (ENDOR)

ENDOR experiments were carried out at 17 K and 20 K using a Bruker EN 5107D2 resonator and an AR 600 W radiofrequency (RF) amplifier (AR 600A225A). Davies ENDOR spectra were recorded using the following microwave pulse sequence: $\pi–T–\pi/2–\tau–\pi–\tau–$echo. An RF pulse of variable frequency was applied during the time interval T. The RF pulse length was chosen based on the nucleus: either ^{1}H (17 µs) or ^{2}H/^{57}Fe (40 µs). The first π-pulse was a rectangular-shaped inversion pulse of 130 ns. Mims ENDOR experiments were carried out at 17 K using the following stimulated-echo pulse sequence: $\pi/2–\tau–\pi/2–$T$–\pi/2–\tau–$echo with τ = 300 ns.

ATR-FTIR spectroscopy

Attenuated total reflectance Fourier transform spectroscopy was performed on a Bruker Tensor II spectrometer (Bruker Optik, Germany), equipped with a nine reflection ZnSe/Si crystal (Microm ATR Vision, Czitek). All measurements were conducted under anoxic conditions (1.5 % H_2, 98.5 % N_2) at 25 °C. The FTIR spectra were recorded from 4000 – 1000 cm^{-1} with a resolution of 2 cm^{-1}. The protein film was dried with a constant gas stream for around 10 minutes and re-humidified with an aerosol by purging a buffer containing compartment.

Expression and purification

E. coli strain BL21 (DE3) ΔiscR was transformed with the expression plasmid pET21b containing the desired gene for protein expression. The codon-optimized CBA5H gene from *Clostridium beijerinckii* (NCBI GenBank: KX147468.1) and the CPI gene from *Clostridium pasteurianum* (NCBI GenBank: WP_004455619.1) was used to express strep-tagged apo-[FeFe]-hydrogenases (lacking the $[2Fe]_H$ subcluster). [2] Expression and purification was conducted under strictly anaerobic conditions as described previously if not stated otherwise. [3] Affinity chromatography was performed using Strep Tacting High-capacity resin (IBA GmBH). The protein concentration was determined by Bradford assay, and purity was verified by SDS-PAGE (polyacrylamide gel electrophoresis), as shown in the Figure below. [4,5] The metal content of apo-CbA5H protein was quantified by ICP-AES (inductively coupled plasma atomic emission spectroscopy) measurements to 12 ± 1 Fe-atoms per monomer in agreement with the literature. [6] Proteins were stored at −80 °C in 100 mM Tris-HCl buffer pH 8 with 2 mM sodium dithionite (NaDT), if not stated otherwise. For NaDT-free protein preparations (termed NaDT-free in the following), sodium dithionite was removed via size exclusion chromatography (NAP 5 column, GE healthcare). The protein solution was stored in 100 mM Tris-HCl buffer pH 8. Details of all the samples used in this work are given in Table S1.

Expression of ^{57}Fe labeled apoprotein
Protein expression was performed in M9 minimal media (without iron source) supplemented with ^{57}Fe (Euroisotope) dissolved in HCl. Approximately 15 mg ^{57}Fe per liter culture was used for the overexpression of the labeled apoprotein. The *E. coli* BL21 (DE3) ΔiscR cells were grown until an OD of 0.6 and then transferred into an anaerobic glovebox. All other steps of expression and purification were conducted as previously described. [3] The ^{57}Fe-labeled apoprotein was reconstituted with the $[2Fe]_H$ mimic synthesized with ^{56}Fe (see below).

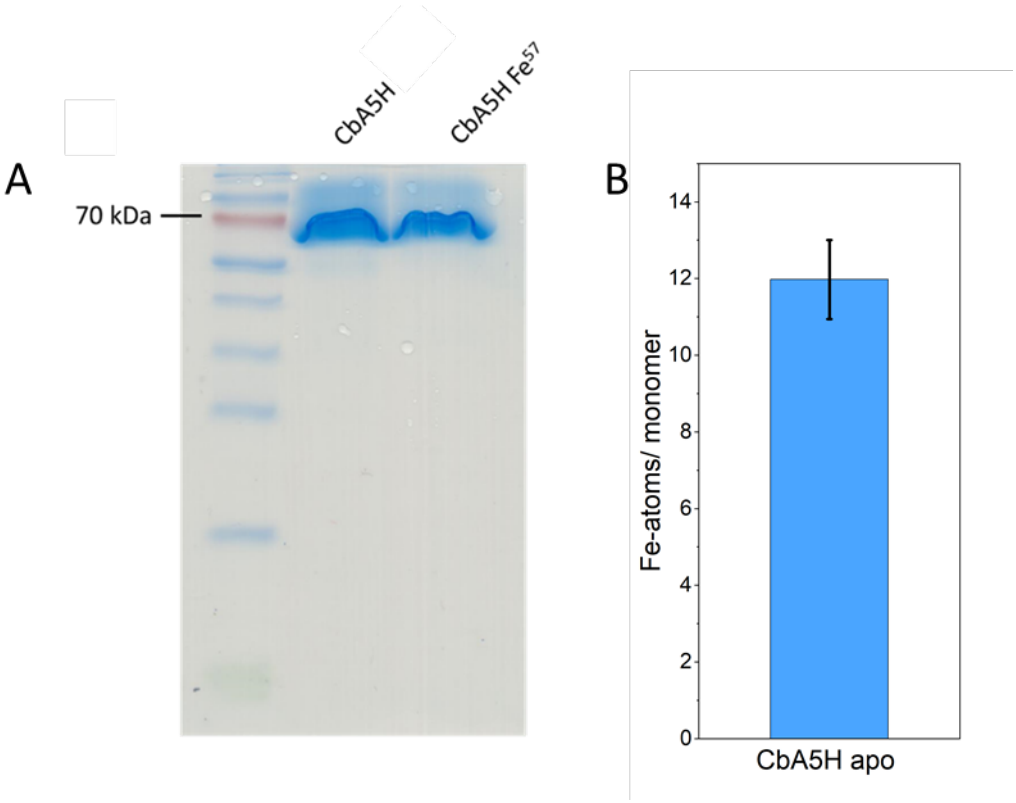

SDS-PAGE and Fe-quantification. (**A**) Lane 1: Protein Marker, Lane 2: CbA5H expressed under standard conditions, Lane 3: ^{57}Fe-labeled CbA5H. The molecular weight of the CbA5H monomer is 75 kDa. (**B**) Fe-atoms quantified by ICP-AES measurements for apo-CbA5H.

***In vitro* maturation**
Apoproteins were incubated on ice for 1 hour with a 10-fold molar excess of the artificially synthesized $[2Fe]_H$ cofactor mimics $[2Fe(SCH_2XCH_2S)(CO)_4(CN)_2]^{2-}$ (X = NH (adt), X = CH_2 (pdt)) to reconstitute active protein as described earlier. [7,8] Holoproteins and excess $[2Fe]_H$ were separated by size exclusion chromatography (NAP 5 column, GE healthcare).

CbA5H sample preparation
For H_2-treated samples, anaerobically isolated CbA5H protein solution was exposed for 45 minutes in a sealed suba tube to a humidified gas stream of 100 % H_2. All O_2-treated samples were initially treated with H_2 and subsequently exposed to a humidified O_2 (100 %) gas stream.

H_2-O_2 cycle of as-isolated CbA5H
For the H_2-O_2 cycle, an anaerobically isolated protein solution of CbA5H (400 µM) was first treated with H_2 (45 min) and then gassed with O_2 (20 min) in two repetitive cycles under the same conditions. Samples were taken after the respective treatment. The ESE-detected Q-band EPR spectra shown in Figure 3 in the main text were recorded in the critically coupled mode with rectangular pulses. The integrated absorption spectra were used as an approximation for the overall signal intensities of paramagnetic species in CbA5H. The intensity of the CbA5H^{H2} signal (trace 1, top) decreased by ~40 % after one cycle with O_2 and H_2 (trace 3) that is in accordance with activity data (see Figure S7). The signal intensity of CbA5H^{O2} (trace 2) decreased by ~5 % after treatment with H_2 and O_2 (trace 4). Note that the signal intensities are only valid for the temperature of 10 K and SRT of 3 ms. The features marked with an asterisk are assumed to arise from O_2-damaged FeS clusters, H_{ox}-CO, and/or background impurities. They are only detectable in the critically coupled mode and at lower temperatures

(compare with Figures S2 and S4). To isolate the $g \approx 2.01$ signal (termed $R^{\bullet ox}$) and determine absolute and relative spin concentrations, the same samples were investigated at 100 K via X-band cw EPR (see Figure S4).

Table S1: Information on sample preparations of CbA5H, apo-CbA5H, and CpI with their respective abbreviations (marked in bold), protein concentrations, appearances in figures (M: main text, S: supplemental information), and presence of $R^{\bullet ox}$.

Sample	Concentration /µM	Figure(s)	$R^{\bullet ox}$ present
apo-CbA5H^{NaDT} apo-CbA5H + 10mM NaDT, 10 % glycerol	350	M2, S2	-
apo-CbA5H^{H2} apo-CbA5H +H_2	730	S6, S12	-
apo-CbA5H^{O2} apo-CbA5H + H_2, + O_2	730	M4, S6, S8, S12	-
CbA5H^{NaDT} CbA5H + 10 mM NaDT, 5 % glycerol	530	M2, S1-2	✓
CbA5H^{air} CbA5H + 10mM NaDT, + O_2, 5 % glycerol	530	S8	✓
CbA5H + 100 mM NaDT, 5 % glycerol	500	S1	✓
H_2-O_2-cycle CbA5H + H_2, + O_2, + H_2, + O_2	400	M3, S3-4	✓
aerobically isolated CbA5H^{H2} CbA5H + H_2	970	S6, S11-12	✓
aerobically isolated CbA5H^{O2} CbA5H + H_2, + O_2	970	S6, S11-12	✓
NaDT-free CbA5H^{H2} CbA5H + H_2	490	S1-2, S5, S8-11, S13, S15	✓
NaDT-free CbA5H^{O2} CbA5H + H_2, + O_2	490	M3-4, S5 S8-11, S13, S15, S17, S19-20	✓
CbA5H$_{D2O}$ CbA5H in deuterated buffer + H_2, + O_2	500	S19-20	✓
CbA5H^{HAR} CbA5H + 1mM HAR	430	S5-9	✓
CbA5H^{HAR} + H_2 CbA5H + 1mM HAR, + H_2	430	S9	✓
^{57}Fe-CbA5H^{O2} ^{57}Fe-labeled apo-CbA5H maturated with $[2^{56}Fe]_H$	400	M5, S17-18, S20	✓
CbA5H-C367D^{O2} CbA5H variant with Cys to Asp exchange at position 367	700	M4, S15	✓
CbA5H(pdt)^{H2} CbA5H maturated with pdt, + H_2	500	S13	-
CbA5H(pdt)^{O2} CbA5H maturated with pdt, + H_2, + O_2	500	M4, S13	-
CpI^{H2} CpI + H_2	270	S10	-
CpI^{O2} CpI + H_2, + O_2	270	M4, S10	-

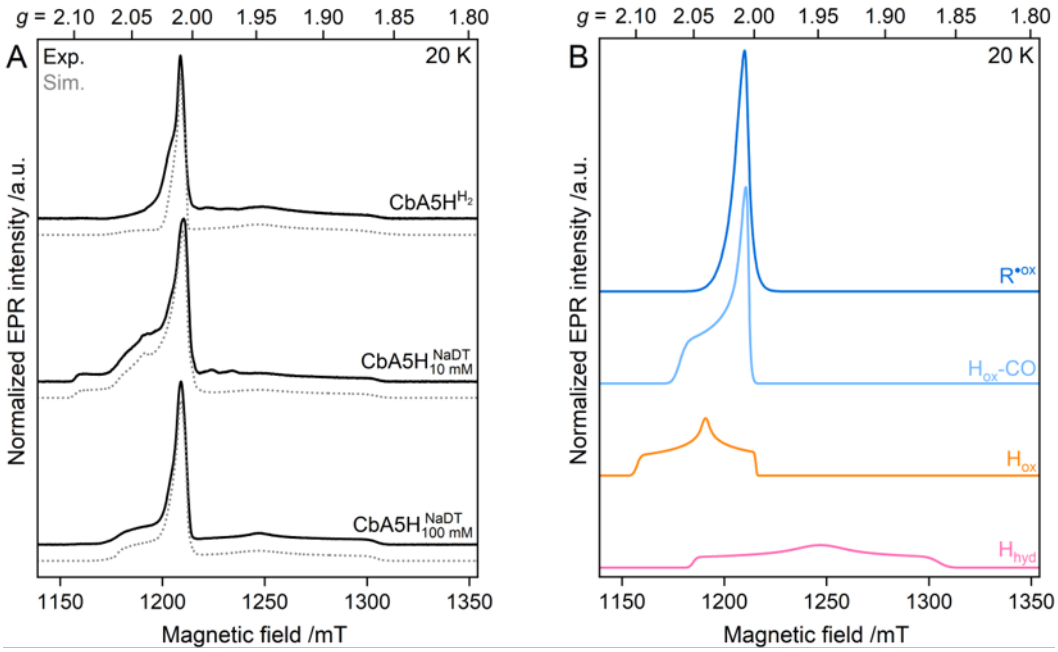

C

Species	Relative weights in %		
	CbA5H^{H2}	CbA5H^{NaDT} (10 mM)	CbA5H^{NaDT} (100 mM)
R$^{\bullet ox}$	51	27	33
H_{ox}-CO	-	31	30
H_{ox}	-	20	-
H_{hyd}	49	22	37

Figure S1. Pulsed EPR spectra (34 GHz, T = 20K) of CbA5H treated with H_2 (NaDT-free) and 10 or 100 mMNaDT. (**A**) Experimental spectra (black traces) and simulations (grey dotted traces) with varying contributions from (**B**) the $g \approx 2.01$ signal (termed R$^{\bullet ox}$, blue), H_{ox}-CO (light blue), H_{ox} (orange), and H_{hyd} (pink). (**C**) Relative weights of the paramagnetic species used in the simulations for the three samples (for g-values, see Table S2). The values are only valid for T = 20 K and an SRT of 0.5 ms. The short SRT was used to suppress R$^{\bullet ox}$ and improve spectral simulations for the remaining species. The full simulations were obtained by simulating four species simultaneously, with their relative weights having an uncertainty of ± 5 %. While the spectrum of CbA5H^{H2} shows contributions from R$^{\bullet ox}$ and H_{hyd}, the 10 mM NaDT-reduced spectrum has additional features of H_{ox} and H_{ox}-CO. Under stronger reducing conditions (100 mM NaDT), H_{hyd} predominates, while the contribution of H_{ox} is negligible. This observation is in accordance with H_{hyd} being only observable at low potentials (< 400 mV) and H_{ox} dominating the hydrogenase EPR spectra at higher potentials. [9] We could isolate R$^{\bullet ox}$ at temperatures above 70 K (see also Figures S2 and S4).

Table S2. Simulation parameters of paramagnetic species observed in CbA5H with $g_1 > g_2 > g_3$. The *g*-values of CbA5H (error given in brackets) were obtained from several different sample preparations recorded at different temperatures and frequencies, where certain species dominated the spectrum (see also Figure S2). Note that *g*-strain was the only line broadening mechanism employed in the simulations. The $R^{\bullet ox\ *}$ species arising in C367D[02] reveals slightly different simulation parameters.

Species	*g*-tensor			*g*-strain		
$R^{\bullet ox}$	2.019(4)	2.010(3)	2.006(3)	0.030	0.010	0.002
$R^{\bullet ox\ *}$	2.015(3)	2.012(3)	2.007(2)	0.012	0.001	0.004
FS4 (axial)	2.09(1)	1.92(1)	1.92(1)	0.03	0.03	0.06
FS4 (rhombic)	2.03(1)	1.94(1)	1.84(1)	0.03	0.01	0.05
H_{ox}	2.099(1)	2.039(1)	1.999(1)	0.007	0.005	0.002
H_{ox}-CO	2.060(4)	2.008(1)	2.006(2)	0.011	0.008	0.002
H_{hyd}	2.050(20)	1.948(1)	1.862(1)	0.006	0.029	0.013

Table S3. *g*-values of paramagnetic H-cluster states observed in CbA5H with $g_1 > g_2 > g_3$ in comparison to literature values. The asterisks mark the species in which *g*-tensors arise from the H_{hyd} state.

Protein	H_{hyd} or H_{trans}			H_{ox}			H_{ox}-CO			Ref.
*Cb*A5H*	2.050(20)	1.948(1)	1.862(1)	2.099(1)	2.039(1)	1.999(1)	2.060(4)	2.008(1)	2.006(2)	this work
*Cr*HydA1*	2.07	1.93	1.88	2.100	2.037	1.996	2.052	2.007	2.007	[10–12]
*Dd*H	2.06	1.96	1.89	2.10	2.04	2.00	2.06	2.00	2.00	[13]
*Dd*V	2.07	1.96	1.89	2.11	2.05	2.00	2.06	2.00	2.00	[14–16]
*Cp*I				2.097	2.0392	1.999	2.0725	2.006	2.006	[17]
*Me*HydA				2.093	2.041	1.999	2.061	2.007	2.007	[18]

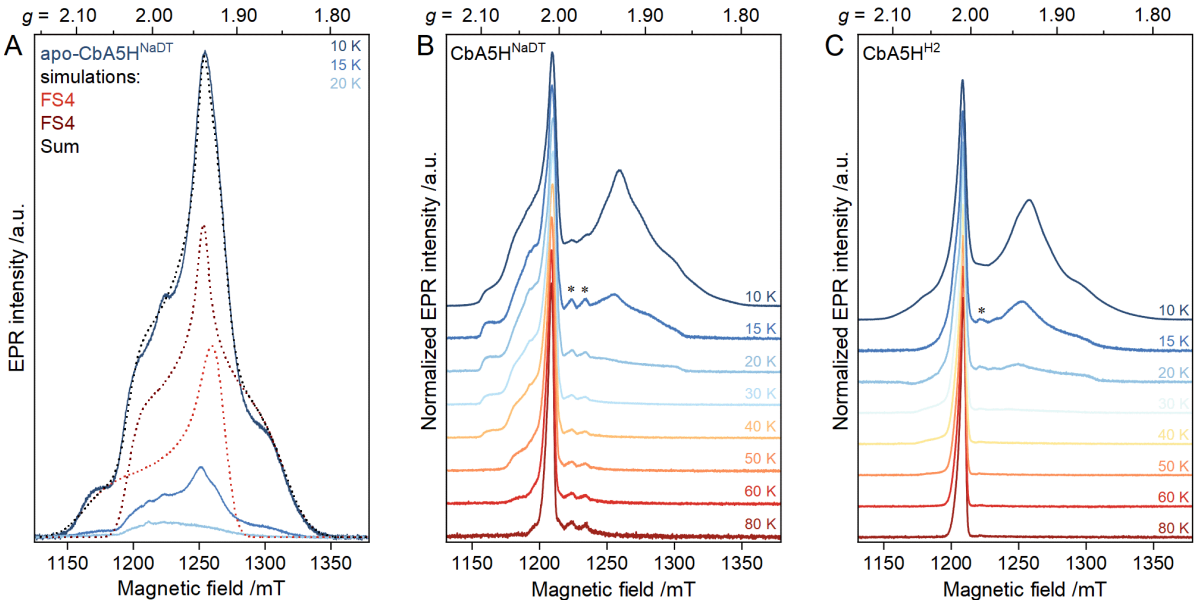

Figure S2. Temperature-dependent pulsed EPR spectra (34 GHz) of reduced apo- and holo-CbA5H. (**A**) reduced (10 mM NaDT) apo-CbA5H, (**B**) reduced (10 mM NaDT) CbA5H and (**C**) H_2-treated, NaDT-free CbA5H. The apo-CbA5H^{NaDT} spectrum at 10 K in A (dark blue) was simulated as a sum (dotted black line) of two contributions from [4Fe4S] clusters (FS4, dotted lines) with rhombic (62 % weight, dark red) and axial (38 % weight, light red) line shape. The simulation parameters are displayed in Table S2. Although there probably exist three [4Fe4S] clusters in the apo-CbA5H, our attempts to simulate the spectrum with three species failed. This might be due to the incomplete reduction of $[4Fe4S]_H$. Note that redox potentiometry or cluster knockouts are necessary to confirm and assign the spectral simulations to their respective cluster. The spectra in B and C were normalized to their maximum signal intensities, and Mn^{2+} impurity signals are marked with asterisks. The EPR spectrum of apo-CbA5H is broadened beyond detection above 20 K, indicating (i) the absence of H-cluster states, (ii) the presence of fast-relaxing $[4Fe4S]^{1+}$ clusters, [19,20], and (iii) lack of accessory $[2Fe2S]^{1+}$ clusters found, e.g., in CpI. [21] In B and C, the rhombic H_{hyd} state is observable up to 25 K, the rhombic signal from H_{ox} is observed below 50 K, and the axial signal of H_{ox}-CO is observed below 60 K. The $g \approx 2.01$ signal (termed $R^{\bullet ox}$) was the only detectable species above 70 K (see Figure S4 and Table S2 for more details).

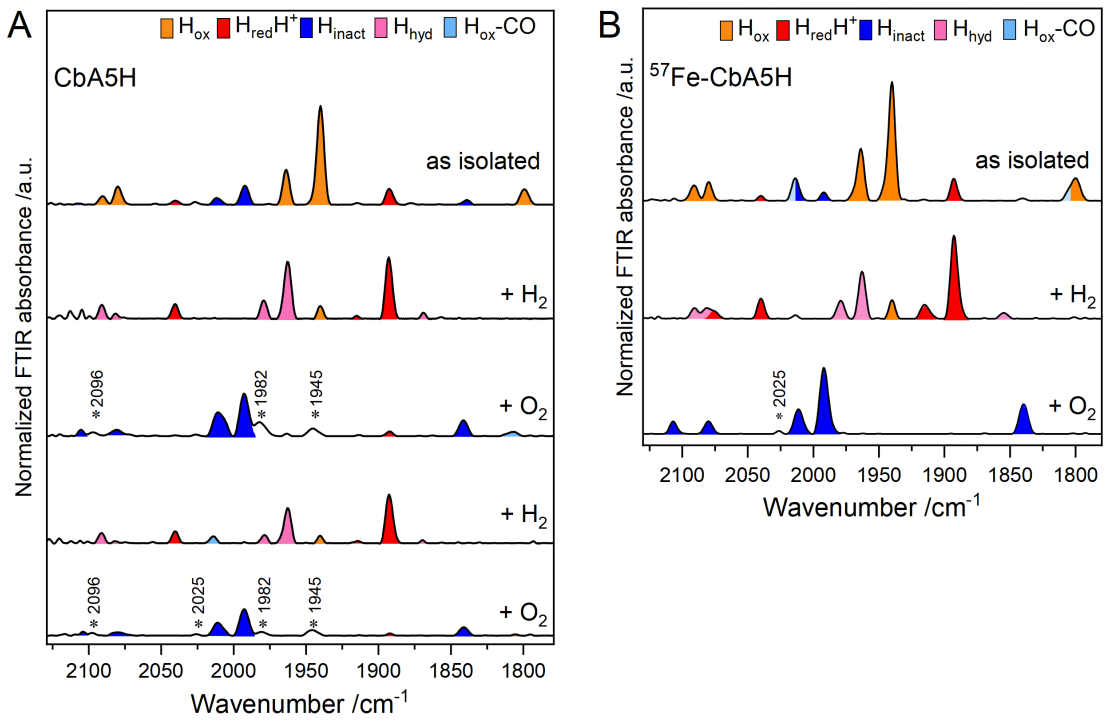

Figure S3. IR-vibrational spectra of CbA5H monitored *via* ATR-FTIR-spectroscopy. (**A**) As-isolated CbA5H protein solution (400 µM, 0.1 M Tris-HCl, pH 8) was purged alternately with H_2 and O_2. The vibrational frequencies are associated with different redox states and are colored accordingly. The contributions of $H_{red}H^+$ and H_{hyd} decreased by approximately 39 % and 47 % during the second H_2 treatment, respectively. The signal intensity of H_{inact} decreased by about 40 % in the second O_2 cycle, indicating that H_{inact} is not directly associated with the $g \approx 2.01$ species (termed $R^{\bullet ox}$), as the latter only decreases by approximately 5–10 % throughout the cycle (see Figure 3 in main text and S4). Asterisks represent unassignable bands, which are suggested to arise from oxygenation of bridging thiolates and were observed to induce a shift of 6–19 cm^{-1}. [22] Swanson *et al.* reported similar shifts for HydA1 after prolonged exposure to O_2. [23] (**B**) IR-vibrational spectra of ^{57}Fe-CbA5H samples utilized for EPR measurements. As-isolated samples were purged with H_2 and subsequently with O_2. Aliquots were taken for EPR and FTIR measurements to verify redox state populations. Approximately 50 % of the cluster intensities remain after O_2 purging compared to the H_2-treated sample. H_2-reduced cluster intensities of ^{57}Fe-CbA5H decrease by about 28 % after treatment with O_2.

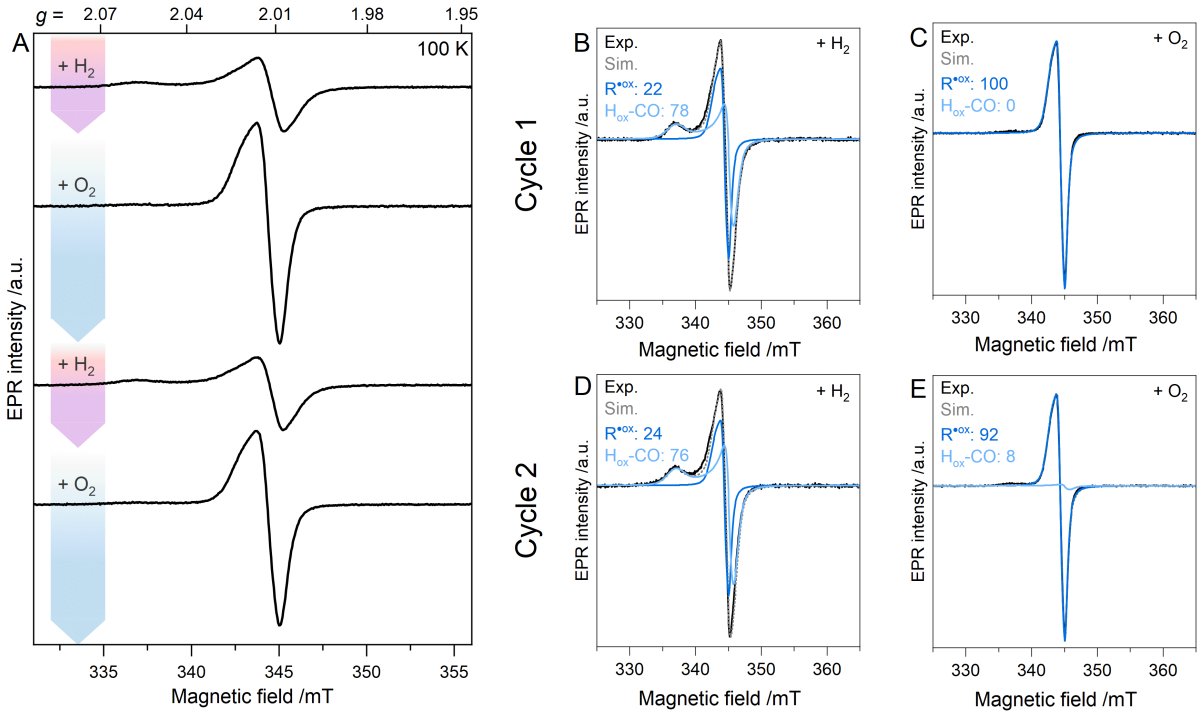

Sample	Spin concentration /spins mol^{-1}	Relative weight /%	
		R•ox	Hox-CO
H_2 (1)	0.077	22	78
O_2 (1)	0.084	100	0
H_2 (2)	0.078	23	76
O_2 (2)	0.079	92	8

Figure S4. Spectral analysis and simulation of cw EPR spectra (9.7 GHz, T = 100 K) within the H_2-O_2 cycle. (**A**) H_2-O_2 cycle of as-isolated CbA5H (see Figure 3 in the main text for pulsed EPR spectra at T = 10 K). (**B–E**) The experimental spectra were simulated with varying contributions of two species, R•ox (blue) and Hox-CO (light blue), with the respective weights (in %) given in the table (see Table S2 for respective *g*-values). The spin concentrations were quantitated by double integration of the cw EPR spectra recorded under non-saturating conditions at X-band and 100 K. The standards for spin quantification were 1 mM CuEDTA and tyrosyl radical, Y_{122}•, residing in *E. coli* class Ia ribonucleotide reductase with a known concentration. We determined R•ox concentrations of at least three distinct CbA5H^{O2} samples from different sample preparations. The highest and lowest amounts were 0.15 and 0.085 spins/mol, respectively, and are in the expected error range of 30 %. [24] The signal intensity of R•ox observed in the shown H_2-O_2 cycle grows by a factor of five upon treatment with O_2 and loses approximately 13 % intensity throughout the cycle. Note that the detected spin concentrations are only valid for the given experimental temperatures. The relative contributions of R•ox and Hox-CO to CbA5H^{H2} at 100 K are 22 % and 78 %, while these values change to 51 % and below 5 %, respectively, when the experiment is conducted at 20 K (Figure 3 and S1). Similar spin concentrations of H-cluster states and variation in optimal temperatures for their EPR detection are observed in other hydrogenases. [13,25] Experimental conditions: 3–10 mW power; 1.28 ms time constant; 80 ms conversion time; 100 s sweep time, 4–5 scans.

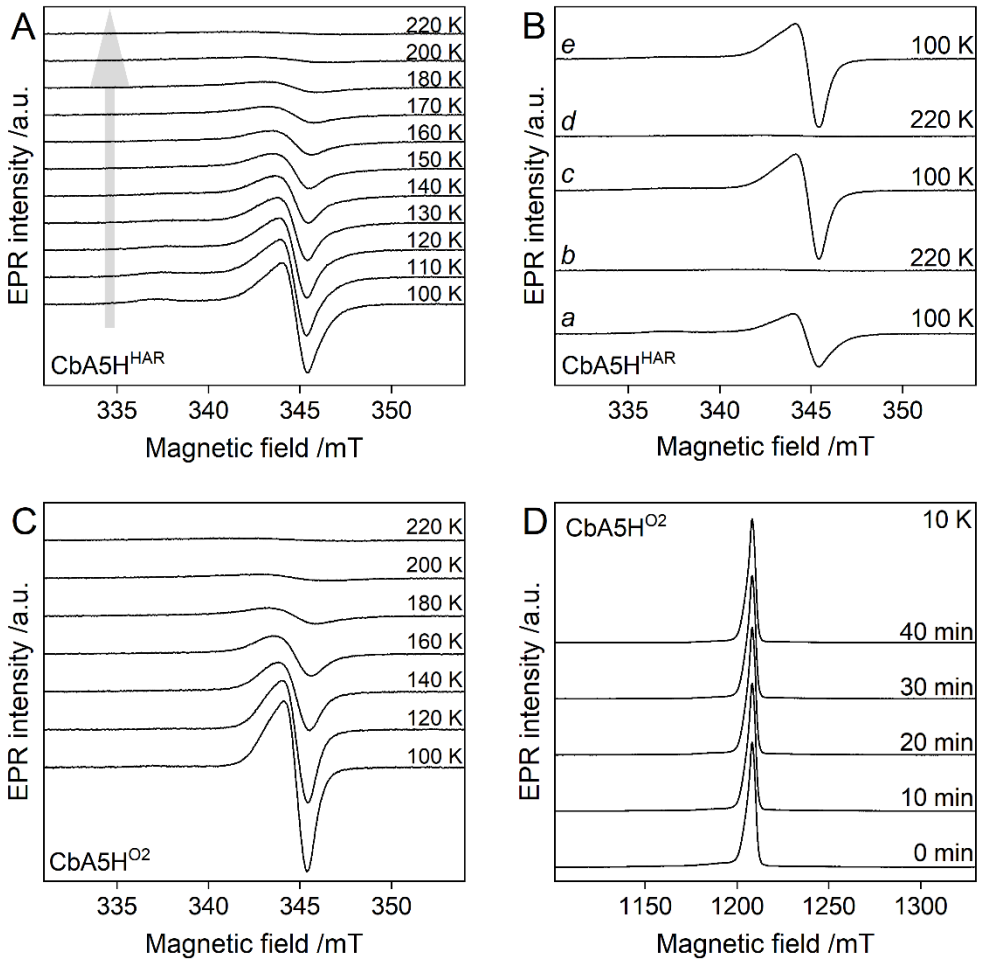

Figure S5. Temperature-dependent EPR spectra of two differently oxidized CbA5H samples with cryo-annealing at T = 220 K and in dry ice. (**A**) Temperature-dependent cw EPR spectra (9.7 GHz, T = 100–220 K) of CbA5H treated with 1 mM HAR were plotted with constant spacing. (As shown in Figure S9, HAR has a similar effect on CbA5H as O_2.) (**B**) Spectra of the same sample were recorded alternately at 100 K and 220 K. Spectra *a* and *b* are the first and last traces shown in A. Spectrum *c* showed a 32 % increase in intensity, possibly due to remaining, previously unreacted HAR from the sample preparation. Spectrum *d* was obtained after 10 min at 220 K. The spectrum *e*, recorded subsequently, showed no signal intensity or line shape change. Experimental conditions: 10 mW power, 1.28 ms time constant, 81 ms conversion time, 77 s sweep time, 5–11 scans. (**C**) Temperature-dependent cw EPR spectra (9.7 GHz, T = 100–220 K) of O_2-oxidized, NaDT-free CbA5H. Experimental conditions: 3 mW power; 1.28 ms time constant; 50 ms conversion time; 50 s sweep time, 3–12 scans. (**D**) Pulsed EPR spectra (34 GHz, T = 10 K) were recorded in a critically coupled cavity with rectangular pulses after 0, 10, 20, 30, and 40 min storage on dry ice (~195 K). The top trace corresponds to a cumulative storage time of 100 min. The measurements shown in panel D were conducted before the ones in C using the same sample. The signal amplitude and shape remained unchanged.

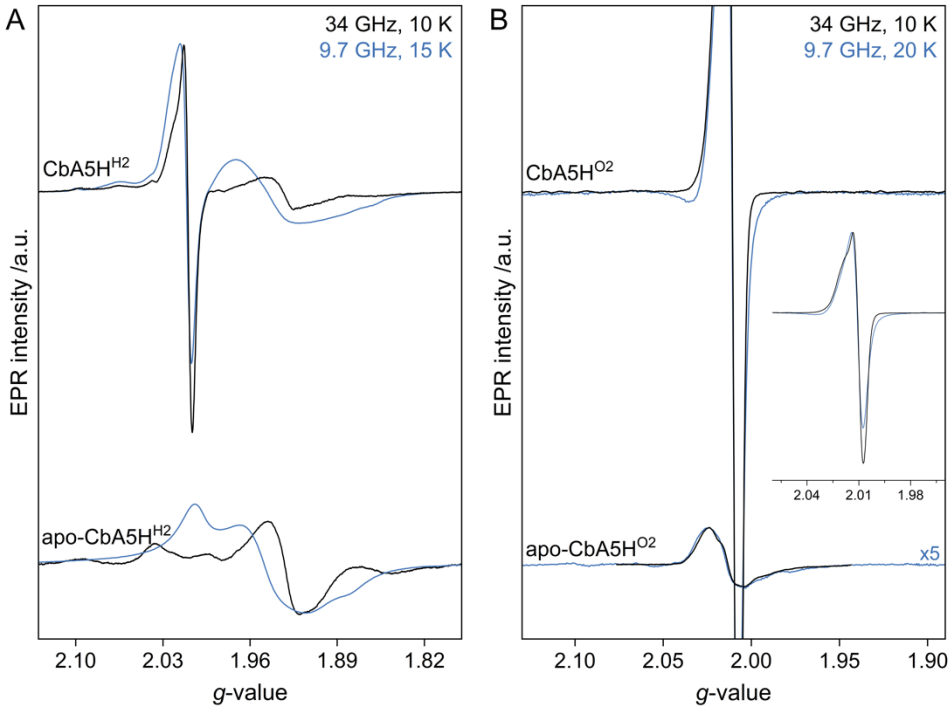

Figure S6. Comparison of cw EPR spectra (9.7 GHz, T = 15–20 K, blue) and pulsed EPR spectra (34 GHz, T = 10 K, black) of anaerobically isolated apo-CbA5H and aerobically isolated holo-CbA5H treated with H_2 or O_2. (**A**) Spectra of CbA5H^{H2} and apo-CbA5H^{H2} and (**B**) spectra of CbA5H^{O2} and apo-CbA5H^{O2} (multiplied by five) with the inset showing the full spectrum of CbA5H^{O2}. All spectra were plotted with a common *g*-scale. The intensities of the pulsed EPR spectra were adjusted to the cw EPR spectra for better comparison. The distinct spectral patterns of apo-CbA5H^{H2} observed at X- and Q-band are a strong indicator of spin-spin interaction between FS4A, FS4B, and $[4Fe4S]_H$. [26,27] This observation is not surprising as these clusters are adjacent to each other (≤ 15 Å apart). [28] In contrast, the spectral line shapes of CbA5H^{O2} and apo-CbA5H^{O2} do not change with the frequency. The cw EPR intensity of CbA5H^{O2}, originating from $R^{\bullet ox}$, is one order of magnitude higher than that of apo-CbA5H^{O2}, which only exhibits residual $[3Fe4S]^+$ clusters due to oxidation damage to [4Fe4S] clusters. [29] Experimental conditions for (i) H_2-reduced samples: 20 K; 1.5 µW power; 100 ms conversion time and 205 s sweep time and (ii) for O_2-oxidized samples: 10 K; 0.47 mW power; 80 ms conversion time and 40 s sweep time.

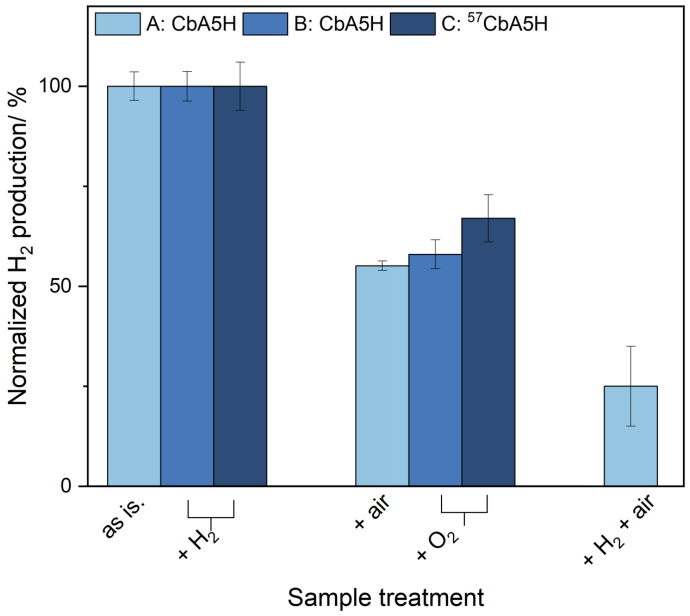

Figure S7: H_2-production activities of CbA5H (wild type and ^{57}Fe-labeled) prior and after exposures to H_2, air and O_2. Hydrogen production activities were determined with a standard assay, as reported earlier. [8] (**A**) H_2-production activities of wild-type CbA5H prior and after air and H_2 exposures. The enzyme stock solution was prepared without NaDT to ensure the absence of oxygen-scavenging reagents. Before further treatment, one aliquot was taken from the stock solution, termed "as isolated" (as is.). Next, the enzyme solution was incubated for 20 min in the air. Aliquots were taken and termed "air". The remaining protein solution was reactivated with 100 % H_2 (45 min) and incubated for an additional 20 min in the air to prepare the aliquot termed "H_2 + air". To determine the hydrogen production activity of previously prepared aliquots, 400 ng enzyme was mixed with 0.1 M potassium phosphate buffer (pH 6.8), 100 mM NaDT and 10 mM methyl viologen. The assay solution was incubated in a sealed suba vessel for 20 min at 37° C under constant shaking. The H_2 production rate was determined via GC-FID (gas chromatography-flame ionization detector). Error bars represent the standard deviations from three technical replicates. (**B, C**) H_2-production activities of wild type and ^{57}Fe-labeled CbA5H before and after exposure to H_2 and O_2. The protein solution was treated with 100 % H_2 (60 min) and incubated for an additional 20 min with 100 % O_2. 400 ng enzyme was mixed with 0.1 M potassium phosphate buffer (pH 6.8), 100 mM NaDT and 10 mM methyl viologen. The assay solution was incubated in a sealed suba vessel for 20 min at 37°C under constant shaking. The H_2 production rate was determined via GC-FID. Activities for H_2-treated CbA5H: 2907 ± 107 µmol H_2 × min^{-1} × mg protein^{-1} and for ^{57}Fe-CbA5H: 2734 ± 163 µmol H_2 × min^{-1} × mg protein^{-1}. After O_2 treatment, the activity decreased by 42 % for CbA5H (1690 ± 60 µmol H_2 × min^{-1} × mg protein^{-1}) and by 33 % for ^{57}Fe-CbA5H (1825 ± 108 µmol H_2 × min^{-1} × mg protein^{-1}).

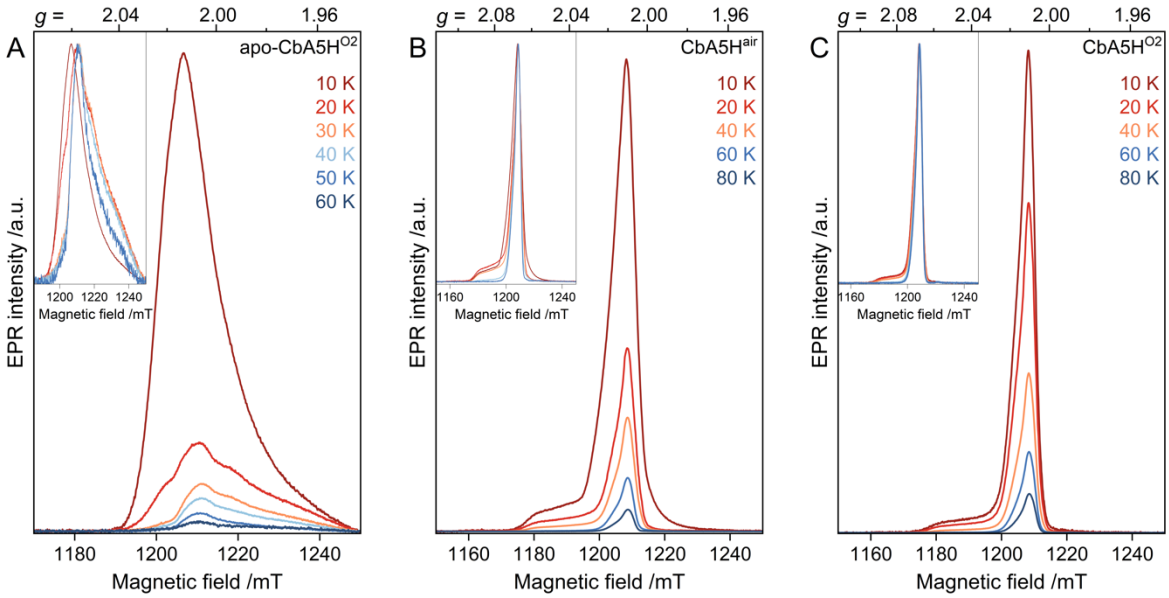

Figure S8. Temperature-dependent pulsed EPR spectra (34 GHz) of oxidized holo- and apo-CbA5H and comparison of air and O_2 for oxidation. (**A**) Spectra of apo-CbA5H^{O2} (SRT: 3.0 – 0.3 ms); (**B**) spectra of air-oxidized holo-CbA5H^{air} (SRT: 25.0 – 0.5 ms); (**C**) spectra of O_2-treated, NaDT-free, holo-CbA5H^{O2} (SRT: 25.0 – 0.5 ms). Note that the third sample had undergone cryo-annealing (see Figure S5 C–D) and thawing. Therefore, it exhibits a contribution from H_{ox}-CO that arises from degraded FeS clusters. This is usually not observed in O_2-oxidized samples (compare Figures S4, S6, and S11). The insets show the spectra normalized to their maximum signal intensity (apo-CbA5H^{O2} measured at 60 K was left out for better visualization due to its low S/N ratio). The spectra of apo-CbA5H^{O2} (A) are observable up to 60 K showing characteristics of an oxidized [3Fe4S]$^{+}$ cluster ($g_{max} \approx 2.03$). [30] In addition to R$^{\bullet ox}$, two more species were detected in holo-CbA5H^{air} (B). First, a minor contribution of the [3Fe4S]$^{+}$ cluster signal was present at 10 K. Second, using air for oxidation led to the formation of H_{ox}-CO, which is observable up to 50 K. At temperatures ≥ 60 K, R$^{\bullet ox}$ is the only observable EPR signal.

Corrigan et al. [6] observed an EPR signal similar to R$^{\bullet ox}$ in an as-isolated CbA5H sample upon oxidation. They ascribed it to a [3Fe4S]$^{+}$ cluster arising from degraded FeS clusters based on free Fe^{3+} present in the oxidized sample. When compared, the spectral features of R$^{\bullet ox}$ are indeed reminiscent of signals typical for oxidized [3Fe4S]$^{1+}$ clusters, including the one observed in apo-CbA5H^{O2}. However, numerous significant properties distinguish it from typical [3Fe4S]$^{1+}$ clusters. First, R$^{\bullet ox}$ is detectable above 100 K (see C). Second, its line shape and temperature dependence are entirely different from those of the [3Fe4S]$^{1+}$ clusters shown in (A) and reported in the literature. [19,30–33] Third, the contribution of R$^{\bullet ox}$ in CbA5H^{O2} is an order of magnitude higher compared to the [3Fe4S]$^{1+}$ cluster observed in apo-CbA5H^{O2} (see also Figure S6). Last, similar amounts of a g = 4.30 signal related to the oxidative degradation of FeS clusters are found in CbA5H^{O2} and apo-CbA5H^{O2} (see Figure S12).

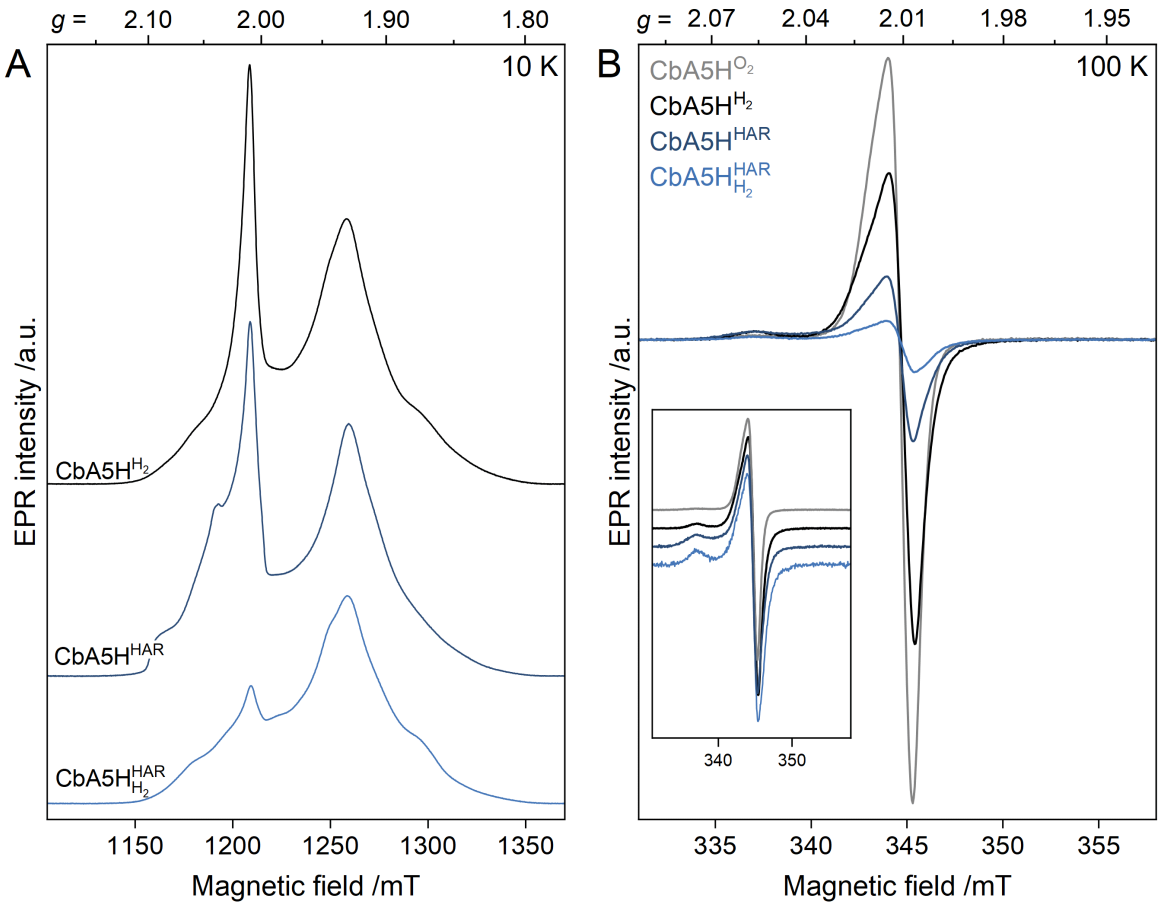

Figure S9. Comparison of EPR spectra of NaDT-free H_2- and O_2-treated CbA5H (CbA5H$^{O2/H2}$) with spectra of CbA5H treated with 1 mM HAR (CbA5H^{HAR}), which was subsequently gassed with H_2 (CbA5H$^{HAR}_{H2}$). (**A**) Pulsed EPR spectra (34 GHz, T = 10 K). Using the mild oxidant HAR, a dominant formation of Hox is observed compared to CbA5H^{H2}. Treating CbA5H^{HAR} with H_2 reduces the signal intensity of R$^{\bullet ox}$. (**B**) Cw EPR spectra recorded at 9.7 GHz and T = 100 K. Spectra normalized to their maximum signal intensity are shown with constant spacings in the inset for better comparison. Suppression of fast-relaxing species at 100 K reveals R$^{\bullet ox}$ in all samples, while CbA5H^{H2} and both HAR-treated samples reveal minor contributions from the H_{ox}-CO state (see $g \approx 2.06$). The signal intensity of R$^{\bullet ox}$ obtained from spectral simulations is approximately 80 % lower in the HAR-treated sample than CbA5H^{O2}. This might arise from different sample preparations, considering the differences between HAR and O_2 regarding the molar ratio, accessibility, and reactivity with the protein. X-band experimental conditions: 10 mW power; 1.28 ms time constant; 81 ms conversion time; 61 s sweep time, 3–9scans.

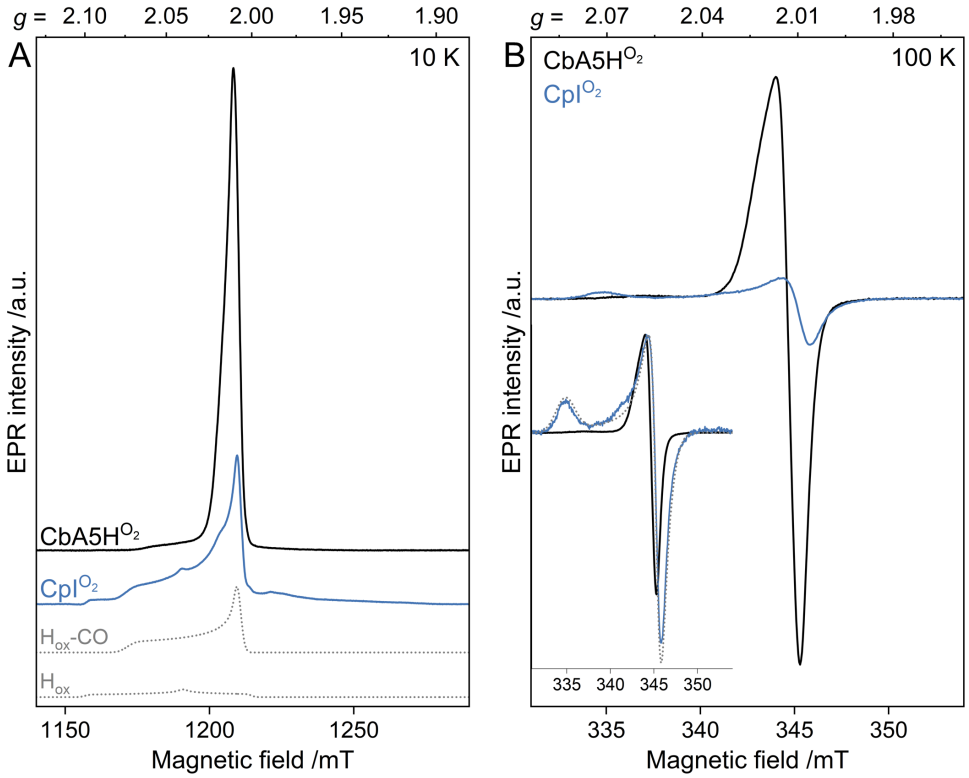

Figure S10. Comparison of EPR spectra of NaDT-free, O_2-oxidized CbA5H^{O2} (black), and CpI^{O2} (blue). The spectra were measured (**A**) via pulsed EPR (34 GHz, T = 10 K) and (**B**) via cw EPR (9.7 GHz, T = 100 K). The latter spectra normalized to their maximum signal intensity are shown in the inset. In contrast to CbA5H^{O2} showing R$^{\bullet ox}$ at both temperatures, the spectrum of CpI^{O2} at 10 K shows contributions from H$_{ox}$ (g =2.10, 2.04, 2.00) and H$_{ox}$-CO (g =2.074, 2.008, 2.006) (simulations shown with grey dotted traces). At 100 K, only a weak signal of H$_{ox}$-CO is observable in CpI (see the grey dotted trace in the inset). X-band experimental conditions for CpI: 3 mW power; 1.28 ms time constant; 80 ms conversion time; 100 s sweep time, 15 scans; for CbA5H^{O2}, see Figure S9.

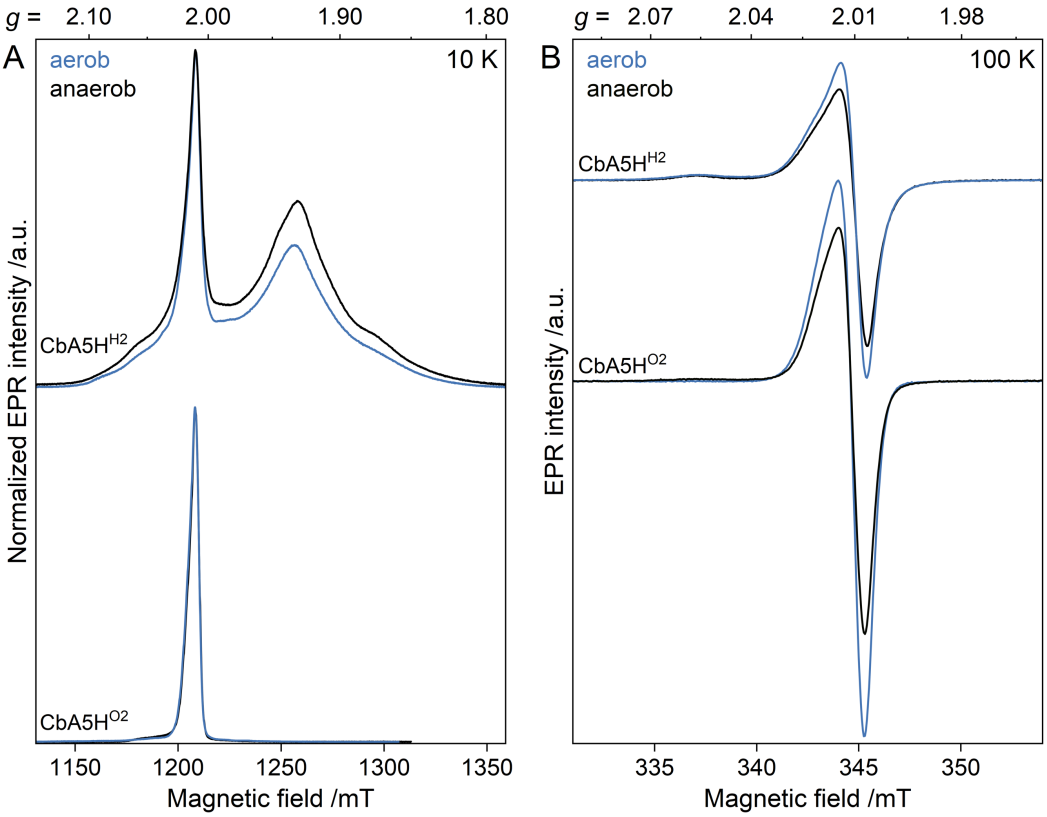

Figure S11. Comparison of EPR spectra of H_2- and O_2-treated CbA5H purified aerobically (blue) and NaDT-free, anaerobically (black). (**A**) Pulsed EPR spectra (34 GHz, T = 10 K) were normalized to their maximum signal intensities to compare the line shapes better. (**B**) Cw EPR spectra (9.7 GHz, T = 100K). At 100 K, spectra of CbA5H^{H2} show a minor contribution from H_{ox}-CO ($g \approx 2.06$). The signal intensities of $R^{\bullet ox}$ obtained via spectral simulations in aerobically purified samples is approximately 22 % higher compared to the anaerobically purified samples. X-band experimental conditions: 10–32 mW power, 1.28–5.12 ms time constant; 60–81 ms conversion time; 45–70 s sweep time, 1–3 scans.

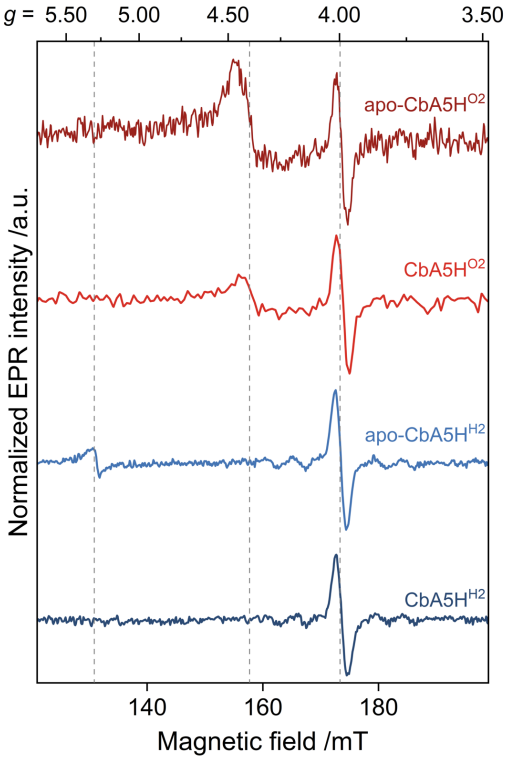

Figure S12. Comparison of cw EPR spectra (9.7 GHz, T = 15–20 K) of apo-CbA5H (730 µM) and holo-CbA5H (970 µM) treated with H_2 and O_2. The grey lines indicate g = 5.3 (left), g = 4.3 (middle, adventitiously bound Fe^{3+} (S = 5/2) [34]) and g = 4 (right, resonator impurity). All spectra were normalized to the resonator impurity signal. The spectrum of $CbA5H^{H2}$ exhibits the resonator impurity only, while apo-$CbA5H^{H2}$ is the only spectrum having a signal at g = 5.3. This indicates the presence of a half-integer high-spin species, as discussed in Ref. [34] and observed in another [FeFe]-hydrogenase under illumination. [13] Spectra of the oxidized samples show varying contributions from adventitiously bound Fe^{3+}. Apo-$CbA5H^{O2}$ has a significantly higher signal intensity at g = 4.3 than holo-$CbA5H^{O2}$. The decreased signal intensity of holo-$CbA5H^{O2}$ at g = 4.3 is noteworthy regarding the $R^{\bullet ox}$ signal, which exhibits one order of magnitude higher signal intensity than the $[3Fe4S]^+$ clusters in apo-$CbA5H^{O2}$ (see Figure S5). Thus, it can be concluded that $R^{\bullet ox}$ is unrelated to the signal intensity at g = 4.3 arising due to degraded FeS clusters. Experimental conditions for (i) H_2-reduced samples: 15 K; 0.47 mW power; 100 ms conversion time and 205 s sweep time and (ii) for O_2-oxidized samples: 15–20 K; 0.047 mW power; 80 ms conversion time and 164 s sweep time.

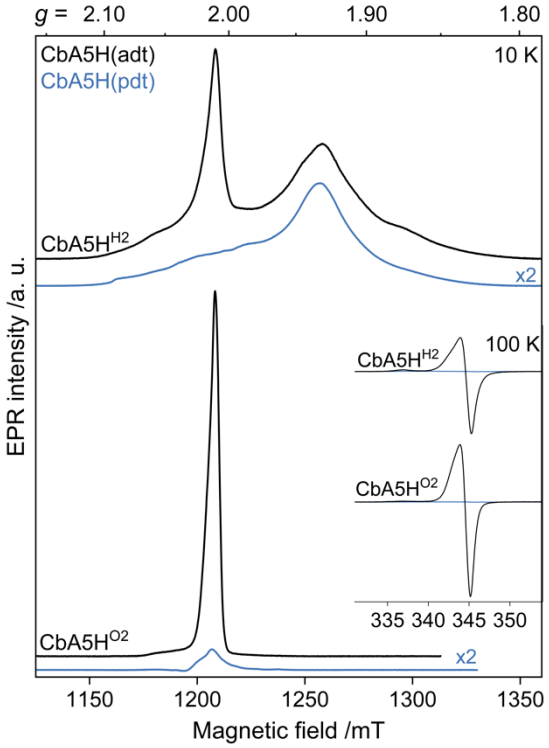

Figure S13. EPR spectra of CbA5H^{H2} and CbA5H^{O2} maturated with adt (490 µM, CbA5H(adt), NaDT-free, black traces) and pdt (500µM, CbA5H(pdt), blue traces). For pulsed EPR spectra (34 GHz, T = 10 K), the intensities of CbA5H(pdt) were multiplied by two for a better comparison of the line shapes. The inset shows the cw EPR spectra (9.7 GHz, T = 100 K) of the same samples. At 10 K, CbA5H(pdt)^{H2} yields H_{ox} as the only paramagnetic H-cluster state and shows contributions from accessory FeS clusters at $g \approx 1.93$. CbA5H(pdt)^{O2} reveals a signal reminiscent of O_2-damaged FeS clusters at lower temperatures. Strikingly, no signal is observed at elevated temperatures in CbA5H(pdt) samples, proving the absence of $R^{\bullet ox}$. X-band experimental conditions: 10 mW power; 1.28 ms time constant; 81 ms conversion time; 77 s sweep time, 3–10 scans.

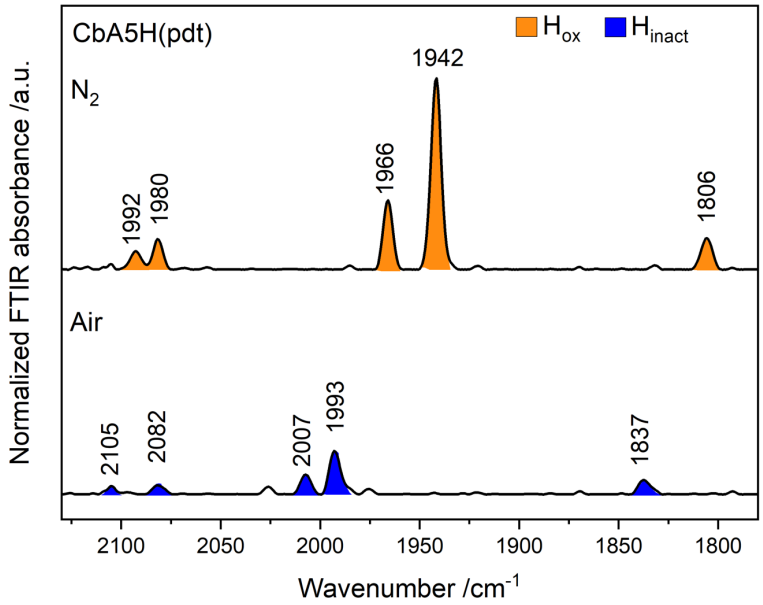

Figure S14. IR-vibrational spectra of CbA5H(pdt) monitored *via* ATR-FTIR-spectroscopy. The upper part of the figure shows CbA5H(pdt) (500 µM, 0.1 M Tris-HCl buffer, pH 8) under a constant stream of N_2 populating the H_{ox} state. The lower part depicts the IR vibrations after purging the same protein film with air (~5 min), showing the presence of H_{inact}.

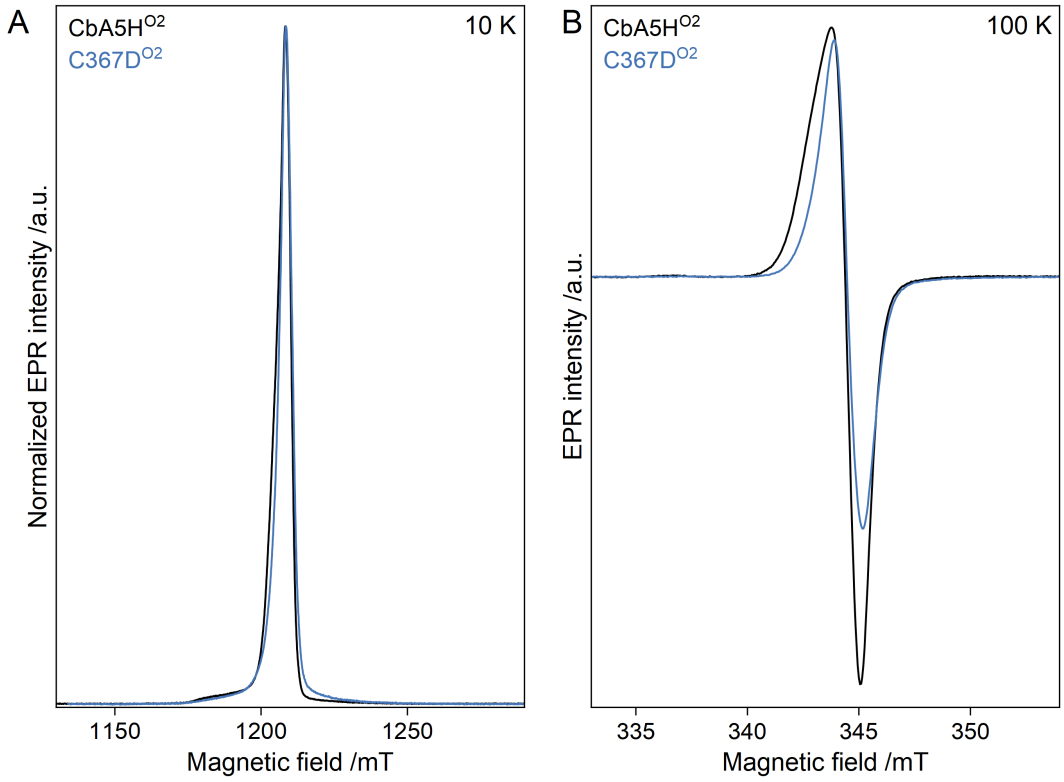

Figure S15. Comparison of EPR spectra of O_2-treated samples of CbA5H (CbA5H^{O2}, NaDT-free, black traces) and its variant C367D (C367D^{O2}, blue traces). (**A**) Pulsed EPR spectra (34 GHz, T = 10 K) were normalized to their maximum signal intensities to compare the line shapes better. (**B**) Cw EPR spectra (9.7 GHz, T = 100K). The C367D variant has a narrower line shape with smaller *g*-values (*g* = 2.015(3), 2.012(3), 2.007(2)). Additionally, its spin concentration decreased by approximately 35 % compared to wild-type CbA5H^{O2}. X-band experimental conditions for C367D: 32 mW power, 1.28 ms time constant; 82 ms conversion time; 62 s sweep time, 2 scans; for CbA5H^{O2}, see Figure S9.

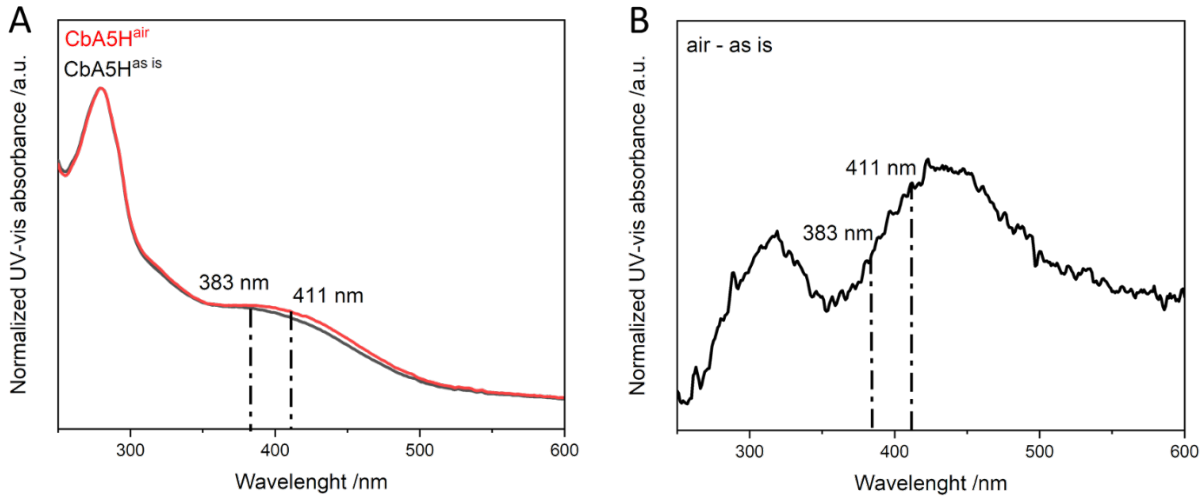

Figure S16. UV-vis and UV-vis difference spectra of as-isolated (black) and air-treated (red) CbA5H. (**A**) Normalized UV-vis spectra (280 nm) of as-isolated protein ($CbA5H^{as\ is}$) and air-treated (10 min) protein solution ($CbA5H^{air}$). The peak at 280 nm represents the absorbance of aromatic amino acids in the protein backbone. Absorbance plateau around 400 nm indicates the presence of FeS clusters. (**B**) UV-vis difference spectra of $CbA5H^{air}$ – $CbA5H^{as\ is}$. Dashed vertical lines indicate expected peak positions for tyrosyl (411 nm) and DOPA (383 nm) radicals which are absent in this spectrum. No decay was observed at 420 nm due to loss of sulfur to iron charge transfer bands. This result shows that the FeS clusters in $CbA5H^{air}$ remain stable upon oxidative treatment and thus, supports the conclusions derived in S8 and S12.

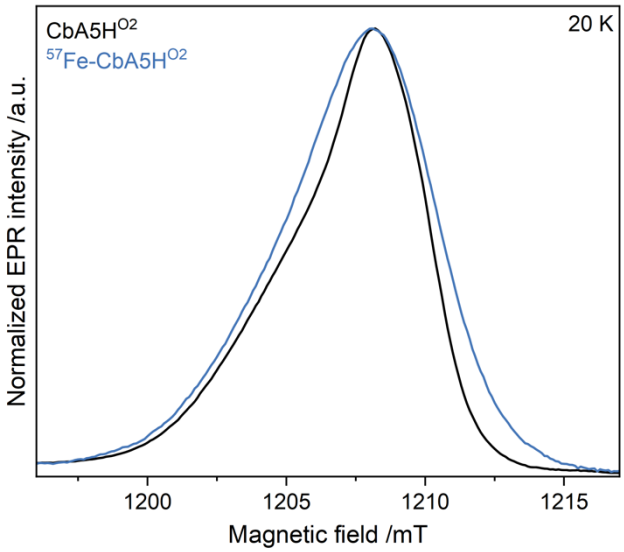

Figure S17. Comparison of pulsed EPR spectra (34 GHz, T = 20 K) of O_2-treated samples of CbA5H (CbA5H^{O2}, NaDT-free, black trace) and ^{57}Fe-labeled CbA5H (^{57}Fe-CbA5H^{O2}, blue traces). The spectra were normalized to their maximum signal intensities to better compare the line shapes. The hyperfine interactions with ^{57}Fe nuclei lead to a broadening of the line shape.

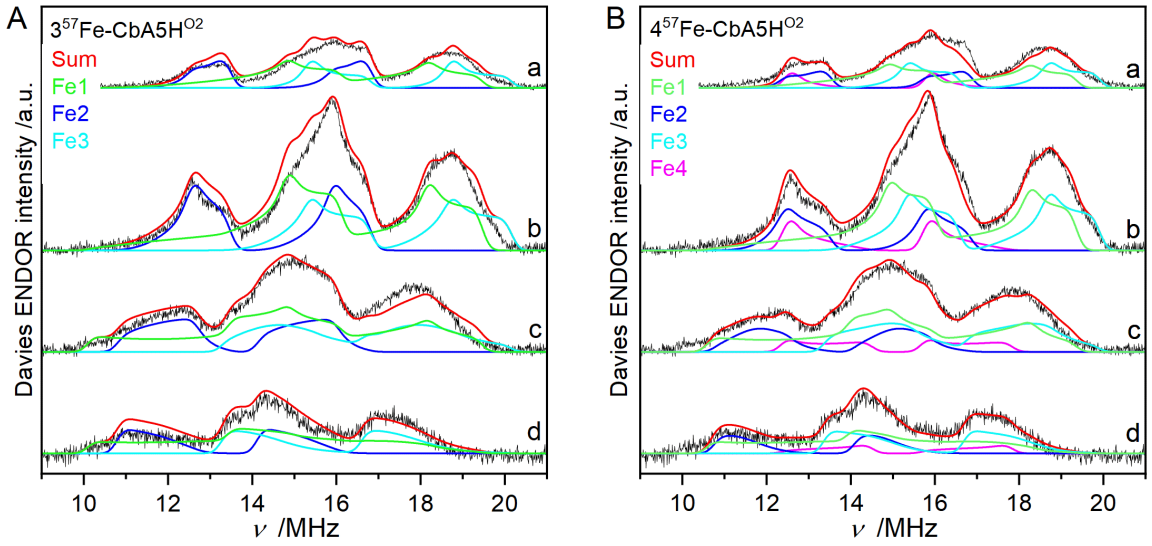

Figure S18. Davies ^{57}Fe ENDOR spectra (Q-band, T = 20 K) of ^{57}Fe-labeled CbA5H^{O2} at different field positions and respective spectral simulations. a: g = 2.008 **b:** g = 2.012 **c:** g = 2.018 **d:** g = 2.022. The simulations were performed with a global fitting function using *salt* in Easy spin and employing (**A**) 3 ^{57}Fe nuclei or (**B**) 4 ^{57}Fe nuclei. The obtained simulation parameters in comparison to literature parameters are displayed in Table S4.

Table S4. Simulation parameters for ^{57}Fe nuclei found in R$^{\bullet ox}$ from ^{57}Fe-labeled CbA5H and in H$_{ox}$-CO from different organisms.

Species	Nuclei	A_x	A_y	A_z	$\lvert A_{iso}\rvert$	φ (deg)	θ (deg)	ψ (deg)	Reference
3Fe-R$^{\bullet ox}$	Fe1	28.5	24.9	30.3	27.9	101	10	6	this work
	Fe2	29.8	34.2	37.0	33.7	89	103	81	
	Fe3	23.5	33.1	35.6	30.7	105	80	59	
4Fe-R$^{\bullet ox}$	Fe1	28.0	32.4	28.5	29.6	62	199	2	this work
	Fe2	28.3	24.8	30.4	27.8	88	0	0	
	Fe3	30.0	34.1	36.5	33.6	89	62	74	
	Fe4	24.5	33.2	35.4	31.0	82	98	60	
H$_{ox}$-CO[a]	Fe1	29.9	35.1	25.1	30.0	8	0	0	[35]
	Fe2	31.2	37.3	31.2	33.2	0	0	0	
	Fe3	28.6	24.7	30.8	28.0	110	0	0	
	Fe4	23.5	29.6	29.8	27.6	20	0	0	
H$_{ox}$-CO[b]	Fe1	-35.4	-35.0	-30.4	33.6	90	185	-	[36]
	Fe2	-34.5	-38.4	-30.7	34.5	90	5	-	
	Fe3	+27.8	+21.8	+30.3	26.7	5	110	-	
	Fe4	+26.7	+23.8	+30.2	27.0	76	-93	-	

[a] from *C. reinhardtii*

[b] from *D. desulfuricans*

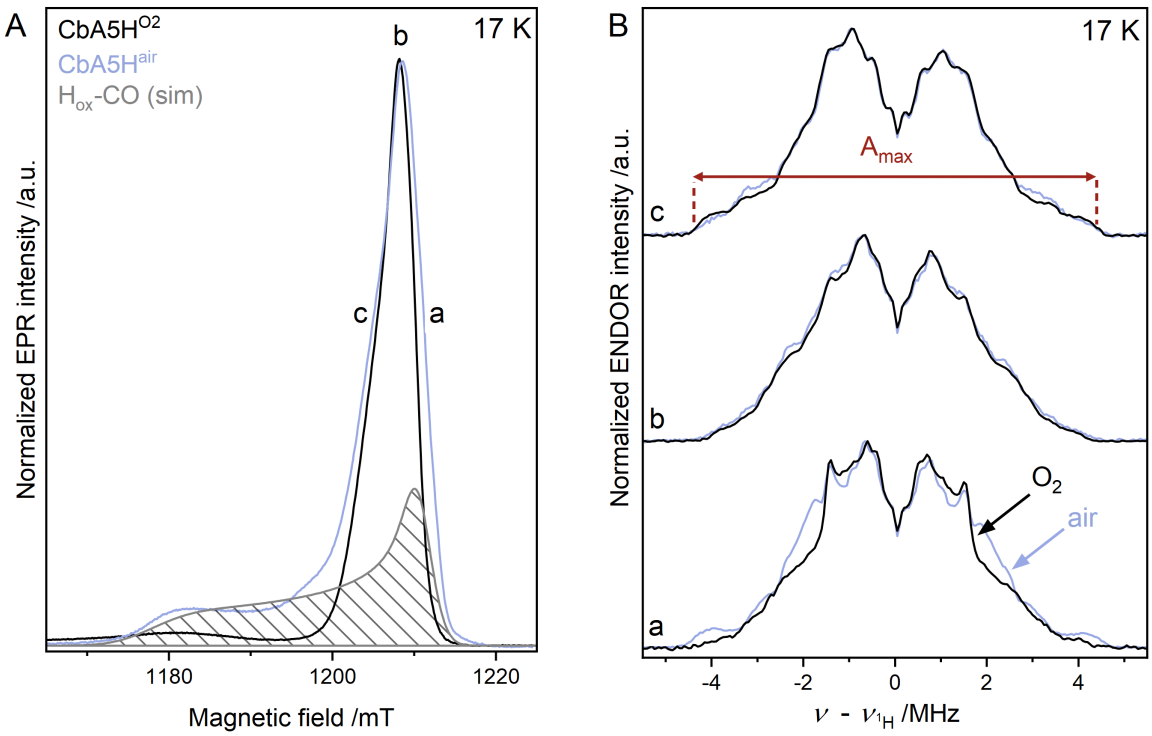

Figure S19. Comparison of EPR and ENDOR spectra of O_2-treated CbA5H (CbA5H^{O2}, NaDT-free, thawed once, black traces) and air-treated CbA5H (CbA5H^{air}, thawed once, blue traces). (**A**) Pulsed EPR spectra (34 GHz, T = 17 K) were normalized to their maximum signal intensities to compare the line shapes better. The simulation of CbA5H^{air} comprises contributions from R$^{\bullet ox}$ (56 % relative weight, not shown) and H_{ox}-CO (44 % relative weight, grey pattern). The field positions **a** (g = 2.008), **b** (g = 2.012) and **c** (g = 2.018) at which the ENDOR spectra were recorded are indicated. (**B**) Proton Davies ENDOR (Q-band, T = 17 K) of CbA5H^{O2} and CbA5H^{air} recorded at the three field positions given in (A). The maximum hyperfine coupling value A_{max} of CbA5H^{O2} is approximately 9 MHz (red arrow). Comparing ^{1}H ENDOR data of CbA5H^{O2} and CbA5H^{air} recorded at positions **c** and **b** revealed only insignificant differences. Yet, ^{1}H ENDOR data of CbA5H^{air} recorded at position **a** shows additional features compared to those of CbA5H^{O2}. These additional low-intensity signals arise from the underlying H_{ox}-CO present in the CbA5H^{air} sample. These data demonstrate unambiguously that the hyperfine couplings detected for CbA5H^{O2} belong solely to R$^{\bullet ox}$. Note that the differences between CbA5H^{O2} and CbA5H^{air} are only prominent at position **a** because the ratio of H_{ox}-CO to R$^{\bullet ox}$ contributing to the ENDOR spectrum at this orientation is the highest, as can be seen in (A). The identical multiplication factors used to normalize the EPR, and ^{1}H ENDOR spectra of ^{57}Fe-CbA5H^{O2} to those of CbA5H^{O2} strongly support the conclusion that the hyperfine couplings observed for CbA5H^{O2} are due to R$^{\bullet ox}$ (see S20).

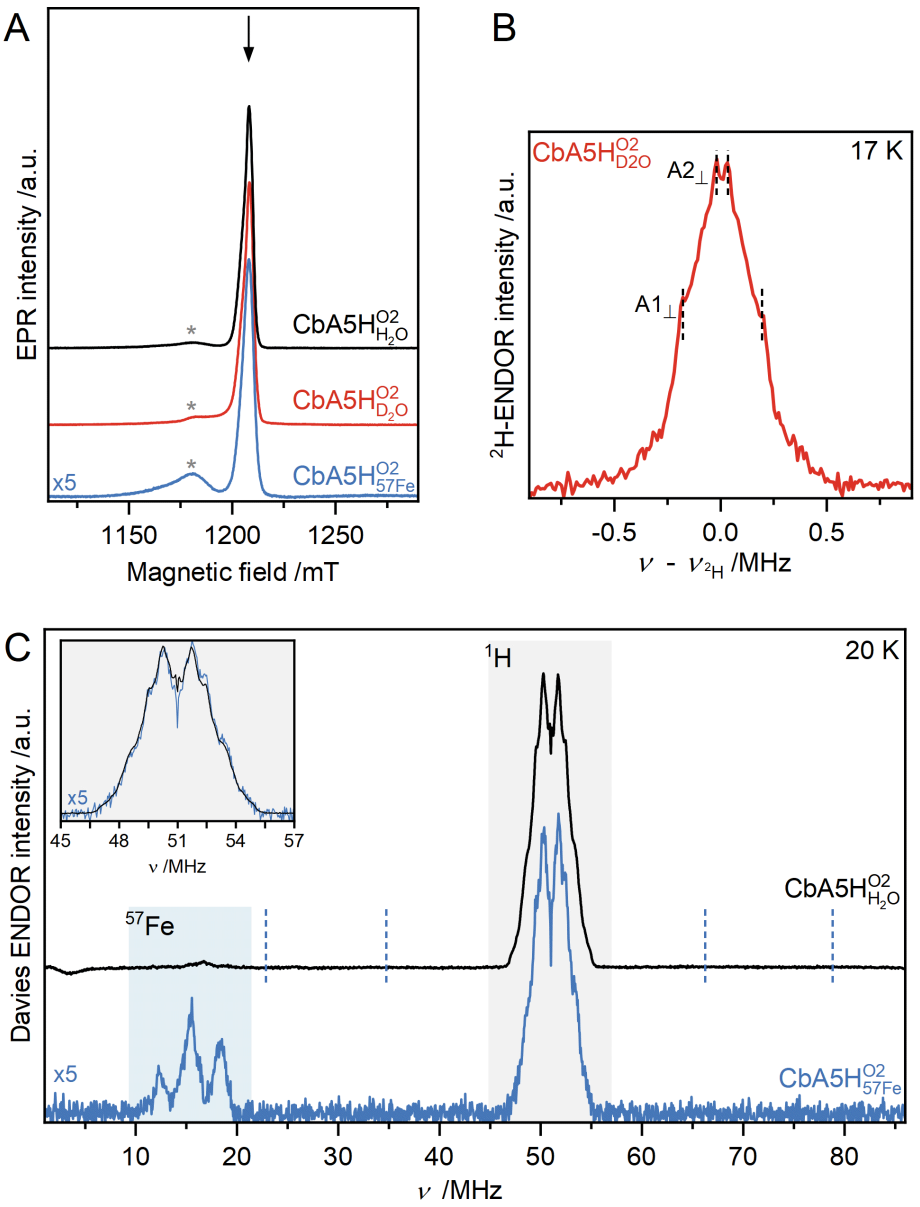

Figure S20. EPR and ENDOR spectra of CbA5H^{O2} in protonated (CbA5H$_{H2O}$) and deuterated (CbA5H$_{D2O}$) buffer and maturated with ^{57}Fe (^{57}Fe-CbA5H) (T = 17/20 K, 34 GHz). The sample of CbA5H$_{H2O}$ had undergone cryo-annealing before the ENDOR experiments (see Figure S5 D). Both CbA5H$_{H2O}$ and CbA5H$_{D2O}$ were subsequently thawed and transferred into 1.6 mm tubes for the ENDOR measurements shown here and in Figure S19. The spectral intensity of ^{57}Fe-CbA5H was multiplied by five in each spectrum. (**A**) ESE-detected EPR spectra (34 GHz, T = 17/20K). The asterisks mark residual H_{ox}-CO and/or resonator impurity signals. The arrow indicates the field position at which the ENDOR spectra were recorded. (**B**) Mims ^{2}H ENDOR spectrum (Q-band, T = 17 K) of CbA5H$_{D2O}$. At least two different couplings are observable as marked by black vertical dashed lines showing the perpendicular components of the hyperfine couplings ($A_\perp$). (**C**) Comparison of Davies ENDOR spectra of CbA5H^{O2} (black trace) and ^{57}Fe-CbA5H^{O2} (blue trace) recorded with a 40 µs RF pulse ranging from 1 to 86 MHz. The inset shows the comparison of hyperfine couplings arising from protons. The almost identical line shapes detected for CbA5H^{O2}, and ^{57}Fe-CbA5H^{O2} show that ^{57}Fe enrichment does not disturb the H-bonding environment and structure of R$^{\bullet ox}$. CbA5H^{O2} does not exhibit strong ^{1}H hyperfine couplings (grey area and inset), which could be associated with tyrosyl and natural DOPA radicals and would be observed at positions marked with vertical dashed blue lines. [37,38] Additionally, the typical ^{14}N hyperfine coupling values observed with natural tryptophanyl radicals are approximately 28 MHz. [39] This coupling would give rise to spectral patterns at $\nu \approx 15$ MHz (blue shaded area). [40] Neither strong ^{1}H nor ^{14}N hyperfine couplings are observed in this spectrum, excluding a typical tyrosyl, DOPA, or tryptophanyl radical as the origin of R$^{\bullet ox}$.

Supporting Discussion on the identity of $R^{\bullet ox}$

Amino-acid-based radicals, e.g., derived from tyrosine, tryptophan, cysteine, and glycine serve as redox centers, generating important metabolites in radical enzymes, such as galactose oxidase ribonucleotide reductase, cytochrome *c* peroxidase, and pyruvate formate-lyase. [41] As the *g*-values of $R^{\bullet ox}$ and its temperature dependence are reminiscent of organic radicals; we investigated whether a redox-active amino acid residue can be the source of the $R^{\bullet ox}$ signal. However, the characteristics of our EPR and UV-vis data conflict with those of typical amino acid radicals. First, the *g*-shifts ($\Delta g_i = g_i - g_e$) of $R^{\bullet ox}$ are too large for a free tyrosyl/modified tyrosyl (natural DOPA or DOPA radical anion), glycyl or tryptophanyl radical but too small to be associated with a thiyl radical. [24,42] Second, distinct peaks related to either tyrosyl or natural DOPA radicals are not observed in the UV-vis spectra of $R^{\bullet ox}$ (Figure S16). Third, ^{1}H Davies ENDOR spectra of $R^{\bullet ox}$ in H_2O and D_2O revealed numerous non-exchangeable proton hyperfine couplings smaller than 10 MHz (Figure S19, the largest hyperfine coupling constant value that is approximately 9 MHz is read between vertical dashed lines). The absence of strong proton and nitrogen hyperfine couplings contrasts the literature data of typical tyrosyl, glycyl, thiyl, and tryptophanyl radicals (Figure S20). [24,43]

Next, we considered sulfur-based radicals because the increased $R^{\bullet ox}$ *g*-anisotropy ($\Delta g = g_3 - g_1 = 13 \cdot 10^{-3}$), usually originating from a large spin-orbit coupling, is indicative of such radicals. [44,45] The *g*-values of $R^{\bullet ox}$ differ from those of disulfide radical anions but agree with *g*-values of sulfinyl or sulfonyl radicals. [44] Similar to $R^{\bullet ox}$, the latter have been observed as reversible intermediates. [46–50] However, the associated proton hyperfine coupling constants are greater than 10 MHz and dominate the line shape at lower frequencies, which is not observed for $R^{\bullet ox}$. Therefore, it is unlikely that $R^{\bullet ox}$ is a typical sulfur-based radical.

Apart from the free amino acid radicals discussed above, several unusual ones have been reported. [41] These include modified amino acids and amino acid radicals having anomalous spectroscopic properties due to their interaction with a close-by metallocofactor. One example is the tryptophan cation radical found in cytochrome *c* peroxidase, namely $Trp191^{\bullet +}$, having a weak exchange coupling with the oxyferryl-heme. [51], [52] Surprisingly, *g*-values of $R^{\bullet ox}$ and $Trp191^{\bullet +}$ are highly similar, and strong ^{14}N hyperfine couplings are absent in both. Yet, the largest proton hyperfine coupling component detected for $Trp191^{\bullet +}$ is higher than that of $R^{\bullet ox}$ (ca. 20 MHz *vs.* 9 MHz).

Last, we note that the reversibility of $R^{\bullet ox}$, and its ENDOR spectrum, showing various proton hyperfine couplings, exclude the possibility of a peroxyl radical. In addition, a semiquinone radical is highly unlikely as the *g*-shifts observed for this radical are remarkably small compared to those of $R^{\bullet ox}$.

References

[1] S. Stoll and A. Schweiger, J. Magn. Reson. **178**, 42 (2006).

[2] M. K. Akhtar and P. R. Jones, Appl. Microbiol. Biotechnol. **78**, 853 (2008).

[3] J. M. Kuchenreuther, C. S. Grady-Smith, A. S. Bingham, S. J. George, S. P. Cramer, and J. R. Swartz, PLoS One **5**, 4 (2010).

[4] M. Bradford, Anal. Biochem. **72**, 248 (1976).

[5] U. K. Laemmli, Nature **227**, 680 (1970).

[6] P. S. Corrigan, J. L. Tirsch, and A. Silakov, J. Am. Chem. Soc. **142**, 12409 (2020).

[7] H. Li and T. B. Rauchfuss, J. Am. Chem. Soc. **124**, 726 (2002).

[8] J. Esselborn et al., Nat. Chem. Biol. **9**, 607 (2013).

[9] D. W. Mulder, Y. Guo, M. W. Ratzloff, and P. W. King, J. Am. Chem. Soc. **139**, 83 (2017).

[10] G. Rao and R. D. Britt, Inorg. Chem. **57**, 10935 (2018).

[11] A. Adamska, A. Silakov, C. Lambertz, O. Rüdiger, T. Happe, E. Reijerse, and W. Lubitz, Angew. Chemie - Int. Ed. **51**, 11458 (2012).

[12] H. Land, M. Senger, G. Berggren, and S. T. Stripp, ACS Catal. **10**, 7069 (2020).

[13] S. P. J. Albracht, W. Roseboom, and E. C. Hatchikian, J. Biol. Inorg. Chem. **11**, 88 (2006).

[14] H. J. Grande, W. R. Dunham, B. Averill, C. Dijk, and R. H. Sands, Eur. J. Biochem. **136**, 201 (1983).

[15] W. R. Hagen, A. van Berkel-Arts, K. M. Krüse-Wolters, W. R. Dunham, and C. Veeger, FEBS Lett. **201**, 158 (1986).

[16] D. S. Patil, S. H. He, J. J. G. Mouras, N. Ravi, D. V. DerVartanian, H. D. Peck, J. LeGall, and B. H. Huynh, J. Inorg. Biochem. **36**, 251 (1989).

[17] B. Bennett, B. J. Lemon, and J. W. Peters, Biochemistry **39**, 7455 (2000).

[18] G. Caserta, A. Adamska-Venkatesh, L. Pecqueur, M. Atta, V. Artero, S. Roy, E. Reijerse, W. Lubitz, and M. Fontecave, Biochim. Biophys. Acta - Bioenerg. **1857**, 1734 (2016).

[19] R. Cammack, *Iron—Sulfur Clusters in Enzymes: Themes and Variations*, in *Advances in Inorganic Chemistry*, Vol. 38 (1992), pp. 281–322.

[20] H. Rupp, K. K. Rao, D. O. Hall, and R. Cammack, Biochim. Biophys. Acta - Protein Struct. **537**, 255 (1978).

[21] M. Atta, M. E. Lafferty, M. K. Johnson, J. Gaillard, and J. Meyer, Biochemistry **37**, 15974 (1998).

[22] T. Liu, B. Li, M. L. Singleton, M. B. Hall, and M. Y. Darensbourg, J. Am. Chem. Soc. **131**, 8296 (2009).

[23] K. D. Swanson et al., J. Am. Chem. Soc. **137**, 1809 (2015).

[24] G. Jeschke, Biochim. Biophys. Acta - Bioenerg. **1707**, 91 (2005).

[25] N. Chongdar, K. Pawlak, O. Rüdiger, E. J. Reijerse, P. Rodríguez-Maciá, W. Lubitz, J. A. Birrell, and H. Ogata, J. Biol. Inorg. Chem. (2019).

[26] M. L. Antonkine, M. S. Koay, B. Epel, C. Breitenstein, O. Gopta, W. Gärtner, E. Bill, and W. Lubitz, Biochim. Biophys. Acta - Bioenerg. **1787**, 995 (2009).

[27] P. Rodríguez-Maciá, K. Pawlak, O. Rüdiger, E. J. Reijerse, W. Lubitz, and J. A. Birrell, J. Am. Chem. Soc. **139**, 15122 (2017).

[28] M. Winkler et al., Nat. Commun. **12**, 756 (2021).

[29] J. A. Imlay, Mol. Microbiol. **59**, 1073 (2006).

[30] J. Telser, H.-I. Lee, and B. M. Hoffman, J. Biol. Inorg. Chem. **5**, 369 (2000).

[31] S. Agarwalla, R. M. Stroud, and B. J. Gaffney, J. Biol. Chem. **279**, 34123 (2004).

[32] M. Saggu, I. Zebger, M. Ludwig, O. Lenz, B. Friedrich, P. Hildebrandt, and F. Lendzian, J. Biol. Chem. **284**, 16264 (2009).

[33] M. T. Pellicer Martinez, J. C. Crack, M. Y. Y. Stewart, J. M. Bradley, D. A. Svistunenko, A. W. B. Johnston, M. R. Cheesman, J. D. Todd, and N. E. Le Brun, Elife **8**, 1 (2019).

[34] W. R. Hagen, *EPR Spectroscopy of Iron—Sulfur Proteins*, in *Advances in Inorganic Chemistry*, Vol. 38 (1992), pp. 165–222.

[35] R. Gilbert-Wilson, J. F. Siebel, A. Adamska-Venkatesh, C. C. Pham, E. Reijerse, H. Wang, S. P. Cramer, W. Lubitz, and T. B. Rauchfuss, J. Am. Chem. Soc. **137**, 8998 (2015).

[36] A. Silakov, E. J. Reijerse, S. P. J. Albracht, E. C. Hatchikian, and W. Lubitz, J. Am. Chem. Soc. **129**, 11447 (2007).

[37] V. Srinivas et al., Nature **563**, 416 (2018).

[38] S. L. Meichsner, Y. Kutin, and M. Kasanmascheff, Angew. Chemie - Int. Ed. **60**, 19155 (2021).

[39] R. Pogni, M. C. Baratto, C. Teutloff, S. Giansanti, F. J. Ruiz-Dueñas, T. Choinowski, K. Piontek, A. T. Martínez, F. Lendzian, and R. Basosi, J. Biol. Chem. **281**, 9517 (2006).

[40] S. M. Musser, Y.-C. Fann, R. J. Gurbiel, B. M. Hoffman, and S. I. Chan, J. Biol. Chem. **272**, 203 (1997).

[41] J. A. Stubbe and W. A. Van Der Donk, Chem. Rev. **98**, 705 (1998).

[42] S. Stoll, *High-Field EPR of Bioorganic Radicals*, in *Electron Paramagnetic Resonance*, Vol. 22 (Royal Society of Chemistry, 2011), pp. 107–154.

[43] M. van Gastel, W. Lubitz, G. Lassmann, and F. Neese, J. Am. Chem. Soc. **126**, 2237 (2004).

[44] N. Babaei Bidmeshki, Y. T. Azar, F. Ziaie, and M. Janbazi, Phys. Chem. Chem. Phys. **23**, 6815 (2021).

[45] S. G. Swarts, D. Becker, S. DeBolt, and M. D. Sevilla, J. Phys. Chem. **93**, 155 (1989).

[46] A. Adrait, M. Öhrström, A.-L. Barra, L. Thelander, and A. Gräslund, Biochemistry **41**, 6510 (2002).

[47] S. G. Reddy, K. K. Wong, C. V. Parast, J. Peisach, R. S. Magliozzo, and J. W. Kozarich, Biochemistry **37**, 558 (1998).

[48] G. Lassmann, M. Kolberg, G. Bleifuss, A. Gräslund, B.-M. Sjöberg, and W. Lubitz, Phys. Chem. Chem. Phys. **5**, 2442 (2003).

[49] M. D. Sevilla, D. Becker, and M. Yan, Int. J. Radiat. Biol. **57**, 65 (1990).

[50] M. Kolberg, G. Bleifuss, B.-M. Sjöberg, A. Gräslund, W. Lubitz, F. Lendzian, and G. Lassmann, Arch. Biochem. Biophys. **397**, 57 (2002).

[51] M. Sivaraja, D. B. Goodin, M. Smith, and B. M. Hoffman, Science **245**, 738 (1989).

[52] A. L. P. Houseman, P. E. Doan, D. B. Goodwin, and B. M. Hoffman, Biochemistry **32**, 4430 (1993).

7

On the Tracks of the Radical Signal $R^{\bullet ox}$

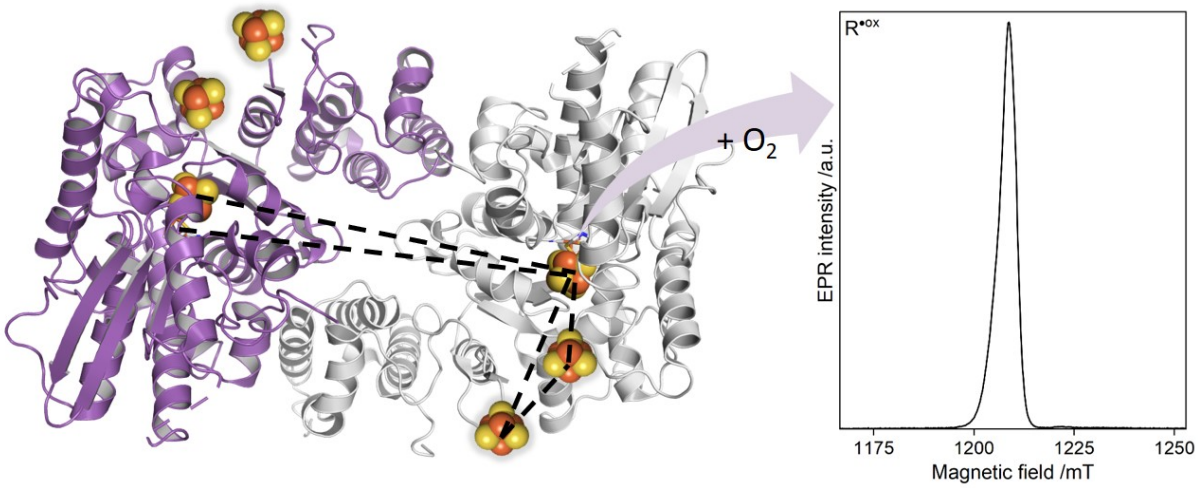

The results presented in Chapter 6 revealed an unprecedented radical signal, termed $R^{\bullet ox}$, which dominates under oxidizing conditions in the oxygen-resistant [FeFe]-hydrogenase CbA5H. The spectral properties of $R^{\bullet ox}$ are different from any identified species thus far and lack evidence for typical organic radicals or iron-sulfur clusters. The obtained hyperfine coupling constants disagree with single [4Fe4S] clusters but are very similar to other H-cluster states, especially H_{ox}-CO. Notably, almost no spectral FTIR or EPR features associated with H_{ox}-CO were observed under oxidizing conditions in this study. Although the spin density distribution of $R^{\bullet ox}$ strongly resembled the H_{ox}-CO state, the absence of corresponding FTIR vibrations prevented a definite assignment of $R^{\bullet ox}$ as a new H-cluster state. Here, the investigation of CbA5H and $R^{\bullet ox}$ is continued to address the open questions. A redox potentiometry of apo-CbA5H is performed to determine the midpoint potentials of the accessory FeS clusters. Moreover, knockout variants of each one of the F-clusters provide an insight into the inter-cluster exchange coupling and the F-cluster's influence on the formation of $R^{\bullet ox}$. The investigation of pH-dependent samples and the (almost) inactive variants C367A and C367D is employed to elucidate the conditions for and mechanism of $R^{\bullet ox}$ formation in dependence of pH, H_2, O_2, and CO-treatment. Eventually, DEER spectroscopy is applied to investigate the distances of $R^{\bullet ox}$ and other species in the two subunits of the dimeric enzyme.

Notably, an only recently published study proposes that $R^{\bullet ox}$ is a CO-bound H-clusters state, similar to H_{ox}-CO, which exhibits distinct spectroscopic properties due to structural perturbation of the protein environment.[311] As the following experiments were performed without this knowledge, the last section evaluates these findings and puts them into context with the here presented results.

7.1 Sample Preparations and Measurement Conditions of CbA5H

The [FeFe]-hydrogenase CbA5H from *C. beijerinckii* was expressed, purified and prepared by Andreas Rutz and Feng Zheng by the Biotechnology AG, Ruhr-University Bochum, as described in Chapter 6 and Rutz et al. [231]. Table 7.1 presents an overview of the distinct sample preparations provided in 2.8 mm quartz tubes. If not stated otherwise, EPR spectra of the frozen sample solutions were recorded as described in Chapter 6.

Table 7.1: Overview of the distinct sample preparations of CbA5H and its variants with their respective abbreviations (marked in bold), protein concentrations, appearances in figures and presence of Rox indicated.

Sample	Concentration µM	Figure(s)	$R^{\bullet ox}$ present
ΔFS4A: C232A C232A + H_2; C232A + H_2, + O_2	170	7.2, 7.3	✓
ΔFS4B: C225A C225A + H_2; C225A + H_2, + O_2	300	7.2, 7.3	✓
CbA5H^{H_2} (pH6) CbA5H + H_2	130	7.4	distinct signal
CbA5H^{O_2} (pH6) CbA5H + H_2, + O_2	130	7.4	-
CbA5H^{H_2} (pH9) CbA5H + H_2	180	7.4	✓
CbA5H^{O_2} (pH9) CbA5H + H_2, + O_2	180	7.4	✓
aerobically isolated CbA5H^{H_2} CbA5H + H_2	970	7.2, 7.3, 7.4	✓
aerobically isolated CbA5H^{O_2} CbA5H + H_2, + O_2	970	7.2, 7.3, 7.4, 7.6	✓
C367D^{H_2} C367D + H_2	347	7.5	✓
C367D^{O_2} C367D + H2, + O2	347	7.5	✓
C367D^{CO} C367D + H_2, + O_2	347	7.5	✓
C367A^{H_2} C367A + H_2	267	7.5	-
C367A^{O_2} C367A + H_2, + O_2	267	7.5	✓
C367A^{CO} C367A + H_2, + CO	267	7.5	-
apo-CbA5H^{H_2} apo-CbA5H + H_2	730	7.2	-
apo-CbA5H^{O_2} CbA5H + H_2, + O_2	730	7.3	-
CbA5H^{NaDT} CbA5H + 10 mM NaDT , + 5 % glycerol	530	7.6	✓
CbA5H^{air} CbA5H + 10 mM NaDT, + air, 5 % glycerol	530	7.6	✓

Redox Potentiometry of apo-CbA5H

The redox potentiometry of apo-CbA5H was performed anaerobically with a final concentration of 200 µM protein and 100 µM redox mediator dyes at room temperature. All herein reported potentials are corrected for the standard hydrogen electrode. After the reaction mixture poised at a potential of -258 mV a first sample was taken. Next, the reaction mixture was reduced with NaDT to a potential of -402 mV and gradually oxidized with FIC to a final potential of -54 mV. Meanwhile every ~ 50 mV a sample was transferred to an EPR tube and immediately frozen in liquid nitrogen. Finally, the sample solution was rereduced with NaDT to a potential of -430 mV, where a sample was taken. The samples were measured with ESE-detected field-sweep experiments with the resonator in the overcoupled mode at 10 K and Q-band frequencies.

DEER Spectroscopy on CbA5H

Preliminary DEER experiments on three distinct samples were performed by myself at one magnetic field position at 20 K. Orientation-selective DEER experiments were performed by Dörte Brandis during the course of her master thesis under my supervision.[312] The respective measurement parameters and details can be found therein.

7.2 Results and Discussion

The following sections provide further insights into the formation and origin of $R^{\bullet ox}$.

7.2.1 Redox Potentiometry Indicates Similar Redox Potentials for F-clusters

To determine the midpoint potentials of the accessory FeS clusters, a redox potentiometry was performed on the catalytically inactive apo-CbA5H lacking the $[2Fe]_H$ subcluster. The use of an inactive hydrogenase (i) facilitates the analysis due to the absent H-cluster states and (ii) prevents catalytic turnover during the potentiometry, which would distort the equilibrium conditions. The $[4Fe]_H$ cluster, however, is expected to be paramagnetic under reducing conditions as well. For the redox potentiometry of apo-CbA5H, samples were taken at potentials between −54 and −430 mV. Previous quantitative EPR experiments were performed with the resonator in the critically coupled mode to ensure the reproducibility of the spin concentration (see also Chapter 3). As the present samples exhibited a very low spin concentration the overcoupled mode was used.

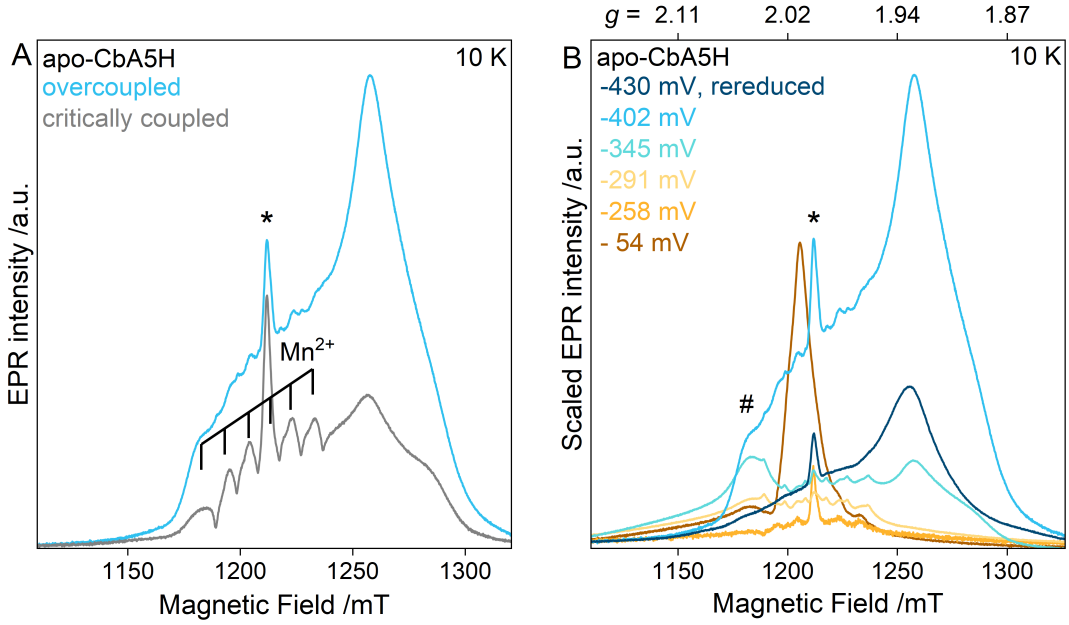

Figure 7.1: ESE-detected EPR spectra ($T = 10$ K, 34 GHz) of redox potentiometry samples of apo-CbA5H poised at distinct potentials. (**A**) Comparison of EPR spectra of a sample poised at -402 mV recorded with the resonator in the overcoupled mode (blue trace) and critically coupled mode (black trace). Background impurities arise from the mediator mix and/or NaDT (marked by an asterisk) and Mn^{2+} as indicated. **(B)** EPR spectra of redox potentiometry samples were scaled for better comparison of their line shapes. The signal arising from the resonator background is marked with a hash sign.

A comparison between both resonator modes is shown in Figure 7.1A, where the spectrum recorded in the overcoupled mode displays a significantly higher signal intensity due to the lower inter-pulse delay of $\tau = 220$ *versus* 650 ns. A longer inter-pulse delay is necessary for the critically coupled mode to circumvent the longer dead time arising from the higher power pulses. Additionally, the hyperfine splitting of Mn^{2+} ($I = 5/2$) in six resonance lines, as well as the impurity arising at $g \approx 2.02$ from the redox mediator dyes and/or NaDT (marked by an asterisk), are less pronounced in comparison to the spectrum recorded with a critically coupled resonator. As the signal intensity is not reproducible with this overcoupled resonator, the spin

concentrations of the redox potentiometry samples can not be sufficiently quantified. Therefore, the following analysis only deals with the spectral features of the recorded EPR spectra and approximates the midpoint potentials.

For comparison of the line shape of the low potential samples, the spectra were scaled for better visualization (Figure 7.1). Under most reductive conditions, at potentials between -430 and -345 mV, a rhombic signal is present around $g_2 = 1.93$, which is attributed to one or more reduced [4Fe4S] clusters. None of the spectra share the same g-values, but the high agreement indicates the presence of similar cluster environments, e.g., an all-cysteine coordination. Moreover, exchange interactions between the clusters observed in Chapter 6 hint at intersecting E_ms and further impede the analysis. The presence of exchange interactions is furthermore supported by broadened features at the outer edges of the spectra. With increasing potentials, from -291 mV up to -101 mV (trace not shown), no signal but the background is observed. Only again at -54 mV a new isotropic signal at $g \approx 2.02$ arises, that can be simulated with $g = 2.029$, 2.015, 2.000 and is assigned to a [3Fe4S] cluster. Measurements at higher temperatures excluded the presence of $R^{\bullet ox}$ in apo-CbA5H, as was shown in Chapter 6. The intensity of the rereduced sample, however, is significantly lowered compared to the sample taken at -430 mV, indicating that a substantial amount of clusters degraded during the potentiometry or due to oxidative treatment. This observation emphasizes one of the disadvantages of prolonged redox titrations at room temperature.

Overall, the midpoint potential for the present [4Fe4S] clusters is estimated to $E_\mathrm{m} \leq -350$ mV, which agrees with [4Fe4S] cluster potentials.[313] Moreover, no further species, but degraded [3Fe4S] clusters were observed at higher potentials. For the deconvolution of the involved clusters and determination of their midpoint potentials a renewed redox potentiometry with higher amounts of paramagnetic clusters and exclusion of manganese is necessary. Especially in hindsight of expected inter-cluster exchange interactions, more frequent withdrawal of samples in a narrower potential range is required for an accurate analysis.

7.2.2 Site-Directed Mutagenesis of F-clusters and Their Impact on $R^{\bullet ox}$ Formation

Next, the impact of the accessory FeS clusters FS4A and FS4B on the activity, magnetic properties of CbA5H, and the formation of $R^{\bullet ox}$ was investigated. Therefore, one of the four ligating cysteine residues was exchanged for alanine for each F-cluster (ΔFS4A: C232A, ΔFS4B: C225A). The resulting variants lack the respective cluster as confirmed by inductively coupled plasma atomic emission spectroscopy (ICP-AES) measurements, showing a loss of each three to four Fe ions in comparison to the wild-type enzyme.[231]

Pulsed EPR spectra of the H_2-treated variants in comparison to the wild-type enzyme and apo-CbA5H are presented in Figure 7.2A. The spectra of both variants exhibit distinct features in the FeS cluster region around $g = 1.93$ compared to the wild-type enzyme, which is attributed to the respective [4Fe4S] cluster-loss. The lower signal intensity of ΔFS4B in the FeS cluster region compared to ΔFS4A may be traced back to FS4B's location in the protein: FS4B is expected to be the entry point for electrons to the H-cluster, which is why the (complete) reduction of FS4A may be prevented by the lack of FS4B.

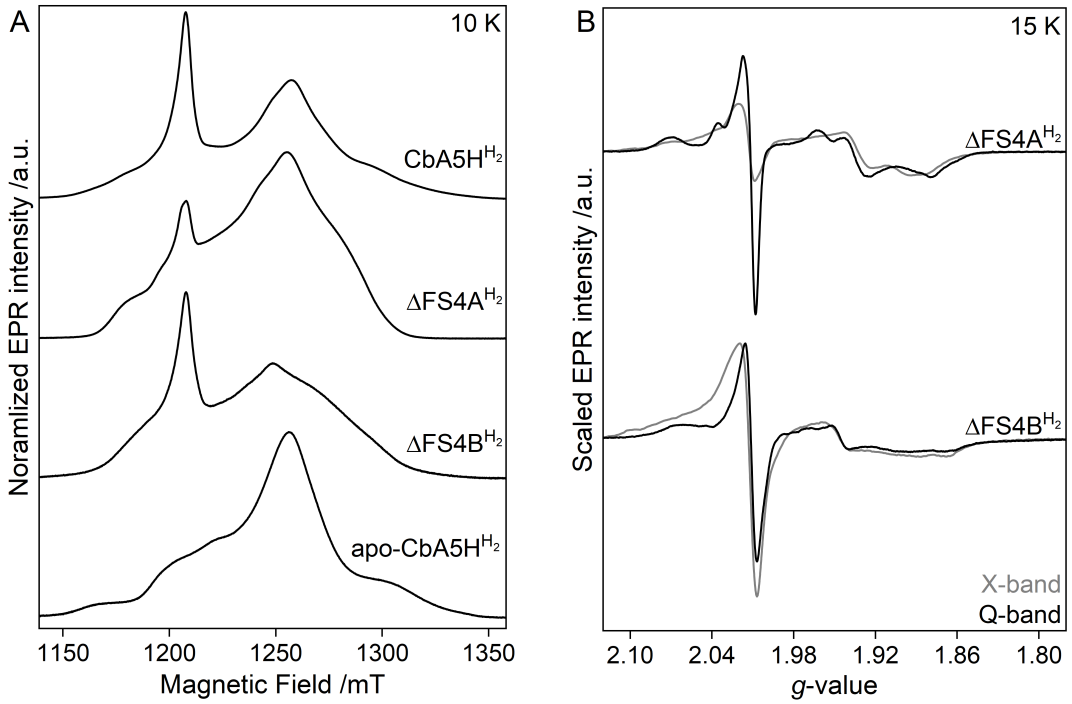

Figure 7.2: ESE-detected EPR spectra ($T = 10\,\mathrm{K}$, 34 GHz) of (**A**) H_2-treated holo-CbA5H, the variants ΔFS4A/B and apo-CbA5H normalized to their maximum signal amplitude. (**B**) Pseudo-modulated spectra of the H_2-treated variants ΔFS4A/B in comparison to CW EPR spectra ($T = 15$ K, 9.5 GHz, grey traces) plotted on a common g-value axis and scaled to the maximum intensity of the FeS cluster region around $g = 1.93$.

Multi-frequency EPR spectra recorded at the X- and Q-band are slightly distinct for ΔFS4A (Figure 7.2B). Distinct spectral features recorded at two microwave frequencies are an indicator for exchange coupling interactions between two or more closely spaced (approximately $\leq 12\,\text{Å}$) paramagnetic species,[252] as is evident for CbA5H.[123] The strength of the exchange coupling is independent of the magnetic field, but gains relative importance at lower frequencies when the field-dependent electron Zeeman interactions appear smaller on the g-value scale.[255] Loss of the proximal FS4A cluster is expected to dissolve any exchange coupling interactions, as the inter-cluster distance between the H-cluster and FS4B is now significantly greater than 12 Å.[123] Thus, the apparent changes in the FeS cluster region are not attributed to exchange interactions between the H-cluster and FS4B but might arise from the distinct measurement conditions (CW, 15 K *versus* pulsed EPR, 10 K) and thus, different relaxation properties of the clusters and H-cluster states. The application of different powers and temperatures at the X-band might resolve this issue. The EPR spectra of ΔFS4B show no frequency dependency in the FeS cluster region, which suggests that no significant exchange coupling occurs between FS4A and the H-cluster, but rather between FS4A and FS4B as was shown for holo- and apo-CbA5H in Chapter 6. In contrast, a broadening in the H-cluster and $R^{\bullet ox}$ region at $g \geq 2$ is more prominent in ΔFS4B than in ΔFS4A. This observation, however, could be caused by an exchange interaction between $R^{\bullet ox}$ or the H-cluster states and FS4A. The involvement of additional H-cluster states, such as H_{hyd} in the FeS region, and expected exchange interactions prevented the spectral simulation with universal g-values for all species.

Interestingly, the H_{ox} state is absent in both variants, which was further confirmed by FTIR measurements, where the H_{hyd}, $H_{red}H^+$, and residual amounts of the H_{ox}-CO state were observed.[231]

Concomitantly, the hydrogen production activity is severely impaired by approximately 95 % in the two variants,[231] indicating that the presence of both F-clusters is essential for the electron transfer to and from the H-cluster and consequently for effective hydrogen turnover. Nevertheless, both variants show a quantitative accumulation of H_{inact} under oxygen exposure and can undergo several cycles of reductive activation and oxidative inactivation, as evidenced by FTIR data.[231] The stability of the (partially) cluster-less variants in the H_{inact} state in conjunction with multiple reactivation cycles indicate that the accessory clusters are not involved in the sensing of oxidative conditions. Notably, temperature-dependent EPR spectra revealed the presence of $R^{\bullet ox}$ in the H_2-treated variants as well (see below).

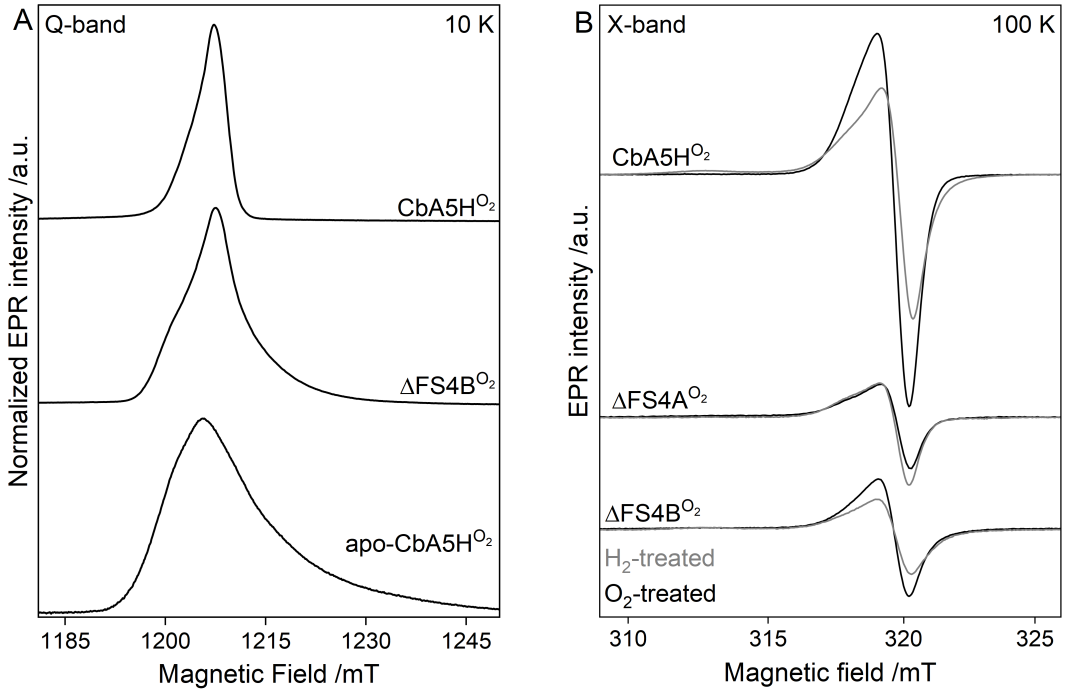

Figure 7.3: EPR spectra of O_2-treated holo-CbA5H, the variants ΔFS4A/B and apo-CbA5H recorded with (**A**) ESE-detected EPR (T = 10 K, 34 GHz) and normalized to their maximum signal amplitude and (**B**) CW EPR (T = 100 K, 9.5 GHz) in comparison to spectra of H_2-treated samples (grey traces) normalized to their protein concentration.

Next, the O_2-treated variants were compared to holo and apo-CbA5H (Figure 7.3). Note, that the sample preparation of ΔFS4A prevented the measurement at Q-band frequencies, presumably due to a low spin concentration. The spectrum of ΔFS4B recorded at 10 K (Figure 7.3A) represents a mixture of $R^{\bullet ox}$ and [3Fe4S] clusters. At elevated temperatures (Figure 7.3B) both variants exhibit $R^{\bullet ox}$ in the H_2- and O_2-treated states but no significant accumulation of H_{ox}-CO. This observation excludes both [4Fe4S] clusters as the origin of $R^{\bullet ox}$ as otherwise, a complete signal loss of $R^{\bullet ox}$ in either variant would have been expected. Additionally, both cluster knockouts do not influence $R^{\bullet ox}$'s line shape, indicating a certain distance between paramagnetic centers. The fivefold decreased signal intensity of the variants in comparison to the wild-type enzyme can possibly be traced back to the reduced activity of the variants and is in conjunction with the necessity of an active H-cluster for the formation of $R^{\bullet ox}$, as was shown in Chapter 6. Notably, $R^{\bullet ox}$'s intensity does not or only little increase upon oxidation in ΔFS4A and ΔFS4B, respectively. This observation is in contrast to the wild-type enzyme, where a three- to fivefold increase of $R^{\bullet ox}$ upon oxidation was observed. The cause for the lack of this increase remains elusive, but might be in conjunction with the reduced enzyme activity.

Overall, both variants exhibit different redox states in comparison to the wild-type enzyme and significantly reduced activity, showing that each accessory [4Fe4S] cluster is necessary for effective hydrogen turnover. Multi-frequency spectra revealed only minor inter-cluster exchange interactions, indicating that most of the exchange interaction arises from interactions between FS4A and FS4B. Moreover, the formation of $R^{\bullet ox}$ is observed in both variants and thus excludes both F-clusters to be the origin of $R^{\bullet ox}$ or influence its spectral line shape. It moreover excludes, that either of the clusters is responsible for the sensing of oxidative conditions leading to the formation of the H_{inact} state. Only the three- to fivefold increase of $R^{\bullet ox}$'s intensity after O_2 treatment is impaired and might provide a hint on the mechanism of $R^{\bullet ox}$ formation. Interestingly, only residual contributions of the H_{ox}-CO state were observed in FTIR and EPR spectral data, highlighting again the distinct emergence of $R^{\bullet ox}$ and H_{ox}-CO.

7.2.3 Insights Into the pH-Dependency of $R^{\bullet ox}$ Formation

CbA5H was shown to convert almost completely into the H_{inact} state when in buffer with pH 6, as evidenced by FTIR spectral data (personal communication with A. Rutz and shown by a recent study[311]). This observation is in line with the low $H_{ox}-H_{inact}$ midpoint potential determined previously.[124] To probe the effects of pH on the formation of $R^{\bullet ox}$, H_2 and O_2-treated samples of CbA5H were prepared in buffer with distinct pH values (simply denoted pH X in the following) and recorded at elevated temperatures (Figure 7.4).

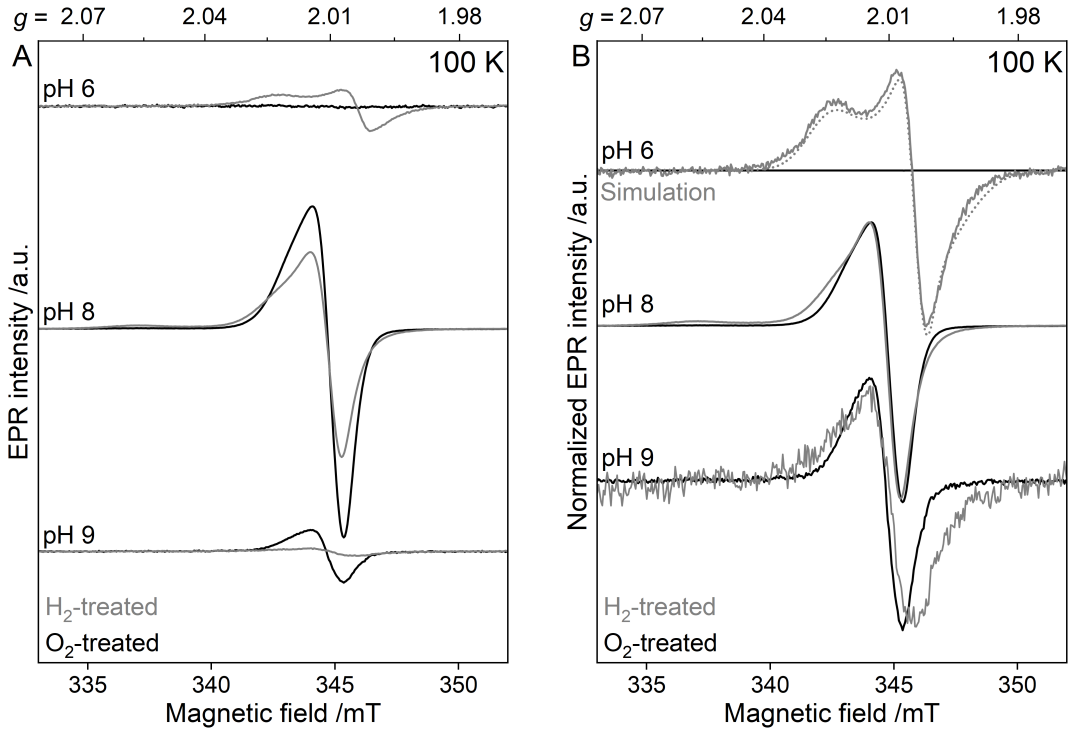

Figure 7.4: CW EPR spectra (T = 100 K, 9.7 GHz) of H_2- and O_2-treated CbA5H in buffers with distinct pH values (**A**) normalized to their protein concentration and (**B**) normalized to their maximum intensity. The simulation of the H_2-treated pH 6 sample is shown as gray dotted trace.

The presence of $R^{\bullet ox}$ was observed in pH 8 and pH 9 samples, whereas its signature is absent in the pH 6^{O_2} sample. Intriguingly, in the pH 6^{H_2} sample a signal with a distinct spectral line shape compared to $R^{\bullet ox}$ is observed. The species can be simulated with $g = 2.024, 2.003, 1.997$.

As a result, the average g-value is decreased from 2.012 ($R^{\bullet ox}$) to 2.008 (pH 6), whereas the g-value range doubles from 0.013 to 0.027, respectively. (Figure 7.4B). Both, the pH 6 and pH 9 samples exhibit a lower signal intensity compared to the wild-type enzyme. The pH 6^{H_2} sample has approximately 40 % lower spin concentration compared to $R^{\bullet ox}$ at pH 8^{H_2}, whereas pH 9^{H_2} has a reduced spin concentration of only 8 %. The latter increases threefold by treatment with O_2 in agreement with the signal intensity increase of the pH 8 samples. Notably, the spectral line shape of pH 9^{H_2} is slightly different compared to $R^{\bullet ox}$, but difficult to analyze due to the low signal intensity.

In the case of pH 6^{H_2}, where the enzyme is thought to be mainly in the H_{inact} state, a novel species, resembling $R^{\bullet ox}$, is observed. The changed line shape is first considered to be caused by the low pH. The acidic conditions may result in the protonation of nearby residues, such as the coordinating C367, and in turn, alter the electronic properties of $R^{\bullet ox}$. The protonation of $[4Fe]_H$ is excluded based on the unchanged FTIR spectral signature, where a concomitant shift of vibrational bands would be anticipated.[173,311] A comparison of the EPR and ENDOR spectra of pH 6^{H_2} in protonated and deuterated buffer may illuminate the occurrence of a protonation event in the vicinity of $R^{\bullet ox}$.

A second hypothesis is based on the assumption, that $R^{\bullet ox}$ is a yet unidentified H-cluster state, with a ligand bound at Fe_d and focused on the order of oxidation and reduction events, that previously led to the observation of $R^{\bullet ox}$. Usually, as-isolated CbA5H was treated with H_2 and subsequently O_2 to yield a substantial amount of $R^{\bullet ox}$. However, when in pH 6 buffer, the as-isolated enzyme transforms immediately to the H_{inact} state, and thereby, the initial H_2 reduction step is omitted. Moreover, the open coordination site is expected to be mainly blocked by the coordinating C367 residue. This observation is in agreement with the low signal intensity of pH 6^{H_2}. The subsequent H_2- and O_2-treatments leave the composition of H-cluster states unchanged, as is evident from accompanying FTIR data (personal communication with A. Rutz). The signal from the $R^{\bullet ox}$ like species, however, vanishes upon further oxidation. On that basis, it is assumed that the species is replaced by C367. Such a displacement, however, has not been observed in the previous sample preparations and may be explained by the duration of oxidation or in the case of pH 6 the time of the enzyme being in the H_{inact} state. Therefore, it would be interesting to investigate the time-dependent formation of $R^{\bullet ox}$ under O_2. Furthermore, no sample preparation of $R^{\bullet ox}$ omitting initial H_2 reduction before O_2 oxidation was investigated by EPR spectroscopy yet. Thus, a preparation of the as-isolated sample of pH 6 and an as-isolated sample treated with O_2 may further elucidate the mechanism and conditions for $R^{\bullet ox}$ formation.

7.2.4 Variants of CbA5H Show That $R^{\bullet ox}$ is Dependent on Oxidation

The H_{inact} formation in CbA5H was shown to be dependent on the presence of the proximal cysteine residue C367 by two variants, where the cysteine residue was exchanged to alanine (C367A) or aspartic acid (C367D).[123] The C367A variant was shown to be inactive, while C367D retains approximately 20 % H_2 production activity, which can be traced back to an impaired proton transfer pathway.[123,162,173] Both variants prevent H_{inact} formation and degrade under aerobic conditions, whereas residual vibrational bands associated with H_{ox} and H_{ox}-CO were observed for C367D after 15 min.[123] As presented in Chapter 6, C367D revealed the presence

of $R^{\bullet ox}$ under O_2-treatment, but exhibited a slightly perturbed line shape indicating that the amino acid exchange occurs in the vicinity of $R^{\bullet ox}$. To further probe the influence of O_2- and CO-treatment on the formation of $R^{\bullet ox}$ in the absence of the H_{inact} state, the H_2-treated variants C367D and C367A were further treated with O_2 or CO.

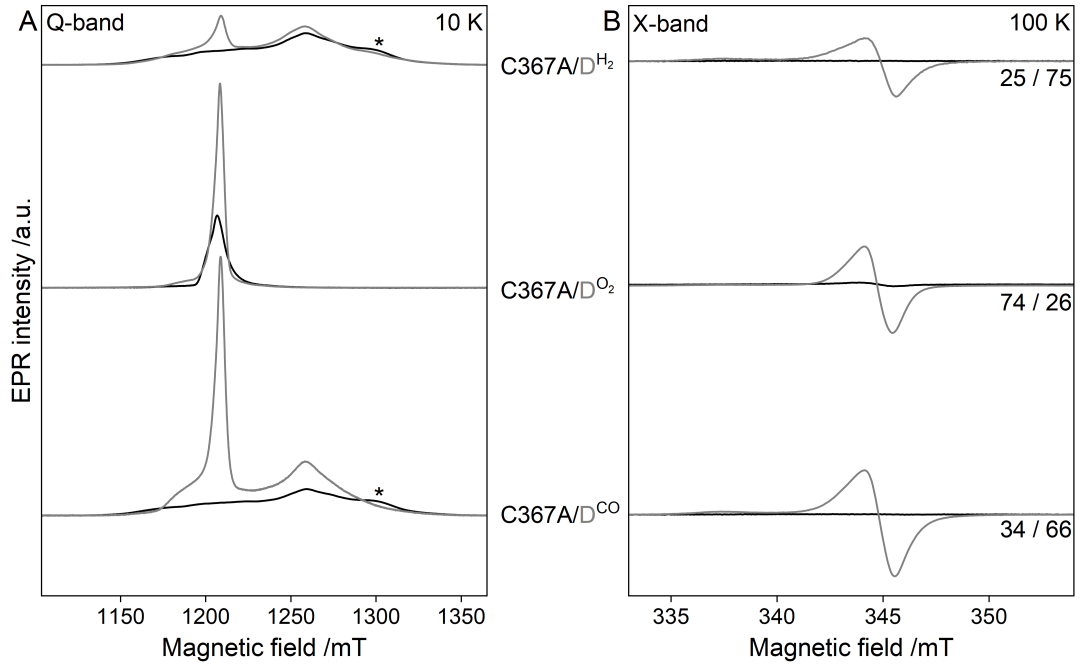

Figure 7.5: EPR spectra of CbA5H variants C367A (black traces) and C367D (gray traces) sequentially treated with H_2-, and either O_2- or CO recorded with (**A**) ESE-detected EPR ($T = 10$ K, 34 GHz) and (**B**) CW EPR ($T = 100$ K, 9.7 GHz). The ratio of $R^{\bullet ox}$ to H_{ox}-CO in C367D obtained from spectral simulations is given on the right. Asterisks mark $g = 1.86$ associated with the H_{hyd} state.

Under H_2 atmosphere, the spectrum of C367D presented in Figure 7.5A reveals a spectrum similar to the wild-type enzyme (compare Chapter 6) at lower temperatures. The presence of $R^{\bullet ox}$* is unambiguously shown at elevated temperatures (see Figure 7.5B and Chapter 6). The following spin concentrations were determined from the spectra recorded at 100 K. While the treatment with O_2 results in a 1.4-fold increase of the overall signal intensity, the CO-treatment increases the overall spin concentration 2.5-fold. Interestingly, the ratio of $R^{\bullet ox}$ to H_{ox}-CO (indicated on the right in Figure 7.5B) increases with O_2, but remains similar under CO. This indicates, that $R^{\bullet ox}$ formation occurs under O_2- and CO-treatment but is favored under oxidizing conditions, where the relative intensity of H_{ox}-CO decreases.

In contrast to C367D, the C367A variant shows almost no signal arising from $R^{\bullet ox}$ or H_{ox}-CO in any of the reduced (H_2, or H_2 +CO) sample preparations, as is evident from the spectra recorded at 100 K (Figure 7.5B). At lower temperatures, the presence of F-clusters and H_{hyd} is detected in the reduced samples, whereas only [3Fe4S] clusters were observed in the oxidized sample. These observations are in agreement with the literature, where a C169A variant of *Cr*HydA1 (C367 in CbA5H) revealed 90 % H_{ox}-O_2 and 85 % H_{hyd} under H_2- and air treatment, respectively.[173] The accumulation of both states is attributed to the impaired proton transfer pathway, that prevents protonation of the amine of the adt bridgehead. Moreover, the open coordination site is suggested to be occupied in H_{ox}-O_2 by O_2, which prevents the binding of external molecules. The H_{ox}-O_2 state is suggested to be EPR silent in conjunction with the present results.[173] Thus, the absence of H_{ox}-CO or $R^{\bullet ox}$ in C367A can possibly be traced back to the blockage of

the open coordination site. The presence of [3Fe4S] clusters in the oxidized state agrees with the degradation of C367A in the absence of H_{inact} formation. Overall, the presented results emphasize again the possibility of $R^{\bullet ox}$ being an H-cluster state having an external ligand bound to the coordination site.

7.2.5 DEER Spectroscopy Shows Distance Related to $R^{\bullet ox}$

In an attempt to narrow down the then unknown location of $R^{\bullet ox}$ in the dimeric enzyme, DEER spectroscopy was applied to determine the distances and relative orientations of the containing paramagnets. The application of DEER spectroscopy to enzymes containing multiple FeS clusters, however, is challenging.[43] First, the delocalized spin density of the FeS clusters varies with the type and environment of the clusters and can hamper further analysis. Second, the bandwidth of DEER pulses only excites a limited range of the broad EPR spectra of FeS clusters. This circumstance requires orientation-selective measurements, i.e., multiple DEER experiments with varying magnetic field positions to account for all molecular orientations. But this issue can also be used to advantage by selectively exciting only the desired species, whose contribution can be altered by varying temperatures exploiting their relaxation properties.

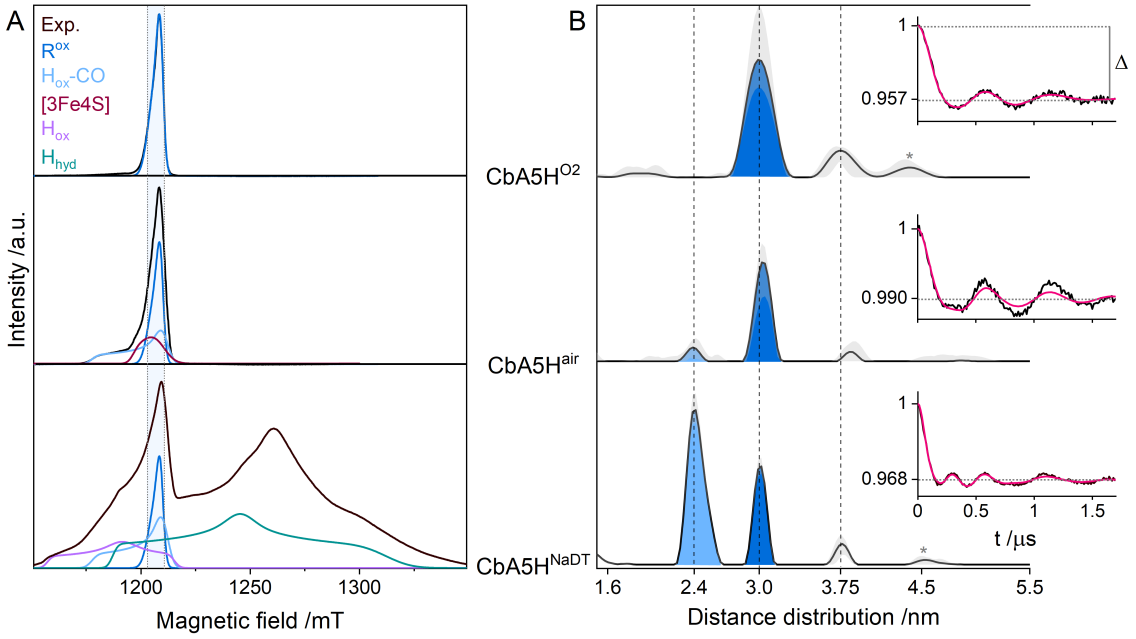

Figure 7.6: EPR spectra and DEER distance distributions of CbA5H^{O_2}, CbA5H^{air}, and CbA5H^{NaDT} derived from summed up DEER traces. **(A)** ESE-detected EPR spectra (6/15 K, 34 GHz) of CbA5H samples (black traces) with respective simulations (colored traces) and the range of applied detection pulses indicated in light blue (1203.5 mT, 1205 mT, 1206.5 mT, 1208 mT, 1209.5 mT, and 1211 mT) with **(B)** their respective distance distributions and error (gray shaded areas) obtained from the fits (pink traces) of the experimental, background-corrected, and summed up DEER spectra over all orientations given in A (black traces, insets). The approximate modulation depth Δ is indicated. Artifacts at 4.5 nm are marked with asterisks.

Here, orientation-selective DEER experiments were performed on three distinct sample preparations of CbA5H, namely CbA5H^{O_2}, CbA5H^{air}, and CbA5H^{red}. The species contributing to each EPR spectrum are shown in Figure 7.6A and are described in more detail in Chapter 6. The excitation bandwidth of the detect pulses is 1.4 mT so that DEER measurements recorded at six different field positions cover all dipolar frequencies of $R^{\bullet ox}$ in respect to the magnetic

field. The fit of the normalized and summed up DEER traces, shown in the insets in Figure 7.6B, represents all molecular orientations of the chosen field positions and yield the respective distance distributions reflecting the inter-spin distances. Each sample exhibits a distance of approximately 3 nm. This distance is expected to arise from two $R^{\bullet ox}$ species within each monomeric unit of the dimer, as the EPR spectrum of $CbA5H^{O_2}$ consists of $R^{\bullet ox}$ only. The width of the peak is considerably small and hints at a localized and rigid paramagnet. In contrast, the distance peak in $CbA5H^{air}$ reveals a slight upshift and reduced peak width, which might hint at a change in the protein structure. Moreover, in $CbA5H^{air}$ a second distance at 2.4 nm is present, which is also reflected in the respective DEER trace. This second distance is attributed to the presence of the H_{ox}-CO state, as is evident from the respective EPR spectrum. Both distances are also observed in $CbA5H^{NaDT}$, whose EPR spectrum exhibits the presence of several additional H-cluster states, such as H_{hyd}, H_{ox}, and H_{ox}-CO, as well as $R^{\bullet ox}$, and the F-clusters. Here, the 2.4 nm distance, however, is the dominating peak. The origin of additional distances around 3.75 and 4.5 nm in all sample preparations is elusive but may be partially caused by background correction artifacts.

To confirm the above-stated assignments, the obtained distances were compared to the available crystal structure of CbA5H in the H_{inact} state shown in Figure 7.7. It soon becomes apparent, that the measured and extracted distances do not coincide. This discrepancy and the assignment of distances are evaluated in the following.

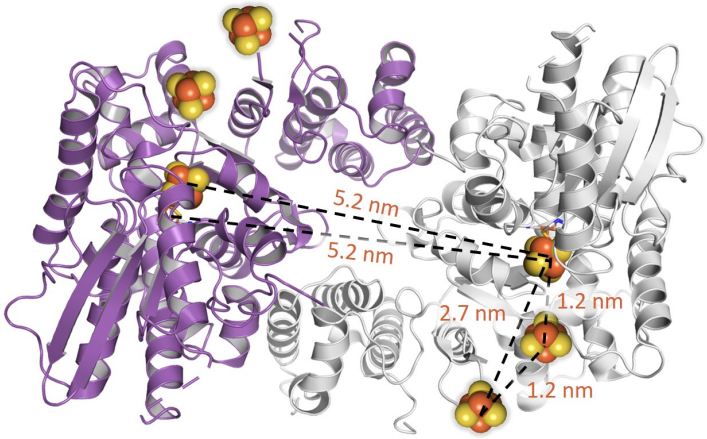

Figure 7.7: Crystal structure of the CbA5H dimer (PDB ID: 6TTL). The positions of the F-clusters, shown as spheres, are approximated. The inter-cluster distances, extracted from the crystal structure, are expected to vary between 0.1 to 0.3 nm depending on the origin of the spin. Atomic colouring: Fe: orange, S: yellow, C: grey, O: red, N: blue.

First, $R^{\bullet ox}$ is considered to be located at or in the direct vicinity of the H-cluster based on the previously presented results. Moreover, under oxidizing conditions, the F-clusters are usually diamagnetic. Residual [3Fe4S] cluster contributions, as observed in $CbA5H^{air}$, are expected to have a too short phase-memory time T_m to contribute to the oscillations. Also, in the case of $CbA5H^{NaDT}$, the reduced F-clusters are not expected to contribute to the DEER modulations as (i) the inter-cluster distances of ≤ 1.2 nm, such as for the FS4A/FS4B or H-cluster/FS4A pairs (Figure 7.7), are usually too small to be detected and (ii) DEER traces of apo-$CbA5H^{O_2}$ and apo-$CbA5H^{NaDT}$ are devoid of any modulations,[312] excluding the $[4Fe]_H$/FS4B pair as well. Thus, the only reasonable explanation for the observed distances is the inter-dimer distance between two H-clusters.

Second, the obtained distance distributions might not reflect the real distances extracted from the crystal structure. This consideration is based on the delocalized spin density distribution of the H-cluster states including $R^{\bullet ox}$. It was already shown with Complex I from *B. taurus*,[43] that elaborate DFT calculations are necessary to account for the various possibilities that a spin can attain in FeS clusters. Therefore, simulations of the DEER traces including spin projection factors are required to account for the delocalized spins and obtain reasonable distances, which is beyond the scope of this work. Nevertheless, additional oscillations of a second distance are clearly observable in the DEER trace when H_{ox}-CO is present.

Third, under the assumption that $R^{\bullet ox}$ and H_{ox}-CO are both located at the H-cluster, it is questionable why two different distances, namely 2.4 nm and 3 nm, are obtained. Three explanations are considered. One, the distance between the two H-clusters moieties, $[4Fe]_H$ and $[2Fe]_H$, is in the range of 0.5 to 1 nm. Thus, both distances might reflect distinct spin density distributions of $R^{\bullet ox}$ and H_{ox}-CO. This hypothesis is also in agreement with the results obtained from $CbA5H^{NaDT}$, where additional H-cluster states, such as H_{hyd} and H_{ox} are expected to contribute to the distance distribution. The latter states have their paramagnetic center either located at $[4Fe]_H$ or $[2Fe]_H$, respectively, which might be reflected in the distinct relative peak intensities. However, $R^{\bullet ox}$ and H_{ox}-CO are expected to exhibit very similar spin density distributions, as shown in the previous chapter, and thus, the 2.4 nm distance observed in $CbA5H^{air}$ is inexplicable. Therefore, the second possibility seems more reasonable: a structural change that the enzyme undergoes upon oxidation, which relocates the source of electron density. In $CbA5H^{O_2}$, the enzyme is assumed to reside entirely in the H_{inact} state. Under air, however, parts of the enzyme are still in the H_{ox}-CO state, reflected in the respective EPR spectrum and associated with the 2.4 nm distance. This observation is in agreement with the distance distribution of $CbA5H^{NaDT}$, where the majority of the enzyme is expected to reside in 'active' states, resulting in a higher 2.4 nm distance peak compared to 3 nm. The relative intensity of 2.4 nm, however, is comparably small. This may be due to turnover conditions, where also several diamagnetic states of the H-cluster, such as H_{red}, are present, which do not contribute to the DEER trace. It is moreover questionable, to which extent faster relaxing species, such as H_{hyd} and H_{ox}, contribute to the DEER spectrum. A closer examination of the refocused echoes should clarify this issue. A third possibility is the appearance of double frequencies in the DEER spectrum. These can arise from insufficient orientation-averaging, e.g. for H_{ox}-CO, and distort the corresponding pake pattern, which induces a false distance in the distance distribution. To circumvent this issue and probe if the 2.4 nm peak represents a real distance, measurements at lower frequencies, such as the X-band, could be performed.

Eventually, the modulation depth of each DEER trace (insets in Figure 7.6B), which depends on the number of pumped B spin pairs, is evaluated. In comparison to $CbA5H^{O_2}$, the modulation depth in $CbA5H^{air}$ is decreased. This observation might be explained by the presence of [3Fe4S] clusters in the EPR spectrum. Although these clusters do not contribute to the DEER modulations, they are an indicator of the degradation of the enzyme. Therefore, one hypothesis is based on the presence of monomers due to degradation, which in turn reduces the modulation depth, as there is no inter-cluster distance to be detected. Moreover, the distinct relaxation properties, as well as anisotropy-dependent relaxation and spectral width of the spin systems might need to be taken into account. This is especially true for H_{ox}-CO, whose spectrum is

not entirely covered by the selected pulse positions. Furthermore, the modulation depth of $CbA5H^{NaDT}$ is reduced as well. As already discussed for the respective peak intensities, the contribution of several underlying H-cluster states prevents a simple analysis. Thus, it can be assumed, that the dimeric enzyme carries each one paramagnetic and one diamagnetic H-cluster state at the same time, which would decrease the modulation depth. A final parameter to be considered is the presence of 5 % glycerol in $CbA5H^{air}$and $CbA5H^{O_2}$, which is not expected to induce significant changes. The usually expected reduction of the T_m time, however, can possibly influence the fraction of contributing species. A uniform sample preparation is considered for the next experiments.

Overall, three distinct samples preparations of CbA5H were investigated with DEER spectroscopy. The two main distances obtained with different peak intensities are associated with the H-cluster states and/or $R^{\bullet ox}$. Although the measured distances do not coincide with the crystal structure, they provide a hint to (i) the presence of $R^{\bullet ox}$ in each monomer of the subunit and (ii) a possible structural change during aerobic inactivation. To further illuminate those hypotheses DEER spectroscopy of samples with an isolated H-cluster state, such as H_{hyd}, H_{ox}, or H_{ox}-CO, or mutations, that prevent dimerization of CbA5H, could be investigated. Moreover, the experiments should be performed at lower frequencies. DEER spectra recorded at the X-band can simplify the analysis, as fewer magnetic field positions would be necessary to excite all molecular orientations. In turn, orientation-selection artifacts can be more likely excluded. For further evaluation of the DEER traces, numerical simulations of the contributing cluster pairs, including g-values, linewidths, spin projection factors, as well as g-axis orientation combinations could be taken into account.

7.3 Is $R^{\bullet ox}$ a CO-Inhibited State?

The recently published study by Corrigan et al. [311] investigates the possibility of dynamic rearrangement of the loop harboring the cysteine residue C367 upon oxidation and the effects of local perturbations on CbA5H's spectral features. The study showed the presence of two distinct states 1 and 2 for the H_{ox} and H_{ox}-CO states in the EPR spectra of CbA5H, respectively. This observation is suggested to be caused by an unusual mobility of the $SCC_{367}P$ loop enabling a fast transition between active and inactive H-cluster states. Intriguingly, their H_{ox}-CO(1) state exhibits the same properties as $R^{\bullet ox}$ in terms of the g-values and relaxation behavior. The different forms observed are ascribed to perturbations of the $[4Fe]_H$ cluster upon rearrangement of the loop, resulting in distinct g-values but overall similar spin states. Therefore, no additional or changed FTIR signatures are observed for each second form. Unfortunately, direct experimental evidence of this hypothesis is lacking thus far.

Therefore, this study is compared to the presented results to clarify if $R^{\bullet ox}$ is H_{ox}-CO(1). The observation of two distinct forms of H_{ox} can neither be confirmed nor refuted by our currently available spectroscopic data, as any sample preparation has an isolated H_{ox} state. Moreover, in our hands, CO-treated samples reveal indeed the presence of $R^{\bullet ox}$ and H_{ox}-CO, but contrarily $R^{\bullet ox}$ is also observed in the air- and O_2-treated samples. Corrigan et al. [311] tried to reproduce our $R^{\bullet ox}$ signal by treating CbA5H with air but observed [3Fe4S] clusters only. One major difference, however, is that we observed $R^{\bullet ox}$ mainly with previous reductive treatment (NaDT or

H_2) and subsequent oxidation, which was neglected by the authors. Nevertheless, this observation supports their hypothesis, that an "inactivation-favorable conformation" is a prerequisite for H_{inact} formation. This furthermore supports their notion that the two H-cluster forms 2 and 1 can be associated with the two active states A_1 and A_2 proposed by Winkler et al. [123], respectively. Further support that $R^{\bullet ox}$ is a CO-inhibited state is provided by the absence of $R^{\bullet ox}$ in pdt-maturated samples. While CbA5H(pdt) can enter the H_{inact} state, the artificial cofactor is known to limit CO-binding to the open coordination site.[151] Similarly, the C367A variant prevents the formation of H_{ox}-CO due to occupancy of the binding site by O_2. In both sample preparation no $R^{\bullet ox}$ is observed either. In contrast, the C367D variant omits H_{inact} formation but reveals the presence of $R^{\bullet ox}$. This observation is reasonable, as the cysteine residue may not bind to the open coordination site, but an accompanying structural change of the neighboring loop under oxidizing conditions is still feasible leading to perturbation of the $[4Fe]_H$ cluster and thus, $R^{\bullet ox}$ formation. Moreover, the presented DEER data, which shows two distances in the reduced, but only one in the oxidized state, may support a conformational change of the enzyme. If those results can be associated with a small local change in the vicinity of the H-cluster needs to be investigated.

While the majority of our results agree with $R^{\bullet ox}$ being H_{ox}-CO, the absence of H_{ox}-CO vibrational bands in our FTIR data refutes them. Similar to Corrigan et al. [311], no new or changed FTIR signatures were observed, that associate $R^{\bullet ox}$ with a new H-cluster state. But most importantly, no FTIR bands associated with H_{ox}-CO were observed in O_2-treated samples. Moreover, the fraction of $R^{\bullet ox}$ in our hands was significantly enhanced by oxidation with O_2. Under the assumption, that $R^{\bullet ox}$ is a CO-inhibited state, the presence and enhancement of H_{ox}-CO signals would have been expected to be observable in the concomitant FTIR data, which is not the case. Another question that arises in this context is the origin of $R^{\bullet ox}$ in O_2- or HAR-treated samples under the exclusion of CO. One reasonable explanation is that oxidation-induced damage triggers the release of CO-ligands from the H-cluster, which in turn bind to the open coordination site of intact H-clusters forming H_{ox}-CO.[184] The absence of FTIR bands associated with H_{ox}-CO in most of our preparations is currently the most compelling evidence against $R^{\bullet ox}$ being H_{ox}-CO(1). This discrepancy can only be explained by a difference in EPR and FTIR data. Further complementary EPR and FTIR studies are necessary to investigate if the recorded spectra reflect the other method in each case. Otherwise, it will be precarious in the future to assign EPR spectral features to respective H-cluster states.

A straightforward experiment to eventually solve the mystery of $R^{\bullet ox}$ is a ^{13}CO-treatment of CbA5H. If $R^{\bullet ox}$ is associated with CO, the resulting spectra should reveal not only H_{ox}-CO but also $R^{\bullet ox}$ exhibiting hyperfine couplings or broadenings due to coupling of the electron spin with ^{13}CO occupying the open coordination site. Furthermore, the release of CO-ligands by degraded clusters could be investigated by isotope-labeling the CO ligands of the H-cluster with ^{13}CO and subsequent treatment with O_2, which would result in ^{13}CO-labeled $R^{\bullet ox}$. The latter experiment would unambiguously show the origin of $R^{\bullet ox}$ in O_2-treated samples.

8

[FeFe]-hydrogenase CpI revisited: Modulation of Intercluster Exchange Coupling as a Tool for Regulation of Catalysis?

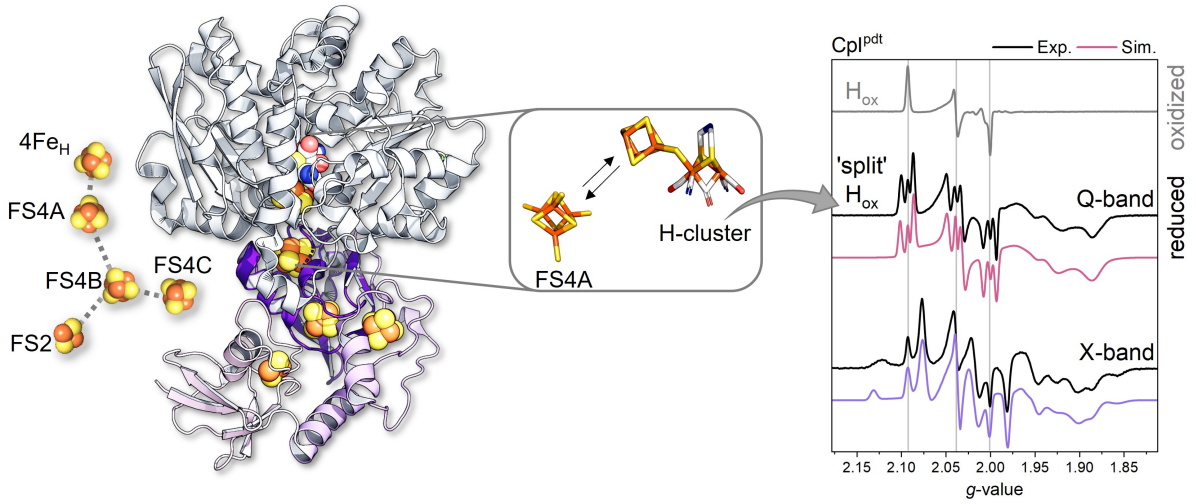

This research is in preparation for submission as:

Heghmanns, M., Brocks, C., Happe, T. and Kasanmascheff, M., *[FeFe]-hydrogenase CpI revisited: modulation of intercluster exchange coupling as a tool for regulation of catalysis*, 2023. The journal is to be determined.

- Claudia Brocks prepared all protein samples and performed and analyzed activity assays and FTIR spectroscopic experiments
- I performed all EPR experiments and analyzed the spectrosopic data
- I wrote the below shown first draft of the manuscript

[FeFe]-hydrogenase CpI revisited: modulation of intercluster exchange coupling as a tool for regulation of catalysis?

Abstract

The [FeFe]-hydrogenase CpI from *Clostridium pasteurianum* has been extensively investigated over the past decades due to its ability to effectively convert hydrogen. The enzyme harbors the H-cluster and a relay of four additional FeS clusters (F-clusters), which were shown to affect the active site through redox anticooperative behavior. Here, we applied multi-frequency and temperature-dependent EPR spectroscopy to unambiguously display the exchange interaction between the H-cluster and proximal F-cluster in CpI. Based on spectral simulations, we determined the associated spin coupling constants and revised some of the earlier reported EPR features. Moreover, we were able to modulate the magnitude of the spin coupling by site-directed mutagenesis of residues in the second coordination sphere of the active site. Compared to the wild-type enzyme, all variants show a decreased coupling interaction between the H-cluster and the proximal F-cluster in conjunction with changed biological properties. We thus focused on determining the factors that influence exchange coupling and how it affects the electronic properties and biological function. Ultimately, our results might provide a tool to further understand and tune the enzyme's catalytic reactivity.

Hydrogenases, mainly found in prokaryotes, catalyze the reversible reduction of protons to molecular hydrogen.[1,2] Within its subclass, [FeFe]-hydrogenases share the same catalytic center, better known as the H-cluster.[3] It consists of a cubane [4Fe4S] cluster ($[4Fe]_H$) with two antiferromagnetically coupled high-spin Fe layers that are scaffolded by four cysteine residues of which one is shared with a binuclear [2Fe2S] cluster ($[2Fe]_H$).[4–9] The distal (Fe_d) and proximal Fe (Fe_p) ions of $[2Fe]_H$ are coordinated by three carbon monoxide (CO) and two cyanide (CN^-) ligands, which exhibit characteristic vibrational bands associated with various redox and protonation states of the H-cluster.[10–12] The $[2Fe]_H$ site is additionally bridged by an azadithiolate (adt) ligand carrying an amine group, that act as a base during hydrogen turnover.[1,5,9] The incorporation of a synthetic $[2Fe]_H$ precursor can circumvent the elaborate, naturally occurring maturation of the H-cluster while providing higher yields of a spectroscopically indistinguishable enzyme,[13,14] and allowing for modifications of the central headgroup.[15] A vacant position at Fe_d enables not only the binding of substrates (H^+, H_2) but also inhibitors (CO, O_2, SH, and CN).[16–23] In conjunction with the complex interplay of the two electronically coupled H-cluster subsites, a multitude of redox and protonation states exists, whose order and involvement in the catalytic cycle are highly debated.[24–29]

One of the first purified and characterized [FeFe]-hydrogenases is CpI from *Clostridium pasteurianum* (*C. pasteurianum),* which has been thoroughly investigated in recent years.[5,21,30–32] The first EPR spectra of CpI were reported in the mid-70s and have been reevaluated since.[33–41] CpI harbors four accessory iron-sulfur (FeS) clusters, termed F-clusters, that serve as electron transfer relays between external redox partners and the catalytic site (Figure 1).[5] The all-cysteine coordinated [4Fe4S] cluster FS4A is proximal to the H-cluster (~7.6 Å), and located 9.4 Å away from the medial cluster FS4B. Two surface domains carry each one additional FeS cluster: FS2, a [2Fe2S] cluster, and FS4C, a [4Fe4S] cluster with an unusual 3Cys1His-ligation, that is considered as the binding site for redox partners.[41,42] The closely arranged FeS clusters can enable efficient electron transfer rates and are also suggested to tune the enzyme's catalytic bias or its oxygen sensitivity.[41,43–47] Under reducing conditions, the FeS clusters in CpI become paramagnetic, exhibiting multiple, overlapping

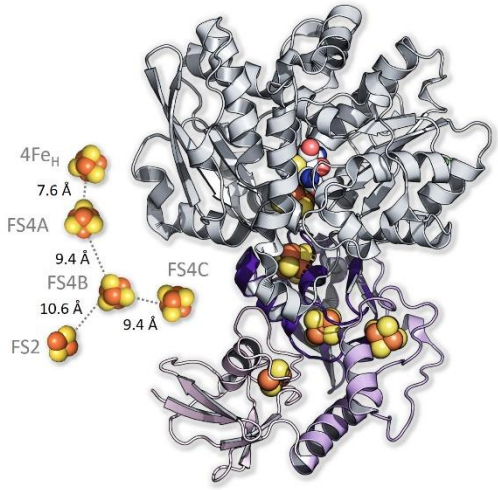

Figure 1: Crystal structure of CpI (PDB ID: 3C8Y). The H-domain (grey), and the F-domain (purple) are shown as ribbons. The accessory FeS clusters and the H-cluster are shown as spheres. Atomic colouring: Fe: orange, S: yellow, C: grey, O: red, N: blue. The distances between the FeS cluster relay are depicted.

species observable with electron paramagnetic resonance (EPR) spectroscopy. A redox titration series monitored with EPR spectroscopy at 9.5 GHz (X-band) was used to differentiate between the FeS cluster signals and to determine their midpoint potentials.[41] The analysis was simplified by maturating the enzyme with an artificial $[2Fe]_H$ carrying a methylene bridgehead (pdt = propane-dithiolate, CpI(pdt)), which shows similar structural[48] and spectral properties, but only residual activity. As the electron is captured at $[4Fe]_H$, the diiron subsite is supposedly limited to two redox states (H_{ox} and H_{red}).[13,14] Subsequent spectroelectrochemical experiments, however, showed redox anticooperative behavior between the H- and F-clusters of CpI(pdt), that were neglected in the previous study.[41,49,50] The involvement of those mutual redox interactions, where the reduction of one cluster lowers the initial potential of a second interacting cluster, results in redox anticooperativity between the H-cluster and FS4A (111 mV) and also between FS4A and FS4B (38 mV). As a result, lower intrinsic midpoint potentials of

CpI(pdt) were determined (-438 mV ($[4Fe4S]_H$), -419 mV (FS4A), and -482 mV (FS4B) at pH 8),[50] than previously reported.[41] These interactions are promoted by the close arrangement of FeS clusters, which can lead to spin coupling interactions, as was shown for the [FeFe]-hydrogenase *Dd*HydAB from *Desulfovibrio desulfuricans*.[49] Therefore, similar interactions have been proposed for CpI, which should be visible in the EPR spectrum and might alter the current allocation of EPR spectral properties and respective potentials.

Spin-spin interactions have been frequently observed in [NiFe] hydrogenases. At low temperatures, the Ni-C and Ni-L state magnetically interact with the proximal $[4Fe4S]^+$ cluster in *A. vinosum*,[51] *C. vinosum*,[52,53] and *D. gigas*,[54–56] leading to a splitting of the EPR lines at lower temperatures (denoted as "split" states). Besides the H-cluster, FeS clusters, such as the two [4Fe4S] clusters in *C. pasteurianum* ferredoxin were shown to couple to each other.[38]

Here, we used EPR spectroscopy to investigate the [FeFe]-hydrogenase CpI maturated with adt and pdt, respectively, in distinct states. Multi-frequency EPR spectra and concomitant simulations unambiguously reveal the presence of exchange coupling interactions between the H-cluster and the proximal [4Fe4S] cluster, FS4A. This is the first report of simulated exchange couplings and determination of their strength in [FeFe]-hydrogenases. Moreover, site-directed mutations of residues in the second coordination sphere of the active site resulted in a decreased exchange coupling. We strive to investigate the determinants of exchange coupling and how they affect electronic properties and biological function.

Results and Discussion

Exchange Interaction Observed Between H_{ox} and FS4A in pdt-maturated Samples

We first investigated CpI maturated with the synthetic mimic pdt (CpI(pdt)). The unprotonatable pdt bridgehead inactivates the enzyme almost completely, and thus, limits the observable H-cluster states and facilitates analysis. Under oxidizing conditions, the EPR spectrum of CpI(pdt) shows the characteristic rhombic EPR signal of the oxidized, active state H_{ox}, whereas the F-clusters are EPR-silent. The electronic structure of the H_{ox} state is best described as a diamagnetic $[4Fe4S]^{2+}$ cluster and a mixed-valence, paramagnetic $[2Fe]_H$ (S = ½) site.[8,57,58] The g-values of H_{ox} determined with spectral simulations are in agreement with the literature.[34,41] At elevated temperatures (40 K) an axial feature with g-values strongly resembling the CO-inhibited H_{ox}-CO state is apparent in substoichiometric amounts (see Supporting Discussion).

Next, we recorded the EPR spectra of CpI(pdt) treated with N_2, which mainly generates the H_{ox} state. Low concentrations of added sodium dithionite mildly reduced the accessory FeS clusters. At low temperatures, the spectra show a complicated pattern (Figure 2) arising from multiple FeS clusters and the H-cluster state H_{ox}. The signals of H_{ox} show a clear splitting centered around the initial g-values up to a temperature of 30 K. The previous study on CpI(pdt) at X-band frequencies attributed those features to the accessory F-clusters.[41] However, these changes arise from exchange interactions between the H-cluster and the proximal [4Fe4S] cluster FS4A, as was recently suggested by Rodriguez et. al,[50] and might also explain the differences observed between apo-CpI and

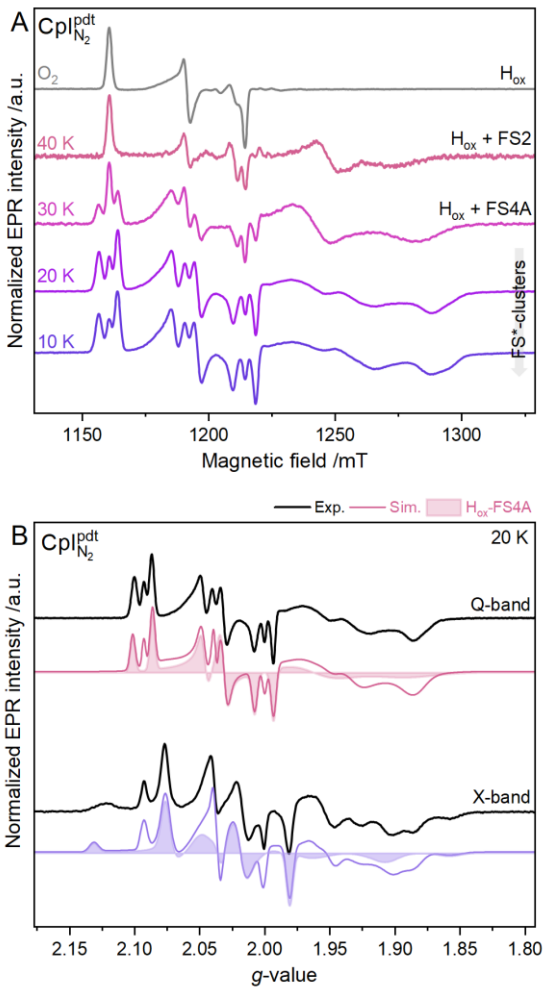

Figure 2: EPR spectra of CpI(pdt). (A) ESE-FS spectra (34 GHz) of CpI(pdt) treated with O_2 (top trace, T = 10 K) and N_2 (T = 10-40 K, purple traces). (B) Comparison of CW EPR (9.5 GHz) and ESE-FS (34 GHz) spectra recorded at 20 K (black traces) and respective total simulations (solid, coloured traces) and simulations of the exchange coupled system H_{ox}-FS4A depicted as filled areas.

CpI(pdt).[41] At lower microwave frequencies, such as 9.5 GHz, the field-dependent electron Zeeman interactions (EZ) are dominated by the frequency-independent exchange interactions J, while the situation can be reversed at higher frequencies, such as 34 GHz.[59] Thus, for $J \leq$ EZ the exchange interactions are farther distributed and might remain unnoticed in earlier studies performed at 9.5 GHz.

To estimate the F-cluster g-values we investigated the spectra of a dithionite-reduced sample of CpI(pdt) exhibiting EPR-active F-clusters only (Figure S1). The absence of any H-cluster state indicates that the enzyme entirely resides in diamagnetic H-cluster states. Temperature-dependent measurements revealed no g-value > 2.09 and contrast the F-cluster g_1-value reported for FS4A at X-band frequencies.[41] As a small degree of redox anticooperativity was observed between FS4A and FS4B, it is suggested that FS4B also interacts with the two distal clusters FS2 and FS4C.[50] Although redox anticooperativity is not necessarily associated with exchange coupling, the latter effect is suggested to affect all F-clusters due to their close arrangement. The overlap of presumably

five different magnetically interacting FeS clusters in apo-CpI (including $[4Fe4S]_H$) impedes a facile assignment of the contributing clusters and their *g*-values. In the following, we, therefore, focus on simulations of the H-cluster/FS4A interaction based on temperature-dependent pulsed Q-band spectra of CpI(pdt) to deconvolute the contributing species independent of literature data. Analysis of spectra recorded at X-band frequencies allow for a more precise determination of exchange coupling interactions.

At a temperature of 40 K, CpI(pdt) exhibits the uncoupled H_{ox} state. The exchange interactions of the H-cluster states are canceled at this temperature, as the interacting cluster is broadened beyond detection. An additional rhombic signal with *g* = 2.041(3), 1.950(1), 1.900(1) (Figure 2, Figure S2, and Table S1) is assigned to FS2, whose slow relaxation properties and *g*-values agree with a distal domain construct harboring FS2 and FS4C only.[41] Upon lowering the temperature to 30 K, the exchange interactions of H_{ox} arise in conjunction with changes in the FeS cluster region, suggesting that the interacting FeS cluster is present ($F_{red}H_{ox}$). Presumably three different states in connection with FS4A and H_{ox} are present (see also Figure S3): $F_{ox}H_{ox}$, with an oxidized FS4A (F_{ox}) giving rise to the uncoupled H_{ox} state, $F_{red}H_{red}$, where the H-cluster is EPR-silent and the uncoupled FS4A cluster (F_{red}) is observed, and $F_{red}H_{ox}$, yielding the exchange coupled FS4A-H_{ox} state. Due to the relatively featureless line shape in the FeS cluster region, we expect FS4B and FS4C to be absent; either they are too fast relaxing to be detected at this temperature or they may be diamagnetic in this sample preparation due to their low redox potential. We thus assigned the most prominent rhombic FeS cluster signal with *g* = 2.032(5), 1.960(2), 1.887(2) to the interacting cluster FS4A. As this cluster species cannot be readily isolated from the full spectrum, the correct assignment of *g*-values is difficult but can be adequately approximated. For example, changes in FS4A *g*-values of ≥ 0.03 result in improper simulations, whereas small *g*-value shifts do not result in significant deviations of *J*. At temperatures of 20 K and lower, the FeS cluster region becomes more complex due to increasing contributions of additional F-clusters and possible exchange interactions between them. The splitting pattern, however, remains unchanged, indicating that only FS4A has an impact on the EPR signature of H_{ox} as suggested previously.[50] Additionally, a third rhombic species was included to account for prominent changes in the FeS cluster region. The *g*-values with *g* = 2.078(5), 1.934(5), 1.885(5) are similar to the FS4C literature data.[41] Moreover, the separation of an expected fourth species arising from FS4B is hampered possibly due to similar properties or inter-cluster exchange interactions. Therefore, the third species is denoted as FS* and comprises all unresolved and possibly exchange-coupled FeS cluster contributions to lower temperatures. An unambiguous assignment of the accessory FeS clusters to unique spectral properties would require a revision of the redox potentiometric data.

To increase the accuracy of our analysis, we recorded CW EPR spectra of the same samples at X-band frequencies and performed multi-frequency simulations (Figure 2). The higher resolution of exchange interactions at lower frequencies enabled a more precise determination of *g*-values and exchange interaction, where even small changes in *g*-values lead to a strong deviation between the experimental and simulated spectrum. For the multi-frequency simulations, the

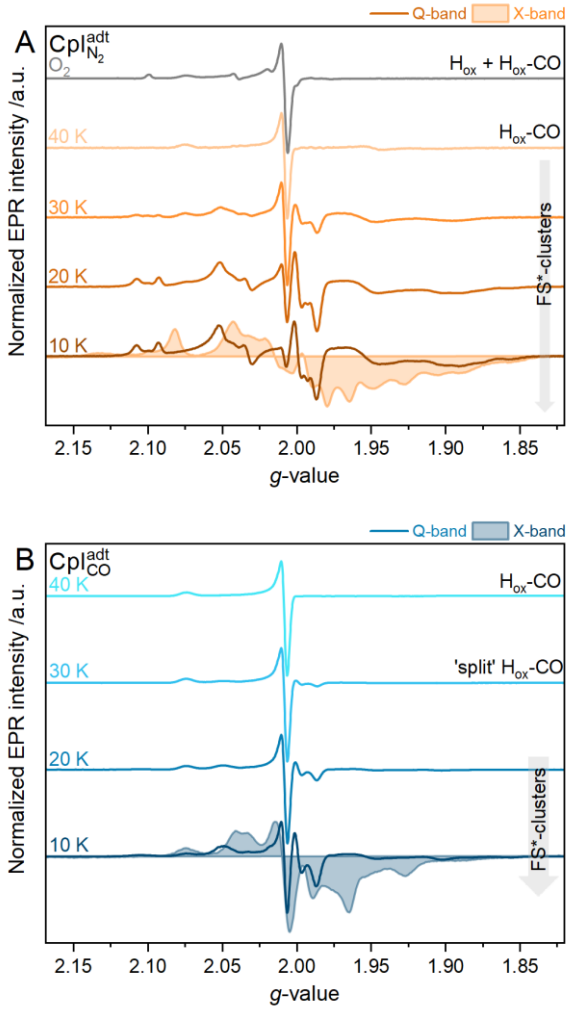

Figure 3: EPR spectra of CpI(adt). ESE-FS spectra (34 GHz) of CpI(adt) treated with O_2 (top trace, *T* = 10 K) and N_2 (*T* = 10-40 K, orange traces) in comparison to a CW EPR spectrum (9.5 GHz) spectra recorded at 10 K (filled area, lower trace).

g-values of all species were kept constant, whereas the *g*-strain was fitted accordingly to the two frequencies. The full simulations for X- and Q-band spectra are shown in Figure 2 (with the single contributions presented in Figure S2) and yielded an isotropic exchange coupling constant $J_{iso} = 8.2 \pm 0.7 \cdot 10^{-3}cm^{-1}$ (see SI for more details on the simulation procedure). The magnitude of the exchange coupling is comparable to the ones found in some [NiFe]-hydrogenases, which exhibit exchange interactions between the active site Ni and the neighboured FeS cluster. For *D. gigas*, the Ni-C state interacts with a $[4Fe4S]^+$ cluster showing splittings with $J_{iso} = 2 \cdot 10^{-3}cm^{-1}$,[56] whereas in *A. aeolicus* the Ni-B state splits with the oxidized or reduced $[4Fe3S]^{5+/3+}$ cluster with $J_{iso} = 10 \cdot 10^{-3}cm^{-1}$ and $J_{iso} = 1.8 \cdot 10^{-3}cm^{-1}$, respectively.[45,60] Fe centers interacting with a radical can exhibit larger exchange couplings of up to 0.72 cm^{-1}, but also values < $10^{-3}cm^{-1}$ have been found.[61] Exchange coupling values for two interacting $[4Fe4S]^+$ clusters are in the range of 4-6 • $10^{-3}cm^{-1}$.[62] All interacting species are usually located within a distance of 7-12 Å.

Exchange Interaction Observed Between H_{ox}/H_{ox}-CO and FS4A in adt-maturated samples

Next, we investigated CpI maturated with the synthetic but naturally occurring adt ligand, termed CpI(adt). The O_2-oxidized EPR spectrum shows in addition to H_{ox} dominant contributions from the H_{ox}-CO state, which is characterized by a CO ligand bound to the open coordination site. The presence of H_{ox}-CO is frequently observed in sample preparations, where degraded H-clusters release CO-ligands which in turn inhibit intact H-clusters.[63] The electronic structure of the CO-inhibited state is similar to H_{ox}, whereas the electron density is suggested to be more distributed, yielding an axial instead of a rhombic signal.[58] The signal of H_{ox}-CO can be isolated at elevated temperatures and agrees with the literature (Table S3).[34,41] Treating the CpI(adt) sample with N_2 induces similar states as in CpI(pdt) but includes the presence of H_{ox}-CO. Accompanying FTIR data verify the absence of other paramagnetic H-cluster states.[64] At lower temperatures, new features arise due to an additional exchange interaction between H_{ox}-CO and FS4A, which significantly affects the FeS cluster region (Figure S4). For the simulation of spectra, the *g*-values of adt- and pdt-maturated samples were kept constant (except H_{ox}). The full and single simulations (see Figure S5 and Table S2) yield isotropic exchange coupling constants J_{iso} = 28 ± 10 10^{-3}cm^{-1} for $F_{red}H_{ox}$-CO and J_{iso} = 8.2 ± 0.7 10^{-3}cm^{-1} for $F_{red}H_{ox}$, while the latter is the same for both adt- and pdt-maturated enzymes. Earlier studies on *Cr*HydA1 already suggested that the wild-type enzyme and pdt mimic show identical inter-cluster exchange interactions between $[2Fe]_H$ and $[4Fe4S]_H$.[65] In $F_{red}H_{ox}$-CO additional dipolar couplings of 1.7, 4.5, -6.3 10^{-3} cm^{-1} needed to be introduced. These results can be explained by the different spin density distributions of the H_{ox} and H_{ox}-CO states, respectively. The different *J*-values of H_{ox}.CO and H_{ox} possibly reflect the state's differences in spin density distribution. In the H_{ox} state, the electron is suggested to reside mainly on $[2Fe]_H$, whereas upon CO-binding the unpaired electron delocalizes leading to a valence-delocalized $[Fe_p^{1.5+}Fe_d^{1.5+}]_H$ with increased spin density on $[4Fe]_H$.[12,58,66] Thus, the anticipated center-to-center distance of the spin density between the H-cluster and FS4A decreases for H_{ox}-CO and explains the stronger exchange coupling observed for $F_{red}H_{ox}$-CO. Moreover, the extensive spin delocalization required the introduction of anisotropic and dipole-dipole interactions. The necessity of these additional contributions is also reflected in the respective simulations, where no longer a simple splitting of the signal is observed but it is perturbed by secondary effects (see single simulations in Figure S5). In comparison to CpI(pdt), the overall simulation is not fitting sufficiently well, which is attributed to the $F_{red}H_{ox}$-CO contribution.

To simplify the spectrum and isolate the H_{ox}-CO contributions, we recorded spectra of CpI(adt) treated with CO and 10 mM NaDT (Figure 3). The spectra readily reveal the exchange interaction between H_{ox}-CO and FS4A. In comparison to the N_2-treated sample, however, only a few accessory F-cluster features are detected. This observation can possibly be explained by (i) inefficient reduction of the F-clusters due to the CO-inhibited H-cluster and (ii) the assumption, that the H-cluster is primarily in the paramagnetic H_{ox}-CO state so that each reduced FS4A cluster is coupled, yielding the dominating $H_{ox}F_{red}$ state with only a few $H_{red}F_{red}$ species present. The spectral sum of CpI(pdt) and CO-treated CpI(adt) is very well in agreement with N_2-treated CpI(adt) (see Figure S4), and highlights the effects of each H-cluster/FS4A interaction on the FeS cluster region. Our efforts to accurately simulate the respective spectra of CO-treated CpI(adt) were unsuccessful. This circumstance can be traced back to the stronger antiferromagnetic exchange coupling between $[4Fe]_H$ and $[2Fe]_H$, which is approximately five times higher in H_{ox}-CO compared to H_{ox} and also reflected in the obtained exchange couplings.[66] Thus, the application of a local spin model accounting for polynuclear clusters is required to accurately determine the strength of the exchange interaction between FS4A and H_{ox}-CO. Nevertheless, our analysis shows, that it is possible to isolate designated exchange interactions with different sample preparations.

Exchange Interaction Between H_{ox} and FS4A is Modulated by Site-directed Mutation

Increasing the oxygen stability of [FeFe]-hydrogenases is a major task to improve the efficiency of hydrogen production applications.[67] In an attempt to engineer more oxygen-stable variants of CpI, Brocks, and coworkers targeted a newly identified water channel in the vicinity of the H-cluster by site-directed mutations of G302A, G302S, and S357T.[64] The novel water channel, W_H, is located between $[4Fe]_H$ and FS4A and connects Fe_d with the $[4Fe]_H$ moiety. It is suggested to be a diffusion pathway for reactive oxygen species formed at Fe_d. The introduction of bulkier and more hydrophilic residues resulted in a constriction of the water channel by the formation of additional H-bonds and in turn an increase in oxygen-stability for G302S and S357T. We investigated all CpI variants maturated with pdt at X- and Q-band frequencies. In comparison to the wild-type enzyme, spectral simulations of all variants show a decreased exchange coupling interaction between FS4A and H_{ox} (Figure 4). In Variant S357T, the exchange coupling is almost reduced by half in comparison to the wild-type enzyme, whereas both Ala and Ser exchanges of G302 result in the same decreased *J*-value independent of the amino acid residue. The simulation parameters for the exchange interactions of the variants (see Tables S3-5 and Table S6 for comparison) are derived from the analysis of multi-frequency spectra (see Figures S6-8). Apart from the exchange interaction, mutagenesis effects are mainly reflected in the changed *g*-values of FS4A (Table S6), pointing to their influence on the electronic environment of the cluster. The overlap of multiple species, however, prevents a detailed analysis of the respective *g*-tensors. Furthermore, minor changes in the spectral line shapes and contributing species of each variant are discussed in the Supporting Information.

Next, we probed if the biological function of the enzymes is affected. Thus, several factors were considered to be influenced by the decreased magnitude of the exchange coupling. The overall H-cluster occupancy, H_2-production activity, and catalytic bias of the variants, however, remained similar to CpI (see Table 1) and are excluded to be affected by a reduced *J*-coupling. Moreover, no correlation between the increased oxygen stability and *J* can be established, confirming that the more oxygen-tolerant variants behave similarly to the wild-type enzyme. Another example of long-range exchange coupling is found in xanthine oxidases, whose spectra exhibit magnetic couplings between Mo(V) and a FeS cluster.[68] In xanthine oxidase from different organisms, no correlation

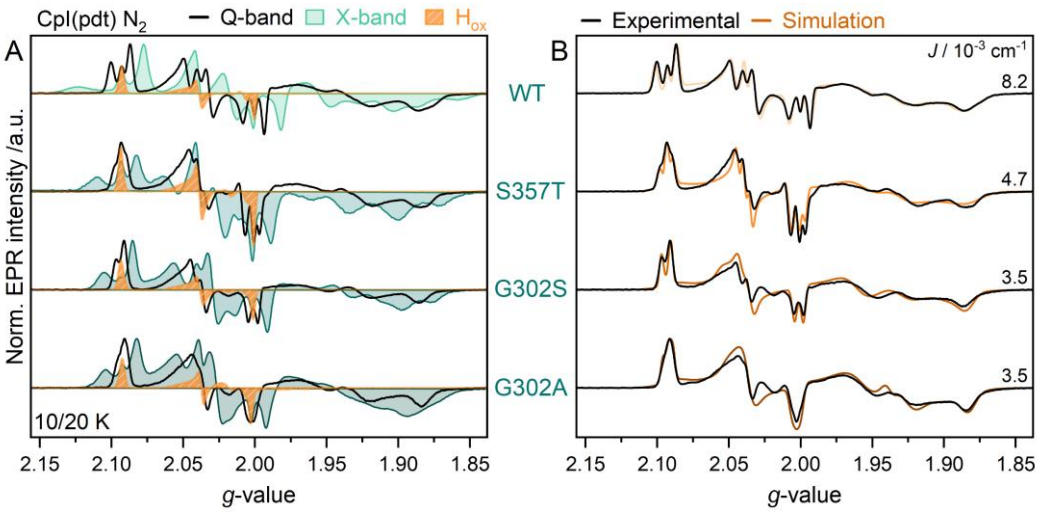

C

Protein	J /10^{-3} cm^{-1}	Distance of OH_{357} to $[4Fe]_H$ / Å	H_2-activity /µmol H_2 mg^{-1} min^{-1}	O_2-stability after injection of O_2 / %
wild-type	8.2 ± 0.07	5.95	2778±358	35
S357T	4.7 ± 0.07	4.85	2355±213	70
G302S	3.5 ± 0.07	4.25	2841±347	55
G302A	3.5 ± 0.07	-	2543±315	30

Figure 4: EPR spectra of CpI(pdt) and its variants. (**A**) ESE-FS spectra (34 GHz, T = 20 K, black traces) of CpI(pdt) treated with N_2 and O_2 (orange traces) in comparison to CW EPR spectra (9.5 GHz, T = 10 K, filled areas) and (**B**) the respective Q-band simulations (brown traces) with the exchange coupling values indicated on the right. The simulation parameters can be found in Tables S3-5. (**C**) Comparison of the exchange coupling values J of CpI and its variants in comparison to selected parameters. The distances were extracted from the crystal structure and present a mean value between conformation A and B.

between the intramolecular electron transfer and the magnitude of J was found.[68] This observation led to the conclusion, that the exchange and electron transfer pathways are distinct. The electron transfer kinetics can be influenced by the redox potentials of the participating species, electronic coupling, and the energy of structural reorganization.[69] Reduced inter- or intra-molecular electron transfers were shown to arise from site-directed variants of the distal [4Fe4S] cluster and resulted in a lowered H_2 production or oxidation activity.[42,70] Here, the H_2-production activity is unchanged but the magnitude of J is decreased in the variants. Therefore, we suggest, that the investigated range of J-values do not significantly influence the electron transfer, which in turn is independent on the exchange coupling between FS4A and the H-cluster.

Exchange pathways between two paramagnetic centers were found, among other factors, to be dependent on the linking atom and the type of bonding, such as σ- and π-bonds.[61,71,72] Knowledge of longer-range interaction, particularly in proteins, remain scarce. Furthermore, multiple factors, such as hydrogen bonding, bulk water, and/or functional groups are suggested to influence the exchange coupling interaction. We thus focused next on how the amino acid exchanges modulate the exchange pathway.

The introduction of the bulkier residue S357T was shown to impair the flexibility of the hydroxyl group OH_{357} by the introduction of two additional H-bonds.[64] These H-bonds constrict the water channel W_H and cause a local desolvation near $4Fe_H$. A similar case is encountered for the G302 variants. Both exchanges show the same decreased J-value independent of the exchanged amino acid. In G302S two additional H-bonds to the protein backbone and OH_{S357} are suggested to form a rigid H-bond network preventing access of bulk water in between FS4A and the H-cluster.[64] Thus, it is tempting to speculate, that the increased rigidity due to additional H-bonds limit the exchange interaction between the two centers. This notion is supported by the distance of OH_{357} to $[4Fe]_H$, which decreases concomitantly with the J-value (Figure 4) and hints at the involvement of OH_{357} in the exchange pathway between $[4Fe]_H$ and FS4A. The role of OH_{357}, bulk water, and/or additional H-bonds might be further elucidated, when a crystal structure for G302A becomes available. Thus far it is suggested that the additional methyl group in G302A may sterically hinder the inter-cluster exchange.

Moreover, the G302S and S357T variants populate two distinct side chain conformations of OH_{357}.[64] A similar observation was made with the wild-type enzyme in a previous study.[73] It was shown, that in the dominant conformation A, populated at more positive potentials, OH_{357} is located 5.6 Å away from $[4Fe]_H$. In the secondary conformation B, populated at more reduced potentials, OH_{357} points towards $[4Fe]_H$ at a 3.4 Å distance. As a result, H_{ox} prefers conformation A, whereas $H_{red}H^+$ prefers conformation B. Thus, the electrostatic effects of OH_{357} were suggested to dynamically tune the redox

properties of the H-cluster.[73] Interestingly, all variants were found to adopt a higher fraction of the $H_{red}H^+$ state under N_2 compared to the wild-type enzyme.[64] This observation agrees well with OH_{357} occupying conformation B as well. Recent findings imply that redox anticooperativity destabilizes the H_{red} state in favor of $H_{red}H^+$.[47,50,74] Therefore, it would be interesting to quantify the amounts of $H_{red}H^+$ in each variant to investigate if a correlation between the electrostatic effect of exchange coupling and the electrostatic repulsion of redox anticooperativity exists.[75] This notion could be supported by further electrochemical studies investigating the redox anticooperativity in the variants. However, a concomitant change in the redox potential of $[4Fe]_H$ and/or FS4A in the variants due to the exchanged amino acids, as might be reflected in the changed *g*-values of FS4A, needs to be considered as well.

Summary

Simulations of temperature-dependent spectra recorded at two different frequencies enabled the partial deconvolution of the H- and F-cluster states in CpI and lead to the revision of earlier reported spectroscopic features. Our study unambiguously demonstrates for the first time highly resolved exchange interactions between the H-cluster and FS4A. Spectral simulation serves to determine the magnitude of the isotropic exchange coupling *J* between H_{ox} and FS4A and provide guidance for its detection in other [FeFe]-hydrogenases. Comparing their magnitude of *J* can contribute to our understanding of the rate-limiting steps and the exchange pathways between the H-cluster and proximal [4Fe4S] cluster. Moreover, the inclusion of a local spin model accounting for polynuclear clusters may provide further insight and eventually elucidate the controversially discussed spin localization in $[2Fe]_H$.

The variants of CpI exhibiting decreased *J*-couplings demonstrate the tunability of the exchange interaction. While the inter-cluster distances are expected to remain the same, the exchange pathway may be modified by the introduction of rigid residues, additional H-bonds, and/or the exclusion of bulk water. Although the present results indicate no correlation between *J* and biochemical features, the understanding of exchange coupling and related spectroscopic properties is essential.

References

[1] W. Lubitz, H. Ogata, O. Rüdiger, E. Reijerse, *Chem. Rev.* **2014**, *114*, 4081–4148.

[2] A. Hemschemeier, T. Happe, *Nat. Rev. Chem.* **2018**, *2*, 231–243.

[3] S. Morra, *Front. Microbiol.* **2022**, *13*, 853626.

[4] M. W. W. Adams, *Biochim. Biophys. Acta BBA - Bioenerg.* **1990**, *1020*, 115–145.

[5] J. W. Peters, *Science* **1998**, *282*, 1853–1858.

[6] W. Lubitz, H. Ogata, O. Rüdiger, E. Reijerse, *Chem. Rev.* **2014**, *114*, 4081–4148.

[7] Y. Nicolet, C. Piras, P. Legrand, C. E. Hatchikian, J. C. Fontecilla-Camps, *Structure* **1999**, *7*, 13–23.

[8] C. V. Popescu, E. Münck, *J. Am. Chem. Soc.* **1999**, *121*, 7877–7884.

[9] A. Silakov, E. J. Reijerse, S. P. J. Albracht, E. C. Hatchikian, W. Lubitz, *J. Am. Chem. Soc.* **2007**, *129*, 11447–11458.

[10] C. Sommer, A. Adamska-Venkatesh, K. Pawlak, J. A. Birrell, O. Rüdiger, E. J. Reijerse, W. Lubitz, *J. Am. Chem. Soc.* **2017**, *139*, 1440–1443.

[11] M. Winkler, M. Senger, J. Duan, J. Esselborn, F. Wittkamp, E. Hofmann, U.-P. Apfel, S. T. Stripp, T. Happe, *Nat. Commun.* **2017**, *8*, 16115.

[12] S. Mebs, R. Kositzki, J. Duan, L. Kertess, M. Senger, F. Wittkamp, U.-P. Apfel, T. Happe, S. T. Stripp, M. Winkler, M. Haumann, *Biochim. Biophys. Acta - Bioenerg.* **2018**, *1859*, 28–41.

[13] J. Esselborn, C. Lambertz, A. Adamska-Venkatesh, T. Simmons, G. Berggren, J. Noth, J. Siebel, A. Hemschemeier, V. Artero, E. Reijerse, M. Fontecave, W. Lubitz, T. Happe, *Nat. Chem. Biol.* **2013**, *9*, 607–609.

[14] G. Berggren, A. Adamska, C. Lambertz, T. R. Simmons, J. Esselborn, M. Atta, S. Gambarelli, J. M. Mouesca, E. Reijerse, W. Lubitz, T. Happe, V. Artero, M. Fontecave, *Nature* **2013**, *499*, 66–69.

[15] J. F. Siebel, A. Adamska-Venkatesh, K. Weber, S. Rumpel, E. Reijerse, W. Lubitz, *Biochemistry* **2015**, *54*, 1474–1483.

[16] G. Goldet, C. Brandmayr, S. T. Stripp, T. Happe, C. Cavazza, J. C. Fontecilla-Camps, F. A. Armstrong, *J. Am. Chem. Soc.* **2009**, *131*, 14979–14989.

[17] A. Kubas, C. Orain, D. De Sancho, L. Saujet, M. Sensi, C. Gauquelin, I. Meynial-Salles, P. Soucaille, H. Bottin, C. Baffert, V. Fourmond, R. B. Best, J. Blumberger, C. Léger, *Nat. Chem.* **2017**, *9*, 88–95.

[18] S. T. Stripp, G. Goldet, C. Brandmayr, O. Sanganas, K. A. Vincent, M. Haumann, F. A. Armstrong, T. Happe, *Proc. Natl. Acad. Sci. U. S. A.* **2009**, *106*, 17331–17336.

[19] P. Rodríguez-Maciá, E. J. Reijerse, M. Van Gastel, S. Debeer, W. Lubitz, O. Rüdiger, J. A. Birrell, *J. Am. Chem. Soc.* **2018**, *140*, 9346–9350.

[20] C. Baffert, M. Demuez, L. Cournac, B. Burlat, B. Guigliarelli, P. Bertrand, L. Girbal, C. Léger, *Angew. Chem. Int. Ed.* **2008**, *47*, 2052–2054.

[21] B. J. Lemon, J. W. Peters, *Biochemistry* **1999**, *38*, 12969–12973.

[22] C. Lambertz, N. Leidel, K. G. V. Havelius, J. Noth, P. Chernev, M. Winkler, T. Happe, M. Haumann, *J. Biol. Chem.* **2011**, *286*, 40614–40623.

[23] J. Duan, A. Hemschemeier, D. J. Burr, S. T. Stripp, E. Hofmann, T. Happe, *Angew. Chem. Int. Ed.* **2023**, *1*, e202216903.

[24] L. S. Mészáros, P. Ceccaldi, M. Lorenzi, H. J. Redman, E. Pfitzner, J. Heberle, M. Senger, S. T. Stripp, G. Berggren, *Chem. Sci.* **2020**, *11*, 4608–4617.

[25] M. Senger, S. Mebs, J. Duan, O. Shulenina, K. Laun, L. Kertess, F. Wittkamp, U. P. Apfel, T. Happe, M. Winkler, M. Haumann, S. T. Stripp, *Phys. Chem. Chem. Phys.* **2018**, *20*, 3128–3140.

[26] M. Senger, K. Laun, F. Wittkamp, J. Duan, M. Haumann, T. Happe, M. Winkler, U.-P. Apfel, S. T. Stripp, *Angew. Chem. Int. Ed.* **2017**, *56*, 16503–16506.

[27] F. Wittkamp, M. Senger, S. T. Stripp, U.-P. Apfel, *Chem. Commun.* **2018**, *54*, 5934–5942.

[28] K. Laun, I. Baranova, J. Duan, L. Kertess, F. Wittkamp, U.-P. Apfel, T. Happe, M. Senger, S. T. Stripp, *Dalton Trans.* **2021**, *50*, 3641–3650.

[29] M. L. K. Sanchez, C. Sommer, E. Reijerse, J. A. Birrell, W. Lubitz, R. B. Dyer, *J. Am. Chem. Soc.* **2019**, *141*, 16064–16070.

[30] J.-S. Chen, L. E. Mortenson, *Biochim Biophys Acta* **1974**, *371*, 283–298.

[31] L. E. Mortenson, G. Nakos, *Biochemistry* **1971**, *10*, 2442–2449.

[32] J. B. Therien, J. H. Artz, S. Poudel, T. L. Hamilton, Z. Liu, S. M. Noone, M. W. W. Adams, P. W. King, D. A. Bryant, E. S. Boyd, J. W. Peters, *Front. Microbiol.* **2017**, *8*, 1–11.

[33] M. W. W. Adams, E. Eccleston, J. B. Howard, *Proc. Natl. Acad. Sci. U. S. A.* **1989**, *86*, 4932–4936.

[34] B. Bennett, B. J. Lemon, J. W. Peters, *Biochemistry* **2000**, *39*, 7455–7460.

[35] M. W. W. Adams, *Biochim. Biophys. Acta BBA - Bioenerg.* **1990**, *1020*, 115–145.

[36] A. T. Kowal, M. W. W. Adams, M. K. Johnson, *J. Biol. Chem.* **1989**, *264*, 4342–4348.

[37] D. L. Erbes, R. H. Burris, W. H. Orme Johnson, *Proc. Natl. Acad. Sci. U. S. A.* **1975**, *72*, 4795–4799.

[38] I. C. Zambrano, A. T. Kowal, L. E. Mortenson, M. W. W. Adams, M. K. Johnson, *J. Biol. Chem.* **1989**, *264*, 20974–20983.

[39] J. Telser, M. J. Benecky, M. W. Adams, L. E. Mortenson, B. M. Hoffman, *J. Biol. Chem.* **1987**, *262*, 6589–6594.

[40] J. Telser, M. J. Benecky, M. W. W. Adams, L. E. Mortenson, B. M. Hoffman, *J. Biol. Chem.* **1986**, *261*, 13536–13541.

[41] J. H. Artz, D. W. Mulder, M. W. Ratzloff, C. E. Lubner, O. A. Zadvornyy, A. X. Levan, S. G. Williams, M. W. W. W. Adams, A. K. Jones, P. W. King, J. W. Peters, *J. Am. Chem. Soc.* **2017**, *139*, 9544–9550.

[42] C. E. Lubner, J. H. Artz, D. W. Mulder, A. Oza, R. J. Ward, S. G. Williams, A. K. Jones, J. W. Peters, I. I. Smalyukh, V. S. Bharadwaj, P. W. King, *Chem. Sci.* **2022**, 4581–4588.

[43] C. Gauquelin, C. Baffert, P. Richaud, E. Kamionka, E. Etienne, D. Guieysse, L. Girbal, V. Fourmond, I. André, B. Guigliarelli, C. Léger, P. Soucaille, I. Meynial-Salles, *Biochim. Biophys. Acta - Bioenerg.* **2018**, *1859*, 69–77.

[44] H. Adamson, M. Robinson, J. J. Wright, L. A. Flanagan, J. Walton, D. Elton, D. J. Gavaghan, A. M. Bond, M. M. Roessler, A. Parkin, *J. Am. Chem. Soc.* **2017**, *139*, 10677–10686.

[45] M.-E. Pandelia, W. Nitschke, P. Infossi, M.-T. Giudici-Orticoni, E. Bill, W. Lubitz, *Proc. Natl. Acad. Sci.* **2011**, *108*, 6097–6102.

[46] P. Wulff, C. Thomas, F. Sargent, F. A. Armstrong, *JBIC J. Biol. Inorg. Chem.* **2016**, *21*, 121–134.

[47] G. Caserta, C. Papini, A. Adamska-Venkatesh, L. Pecqueur, C. Sommer, E. Reijerse, W. Lubitz, C. Gauquelin, I. Meynial-Salles, D. Pramanik, V. Artero, M. Atta, M. del Barrio, B. Faivre, V. Fourmond, C. Léger, M. Fontecave, *J. Am. Chem. Soc.* **2018**, *140*, 5516–5526.

[48] J. Esselborn, N. Muraki, K. Klein, V. Engelbrecht, N. Metzler-Nolte, U. P. Apfel, E. Hofmann, G. Kurisu, T. Happe, *Chem. Sci.* **2016**, *7*, 959–968.

[49] P. Rodríguez-Maciá, K. Pawlak, O. Rüdiger, E. J. Reijerse, W. Lubitz, J. A. Birrell, *J. Am. Chem. Soc.* **2017**, *139*, 15122–15134.

[50] P. Rodríguez-Maciá, N. Breuer, S. Debeer, J. A. Birrell, *ACS Catal.* **2020**, *10*, 13084–13095.

[51] J. W. Van Der Zwaan, S. P. J. Albracht, R. D. Fontijn, P. Mul, *Eur. J. Biochem.* **1987**, *169*, 377–384.

[52] S. P. J. Albracht, J. W. Van Der Zwaan, R. D. Fontijn, *BBA - Bioenerg.* **1984**, *766*, 245–258.

[53] K. K. Surerus, E. Münck, M. Chen, J. W. van der Zwaan, M. Kolk, E. C. Duin, F. M. Rusnak, S. P. J. Albracht, *Biochemistry* **1994**, *33*, 4980–4993.

[54] R. Cammack, D. S. Patil, V. M. Fernandez, *Biochem. Soc. Trans.* **1985**, *13*, 572–578.

[55] M. Teixeira, I. Moura, A. V. Xavier, B. H. Huynh, D. V. DerVartanian, H. D. Peck, J. LeGall, J. J. Moura, *J. Biol. Chem.* **1985**, *260*, 8942–8950.

[56] B. Guigliarelli, C. More, A. Foumel, M. Asso, P. Bertrand, E. Claude Hatchikian, R. Williams, R. Cammack, *Biochemistry* **1995**, *34*, 4781–4790.

[57] A. S. Pereira, P. Tavares, I. Moura, J. J. G. Moura, B. H. Huynh, *J. Am. Chem. Soc.* **2001**, *123*, 2771–2782.

[58] W. K. Myers, T. A. Stich, D. L. M. Suess, J. M. Kuchenreuther, J. R. Swartz, R. D. Britt, *J. Am. Chem. Soc.* **2014**, *136*, 12237–12240.

[59] A. Bencini, D. Gatteschi, *Electron Paramagnetic Resonance of Exchange Coupled Systems*, Springer Berlin Heidelberg, **1990**.

[60] M. E. Pandelia, D. Bykov, R. Izsak, P. Infossi, M. T. Giudici-Orticoni, E. Bill, F. Neese, W. Lubitz, *Proc. Natl. Acad. Sci. U. S. A.* **2013**, *110*, 483–488.

[61] A. Fournel, S. Gambarelli, B. Guigliarelli, C. More, M. Asso, G. Chouteau, R. Hille, P. Bertrand, *J. Chem. Phys.* **1998**, *109*, 10905–10913.

[62] C. More, P. Camensuli, F. Dole, B. Guigliarelli, M. Asso, A. Fournel, P. Bertrand, P. Betrand, *J. Biol. Inorg. Chem.* **1996**, *1*, 152–161.

[63] M. Senger, S. Mebs, J. Duan, F. Wittkamp, U. P. Apfel, J. Heberle, M. Haumann, S. T. Stripp, *Proc. Natl. Acad. Sci. U. S. A.* **2016**, *113*, 8454–8459.

[64] C. Brocks, C. Das, J. Duan, S. Yadav, U. P. Apfel, S. Ghosh, E. Hofmann, M. Winkler, V. Engelbrecht, L. V. Schäfer, T. Happe, *Manuscr. Submitt. Publ.* **2023**.

[65] A. Adamska-Venkatesh, T. R. Simmons, J. F. Siebel, V. Artero, M. Fontecave, E. Reijerse, W. Lubitz, *Phys. Chem. Chem. Phys.* **2015**, *17*, 5421–5430.

[66] A. T. Fiedler, T. C. Brunold, *Inorg. Chem.* **2005**, *44*, 9322–9334.

[67] M. L. Ghirardi, *Photosynth. Res.* **2015**, *125*, 383–393.

[68] D. J. Lowe, R. C. Bray, *Biochem. J.* **1978**, *169*, 471–479.

[69] R. A. Marcus, N. Sutin, *Biochim. Biophys. Acta BBA - Rev. Bioenerg.* **1985**, *811*, 265–322.

[70] S. Dementin, V. Belle, P. Bertrand, B. Guigliarelli, G. Adryanczyk-Perrier, A. L. De Lacey, V. M. Fernandez, M. Rousset, C. Léger, *J. Am. Chem. Soc.* **2006**, *128*, 5209–5218.

[71] G. R. Eaton, S. S. Eaton, *Acc. Chem. Res.* **1988**, *21*, 107–113.

[72] P. J. González, M. G. Rivas, A. L. Pérez, C. D. Brondino, *J. Magn. Reson. Open* **2023**, *16–17*, 100117.

[73] J. H. Artz, O. A. Zadvornyy, D. W. Mulder, S. M. Keable, A. E. Cohen, M. W. Ratzloff, S. G. Williams, B. Ginovska, N. Kumar, J. Song, S. E. McPhillips, C. M.

Davidson, A. Y. Lyubimov, N. Pence, G. J. Schut, A. K. Jones, S. M. Soltis, M. W. W. Adams, S. Raugei, P. W. King, J. W. Peters, *J. Am. Chem. Soc.* **2020**, *142*, 1227–1235.

[74] J. A. Birrell, P. Rodríguez-Maciá, E. J. Reijerse, M. A. Martini, W. Lubitz, *Coord. Chem. Rev.* **2021**, *449*, 214191.

[75] L. I. Krishtalik, *Arch. Biochem. Biophys.* **1985**, *243*, 701–702.

SUPPLEMENTAL INFORMATION

Methods

Sample Preparation

A detailed description of the sample preparation can be found in Brocks et al..[1]

Site-directed mutagenesis: To generate hydrogenase-encoding sequences with modified codons, the Quik Change method was employed.[2] Mismatch primer pairs (ordered at Sigma-Aldrich) were used to amplify the expression plasmid pET21b-CpI. The parental DNA template was digested (DpnI; Thermo Fisher Scientific) and the PCR product was introduced into *E. coli* DH5α using the heat-shock method. *Expression and purification:* For the expression of CpI apo-hydrogenases sequences, the expression plasmids with the respective hydrogenase sequences were introduced into *E. coli* strain BL21 (DE3) ΔiscR.[3] Expression and subsequent protein purification were done as already reported.[3] To avoid any O_2 contamination, the Coy Laboratory Anaerobic vinyl tent (98.5 % N_2, 1.5 % H_2) was used. The protein was eluted in 0.1 M Tris-HCl pH 8 buffer, containing 2 mM of sodium dithionite (NaDT). *In vitro maturation of [FeFe]-hydrogenases:* Purified apo-CpI proteins, lacking the $[2Fe]_H$-subcluster, were maturated in vitro with the synthetic mimic of the native $[2Fe]_H$-complex carrying an azadithiolate ligand (adt) or propanedithiolate ligand (pdt) as reported before.[4,5] The samples for EPR spectroscopy were either gassed with N_2 for 60 min, O_2 for 20 min, or CO for 30 min and transferred to 2.8 mm Quartz tubes.
In vitro H_2 production assay: To determine the specific H_2 production activities of wild-type CpI and variants, 400 ng of holo proteins in 0.1 M KPI pH 6.8 were mixed with methyl viologen (MV) as an electron mediator (10 mM) and NaDT as sacrificial electron donor (100 mM) in 8-ml headspace vials. The vials were sealed airtight with red Suba-Seal septa and the headspace of each vial was purged with 100 % argon for 5 min. After incubating the reaction mixtures in a shaking water bath (100 rpm) at 37 °C for 20 minutes, H_2 was quantified in 400 µl of the headspace of each sample by gas chromatography (GC-2010, Shimadzu).

Continuous Wave X-band EPR spectroscopy

X-band (9.5 GHz) continuous wave electron paramagnetic resonance (EPR) experiments were performed on a Bruker Elexsys E500 spectrometer fitted with an Oxford Instruments ESR-900 helium-gas flow for cryogenic temperature studies. The experimental parameters were as follows: 100 kHz modulation frequency, 3 G modulation amplitude, 82 ms conversion time, 1.28 ms time constant, 0.1-10 mW microwave power, and 1-10 scans. The spectra were normalized, processed, and baseline-corrected using Matlab.

Pulsed Q-band EPR spectroscopy

Q-band (34 GHz) pulsed EPR measurements were carried out using a Bruker Elexsys E580 spectrometer equipped with a 150 W TWT amplifier, Bruker ER 5106QT-2 resonator, Bruker SpinJet AWG, Oxford Instruments CF935 continuous-flow helium cryostat and Oxford Instruments MercuryiTC temperature controller using a Hahn-echo pulse sequence (electron spin echo-field sweep, ESE-FS). One to five scans were taken for each spectrum with gaussian pulse lengths of $\pi/2$ = 11-15 ns and π = 22-30 ns, respectively, an interpulse delay of 250-260 ns, a shot repetition time between 0.5 and 2 ms, and a microwave power of 20 mW. The spectra were normalized, processed, and baseline-corrected using Matlab.

Theoretical Background and Simulation of Exchange Coupled Systems

Electron-electron interactions can occur due to the direct overlap of orbitals or interaction between them via mediating atoms, or through dipole-dipole interaction when the paramagnets are farther apart.[6,7] Isotropic exchange interactions between two spins S_1 and S_2 can be described by the spin Hamiltonian: $H_{ex} = J S_1 S_2$, where J is the isotropic exchange interaction.

The simulation of spectra was performed with the pepper function of *EasySpin*[8] including 4-7 distinct systems, whose *g*-values were kept constant for each variant at X- and Q-band frequencies and distinct temperatures. At elevated temperatures, some *g*-values could be obtained from spectra where species were isolated due to slower relaxation. For H_{ox}-FS4A the simulation of the X- and Q-band data was fitted sufficiently with an isotropic exchange coupling *J*. The inclusion and least-square fitting of dipolar, symmetric, or antisymmetric interactions did not significantly alter the spectrum or changed the exchange interaction, but significantly increased simulation times and uncertainties. Least-square simulations of CpI(pdt) at 30 K performed with and without the contribution of FS2 yielded an error for the *J*-value of H_{ox}-FS4A of $\Delta J = \pm 0.7 \bullet 10^{-3}$ cm^{-1} and is only marginally influenced by changes in the FS4A *g*-values (even setting FS4A's $g_x = 2.08$). The *g*-values of the FS4A cluster likewise showed only small changes ($\Delta g = \pm 0.01$) until there is a significant deterioration of the fit H_{ox}-FS4A. Simulations of the X-band CW EPR spectra reacted even more sensitively to changes in *g*- and *J*-values. The pulsed Q-band EPR spectra were pseudo-modulated with a modulation amplitude of 2 mT. To account for changes in *g*-strain/line width, the simulations of CW EPR spectra were performed with 1 mT modulation amplitude. The *g*-strain was adjusted for each system and additionally, the *g*-strain of the coupled system was varied independently from the uncoupled species to account for additional exchange broadening. The RMSD value for all simulations was usually below 0.07. To enable the feasibility of simulations at lower temperatures, FS* was introduced, which accounts for all unresolved FeS cluster contributions and thus, can not be associated with a definite species. Thus, FS* varies for each variant. The introduction of FS* is not expected to influence the exchange coupling *J*, whose determination is the primary goal of this study. For the simulation of H_{ox}-CO-FS4A, isotropic exchange couplings resulted in an insufficient fit. The introduction of anisotropic and asymmetric terms, which were implemented by the usage of the EasySpin function *ee*, however, are expected to be negligible in systems exhibiting only weak exchange interactions. Therefore, the additional contribution is expected to arise from dipole-dipole interactions.[9] The resulting simulations, however, do not fit sufficiently well and result in a higher RMSD value > 1. Due to the delocalized spin density in FeS clusters and the additional exchange interaction between $[4Fe]_H$ and $[2Fe]_H$,[10] no further information is derived from this simple model. Nevertheless, Bertrand et al.[11] and More et al.[12] showed that the dipole model is a good approximation for a local spin model. The latter implements spin projection factors accounting for the delocalized spin densities in FeS clusters, which currently extend the scope of this work.

Presence of H_{ox}-CO in pdt-maturated enzymes

CpI(pdt) treated with N_2 reveals a small contribution from H_{ox}-CO, which is more pronounced at elevated temperatures. H_{ox}-CO was previously not observed in pdt-maturated samples and is absent in the corresponding FTIR data. The absence of H_{ox}-CO is attributed to a non-accessibility of CO to the open coordination site and suggested to arise from sterical hindrance due to the larger methylene bridgehead or the inability of the unprotonatable bridgehead to form hydrogen bonds with the protein surrounding leading to the relocation of the bridgehead position.[13,14] Another study proposes a lacking hydrogen bond between the pdt bridgehead and an apical CN^- ligand as a cause for reduced H_{ox}-CO formation.[15] Nevertheless, the same study was able to convert pdt-maturated CpI into the H_{ox}-CO state. EPR spectroscopy may be a more sensitive method, which enables the detection of lower fractions of H_{ox}-CO compared to FTIR spectroscopy. Thus, the presence of H_{ox}-CO observed by Artz et al. in their redox potentiometry on CpI(pdt) might be reasonable.[16]

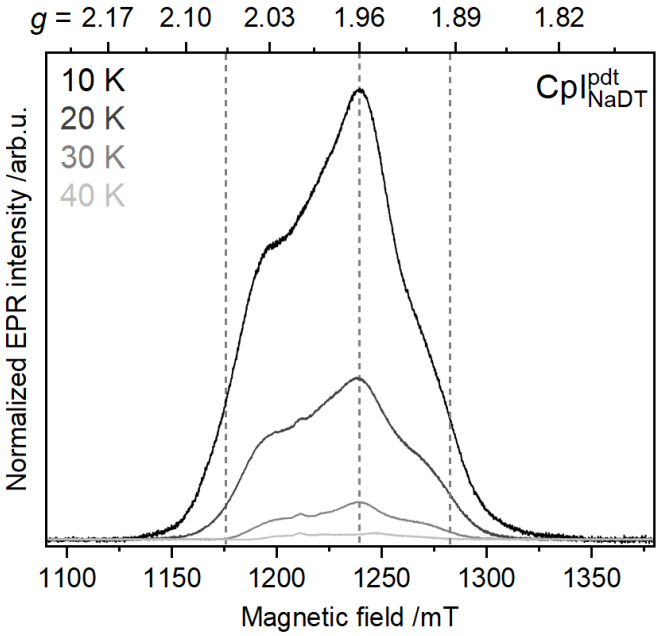

Figure S1: ESE-FS detected EPR spectra (34 GHz, *T* = 10-40 K) of CpI(pdt) treated with 10 mM NaDT. The approximate *g*-values of the spectrum recorded at 10 K are indicated by dashed grey lines.

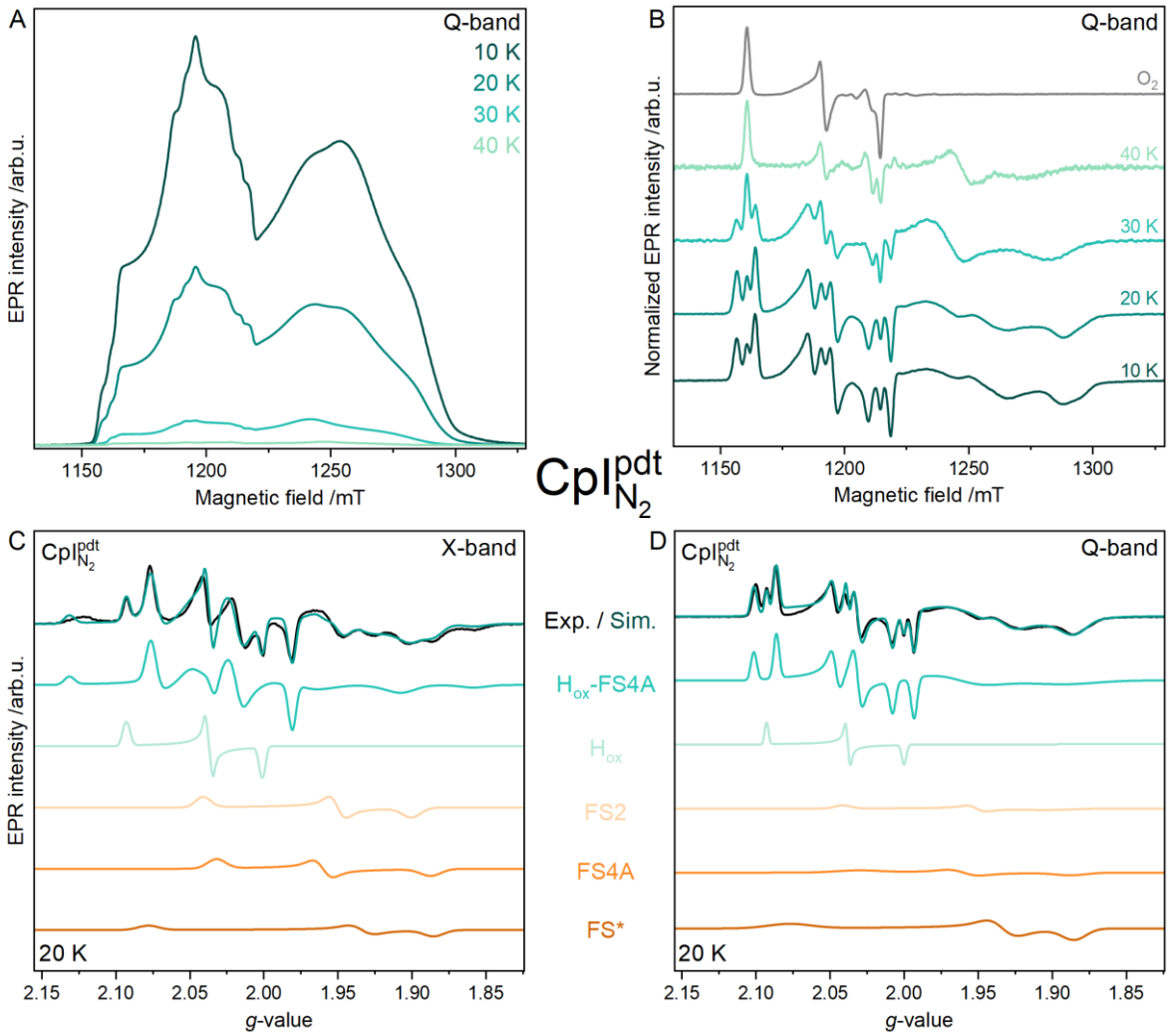

Figure S2: EPR spectra of wild-type CpI(pdt) treated with N_2 and respective simulations. (**A**) Temperature-dependent absorption pulsed EPR spectra (34 GHz). (**B**) Temperature-dependent pseudo-modulated pulsed EPR spectra (34 GHz) of CpI(pdt) treated with O_2 (T = 10 K, top trace) and treated with N_2 recorded at different temperatures normalized to their maximum signal amplitude. The asterisks mark unknown signal contributions. (**C**) CW EPR spectrum (9.5 GHz, T = 30 K, 0.1 mW microwave power) and (**D**) pseudo-modulated pulsed EPR spectrum (34 GHz, T = 20 K) (experimental trace shown in black) and their respective total simulation (colored top trace) and the single contributions as indicated in the center. The respective simulation parameters are listed in Table S1.

Table S1: Simulation parameters of wild-type CpI(pdt) with distinct *g*-strain (if any) and weight percentage used for the spectral simulations at X-band (upper row) and Q-band (lower row), respectively.

System	*g*-tensor			*g*-strain			Weight /%	*J* /10^{-3} cm^{-1}
$F_{red}H_{ox}$	H_{ox} + FS4A			slightly changed			17 18	8.2 ± 0.7
H_{ox}	2.093	2.039	2.001	0.003	0.004	0.003	10	-
				0.003	0.004	0.003	9	
FS4A	2.032	1.960	1.888	0.032	0.014	0.015	30	
				0.035	0.020	0.024	16	
FS2	2.041	1.950	1.900	0.015	0.012	0.014	22	
				0.012	0.012	0.037	10	
FS*	2.067	1.934	1.885	0.034	0.016	0.015	20	
				0.034	0.019	0.019	46	

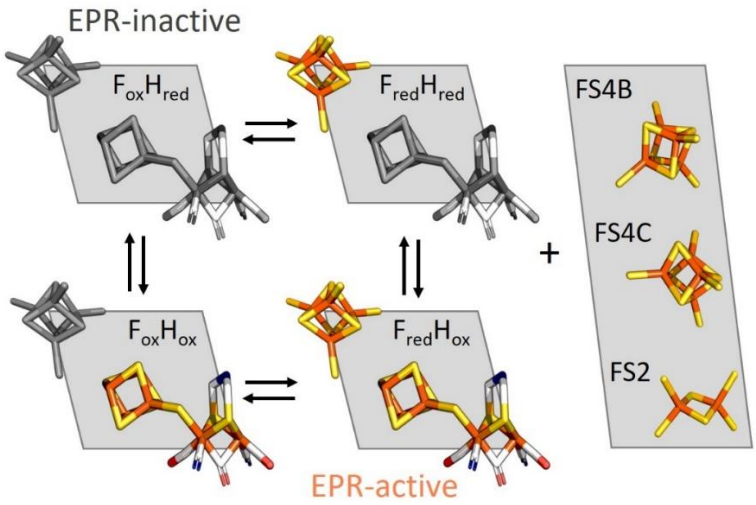

Figure S3: Coupling scheme of the H-cluster (here based on H_{ox}) and the proximal [4Fe4S] cluster FS4A. Further paramagnetic species are the accessory FeS clusters, FS4B, FS4C, and FS2. The FeS clusters are shown as spheres, where gray-colored clusters are diamagnetic and colored clusters are paramagnetic. Atomic coloring: Fe: orange, S: yellow, C: grey, O: red, N: blue.

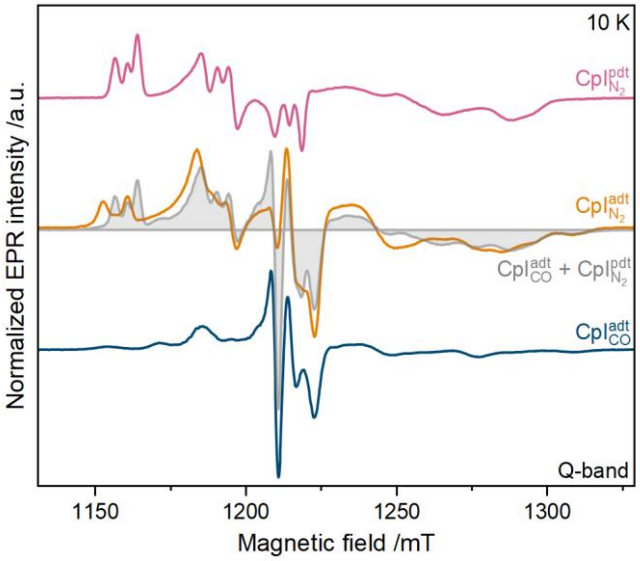

Figure S4: Comparison of ESE-FS spectra (34 GHz, T = 10 K) of different sample preparations of CpI(adt) and CpI(pdt). The sum (grey filled area) of CpI(pdt) treated with N_2 (pink trace) and CpI(adt) treated with CO (blue trace) is very similar to CpI(adt) treated with N_2 (orange trace) in consideration of the slightly distinct *g*-values observed for H_{ox} in adt- and pdt-maturated enzymes. This observation highlights that two distinct total simulations reflect the whole system.

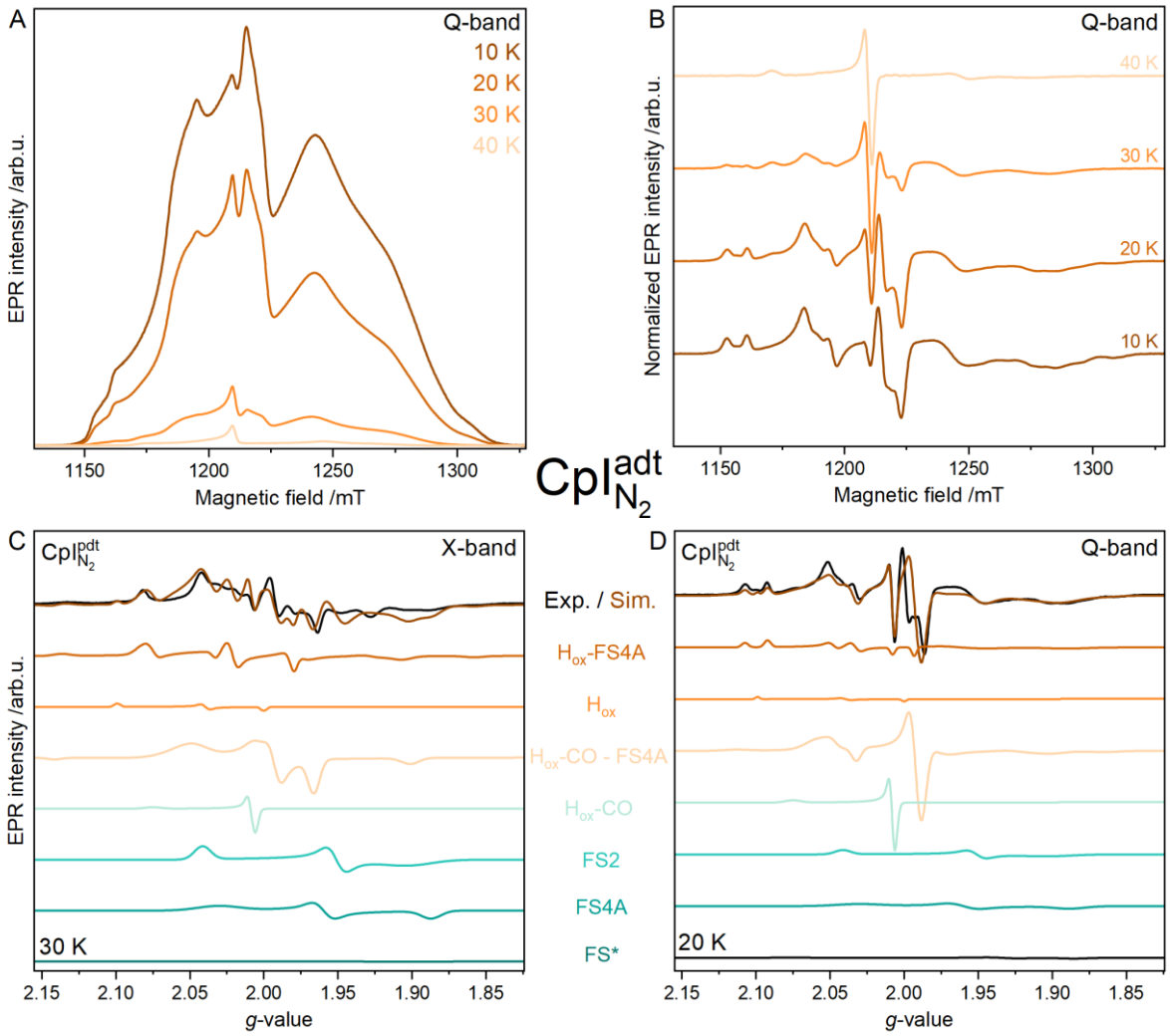

Figure S5: EPR spectra of wild-type CpI(adt) treated with N_2 and respective simulations. (**A**) Temperature-dependent absorption pulsed EPR spectra (34 GHz). (**B**) Temperature-dependent pseudo-modulated pulsed EPR spectra (34 GHz) of CpI(pdt) treated with N_2 recorded at different temperatures normalized to their maximum signal amplitude. The asterisks mark unknown signal contributions. (**C**) CW EPR spectrum (9.5 GHz, T = 30 K, 1 mW microwave power) and (**D**) pseudo-modulated pulsed EPR spectrum (34 GHz, T = 20 K) (experimental trace shown in black) and their respective total simulation (colored top trace) and the single contributions as indicated in the center. The respective simulation parameters are listed in Table S2.

Table S2: Simulation parameters for wild-type CpI(adt) with distinct *g*-strain (if any) and weight percentage used for the spectral simulations at X-band (upper row) and Q-band (lower row), respectively. The $F_{red}H_{ox}$-CO system has an additional dipolar contribution to the exchange coupling indicated below *J*.

System	*g*-tensor			*g*-strain			Weight /%	*J* /10^{-3} cm^{-1}
$F_{red}H_{ox}$	H_{ox} + FS4A			slightly changed			9 8	8.2 ± 0.7
H_{ox}	2.099	2.040	2.000	0.003	0.004	0.003	2	-
				0.002	0.006	0.003	2	
FS4A	2.032	1.960	1.888	0.032	0.014	0.015	31	
				0.035	0.020	0.024	32	
FS2	2.041	1.950	1.900	0.012	0.012	0.037	40	
				0.012	0.012	0.037	27	
FS*	2.078	1.934	1.885	0.034	0.016	0.015	0	
				0.034	0.019	0.019	1	
$F_{red}H_{ox}$-CO	H_{ox}-CO + FS4A			slightly changed			15 23	28.1 ± 0.7 1.7, 4.5, -6.1
H_{ox}-CO	2.075	2.008	2.007	0.012	0.003	0.004	3	-
				0.012	0.003	0.004	8	

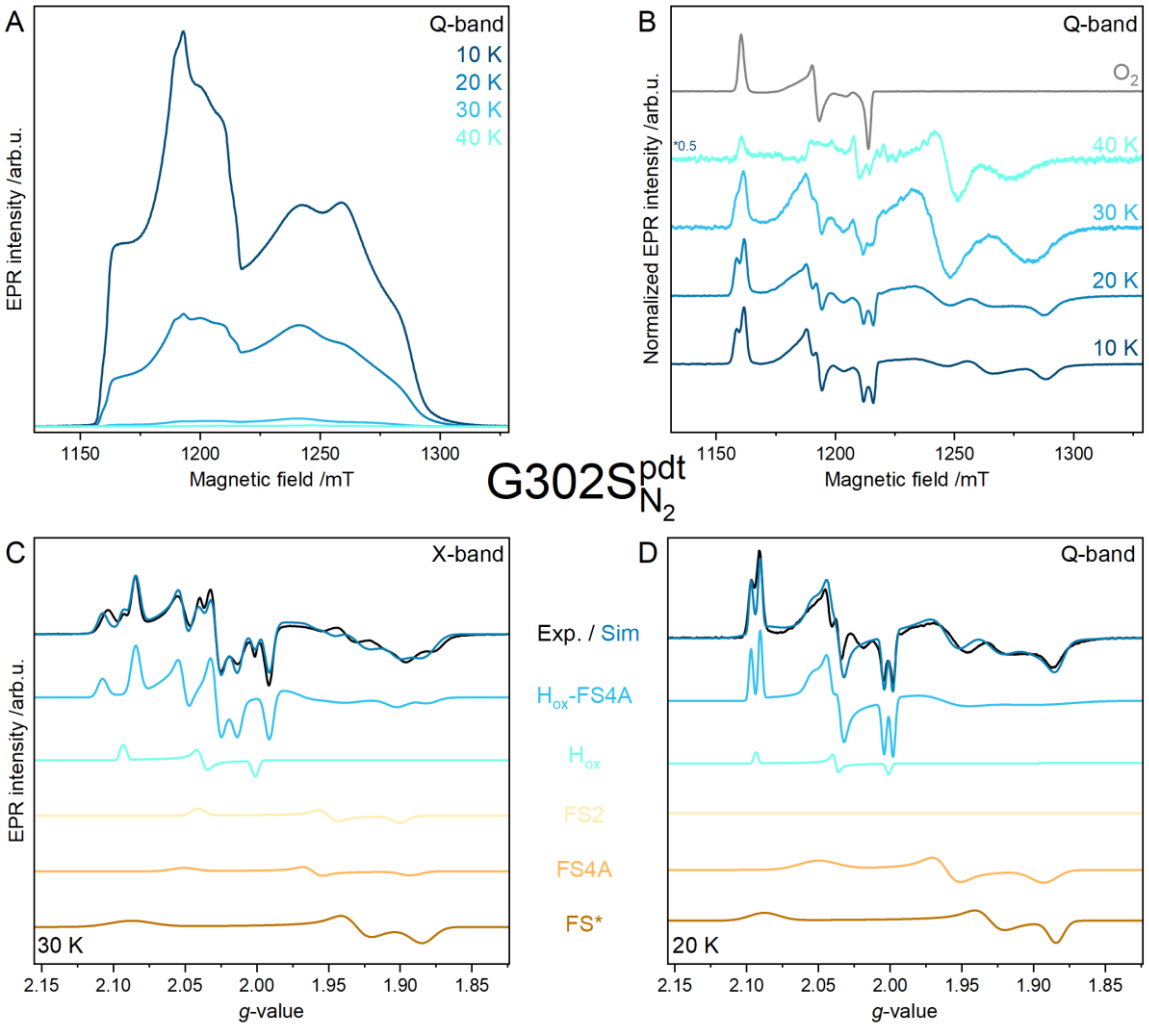

Figure S6: EPR spectra of CpI variant G302S(pdt) treated with N_2 and respective simulations. (**A**) Temperature-dependent absorption pulsed EPR spectra (34 GHz). (**B**) Temperature-dependent pseudo-modulated pulsed EPR spectra (34 GHz) of G302S(pdt) treated with O_2 (T = 10 K, top trace) and treated with N_2 recorded at different temperatures normalized to their maximum signal amplitude. The asterisks mark unknown signal contributions. (**C**) CW EPR spectrum (9.5 GHz, T = 30 K, 10 mW microwave power) and (**D**) pseudo-modulated pulsed EPR spectrum (34 GHz, T = 20 K) (experimental trace shown in black) and their respective total simulation (colored top trace) and the single contributions as indicated in the center. The respective simulation parameters are listed in Table S3.

Table S3: Simulation parameters for CpI variant G302S(pdt) with distinct *g*-strain (if any) and weight percentage used for the spectral simulations at X-band (upper row) and Q-band (lower row), respectively.

System	*g*-tensor			*g*-strain			Weight /%	*J* /10^{-3} cm^{-1}
$F_{red}H_{ox}$	H_{ox} + FS4A			slightly changed			21 15	3.5 ± 0.7
H_{ox}	2.093	2.038	2.001	0.003	0.006	0.004	7	-
				0.002	0.003	0.003	3	
FS4A	2.051	1.961	1.893	0.020	0.012	0.016	11	
				0.031	0.018	0.021	41	
FS2	2.041	1.950	1.900	0.010	0.012	0.012	12	
				0.012	0.012	0.037	0	
FS*	2.088	1.931	1.884	0.034	0.019	0.019	49	
				0.024	0.019	0.012	41	

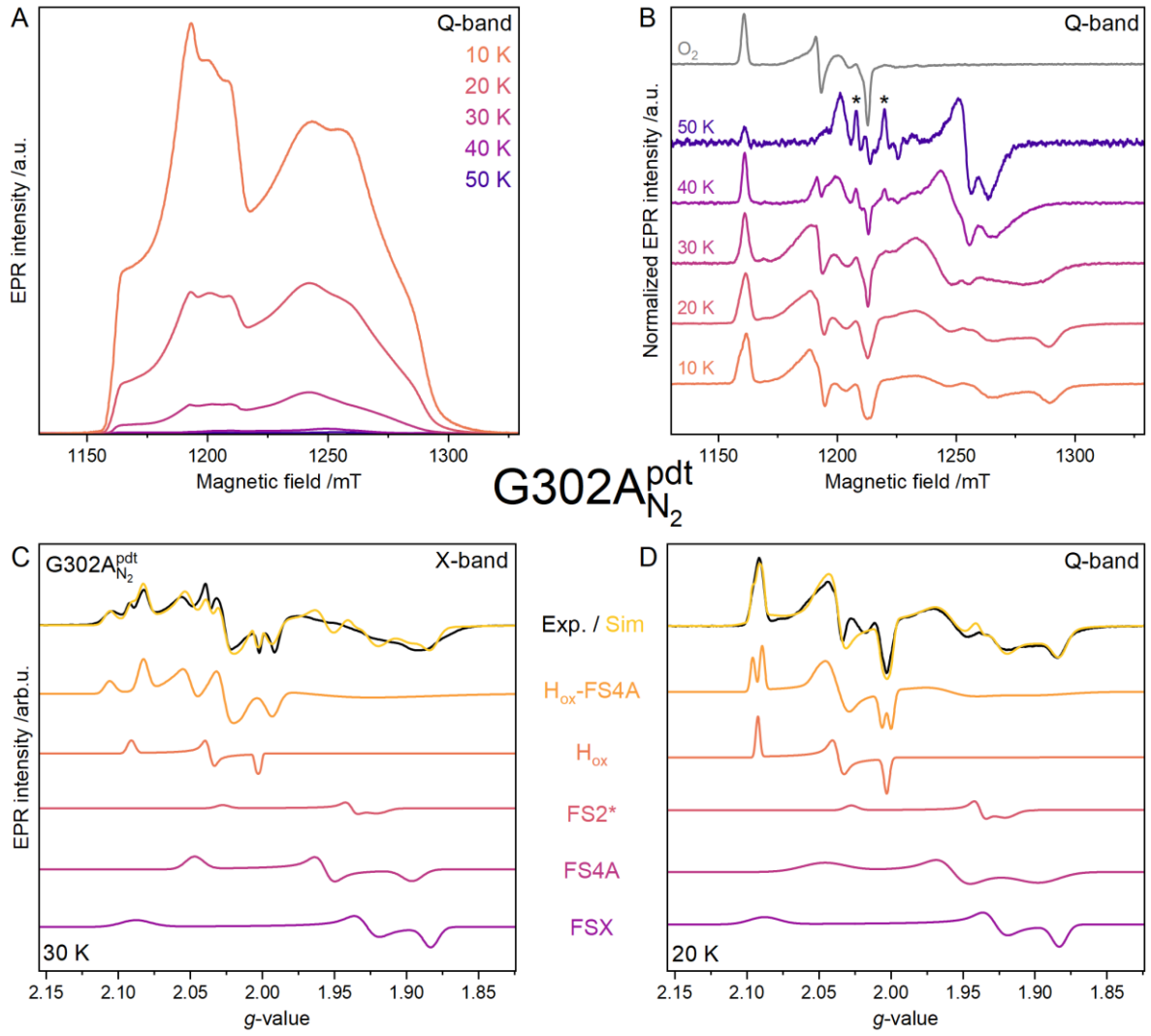

Figure S7: EPR spectra of CpI variant G302A(pdt) treated with N_2 and respective simulations. (**A**) Temperature-dependent absorption pulsed EPR spectra (34 GHz). (**B**) Temperature-dependent pseudo-modulated pulsed EPR spectra (34 GHz) of CpI(pdt) treated with O_2 (T = 10 K, top trace) and treated with N_2 recorded at different temperatures normalized to their maximum signal amplitude. The asterisks mark unknown signal contributions. (**C**) CW EPR spectrum (9.5 GHz, T = 30 K, 1 mW microwave power) and (**D**) pseudo-modulated pulsed EPR spectrum (34 GHz, T = 20 K) (experimental trace shown in black) and their respective total simulation (colored top trace) and the single contributions as indicated in the center. The respective simulation parameters are listed in Table S4.

Table S4: Simulation parameters for CpI variant G302A(pdt) with distinct *g*-strain (if any) and weight percentage used for the spectral simulations at X-band (upper row) and Q-band (lower row), respectively.

System	*g*-tensor			*g*-strain			Weight /%	*J* /10^{-3} cm^{-1}
$F_{red}H_{ox}$	H_{ox} + FS4A			slightly changed			16 10	3.5 ± 0.7
H_{ox}	2.092	2.037	2.003	0.005	0.004	0.002	7	-
				0.002	0.007	0.004	9	
FS4A	2.047	1.957	1.896	0.014	0.012	0.016	31	
				0.036	0.021	0.032	41	
FS2*	2.028	1.938	1.919	0.010	0.007	0.015	5	
				0.010	0.007	0.015	6	
FS*	2.088	1.928	1.883	0.024	0.016	0.012	41	
				0.024	0.016	0.012	34	

Supporting Discussion on G302A

In comparison to the wild-type enzyme and other variants, G302A exhibits changed relaxation properties of at least one FeS cluster at elevated temperatures. At 50 K a dominant signal with *g* = 2.03, 1.93, 1.91 can be observed. Owing to the slightly changed *g*-values compared to FS2 in the wild-type enzyme and the slow relaxation properties, the signal is attributed to a distinct type of [2Fe2S] cluster, denoted as FS2*. This deviation may arise from long-range structural changes, affecting the electronic properties of FS2.

At lower temperatures, the FS* signal exhibits distinct *g*-values as well. The poor fit in the FeS cluster region of the X-band simulation can presumably be traced back to an increased exchange interaction between the FeS clusters, leading to an enhanced broadening due to the appearance of additional features.

Interestingly, the exchange interaction sets in at a lower temperature compared to the wild-type enzyme. The decoupling of H_{ox} and FS4A caused by the lower exchange coupling observed in G302A may lift the relaxation dependency, leading to a faster relaxation, and thus, lower temperatures are required for the observation of either species.

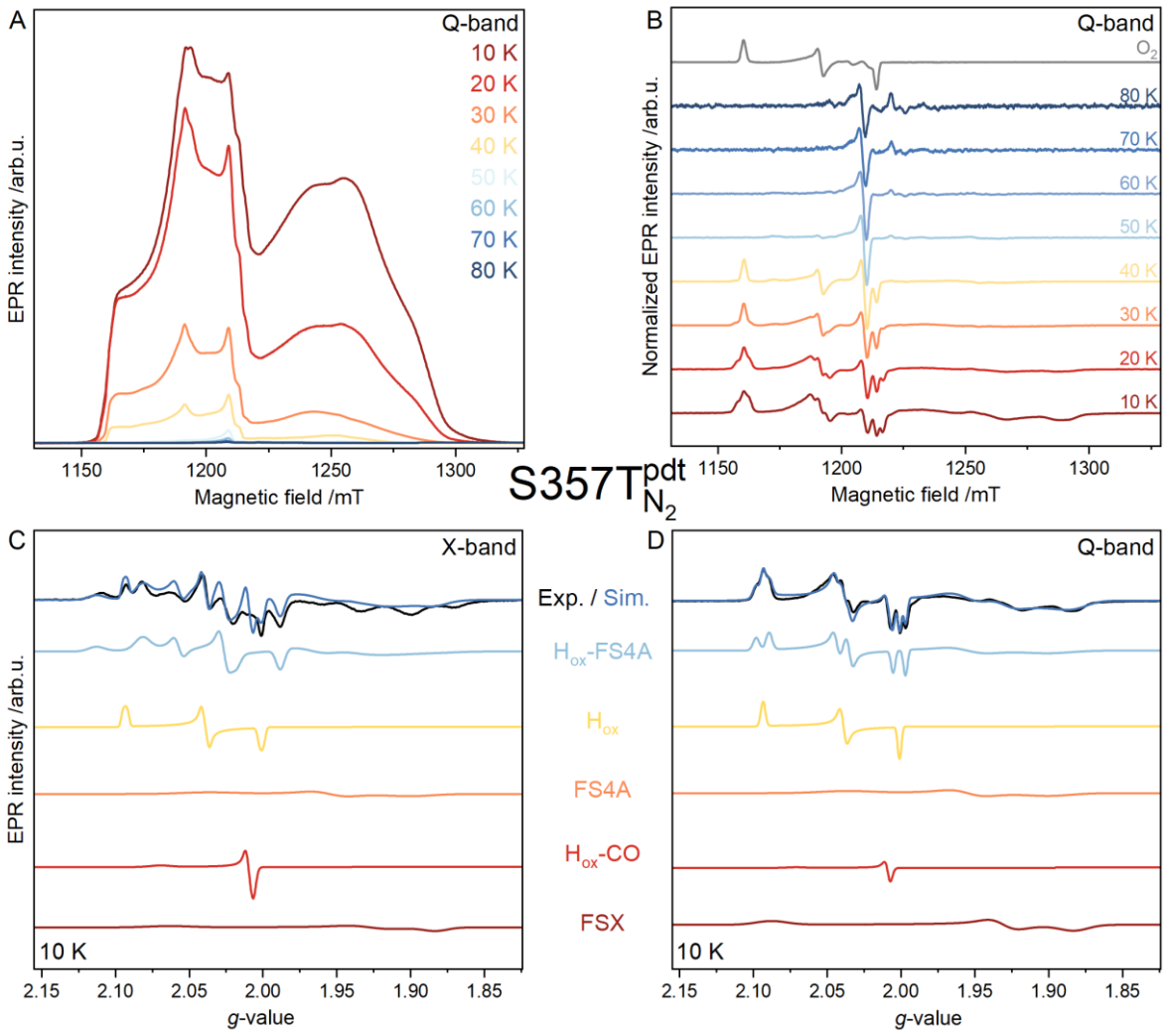

Figure S8: EPR spectra of CpI variant S357T(pdt) treated with N_2 and respective simulations. (**A**) Temperature-dependent absorption pulsed EPR spectra (34 GHz). (**B**) Temperature-dependent pseudo-modulated pulsed EPR spectra (34 GHz) of CpI(pdt) treated with O_2 (T = 10 K, top trace) and treated with N_2 recorded at different temperatures normalized to their maximum signal amplitude. The asterisks mark unknown signal contributions. (**C**) CW EPR spectrum (9.5 GHz, T = 10 K, 1 mW microwave power) and (**D**) pseudo-modulated pulsed EPR spectrum (34 GHz, T = 10 K) (experimental trace shown in black) and their respective total simulation (colored top trace) and the single contributions as indicated in the center. The respective simulation parameters are listed in Table S5.

Table S5: Simulation parameters for CpI variant S357T(pdt) with distinct *g*-strain (if any) and weight percentage used for the spectral simulations at X-band (upper row) and Q-band (lower row), respectively.

System	*g*-tensor			*g*-strain			Weight /%	*J* /10^{-3} cm^{-1}
$F_{red}H_{ox}$	H_{ox} + FS4A			slightly changed			22 13	4.7 ± 0.7
H_{ox}	2.093	2.039	2.001	0.002	0.003	0.002	22	-
				0.003	0.004	0.002	16	
FS4A	2.039	1.955	1.898	0.041	0.023	0.034	25	
				0.041	0.023	0.034	26	
FS2*	2.028	1.938	1.919	0.010	0.007	0.015	1	
				0.012	0.012	0.037	0	
FS*	2.064	1.928	1.883	0.034	0.028	0.018	25	
				0.024	0.019	0.022	44	

Supporting Discussion on S357T

The *g*-values of FS2 are changed in comparison to the wild-type enzyme, similarly as observed in G302S. Moreover, S357T is the only variant that shows a small amount of H_{ox}-CO at elevated temperatures. The presence of H_{ox}-CO is supported by O_2-treated samples, where at elevated temperatures the H_{ox}-CO state can be isolated (see Figure S9), and strongly resembles the CO-treated state from CpI(adt). Although structural differences in the direct vicinity of the active sites of, e.g., CpI(adt) and CpI(pdt), have been excluded from a comparison of crystal structures, the resolution of the respective structures may have been too low for the observation of minor structural changes. A recent high-resolution study for CpI(adt) for example, revealed distinct positions for S357 in CpI(adt) crystals.[17] Furthermore, at temperatures above 60 K a second signal is observable, which resembles an organic radical,[18] R^{ox} from CbA5H,[19] or a [3Fe4S] cluster.[20] However, the signal intensity is comparably low.

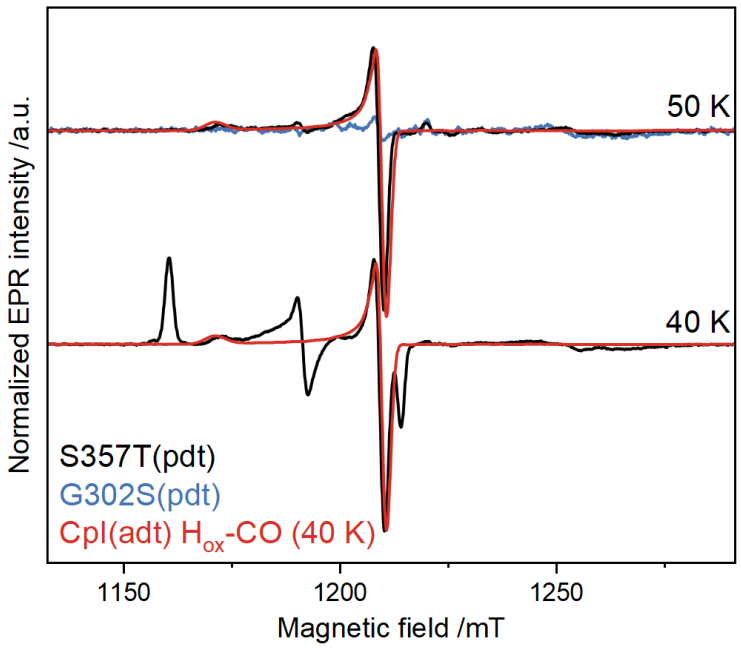

Figure S9: ESE-FS spectra (34 GHz, *T* = 40/50 K) of N_2-treated S357T(pdt) (black trace) and G302S(pdt) (blue trace) in comparison to the H_{ox}-CO state from CpI(adt) (red trace) induced by exposure with CO and recorded at 40 K.

Table S6: Comparison of *g*-values and exchange coupling constants for the magnetically coupled $F_{red}H_{ox}$ state of CpI(pdt) and its variants.

Enzyme	H_{ox}			FS4A			J /10^{-3} cm^{-1}
CpI	2.093	2.039	2.001	2.032	1.960	1.888	8.2
S357T	2.093	2.039	2.001	2.039	1.955	1.898	4.7
G302S	2.094	2.038	2.001	2.051	1.961	1.893	3.5
G302A	2.092	2.037	2.003	2.047	1.957	1.896	3.5

Literature

[1] C. Brocks, C. Das, J. Duan, S. Yadav, U. P. Apfel, S. Ghosh, E. Hofmann, M. Winkler, V. Engelbrecht, L. V. Schäfer, T. Happe, *Manuscr. Submitt. Publ.* **2023**.

[2] L. Zheng, *Nucleic Acids Res.* **2004**, *32*, e115–e115.

[3] J. M. Kuchenreuther, C. S. Grady-Smith, A. S. Bingham, S. J. George, S. P. Cramer, J. R. Swartz, *PLoS ONE* **2010**, *5*, 4–10.

[4] J. Esselborn, C. Lambertz, A. Adamska-Venkatesh, T. Simmons, G. Berggren, J. Noth, J. Siebel, A. Hemschemeier, V. Artero, E. Reijerse, M. Fontecave, W. Lubitz, T. Happe, *Nat. Chem. Biol.* **2013**, *9*, 607–609.

[5] H. Li, T. B. Rauchfuss, *J. Am. Chem. Soc.* **2002**, *124*, 726–727.

[6] G. R. Eaton, S. S. Eaton, in *Spin Labeling Theory Appl.* (Eds.: L.J. Berliner, J. Reuben), Springer US, Boston, MA, **1989**, pp. 339–397.

[7] A. Bencini, D. Gatteschi, *Electron Paramagnetic Resonance of Exchange Coupled Systems*, Springer Berlin Heidelberg, **1990**.

[8] S. Stoll, A. Schweiger, *J. Magn. Reson.* **2006**, *178*, 42–55.

[9] P. J. González, M. G. Rivas, A. L. Pérez, C. D. Brondino, *J. Magn. Reson. Open* **2023**, *16–17*, 100117.

[10] C. V. Popescu, E. Münck, *J. Am. Chem. Soc.* **1999**, *121*, 7877–7884.

[11] P. Bertrand, P. Camensuli, C. More, B. Guigliarelli, *J Am Chem Soc* **1996**, *118*, 1426–1434.

[12] C. More, P. Camensuli, F. Dole, B. Guigliarelli, M. Asso, A. Fournel, P. Bertrand, P. Betrand, *J. Biol. Inorg. Chem.* **1996**, *1*, 152–161.

[13] A. Adamska-Venkatesh, D. Krawietz, J. Siebel, K. Weber, T. Happe, E. Reijerse, W. Lubitz, *J. Am. Chem. Soc.* **2014**, *136*, 11339–11346.

[14] J. Esselborn, N. Muraki, K. Klein, V. Engelbrecht, N. Metzler-Nolte, U. P. Apfel, E. Hofmann, G. Kurisu, T. Happe, *Chem. Sci.* **2016**, *7*, 959–968.

[15] J. Duan, S. Mebs, K. Laun, F. Wittkamp, J. Heberle, T. Happe, E. Hofmann, U. P. Apfel, M. Winkler, M. Senger, M. Haumann, S. T. Stripp, *ACS Catal.* **2019**, *9*, 9140–9149.

[16] J. H. Artz, D. W. Mulder, M. W. Ratzloff, C. E. Lubner, O. A. Zadvornyy, A. X. Levan, S. G. Williams, M. W. W. W. Adams, A. K. Jones, P. W. King, J. W. Peters, *J. Am. Chem. Soc.* **2017**, *139*, 9544–9550.

[17] J. H. Artz, O. A. Zadvornyy, D. W. Mulder, S. M. Keable, A. E. Cohen, M. W. Ratzloff, S. G. Williams, B. Ginovska, N. Kumar, J. Song, S. E. McPhillips, C. M. Davidson, A. Y. Lyubimov, N. Pence, G. J. Schut, A. K. Jones, S. M. Soltis, M. W. W. Adams, S. Raugei, P. W. King, J. W. Peters, *J. Am. Chem. Soc.* **2020**, *142*, 1227–1235.

[18] G. Jeschke, *Biochim. Biophys. Acta - Bioenerg.* **2005**, *1707*, 91–102.

[19] M. Heghmanns, A. Rutz, Y. Kutin, V. Engelbrecht, M. Winkler, T. Happe, M. Kasanmascheff, *Chem. Sci.* **2022**, *13*, 7289–7294.

[20] J. Telser, H.-I. Lee, B. M. Hoffman, *J. Biol. Inorg. Chem.* **2000**, *5*, 369–380.

9

Conclusion and Outlook

Many fundamental studies on FeS proteins were carried out in the past decades with EPR spectroscopy, elucidating some of the magnetic properties, direct and indirect environmental influences, and correlated spectral properties of their FeS clusters. With the rapidly increasing technical and biochemical advancements, multi-frequency approaches, cryo-free systems, higher microwave power, and a toolbox for site-directed manipulations, including mutagenesis, artificial maturation, and isotope-labeling, became readily available. These developments can be exploited to investigate and reevaluate the spectral properties and related functions of new and known FeS clusters.

As is readily evident from simple ferredoxins, the fine-tuning of midpoint potentials, either by inherent structural features or changes in the secondary coordination sphere, is complex and difficult to generalize. Our establishment of pulsed EPR-monitored redox potentiometry at higher frequencies is expected to contribute to the investigation of multi-cluster enzymes by reducing the required protein concentration, providing higher resolution and the possibility of deconvoluting multiple paramagnetic species in one sample preparation.

The subsequent investigation of apo-HydA1, apo-HydA2 and HydF, each carrying a single [4Fe4S] cluster, emphasized once more the case-sensitive dependence of the protein environment and buffer effects on their spectral properties. In particular, the temperature-dependence of the [4Fe4S] cluster, its solvation environment and its behavior under oxygen exposure require further investigation.

The characterization of the [FeFe]-hydrogenase CbA5H with EPR spectroscopy posed another challenge, as from the start of the experiments, a high-resolution crystal structure was missing. The assignment of EPR features to an unknown structure is difficult and requires an interdisciplinary approach. However, methods, such as (isotope-labeled) ENDOR and DEER combined with site-directed mutagenesis, provide valuable insight into the direct environment of the paramagnets and their interaction with distant clusters, respectively, and might in the end experimentally prove the origin of $R^{\bullet ox}$.

The advantages of higher microwave frequencies were shown by means of the [FeFe]-hydrogenase CpI. Although spin-coupling interactions have been long anticipated for these enzymes, their strength was unknown. A multi-frequency approach enabled the simulation and quantification of exchange coupling interactions between the H-cluster and FS4A. Moreover, site-directed variants showed a decreased coupling interaction, which can be associated with a changed exchange pathway. Although the biological function appears to be unaffected in the investigated enzymes, knowledge about the clusters' interaction and how to use it for advantage might be essential for further optimization of H_2 production.

Overall, the investigation of multiple clusters from distinct proteins at higher frequencies helped to expand our library of spectroscopic features related to environmental factors and contributes to our understanding of their yet elusive and hardly predictable characteristics.

Bibliography

[1] J. Olejarz, Y. Iwasa, A. H. Knoll, M. A. Nowak, *Nat Commun* **2021**, *12*, 3985, DOI 10.1038/s41467-021-23286-7.

[2] H. Beinert, *J. Biol. Inorg. Chem.* **2000**, *5*, 2–15, DOI 10.1007/s007750050002.

[3] H. Beinert, *Science* **1997**, *277*, 653–659, DOI 10.1126/science.277.5326.653.

[4] B. Zhang et al., *Proc. Natl. Acad. Sci. U. S. A.* **2012**, *109*, 15734–15739, DOI 10.1073/pnas.1208787109.

[5] R. H. Holm, W. Lo, *Chem. Rev.* **2016**, *116*, 13685–13713, DOI 10.1021/acs.chemrev.6b00276.

[6] E. S. Boyd, K. M. Thomas, Y. Dai, J. M. Boyd, F. W. Outten, *Biochemistry* **2014**, *53*, 5834–5847, DOI 10.1021/bi500488r.

[7] M. A. Wallace et al., *J. Biol. Chem.* **2004**, *279*, 32055–32062, DOI 10.1074/jbc.M403590200.

[8] V. R. Sutton et al., *Biochemistry* **2004**, *43*, 791–798, DOI 10.1021/bi0357053.

[9] B. Halliwell, J. M. Gutteridge, *Biochem J* **1984**, *219*, 1–14, DOI 10.1042/bj2190001.

[10] N. Khoroshilova, C. Popescu, E. Münck, H. Beinert, P. J. Kiley, *Proc. Natl. Acad. Sci. U.S.A.* **1997**, *94*, 6087–6092, DOI 10.1073/pnas.94.12.6087.

[11] J. A. Imlay, *Mol. Microbiol.* **2006**, *59*, 1073–1082, DOI 10.1111/j.1365-2958.2006.05028.x.

[12] M. J. Lukey et al., *J. Am. Chem. Soc.* **2011**, *133*, 16881–16892, DOI 10.1021/ja205393w.

[13] Y. Nicolet, J. C. Fontecilla-Camps in *Iron-Sulfur Clusters in Chemistry and Biology*, De Gruyter, **2014**, pp. 239–266, DOI 10.1515/9783110308426.239.

[14] J. M. Mouesca, L. Noodleman, D. A. Case, B. Lamotte, *Inorg. Chem.* **1995**, *34*, 4347–4359, DOI 10.1021/ic00121a013.

[15] D. C. Rees, *Annu. Rev. Biochem.* **2002**, *71*, 221–246, DOI 10.1146/annurev.biochem.71.110601.135406.

[16] C. Schumann, J. Fernández Méndez, G. Berggren, P. Lindblad, *Front. Microbiol.* **2023**, *14*, 1179607, DOI 10.3389/fmicb.2023.1179607.

[17] W. Lubitz, H. Ogata, O. Rüdiger, E. Reijerse, *Chem. Rev.* **2014**, *114*, 4081–4148, DOI 10.1021/cr4005814.

[18] M. C. Kennedy et al., *Proc Natl Acad Sci USA* **1987**, *84*, 8854–8858, DOI 10.1073/pnas.84.24.8854.

[19] M. K. Johnson, *Curr. Opin. Chem. Biol.* **1998**, *2*, 173–181, DOI 10.1016/S1367-5931(98)80058-6.

[20] H. Beinert, P. J. Kiley, *Curr. Opin. Chem. Biol.* **1999**, *3*, 152–157, DOI 10.1016/S1367-5931(99)80027-1.

[21] M. Atta et al., *Curr. Opin. Struct. Biol.* **2010**, *20*, 684–692, DOI 10.1016/j.sbi.2010.09.009.

[22] Y. Wu, R. M. Brosh, *Nucleic Acids Res* **2012**, *40*, 4247–4260, DOI 10.1093/nar/gks039.

[23] P. Gaudu, N. Moon, B. Weiss, *J. Biol. Chem.* **1997**, *272*, 5082–5086, DOI 10.1074/jbc.272.8.5082.

[24] J. Crack, J. Green, A. J. Thomson, *J. Biol. Chem.* **2004**, *279*, 9278–9286, DOI 10.1074/jbc.M309878200.

[25] T. A. Rouault, *Nat Chem Biol* **2006**, *2*, 406–414, DOI 10.1038/nchembio807.

[26] A. S. Fleischhacker, P. J. Kiley, *Curr. Opin. Chem. Biol.* **2011**, *15*, 335–341, DOI 10.1016/j.cbpa.2011.01.006.

[27] J. Couturier, B. Touraine, J.-F. Briat, F. Gaymard, N. Rouhier, *Front. Plant Sci.* **2013**, *4*, 1–22, DOI 10.3389/fpls.2013.00259.

[28] L. Mortenson, R. Valentine, J. Carnahan, *Biochem. Biophys. Res. Commun.* **1962**, *7*, 448–452, DOI 10.1016/0006-291X(62)90333-9.

[29] R. C. Valentine, *Bacteriol. Rev.* **1964**, *28*, 497–517, DOI 10.1128/br.28.4.497-517.1964.

[30] J. W. Peters, *Science* **1998**, *282*, 1853–1858, DOI 10.1126/science.282.5395.1853.

[31] A. D. Read, R. E. Bentley, S. L. Archer, K. J. Dunham-Snary, *Redox Biology* **2021**, *47*, 102164, DOI 10.1016/j.redox.2021.102164.

[32] C. C. Page, C. C. Moser, P. L. Dutton, *Curr. Opin. Chem. Biol.* **2003**, *7*, 551–556, DOI 10.1016/j.cbpa.2003.08.005.

[33] F. Capozzi, S. Ciurli, C. Luchinat in *Metal Sites in Proteins and Models Redox Centres*, *Vol. 90*, (Eds.: M. J. Clarke et al.), Springer Berlin Heidelberg, **1998**, pp. 127–160, DOI 10.1007/3-540-62888-6_5.

[34] R. H. Sands, H. Beinert, *Biochem. Biophys. Res. Commun.* **1960**, *3*, 47–52, DOI 10.1016/0006-291X(60)90101-7.

[35] K. Tagawa, D. I. Arnon, *Nature* **1962**, *195*, 537–543, DOI 10.1038/195537a0.

[36] J. F. Gibson, D. O. Hall, J. H. Thornley, F. R. Whatley, *Proc. Natl. Acad. Sci. U. S. A.* **1966**, *56*, 987–990, DOI 10.1073/pnas.56.3.987.

[37] J. Telser, H.-I. Lee, B. M. Hoffman, *J. Biol. Inorg. Chem.* **2000**, *5*, 369–380, DOI 10.1007/PL00010666.

[38] A. H. Priem et al., *J. Biol. Inorg. Chem.* **2005**, *10*, 417–424, DOI 10.1007/s00775-005-0656-2.

[39] T. Maly et al., *Biochim. Biophys. Acta - Bioenerg.* **2009**, *1787*, 584–592, DOI 10.1016/j.bbabio.2009.02.003.

[40] G. E. Cutsail, P. E. Doan, B. M. Hoffman, J. Meyer, J. Telser, *J. Biol. Inorg. Chem.* **2012**, *17*, 1137–1150, DOI 10.1007/s00775-012-0927-7.

[41] G. E. Cutsail, J. Telser, B. M. Hoffman, *Biochim. Biophys. Acta - Mol. Cell Res.* **2015**, *1853*, 1370–1394, DOI 10.1016/j.bbamcr.2015.01.025.

[42] W. R. Hagen, *Biomolecular EPR Spectroscopy*, CRC Press, Boca Raton, **2008**, DOI 10.1201/9781420059588.

[43] M. M. Roessler et al., *Proc. Natl. Acad. Sci.* **2010**, *107*, 1930–1935, DOI 10.1073/pnas.0908050107.

[44] J. H. Artz et al., *J. Am. Chem. Soc.* **2017**, *139*, 9544–9550, DOI 10.1021/jacs.7b02099.

[45] K. H. Richardson et al., *Nat Commun* **2021**, *12*, 5387, DOI 10.1038/s41467-021-25527-1.

[46] S. P. Albracht, W. Roseboom, E. C. Hatchikian, *J. Biol. Inorg. Chem.* **2006**, *11*, 88–101, DOI 10.1007/s00775-005-0039-8.

[47] A. Silakov, B. Wenk, E. Reijerse, W. Lubitz, *Phys. Chem. Chem. Phys.* **2009**, *11*, 6592–6599, DOI 10.1039/b905841a.

[48] J. J. Wright, E. Salvadori, H. R. Bridges, J. Hirst, M. M. Roessler, *J. Inorg. Biochem.* **2016**, *162*, 201–206, DOI 10.1016/j.jinorgbio.2016.04.025.

[49] E. I. Stiefel, G. N. Graham in *Bioinorganic Chemistry*, **1994**, DOI 10.1039/b818285j.

[50] A. G. Sykes, R. Cammack in *Advances in Inorganic Chemistry*, Academic Press, **1999**, DOI 10.1002/0470862106.ia116.

[51] *The Molecular Biology of Chloroplasts and Mitochondria in Chlamydomonas*, (Eds.: J. D. Rochaix et al.), Springer Netherlands, Dordrecht, **1998**, DOI 10.1007/0-306-48204-5.

[52] J. D. Rochaix, *FEBS Lett.* **2002**, *529*, 34–38, DOI 10.1016/S0014-5793(02)03181-2.

[53] E. A. Peden et al., *J. Biol. Chem.* **2013**, *288*, 35192–35209, DOI 10.1074/jbc.M113.483727.

[54] W. Yang et al., *Proc. Natl. Acad. Sci.* **2015**, *112*, 14978–14983, DOI 10.1073/pnas.1515240112.

[55] A. Sawyer, M. Winkler, *Photosynth. Res.* **2017**, *134*, 307–316, DOI 10.1007/s11120-017-0409-4.

[56] A. Günzel, V. Engelbrecht, T. Happe, *JBIC J. Biol. Inorg. Chem.* **2022**, *27*, 631–640, DOI 10.1007/s00775-022-01956-1.

[57] I. Bertini, C. Luchinat, A. Provenzani, A. Rosato, P. R. Vasos, *Proteins Struct. Funct. Genet.* **2002**, *46*, 110–127, DOI 10.1002/prot.10009.

[58] M. Schorsch et al., *Proc. Natl. Acad. Sci.* **2018**, *115*, 12111–12120, DOI 10.1073/pnas.1810379115.

[59] V. Subramanian et al., *Plant Physiol* **2019**, *181*, 426–441, DOI 10.1104/pp.19.00457.

[60] A. M. Terauchi et al., *J. Biol. Chem.* **2009**, *284*, 25867–25878.

[61] D. S. Gorman, R. P. Levine, *Plant Physiol.* **1966**, *41*, 1643–1647, DOI 10.1104/pp.41.10.1643.

[62] F. Galván, A. J. Márquez, E. Fernández, *Z. Für Naturforschung C* **1985**, *40*, 373–378, DOI 10.1515/znc-1985-5-615.

[63] K. Fukuyama, *Photosynth. Res.* **2004**, *81*, 289–301, DOI 10.1023/B:PRES.0000036882.19322.0a.

[64] H. Lu, Z. Li, M. Li, D. Duanmu in *Microbial Photosynthesis*, (Ed.: Q. Wang), Springer, Singapore, **2020**, pp. 121–136, DOI 10.1007/978-981-15-3110-1_6.

[65] E. Eroglu, A. Melis, *Int. J. Hydrog. Energy* **2016**, *41*, 12772–12798, DOI 10.1016/j.ijhydene.2016.05.115.

[66] S. B. Mellor, K. Vavitsas, A. Z. Nielsen, P. E. Jensen, *Photosynth. Res.* **2017**, *134*, 329–342, DOI 10.1007/s11120-017-0364-0.

[67] G. Hanke, P. Mulo, *Plant Cell Environ.* **2013**, *36*, 1071–1084, DOI 10.1111/pce.12046.

[68] I. Rasul et al., *Algae Based Polym. Blends Compos.* **2017**, 301–334, DOI 10.1016/b978-0-12-812360-7.00008-2.

[69] T. Happe, A. Hemschemeier, M. Winkler, A. Kaminski, *Trends Plant Sci.* **2002**, *7*, 246–250, DOI 10.1016/S1360-1385(02)02274-4.

[70] M. Forestier et al., *Eur. J. Biochem.* **2003**, *270*, 2750–2758, DOI 10.1046/j.1432-1033.2003.03656.

[71] A. Melis, T. Happe, *Plant Physiology* **2001**, *127*, 740–748, DOI 10.1104/pp.010498.

[72] T. Happe, J. D. Naber, *Eur. J. Biochem.* **1993**, *214*, 475–481, DOI 10.1111/j.1432-1033.1993.tb17944.x.

[73] A. R. Grossman et al., *New Phytol.* **2011**, *190*, 279–288, DOI 10.1111/j.1469-8137.2010.03534.x.

[74] A. R. Limongi et al., *Applied Sciences* **2021**, *11*, 1616, DOI 10.3390/app11041616.

[75] D. Nagarajan, C.-D. Dong, C.-Y. Chen, D.-J. Lee, J.-S. Chang, *Biotechnol. J.* **2021**, *16*, 2000124, DOI 10.1002/biot.202000124.

[76] C. H. Chang, P. W. King, M. L. Ghirardi, K. Kim, *Biophys. J.* **2007**, *93*, 3034–3045, DOI 10.1529/biophysj.107.108589.

[77] S. Rumpel et al., *ChemBioChem* **2015**, *16*, 1663–1669, DOI 10.1002/cbic.201500130.

[78] C. Léger, P. Bertrand, *Chem. Rev.* **2008**, *108*, 2379–2438, DOI 10.1021/cr0680742.

[79] F. A. Armstrong, J. N. Butt, A. Sucheta, *Methods Enzymol.* **1993**, *227*, 479–500, DOI 10.1016/0076-6879(93)27020-H.

[80] J. A. Birrell, C. Laurich, E. J. Reijerse, H. Ogata, W. Lubitz, *Biochemistry* **2016**, *55*, 4344–4355, DOI 10.1021/acs.biochem.6b00341.

[81] P.-L. Hagedoorn, L. van der Weel, W. R. Hagen, *J. Vis. Exp.* **2014**, 51611, DOI 10.3791/51611.

[82] P. Leslie Dutton in *Methods in Enzymology*, *Vol. 54*, Academic Press, **1978**, pp. 411–435, DOI 10.1016/S0076-6879(78)54026-3.

[83] G. Zanetti, C. Binda, A. Aliverti, *Encycl. Inorg. Bioinorg. Chem.* **2011**, 1–12, DOI 10.1002/9781119951438.eibc0564.

[84] P. Hosseinzadeh, Y. Lu, *Biochim. Biophys. Acta - Bioenerg.* **2016**, *1857*, 557–581, DOI 10.1016/j.bbabio.2015.08.006.

[85] D. W. Bak, S. J. Elliott, *Curr. Opin. Chem. Biol.* **2014**, *19*, 50–58, DOI 10.1016/j.cbpa.2013.12.015.

[86] J. Liu et al., *Chem. Rev.* **2014**, *114*, 4366–4369, DOI 10.1021/cr400479b.

[87] A. Riedel et al., *J. Biol. Chem.* **1995**, *270*, 30869–30873, DOI 10.1074/jbc.270.52.30869.

[88] P. Gou et al., *Biochemistry* **2006**, *45*, 14389–14396, DOI 10.1021/bi061779d.

[89] J. A. Birrell, K. Morina, H. R. Bridges, T. Friedrich, J. Hirst, *Biochem. J.* **2013**, *456*, 139–146, DOI 10.1042/BJ20130606.

[90] M. Vidakovic, G. Fraczkiewicz, B. C. Dave, R. S. Czernuszewicz, J. P. Germanas, *Biochemistry* **1995**, *34*, 13906–13913, DOI 10.1021/bi00042a023.

[91] H. Uhlmann, R. Bernhardt, *Journal of Biological Chemistry* **1995**, *270*, 29959–29966, DOI 10.1074/jbc.270.50.29959.

[92] A. Aliverti, W. R. Hagen, G. Zanetti, *FEBS Lett.* **1995**, *368*, 220–224, DOI 10.1016/0014-5793(95)00648-S.

[93] K. Chen et al., *J. Biol. Chem.* **1999**, *274*, 36479–36487, DOI 10.1074/jbc.274.51.36479.

[94] L. Mosebach et al., *Photosynth. Res.* **2017**, *134*, 291–306, DOI 10.1007/s11120-017-0408-5.

[95] M. Boehm et al., *Photosynth. Res.* **2016**, *128*, 45–57, DOI 10.1007/s11120-015-0198-6.

[96] V. Fourmond, N. Plumeré, C. Léger, *Nat Rev Chem* **2021**, *5*, 348–360, DOI 10.1038/s41570-021-00268-3.

[97] S. Morra, *Front Microbiol* **2022**, *13*, 853626, DOI 10.3389/fmicb.2022.853626.

[98] J. Meyer, *Cell. Mol. Life Sci.* **2007**, *64*, 1063, DOI 10.1007/s00018-007-6477-4.

[99] J. W. Peters et al., *Biochim. Biophys. Acta - Mol. Cell Res.* **2015**, *1853*, 1350–1369, DOI 10.1016/j.bbamcr.2014.11.021.

[100] J. T. Kleinhaus, F. Wittkamp, S. Yadav, D. Siegmund, U.-P. Apfel, *Chem. Soc. Rev.* **2021**, *50*, 1668–1784, DOI 10.1039/D0CS01089H.

[101] S. Shima, U. Ermler, *Eur. J. Inorg. Chem.* **2011**, *2011*, 963–972, DOI 10.1002/ejic.201000955.

[102] C. Wang, Z. Lai, G. Huang, H.-J. Pan, *Chem. – Eur. J.* **2022**, *28*, e202201499, DOI 10.1002/chem.202201499.

[103] H. Ogata, W. Lubitz, Y. Higuchi, *J Biochem* **2016**, *160*, 251–258, DOI 10.1093/jb/mvw048.

[104] C. Madden et al., *J. Am. Chem. Soc.* **2012**, *134*, 1577–1582, DOI 10.1021/ja207461t.

[105] M. W. Adams, *Biochim. Biophys. Acta BBA - Bioenerg.* **1990**, *1020*, 115–145, DOI 10.1016/0005-2728(90)90044-5.

[106] M. Stephenson, L. H. Stickland, *Biochem J* **1931**, *25*, 205–214, DOI 10.1042/bj0250205.

[107] L. Girbal et al., *Appl Environ Microbiol* **2005**, *71*, 2777–2781, DOI 10.1128/AEM.71.5.2777-2781.2005.

[108] P. W. King, M. C. Posewitz, M. L. Ghirardi, M. Seibert, *J. Bacteriol.* **2006**, *188*, 2163–2172, DOI 10.1128/JB.188.6.2163-2172.2006.

[109] J. M. Kuchenreuther et al., *PLoS ONE* **2010**, *5*, 4–10, DOI 10.1371/journal.pone.0015491.

[110] G. Berggren et al., *Nature* **2013**, *499*, 66–69, DOI 10.1038/nature12239.

[111] J. Esselborn et al., *Nat. Chem. Biol.* **2013**, *9*, 607–609, DOI 10.1038/nchembio.1311.

[112] J. W. Sidabras, S. T. Stripp, *J Biol Inorg Chem* **2023**, *28*, 355–378, DOI 10.1007/s00775-023-01992-5.

[113] K. Wang et al., *Front. Energy Res.* **2021**, *9*, 660399, DOI 10.3389/fenrg.2021.660399.

[114] S. P. Arimbrathodi, M. A. Javed, M. A. Hamouda, A. Aly Hassan, M. E. Ahmed, *Water* **2023**, *15*, 185, DOI 10.3390/w15010185.

[115] P. M. Vignais, B. Billoud, *Chem. Rev.* **2007**, *107*, 4206–4272, DOI 10.1021/cr050196r.

[116] M. Calusinska, T. Happe, B. Joris, A. Wilmotte, *Microbiology* **2010**, *156*, 1575–1588, DOI 10.1099/mic.0.032771-0.

[117] C. Greening et al., *ISME J* **2016**, *10*, 761–777, DOI 10.1038/ismej.2015.153.

[118] H. Land, M. Senger, G. Berggren, S. T. Stripp, *ACS Catal.* **2020**, *10*, 7069–7086, DOI 10.1021/acscatal.0c01614.

[119] D. W. Mulder et al., *Nature* **2010**, *465*, 248–251, DOI 10.1038/nature08993.

[120] C. C. Moser, C. C. Page, R. Farid, P. L. Dutton, *J Bioenerg Biomembr* **1995**, *27*, 263–274, DOI 10.1007/BF02110096.

[121] C. C. Page, C. C. Moser, X. Chen, P. L. Dutton, *Nature* **1999**, *402*, 47–52, DOI 10.1038/46972.

[122] S. Morra, M. Arizzi, F. Valetti, G. Gilardi, *Biochemistry* **2016**, *55*, 5897–5900, DOI 10.1021/acs.biochem.6b00780.

[123] M. Winkler et al., *Nat. Commun.* **2021**, *12*, 756, DOI 10.1038/s41467-020-20861-2.

[124] P. S. Corrigan, J. L. Tirsch, A. Silakov, *J. Am. Chem. Soc.* **2020**, *142*, 12409–12419, DOI 10.1021/jacs.0c04964.

[125] J. B. Therien et al., *Front. Microbiol.* **2017**, *8*, 1–11, DOI 10.3389/fmicb.2017.01305.

[126] A. Möglich, R. A. Ayers, K. Moffat, *Structure* **2009**, *17*, 1282–1294, DOI 10.1016/j.str.2009.08.011.

[127] N. Chongdar et al., *J. Am. Chem. Soc.* **2018**, *140*, 1057–1068, DOI 10.1021/jacs.7b11287.

[128] H. Land et al., *Chem. Sci.* **2020**, *11*, 12789–12801, DOI 10.1039/D0SC03319G.

[129] R. D. Britt, L. Tao, G. Rao, N. Chen, L.-P. Wang, *ACS Bio Med Chem Au* **2021**, *2*, 11–21, DOI 10.1021/acsbiomedchemau.1c00035.

[130] J. Balk, T. A. Schaedler, *Annu. Rev. Plant Biol.* **2014**, *65*, 125–153, DOI 10.1146/annurev-arplant-050213-035759.

[131] K. Esquilin-Lebron, S. Dubrac, F. Barras, J. M. Boyd, *mBio*, *12*, e02425–21, DOI 10.1128/mBio.02425-21.

[132] D. W. Mulder et al., *Biochemistry* **2009**, *48*, 6240–6248, DOI 10.1021/bi9000563.

[133] D. L. M. Suess, R. D. Britt, *Top Catal* **2015**, *58*, 699–707, DOI 10.1007/s11244-015-0412-y.

[134] A. Pagnier et al., *Angew. Chem. Int. Ed.* **2022**, *61*, e202203413, DOI 10.1002/anie.202203413.

[135] E. M. Shepard et al., *Proc. Natl. Acad. Sci.* **2010**, *107*, 10448–10453, DOI 10.1073/pnas.1001937107.

[136] J. M. Kuchenreuther et al., *Science* **2013**, *342*, 472–475, DOI 10.1126/science.1241859.

[137] J. M. Kuchenreuther et al., *Science* **2014**, *343*, 424–427, DOI 10.1126/science.1246572.

[138] P. Dinis et al., *Proc Natl Acad Sci U S A* **2015**, *112*, 1362–1367, DOI 10.1073/pnas.1417252112.

[139] G. Rao, N. Chen, D. A. Marchiori, L.-P. Wang, R. D. Britt, *Biochemistry* **2022**, *61*, 107–116, DOI 10.1021/acs.biochem.1c00619.

[140] L. Tao et al., *J. Am. Chem. Soc.* **2020**, *142*, 10841–10848, DOI 10.1021/jacs.0c03802.

[141] R. Rohac et al., *J. Am. Chem. Soc.* **2021**, *143*, 8499–8508, DOI 10.1021/jacs.1c03367.

[142] Y. Zhang, L. Tao, T. J. Woods, R. D. Britt, T. B. Rauchfuss, *J. Am. Chem. Soc.* **2022**, *144*, 1534–1538, DOI 10.1021/jacs.1c12506.

[143] G. Rao, L. Tao, R. D. Britt, *Chem. Sci.* **2020**, *11*, 1241–1247, DOI 10.1039/C9SC05900H.

[144] B. Balci et al., *Chem. Commun.* **2023**, *59*, 8929–8932, DOI 10.1039/D3CC02169F.

[145] J. Esselborn et al., *Chem. Sci.* **2016**, *7*, 959–968, DOI 10.1039/c5sc03397g.

[146] O. Lampret et al., *Proc Natl Acad Sci U S A* **2019**, *116*, 15802–15810, DOI 10.1073/pnas.1908121116.

[147] S. A. Freibert et al., *Methods Enzymol.* **2018**, *599*, 197–226, DOI 10.1016/bs.mie.2017.11.034.

[148] G. Caserta et al., *Nat. Chem. Biol.* **2017**, *13*, 779–784, DOI 10.1038/nchembio.2385.

[149] B. Németh, C. Esmieu, H. J. Redman, G. Berggren, *Dalton Trans.* **2019**, *48*, 5978–5986, DOI 10.1039/C8DT04294B.

[150] J. F. Siebel et al., *Biochemistry* **2015**, *54*, 1474–1483, DOI 10.1021/bi501391d.

[151] J. Duan et al., *ACS Catal.* **2019**, *9*, 9140–9149, DOI 10.1021/acscatal.9b02203.

[152] A. Adamska-Venkatesh et al., *Phys. Chem. Chem. Phys.* **2015**, *17*, 5421–5430, DOI 10.1039/c4cp05426a.

[153] A. Adamska-Venkatesh et al., *J. Am. Chem. Soc.* **2014**, *136*, 11339–11346, DOI 10.1021/ja503390c.

[154] Y. Nicolet, C. Piras, P. Legrand, C. E. Hatchikian, J. C. Fontecilla-Camps, *Structure* **1999**, *7*, 13–23, DOI 10.1016/S0969-2126(99)80005-7.

[155] C. V. Popescu, E. Münck, *J. Am. Chem. Soc.* **1999**, *121*, 7877–7884, DOI 10.1021/ja991243y.

[156] A. Silakov, E. J. Reijerse, S. P. J. Albracht, E. C. Hatchikian, W. Lubitz, *J. Am. Chem. Soc.* **2007**, *129*, 11447–11458, DOI 10.1021/ja072592s.

[157] J. W. Tye et al., *Inorg. Chem.* **2005**, *44*, 5550–5552, DOI 10.1021/ic050402d.

[158] M. L. Singleton, N. Bhuvanesh, J. H. Reibenspies, M. Y. Darensbourg, *Angew. Chem. Int. Ed.* **2008**, *47*, 9492–9495, DOI 10.1002/anie.200803939.

[159] M. Haumann, S. T. Stripp, *Acc. Chem. Res.* **2018**, *51*, 1755–1763, DOI 10.1021/acs.accounts.8b00109.

[160] A. S. Pandey, T. V. Harris, L. J. Giles, J. W. Peters, R. K. Szilagyi, *J. Am. Chem. Soc.* **2008**, *130*, 4533–4540, DOI 10.1021/ja711187e.

[161] A. J. Cornish, K. Gärtner, H. Yang, J. W. Peters, E. L. Hegg, *J. Biol. Chem.* **2011**, *286*, 38341–38347, DOI 10.1074/jbc.M111.254664.

[162] J. Duan et al., *Nat Commun* **2018**, *9*, 4726, DOI 10.1038/s41467-018-07140-x.

[163] C. Baffert et al., *Angew. Chem. Int. Ed.* **2008**, *47*, 2052–2054, DOI 10.1002/anie.200704313.

[164] J. Duan et al., *Angew. Chem. Int. Ed.* **2023**, *1*, e202216903, DOI 10.1002/anie.202216903.

[165] G. Goldet et al., *J. Am. Chem. Soc.* **2009**, *131*, 14979–14989, DOI 10.1021/ja905388j.

[166] A. Kubas et al., *Nat. Chem.* **2017**, *9*, 88–95, DOI 10.1038/nchem.2592.

[167] C. Lambertz et al., *Journal of Biological Chemistry* **2011**, *286*, 40614–40623, DOI 10.1074/jbc.M111.283648.

[168] B. J. Lemon, J. W. Peters, *Biochemistry* **1999**, *38*, 12969–12973, DOI 10.1021/bi9913193.

[169] P. Rodríguez-Maciá et al., *J. Am. Chem. Soc.* **2018**, *140*, 9346–9350, DOI 10.1021/jacs.8b04339.

[170] S. Stripp, O. Sanganas, T. Happe, M. Haumann, *Biochemistry* **2009**, *48*, 5042–5049, DOI 10.1021/bi900010b.

[171] Y. Nicolet, B. J. Lemon, J. C. Fontecilla-Camps, J. W. Peters, *Trends in Biochemical Sciences* **2000**, *25*, 138–143, DOI 10.1016/S0968-0004(99)01536-4.

[172] T. Hiromoto, E. Warkentin, J. Moll, U. Ermler, S. Shima, *Angew. Chem. Int. Ed.* **2009**, *48*, 6457–6460, DOI 10.1002/anie.200902695.

[173] S. Mebs et al., *Biochim. Biophys. Acta - Bioenerg.* **2018**, *1859*, 28–41, DOI 10.1016/j.bbabio.2017.09.003.

[174] C. Sommer et al., *J. Am. Chem. Soc.* **2017**, *139*, 1440–1443, DOI 10.1021/jacs.6b12636.

[175] M. Winkler et al., *Nat. Commun.* **2017**, *8*, 16115, DOI 10.1038/ncomms16115.

[176] K. Laun et al., *Dalton Trans.* **2021**, *50*, 3641–3650, DOI 10.1039/D1DT00110H.

[177] L. S. Mészáros et al., *Chem. Sci.* **2020**, *11*, 4608–4617, DOI DOI:10.1039/d0sc00512f.

[178] M. L. K. Sanchez et al., *J. Am. Chem. Soc.* **2019**, *141*, 16064–16070, DOI 10.1021/jacs.9b08348.

[179] M. Senger et al., *Angew. Chem. Int. Ed.* **2017**, *56*, 16503–16506, DOI 10.1002/anie.201709910.

[180] M. Senger et al., *Phys. Chem. Chem. Phys.* **2018**, *20*, 3128–3140, DOI 10.1039/c7cp04757f.

[181] F. Wittkamp, M. Senger, S. T. Stripp, U.-P. Apfel, *Chem. Commun.* **2018**, *54*, 5934–5942, DOI 10.1039/C8CC01275J.

[182] J. A. Birrell, P. Rodríguez-Maciá, E. J. Reijerse, M. A. Martini, W. Lubitz, *Coordination Chemistry Reviews* **2021**, *449*, 214191, DOI 10.1016/j.ccr.2021.214191.

[183] D. W. Mulder et al., *J. Am. Chem. Soc.* **2013**, *135*, 6921–6929, DOI 10.1021/ja4000257.

[184] M. Senger et al., *Proc. Natl. Acad. Sci. U. S. A.* **2016**, *113*, 8454–8459, DOI 10.1073/pnas.1606178113.

[185] A. S. Pereira, P. Tavares, I. Moura, J. J. Moura, B. H. Huynh, *J. Am. Chem. Soc.* **2001**, *123*, 2771–2782, DOI 10.1021/ja003176+.

[186] M. Bruschi, C. Greco, P. Fantucci, L. De Gioia, *Inorg. Chem.* **2008**, *47*, 6056–6071, DOI 10.1021/ic8006298.

[187] A. T. Fiedler, T. C. Brunold, *Inorg. Chem.* **2005**, *44*, 9322–9334, DOI 10.1021/ic050946f.

[188] G. Rao, R. D. Britt, *Inorg. Chem.* **2018**, *57*, 10935–10944, DOI 10.1021/acs.inorgchem.8b01557.

[189] W. K. Myers et al., *J. Am. Chem. Soc.* **2014**, *136*, 12237–12240, DOI 10.1021/ja507046w.

[190] M. Razavet et al., *Chem. Commun.* **2002**, *2*, 700–701, DOI 10.1039/b111613b.

[191] A. Silakov, B. Wenk, E. Reijerse, S. P. Albracht, W. Lubitz, *J. Biol. Inorg. Chem.* **2009**, *14*, 301–313, DOI 10.1007/s00775-008-0449-5.

[192] M. Senger et al., *Inorg. Chem.* **2022**, *61*, 10036–10042, DOI 10.1021/acs.inorgchem.2c00954.

[193] S. Mebs et al., *Inorg. Chem.* **2019**, *58*, 4000–4013, DOI 10.1021/acs.inorgchem.9b00100.

[194] B. Bennett, B. J. Lemon, J. W. Peters, *Biochemistry* **2000**, *39*, 7455–7460, DOI 10.1021/bi992583z.

[195] A. Silakov, C. Kamp, E. Reijerse, T. Happe, W. Lubitz, *Biochemistry* **2009**, *48*, 7780–7786, DOI 10.1021/bi9009105.

[196] E. Reijerse, J. A. Birrell, W. Lubitz, *J. Phys. Chem. Lett.* **2020**, *11*, 4597–4602, DOI 10.1021/acs.jpclett.0c01352.

[197] K. Laun et al., *Molecules* **2018**, *23*, 1–13, DOI 10.3390/molecules23071669.

[198] S. Zilberman, E. I. Stiefel, M. H. Cohen, R. Car, *J. Phys. Chem. B* **2006**, *110*, 7049–7057, DOI 10.1021/jp056551z.

[199] J. Telser, M. J. Benecky, M. W. Adams, L. E. Mortenson, B. M. Hoffman, *J. Biol. Chem.* **1986**, *261*, 13536–13541.

[200] J. Telser, M. J. Benecky, M. W. Adams, L. E. Mortenson, B. M. Hoffman, *J. Biol. Chem.* **1987**, *262*, 6589–6594, DOI 10.1016/s0021-9258(18)48282-8.

[201] C. Greco, M. Bruschi, P. Fantucci, U. Ryde, L. De Gioia, *J. Am. Chem. Soc.* **2011**, *133*, 18742–18749, DOI 10.1021/ja205542k.

[202] M. A. Martini et al., *Chem. Sci.* **2023**, *14*, 2826–2838, DOI 10.1039/D2SC06098A.

[203] S. Katz et al., *Chem. Sci.* **2016**, *7*, 6746–6752, DOI 10.1039/C6SC01098A.

[204] B. Németh et al., *J Biol Inorg Chem* **2020**, *25*, 777–788, DOI 10.1007/s00775-020-01799-8.

[205] Y. Nicolet et al., *J. Am. Chem. Soc.* **2001**, *123*, 1596–1601, DOI 10.1021/ja0020963.

[206] S. Mebs et al., *J. Am. Chem. Soc.* **2017**, *139*, 12157–12160, DOI 10.1021/jacs.7b07548.

[207] E. J. Reijerse et al., *J. Phys. Chem. Lett.* **2019**, *10*, 6794–6799, DOI 10.1021/acs.jpclett.9b02354.

[208] P. E. M. Siegbahn, R.-Z. Liao, *J. Phys. Chem. A* **2020**, *124*, 10540–10549, DOI 10.1021/acs.jpca.0c08705.

[209] J. A. Birrell et al., *J. Am. Chem. Soc.* **2020**, *142*, 222–232, DOI 10.1021/jacs.9b09745.

[210] S. T. Stripp, S. Mebs, M. Haumann, *Inorg. Chem.* **2020**, *59*, 16474–16488, DOI 10.1021/acs.inorgchem.0c02316.

[211] A. Adamska et al., *Angew. Chem. Int. Ed.* **2012**, *51*, 11458–11462, DOI 10.1002/anie.201204800.

[212] C. Lorent et al., *J. Am. Chem. Soc.* **2020**, *142*, 5493–5497, DOI 10.1021/jacs.9b13075.

[213] D. W. Mulder et al., *J. Am. Chem. Soc.* **2014**, *136*, 15394–15402, DOI 10.1021/ja508629m.

[214] D. W. Mulder, Y. Guo, M. W. Ratzloff, P. W. King, *J. Am. Chem. Soc.* **2017**, *139*, 83–86, DOI 10.1021/jacs.6b11409.

[215] E. J. Reijerse et al., *J. Am. Chem. Soc.* **2017**, *139*, 4306–4309, DOI 10.1021/jacs.7b00686.

[216] P. Rodríguez-Maciá, N. Breuer, S. Debeer, J. A. Birrell, *ACS Catal.* **2020**, *10*, 13084–13095, DOI 10.1021/acscatal.0c02771.

[217] J. Cohen, K. Kim, P. King, M. Seibert, K. Schulten, *Structure* **2005**, *13*, 1321–1329, DOI 10.1016/j.str.2005.05.013.

[218] A. R. Finkelmann, M. T. Stiebritz, M. Reiher, *Chem. Sci.* **2014**, *5*, 215–221, DOI 10.1039/c3sc51700d.

[219] M. T. Stiebritz, M. Reiher, *Inorg. Chem.* **2009**, *48*, 7127–7140, DOI 10.1021/ic9002127.

[220] K. D. Swanson et al., *J. Am. Chem. Soc.* **2015**, *137*, 1809–1816, DOI 10.1021/ja510169s.

[221] J. Esselborn, L. Kertess, U. P. Apfel, E. Hofmann, T. Happe, *J. Am. Chem. Soc.* **2019**, *141*, 17721–17728, DOI 10.1021/jacs.9b07808.

[222] M. K. Bruska, M. T. Stiebritz, M. Reiher, *J. Am. Chem. Soc.* **2011**, *133*, 20588–20603, DOI 10.1021/ja209165r.

[223] V. Fourmond et al., *Nat. Chem.* **2014**, *6*, 336–342, DOI 10.1038/nchem.1892.

[224] C. Orain et al., *J. Am. Chem. Soc.* **2015**, *137*, 12580–12587, DOI 10.1021/jacs.5b06934.

[225] W. Roseboom, A. L. De Lacey, V. M. Fernandez, E. C. Hatchikian, S. P. Albracht, *J. Biol. Inorg. Chem.* **2006**, *11*, 102–118, DOI 10.1007/s00775-005-0040-2.

[226] P. Rodríguez-Maciá et al., *Angew. Chem. Int. Ed.* **2020**, *59*, 16786–16794, DOI 10.1002/anie.202005208.

[227] C. Felbek et al., *ACS Catal.* **2021**, *11*, 15162–15176, DOI 10.1021/acscatal.1c04838.

[228] B. H. Huynh, M. H. Czechowski, H. J. Kruger, *Proc. Natl. Acad. Sci. U. S. A.* **1984**, *81*, 3728–3732, DOI 10.1073/pnas.81.12.3728.

[229] P. P. Liebgott et al., *Nat. Chem. Biol.* **2010**, *6*, 63–70, DOI 10.1038/nchembio.276.

[230] J. H. Artz et al., *J. Am. Chem. Soc.* **2020**, *142*, 1227–1235, DOI 10.1021/jacs.9b08756.

[231] A. Rutz et al., *ACS Catal.* **2022**, 856–865, DOI 10.1021/acscatal.2c04031.

[232] A. Fasano, A. Bailly, J. Wozniak, V. Fourmond, C. Léger, Catalytic Bias and Redox-Driven Inactivation of Ancestral FeFe Hydrogenases from Group B2, **2023**, DOI 10.1101/2023.06.23.541094.

[233] G. Caserta et al., *J. Am. Chem. Soc.* **2018**, *140*, 5516–5526, DOI 10.1021/jacs.8b01689.

[234] T. Lautier et al., *Faraday Discuss.* **2011**, *148*, 385–407, DOI 10.1039/c004099c.

[235] S. V. Hexter, F. Grey, T. Happe, V. Climent, F. A. Armstrong, *Proc. Natl. Acad. Sci. U.S.A.* **2012**, *109*, 11516–11521, DOI 10.1073/pnas.1204770109.

[236] C. Gauquelin et al., *Biochim. Biophys. Acta - Bioenerg.* **2018**, *1859*, 69–77, DOI 10.1016/j.bbabio.2017.08.010.

[237] P. Rodríguez-Maciá et al., *J. Am. Chem. Soc.* **2017**, *139*, 15122–15134, DOI 10.1021/jacs.7b08193.

[238] E. K. Zavoisky, *J. Phys.* **1944**, *9*, 211–216.

[239] K. M. Salikhov, N. E. Zavoiskaya, *Reson* **2015**, *20*, 963–968, DOI 10.1007/s12045-015-0264-6.

[240] A. Schweiger, G. Jeschke, A. Schweiger, G. Jeschke, *Principles of Pulse Electron Paramagnetic Resonance*, Oxford University Press, Oxford, New York, **2001**.

[241] J. A. Weil, J. R. Bolton, *Electron Paramagnetic Resonance: Elementary Theory and Practical Applications*, 2nd ed, Wiley & Sons Ltd, Hoboken, N.J, **2007**.

[242] D. Goldfarb, *EPR Spectroscopy: Fundamentals and Methods*, Wiley & Sons Ltd, **2018**.

[243] W. Gerlach, O. Stern, *Z. Für Phys.* **1922**, *9*, 349–352, DOI http://dx.doi.org/10.1007/BF01326984.

[244] H. C. Ohanian, *Am. J. Phys.* **1986**, *54*, 500–505, DOI 10.1119/1.14580.

[245] A. Abragam, M. H. L. Pryce, *Proc. R. Soc. Lond. Ser. Math. Phys. Eng. Sci.* **1951**, *205*, 135–153, DOI 10.1098/rspa.1951.0022.

[246] M. Mostafanejad, *Int. J. Quantum Chem.* **2014**, *114*, 1495–1512, DOI 10.1002/qua.24721.

[247] B. Odom, D. Hanneke, B. D'Urso, G. Gabrielse, *Phys. Rev. Lett.* **2006**, *97*, 030801, DOI 10.1103/PhysRevLett.97.030801.

[248] N. S. Hosmane in *Advanced Inorganic Chemistry*, (Ed.: N. S. Hosmane), Academic Press, Boston, **2017**, pp. 3–13, DOI 10.1016/B978-0-12-801982-5.00001-1.

[249] D. T. Petasis, M. P. Hendrich in *Iron-Sulfur Clusters in Chemistry and Biology: Characterization, Properties and Applications*, *Vol. 1*, **2017**, pp. 135–162, DOI 10.1515/9783110480436-005.

[250] A. Bencini, D. Gatteschi, *Comments on Inorganic Chemistry* **1985**, *4*, 99–111, DOI 10.1080/02603598508072254.

[251] B. R. McGarvey, *J. Phys. Chem.* **1967**, *71*, 51–66, DOI 10.1021/j100860a007.

[252] A. Bencini, D. Gatteschi, *Electron Paramagnetic Resonance of Exchange Coupled Systems*, *Vol. 53*, Springer Berlin Heidelberg, **1990**, DOI 10.1007/978-3-642-74599-7.

[253] G. R. Eaton, S. S. Eaton in *Spin Labeling: Theory and Applications*, (Eds.: L. J. Berliner, J. Reuben), Biological Magnetic Resonance, Springer US, Boston, MA, **1989**, pp. 339–397, DOI 10.1007/978-1-4613-0743-3_7.

[254] P. J. González, M. G. Rivas, A. L. Pérez, C. D. Brondino, *Journal of Magnetic Resonance Open* **2023**, *16–17*, 100117, DOI 10.1016/j.jmro.2023.100117.

[255] A. Fournel et al., *J. Chem. Phys.* **1998**, *109*, 10905–10913, DOI 10.1063/1.477786.

[256] G. Jeschke in *ESR Spectroscopy in Membrane Biophysics*, Biological Magnetic Resonance, Springer US, Boston, MA, **2007**, pp. 17–47, DOI 10.1007/978-0-387-49367-1_2.

[257] P. E. Spindler, P. Schöps, A. M. Bowen, B. Endeward, T. F. Prisner, *eMagRes* **2016**, *5*, 1477–1492, DOI 10.1002/9780470034590.emrstm1520.

[258] J. S. Hyde, M. Pasenkiewicz-Gierula, A. Jesmanowicz, W. E. Antholine, *Appl Magn Reson* **1990**, *1*, 483–496, DOI 10.1007/BF03166028.

[259] E. L. Hahn, *Phys. Rev.* **1950**, *80*, 580–594, DOI 10.1103/PhysRev.80.580.

[260] G. Jeschke, Einführung in Die ESR-Spektroskopie: Ein Vorlesungsskript, **2006**.

[261] D. M. Murphy, R. D. Farley, *Chem. Soc. Rev.* **2006**, *35*, 249–268, DOI 10.1039/b500509b.

[262] E. R. Davies, *Physics Letters A* **1974**, *47*, 1–2, DOI 10.1016/0375-9601(74)90078-4.

[263] W. B. Mims, *Proc. R. Soc. Lond. Ser. Math. Phys. Sci.* **1965**, *283*, 452–457, DOI 10.1098/rspa.1965.0034.

[264] G. Jeschke, Y. Polyhach, *Phys. Chem. Chem. Phys.* **2007**, *9*, 1895, DOI 10.1039/b614920k.

[265] O. Schiemann, T. F. Prisner, *Quart. Rev. Biophys.* **2007**, *40*, 1–53, DOI 10.1017/S003358350700460X.

[266] G. Jeschke, M. Pannier, A. Godt, H. Spiess, *Chemical Physics Letters* **2000**, *331*, 243–252, DOI 10.1016/S0009-2614(00)01171-4.

[267] G. Jeschke, *Annu. Rev. Phys. Chem.* **2012**, *63*, 419–446, DOI 10.1146/annurev-physchem-032511-143716.

[268] R. Ward, O. Schiemann in *Encyclopedia of Biophysics*, Springer, Berlin, Heidelberg, **2013**, pp. 1116–1123, DOI 10.1007/978-3-642-16712-6_662.

[269] B. E. Bode et al., *J. Am. Chem. Soc.* **2007**, *129*, 6736–6745, DOI 10.1021/ja065787t.

[270] P. Bertrand, P. Camensuli, C. More, B. Guigliarelli, *J. Am. Chem. Soc* **1996**, *118*, 1426–1434.

[271] L. Noodleman, T. Lovell, T. Liu, F. Himo, R. A. Torres, *Curr. Opin. Chem. Biol.* **2002**, *6*, 259–273, DOI 10.1016/S1367-5931(02)00309-5.

[272] H. Beinert, M. C. Kennedy, C. D. Stout, *Chem. Rev.* **1996**, *96*, 2335–2373, DOI 10.1021/cr950040z.

[273] L. Noodleman, C. Y. Peng, D. A. Case, J. M. Mouesca, *Coord. Chem. Rev.* **1995**, *144*, 199–244, DOI 10.1016/0010-8545(95)07011-L.

[274] T. Ichiye, *Charact. Prop. Appl.* **2017**, *1*, 11–19, DOI 10.1515/9783110480436-002.

[275] B. A. Skeel, D. L. M. Suess, *J. Am. Chem. Soc.* **2023**, *145*, 10376–10395, DOI 10.1021/jacs.3c02412.

[276] W. R. Hagen, *J. Biol. Inorg. Chem.* **2018**, *23*, 623–634, DOI 10.1007/s00775-018-1543-y.

[277] R. Cammack, F. MacMillan in *Metals in Biology: Applications of High-Resolution EPR to Metalloenzymes*, (Eds.: G. Hanson, L. Berliner), Biological Magnetic Resonance, Springer, New York, NY, **2010**, pp. 11–44, DOI 10.1007/978-1-4419-1139-1.

[278] C. Achim, E. L. Bominaar, J. Meyer, J. Peterson, E. Münck, *J. Am. Chem. Soc.* **1999**, *121*, 3704–3714, DOI 10.1021/ja983980k.

[279] B. Guigliarelli, P. Bertrand, *Adv. Inorg. Chem.* **1999**, *47*, 421–497, DOI 10.1016/S0898-8838(08)60084-7.

[280] Y. Guo, J. Li in *Characterization, Properties and Applications*, *Vol. 1*, **2017**, pp. 77–134, DOI 10.1515/9783110480436-004.

[281] W. R. Hagen, *Dalton Trans.* **2006**, 4415–4434, DOI 10.1039/b608163k.

[282] L. Kertess et al., *Chem. Sci.* **2017**, *8*, 8127–8137, DOI 10.1039/c7sc03444j.

[283] V. Engelbrecht et al., *International Journal of Hydrogen Energy* **2021**, *46*, 7165–7175, DOI 10.1016/j.ijhydene.2020.11.231.

[284] S. Stoll, A. Schweiger, *J. Magn. Reson.* **2006**, *178*, 42–55, DOI 10.1016/j.jmr.2005.08.013.

[285] I. Czech, A. Silakov, W. Lubitz, T. Happe, *FEBS Lett.* **2010**, *584*, 638–642, DOI 10.1016/j.febslet.2009.12.016.

[286] N. A. Sieracki, H. J. Hwang, M. K. Lee, D. K. Garner, Y. Lu, *Chem. Commun.* **2008**, 823–825, DOI 10.1039/b714446f.

[287] A. C. Brown, D. L. M. Suess, *J. Am. Chem. Soc.* **2023**, *145*, 2075–2080, DOI 10.1021/jacs.2c13126.

[288] P. Berto et al., *Biochim. Biophys. Acta - Bioenerg.* **2012**, *1817*, 2149–2157, DOI 10.1016/j.bbabio.2012.09.004.

[289] D. F. Becker, U. Leartsakulpanich, K. K. Surerus, J. G. Ferry, S. W. Ragsdale, *J. Biol. Chem.* **1998**, *273*, 26462–26469, DOI 10.1074/jbc.273.41.26462.

[290] D. P. Bhave et al., *J. Biol. Chem.* **2011**, *286*, 1216–1226, DOI 10.1074/jbc.M110.193722.

[291] S. W. Ragsdale, P. A. Lindahl, E. Münck, *J. Biol. Chem.* **1987**, *262*, 14289–14297, DOI 10.1016/S0021-9258(18)47936-7.

[292] G. S. Wilson in *Methods in Enzymology*, Biomembranes - Part E: Biological Oxidations, Academic Press, **1978**, pp. 396–410, DOI 10.1016/S0076-6879(78)54025-1.

[293] M. A. Martini et al., *J. Am. Chem. Soc.* **2021**, *143*, 18159–18171, DOI 10.1021/jacs.1c07322.

[294] B. Németh, H. Land, A. Magnuson, A. Hofer, G. Berggren, *J. Biol. Chem.* **2020**, *295*, 11891–11901, DOI 10.1074/jbc.RA119.011419.

[295] M. K. Fenwick et al., *Nat Commun* **2015**, *6*, 6480, DOI 10.1038/ncomms7480.

[296] F. Vallese et al., *J Biol Chem* **2012**, *287*, 36544–36555, DOI 10.1074/jbc.M112.388900.

[297] J. M. Kuchenreuther, R. D. Britt, J. R. Swartz, *PLOS ONE* **2012**, *7*, e45850, DOI 10.1371/journal.pone.0045850.

[298] X. Brazzolotto et al., *J. Biol. Chem.* **2006**, *281*, 769–774, DOI 10.1074/jbc.M510310200.

[299] L. Cendron et al., *J Biol Chem* **2011**, *286*, 43944–43950, DOI 10.1074/jbc.M111.281956.

[300] N. Joshi et al., *FEBS Lett.* **2012**, *586*, 3939–3943, DOI 10.1016/j.febslet.2012.09.028.

[301] E. M. Shepard, A. S. Byer, J. N. Betz, J. W. Peters, J. B. Broderick, *Biochemistry* **2016**, *55*, 3514–3527, DOI 10.1021/acs.biochem.6b00528.

[302] I. Czech et al., *FEBS Lett.* **2011**, *585*, 225–230, DOI 10.1016/j.febslet.2010.11.052.

[303] M. Albertini et al., *Top. Catal.* **2015**, *58*, 708–718, DOI 10.1007/s11244-015-0413-x.

[304] R. Haas et al., *ChemBioChem* **2023**, *24*, e202300222, DOI 10.1002/cbic.202300222.

[305] A. G. Scott et al., *Dalton Trans.* **2018**, *47*, 9521–9535, DOI 10.1039/c8dt01654b.

[306] E. M. Shepard et al., *Biochemistry* **2017**, *56*, 3234–3247, DOI 10.1021/acs.biochem.7b00169.

[307] R. E. Duderstadt, C. R. Staples, P. S. Brereton, M. W. Adams, M. K. Johnson, *Biochemistry* **1999**, *38*, 10585–10593, DOI 10.1021/bi990670l.

[308] R. C. Conover et al., *J. Biol. Chem.* **1990**, *265*, 8533–8541, DOI 10.1016/S0021-9258(19)38921-5.

[309] S. Agarwalla, R. M. Stroud, B. J. Gaffney, *J. Biol. Chem.* **2004**, *279*, 34123–34129, DOI 10.1074/jbc.M405702200.

[310] T. Iwasaki et al., *J. Biol. Chem.* **2002**, *277*, 39642–39648, DOI 10.1074/jbc.M207312200.

[311] P. S. Corrigan, S. H. Majer, A. Silakov, *J. Am. Chem. Soc.* **2023**, *145*, 11033–11044, DOI 10.1021/jacs.2c13458.

[312] D. Brandis, MA thesis, TU Dortmund, **2021**.

[313] P. Zanello, *J. Struct. Biol.* **2018**, *202*, 264–274, DOI 10.1016/j.jsb.2018.03.008.

Acknowledgments

First and foremost, I am deeply grateful to my supervisor Prof. Müge Kasanmascheff. Despite her lasting passion for RNR, she worked her way into the realms of FeS clusters and [FeFe]-hydrogenases providing continuous support throughout my thesis journey. Her confidence in my abilities greatly contributed to my personal and academic development. I am thankful for her insightful ideas and contagious dedication throughout all projects, while valuing my opinion and giving me free rein for independent research. Furthermore, she facilitated my participation in numerous conferences to engage with the scientific community.

My sincere thanks goes to Prof. Thomas Happe for the possibility to investigate a multitude of new and exciting FeS proteins. This fruitful collaboration is also owed to his past and present group members providing a constant stream of samples, ideas and stimulating discussions. Therefore, I would especially like to thank Alexander Günzel, Andreas Rutz, Astrit Veliju, Kristina Liedtke, Claudia Brocks, Feng Zheng, Martin Winkler, and Vera Engelbrecht, without whom this thesis would not have been possible.

A special thanks goes to Dr. Yury Kutin, who patiently answered every possible EPR-related question. His thoughtful and critical examinations greatly contributed to the quality of my studies. Moreover, I want to thank my extremely dedicated master student Dörte Brandis, who measured countless spectra and was a great help in the lab. I am also very grateful for my fellow labmembers, especially Shari Meichsner, Simon Schumann and Victor Selve, for all the (non-)scientific conversations, encouragements, and celebrations of the ups and downs.

Moreover, I would like to acknowledge the generous financial support provided by the Cluster of Excellence RESOLV funded by the Deutsche Forschungsgemeinschaft under Germany's Excellence Strategy - EXC-2033 - Projektnummer 390677874, which promoted my scientific development and allowed me to present my research nationally and internationally.

I also thank MOSBRI and the BIP at the National Center for Scientific Research in Marseille, especially Emilien Etienne and Guillaume Gerbaud, for their warm welcome, support, and access to their resources and facilities, which have been very rewarding.

I also want to thank my friends, especially the WG39 crew, who always had an open ear and beer for me.

Moreover, I am deeply grateful for my partner in crime, Justin, for his everlasting support and who always kept a cool head while I was loosing mine.

Als letztes möchte ich mich bei meiner Familie bedanken, insbesondere bei meinen Omis Gertrud und Helene, meinem Opa Manfred, meiner Tante Bine, meinen Eltern, und meinen Brüdern, die mich mein ganzes Leben lang ermutigten, unterstützten und immer an mich geglaubt haben.